

*Nasa CR 65534<sup>4</sup>*

FR66-14-117

FINAL REPORT  
FOR  
A STUDY OF APOLLO  
ANTENNA AND SIGNAL  
PERFORMANCE IN CERTAIN  
ATMOSPHERES

CONTRACT NO. NAS9-5228

PREPARED BY  
HUGHES AIRCRAFT COMPANY  
GROUND SYSTEMS GROUP  
FULLERTON, CALIFORNIA

**LIBRARY COPY**

MAY 3 1966

MANNED SPACECRAFT CENTER  
HOUSTON, TEXAS

GPO PRICE \$ \_\_\_\_\_

CFSTI PRICE(S) \$ \_\_\_\_\_

Hard copy (HC) 3.25

Microfiche (MF) 1.00

ff 653 July 65

FOR  
NASA/MANNED SPACECRAFT CENTER  
HOUSTON, TEXAS

**N66 39935**

FACILITY FORM 802

(ACCESSION NUMBER)

176

(PAGES)

CR-65534

(NASA CR OR TMX OR AD NUMBER)

(THRU)

1

(CODE)

(CATEGORY)

07

FR66-14-117

FINAL REPORT  
FOR  
A STUDY OF APOLLO  
ANTENNA AND SIGNAL  
PERFORMANCE IN CERTAIN  
ATMOSPHERES

CONTRACT NO. NAS9-5228

PREPARED BY  
HUGHES AIRCRAFT COMPANY  
GROUND SYSTEMS GROUP  
FULLERTON, CALIFORNIA

FOR  
NASA/MANNED SPACECRAFT CENTER  
HOUSTON, TEXAS

21 April 1966

## ABSTRACT

This report covers a study of the factors affecting the polarization and signal transfer of the Apollo Telecommunications link. The effect of the various factors upon the performance of the Apollo system are considered. This is accomplished by first making a comprehensive literature search to determine what information is currently available which is applicable to the Apollo link. From this basis additional analysis and some experimental work is carried out on those problems not covered in the literature.

It was found that the principal factors limiting performance of the telecommunications link are: 1) Off axis ellipticity of the spacecraft antennas resulting in power transfer loss; 2) Multipath propagation at low angles resulting in boresight tracking errors and increased noise which limits the region of track and communication near the horizon; 3) Plasma sheath formation during reentry.

Details analysis of the first two factors is made, and some consideration given to means of reducing these effects for improved system performance.

## CONTENTS

	Page
1. INTRODUCTION .....	1
1.1 SCOPE AND PURPOSE.....	1
1.2 SUMMARY OF WORK PERFORMED .....	1
2. LITERATURE SEARCH.....	3
2.1 SPACECRAFT .....	3
2.2 GROUND SYSTEM .....	4
2.3 MEDIUM .....	4
2.4 COMMUNICATION SYSTEM .....	5
3. PARAMETER ANALYSIS.....	7
3.1 WAVE POLARIZATION CHARACTERISTICS.....	7
3.2 POWER LOSS BETWEEN ARBITRARILY POLARIZED ANTENNAS .....	14
3.3 IONOSPHERIC POLARIZATION EFFECTS .....	16
3.3.1 Faraday Rotation .....	16
3.3.2 Effect on Polarization Ellipticity.....	24
3.4 MULTIPATH .....	25
3.4.1 Pattern Analysis .....	25
3.4.2 Experimental Measurement of Boresight Errors .....	30
3.4.3 Signal/Noise Effects.....	30
3.5 PLASMA .....	40



## CONTENTS (Continued)

	Page
4. SYSTEM PERFORMANCE ANALYSIS .....	43
4.1 EFFECT OF POLARIZATION PARAMETERS ON TRACKING .....	43
4.1.1 Mission Geometry .....	43
4.1.2 Phase Lock Loop Performance as a Function of Spacecraft Motion .....	50
4.1.3 Effect of Phase Errors on Angle Tracking .....	56
4.1.4 Range Rate Errors .....	60
4.2 EFFECT OF POLARIZATION PARAMETERS ON RANGING .....	62
4.2.1 Spacecraft Phase Errors .....	62
4.2.2 Ranging Errors .....	63
5. CONCLUSIONS AND RECOMMENDATIONS .....	69
5.1 CONCLUSIONS .....	69
5.2 METHODS FOR IMPROVING SYSTEM PERFORMANCE .....	70
5.3 RECOMMENDATIONS .....	77
6. REFERENCES .....	79
7. BIBLIOGRAPHY .....	81
7.1 SPACECRAFT .....	81
7.2 GROUND SYSTEM .....	82
7.3 MEDIUM .....	83
7.4 COMMUNICATION SYSTEM .....	85
8. APPENDICES .....	

## ILLUSTRATIONS

Figure		Page
1	Polarization Ellipse . . . . .	8
2	Cross Polarization vs Ellipticity . . . . .	12
3	Ellipticity vs Phase Between Two Linear Polarized Components .	
4	Polarization Patterns . . . . .	15
5	Plane Wave in Ionosphere . . . . .	16
6	Electron Density versus Height . . . . .	20
7	Earth's Magnetic Field . . . . .	21
8	Faraday Rotation Geometry . . . . .	21
9	Earth Orbit Geometry . . . . .	23
10	Components of Circularly Polarized Wave . . . . .	25
11	Multipath Image Geometry . . . . .	26
12	Error Pattern Above a Ground Plane, Elevation = $0^\circ$ . . . . .	32
13	Error Pattern Above a Ground Plane, Elevation = $10^\circ$ . . . . .	33
14	Error Pattern Above a Ground Plane, Elevation = $16^\circ$ . . . . .	34
15	Error Pattern Above a Ground Plane, Elevation = $22^\circ$ . . . . .	35
16	One Way Attenuation through Atmosphere . . . . .	37
17	Antenna Sidelobe Radiating into Ground at Low Elevation Angles . . . . .	38
18	Radiation Pattern — Circular Aperture . . . . .	38
19	Plasma Frequency versus Mach Number and Electron Density . . . . .	41
20	Apollo Re-entry Trajectories . . . . .	42
21	Axial Ratio vs Angle Off Boresight (Wide Mode) . . . . .	45
22	Axial Ratio vs Angle Off Boresight (Medium Mode) . . . . .	46
23	Axial Ratio vs Angle Off Boresight (Narrow Mode) . . . . .	47
24	Spacecraft Tracking at 2500 Nautical Miles . . . . .	48
25	Worst Case Tracking at 28,000 Nautical Miles . . . . .	49
26	Apollo Ground Receiver — Static Phase Error vs Range . . . . .	52
27	Doppler Frequency vs Range . . . . .	53
28	Apollo Ground Receiver — Phase Jitter vs. Range . . . . .	54

# ILLUSTRATIONS (Continued)

Figure		Page
29	Apollo Ground Receiver — Total Phase Error vs Range . . . . .	55
30	Sum and Difference Monopulse System . . . . .	57
31	Boresight Shift Due to Pre-Comparator and Post Comparator Phase Shifts . . . . .	58
32	Phase Sensitive Detector — De-Sensitization vs Phase Error . . . . .	61
33	Apollo Spacecraft — Static Phase Error vs Range . . . . .	64
34	Apollo Spacecraft — Phase Jitter vs Range . . . . .	65
35	Apollo Spacecraft — Total Phase Error vs Range . . . . .	66
36	Apollo Communication Link — Two Way Phase Error vs Range . . . . .	67
37	Polarization Control Circuitry . . . . .	71
38	Linear Polarization Sensing and Polarization Control Scheme .	72
39	Circular Component Sensing . . . . .	73
40	Circular Component Sensing Utilizing Antenna Feed for Tilt Angle Control . . . . .	74
41	Reflection Coefficient vs Grazing Angle for a Smooth Sea . . . .	76
42	Reducing Lower Sidelobes to Reduce Multipath Effects . . . . .	77

## TABLES

Table		Page
1	Multipath Effects . . . . .	29
2	Boresight Measurements . . . . .	36
3	Predicted RMS Velocity Error and Spacecraft Roll Error Contribution . . . . .	62

**Section One**  
**INTRODUCTION**

## Section One

### 1. INTRODUCTION

#### 1.1 SCOPE AND PURPOSE

This report documents a study performed during the period of 21 September 1965 thru 21 April 1966 on the factors which govern and affect the polarization characteristics of R. F. telecommunication signals between earth and the Apollo space vehicles. The study consisted of a literature survey and evaluation of existing data, analysis and experimental tests on those factors not well documented in the literature, and evaluation of the polarization and signal transfer effects on the telecommunications system.

The purpose of this study was to provide a comprehensive understanding of the factors which affect the Apollo Telecommunications link, and investigate the use of polarization control to enhance the system operation, particularly during low angle tracking.

#### 1.2 SUMMARY OF WORK PERFORMED

The work accomplished during this period consists of three items. First, a critical evaluation was made of the existing literature, resulting in a fairly comprehensive bibliography of material which is included for further study by those interested.

Second, a detailed analysis was made of the various factors affecting signal transfer, external to the hardware of the Apollo communications system. This analysis consists of a consideration of the factors of wave polarization characteristics, power transfer between arbitrarily polarized antennas, ionospheric polarization effects, multipath propagation, and plasma effects.

The third portion of the study consists of an evaluation of the magnitude of the various effects in relation to the mission geometry and upon the performance of the system. Specifically the errors encountered in angle, range, and range rate

tracking are considered. Techniques of reducing the system losses due to polarization mismatch effects and multipath are considered.

**Section Two**  
**LITERATURE SEARCH**

## Section Two

### 2. LITERATURE SEARCH

As background material for this study, an extensive literature search was performed to determine what information is presently available which is applicable to the problems encountered in the Apollo network from a signal performance viewpoint. This search was generally categorized into four main areas:

1) Spacecraft, 2) Ground System, 3) Medium, 4) Communications System. Although overlapping of these areas was inevitable, the literature has been separated into these general headings in the resulting bibliography. A brief discussion of each area of search follows below, indicating those areas which required further analysis. A comprehensive bibliography is included in Section 7 of this report.

#### 2.1 SPACECRAFT

The motion of the spacecraft and of the spacecraft antennas is well documented in the literature (references 6 and 7 in the bibliography). The effect of any spacecraft antenna movement on data transfer due to signal polarization change is not documented in the literature and required further investigation.

There is substantial information in the literature concerning the radiation characteristics of antennas covered by plasma sheaths. However, most is of a general and academic nature and cannot be easily applied to the Apollo re-entry problem. Reference 9 of the literature survey defines the communication blackout problem with respect to the Apollo mission in general terms. The effects of this plasma shield on communications is well known; however, additional work is necessary to determine ways to reduce or eliminate the blackout problem. This was not an item of this study.



## 2.2 GROUND SYSTEM

Characteristics of the Apollo ground system antennas except for the two 12-foot re-entry antennas are well documented in this section of the literature survey (see references 1, 2, 3, and 4). Characteristics of the 30-foot shipboard antennas are available from measurements made at Hughes. This information is sufficient to determine the effect of the antenna characteristics on information transfer.

References 19, 20, and 22 in the Medium section of the literature survey discuss the complex scattering problem (multipath) when propagating at zero and below zero angles over various terrain and sea water. However, it appears there is very little information available on the effect of multipath, prevalent during low angle tracking, on the radiation characteristics of antennas; specifically, those employed by the MSFN for the Apollo program. Further detailed analysis and experimental measurements of this item are considered in Section 3.

Further study of the multipath problem would seem to be warranted, including actual field probe measurements over various types of terrain, and performance study and correlation of data from existing sites. Measurements which could be made with an operational system would provide valuable data for analyzing the problem and establishing design criteria for reducing the multipath problem.

## 2.3 MEDIUM

The effects of wave propagation through the magneto-ionic medium of the ionosphere, specifically with respect to Faraday rotation, are well documented in the literature. The references found to be most useful in this phase of the study are references 1, 12, 14, 18, 24, 25, and 26 in the bibliography. To our knowledge, however, there is no information available concerning the effects of Faraday rotation on doppler frequency measurements for an orbiting spacecraft. Further analysis of this factor was made and specific results are included in this report.

Reference 8 in the literature section under the heading Communications System provides a thorough explanation of power loss in a communication link due to polarization rotation. This topic has also been considered in some detail. Results of a computer program to provide reference data are included in this report.

## 2.4 COMMUNICATIONS SYSTEM

References 10, 13, 16, 17, 18 and 19 in this section of the bibliography provided a thorough enough system description to fulfill the objectives of this study.

To provide a better understanding of the Apollo tracking and communications system, a review was made of phase-locked loops, a critical item in the operation of the system. Details of this investigation are included in Appendix IV.

Evaluation of the magnitude of the effect of each factor affecting polarization characteristics upon the system performance has not been previously documented. Section 4 of this report details the system performance evaluation.

**Section Three**

**PARAMETER ANALYSIS**

## Section Three

### 3. PARAMETER ANALYSIS

This section of the report contains a summary of the major items affecting wave polarization, signal transfer, and boresight characteristics in the Apollo communications link external to the system equipment. Detailed analysis is made of wave polarization, power transfer, ionospheric effects, and multipath, and data provided in the form of charts and graphs for application to system calculations. Determination is made of the magnitude of the various effects in the Apollo link.

#### 3.1 WAVE POLARIZATION

In general, the energy transmitted or received by an antenna is elliptically polarized, linear and circular polarization being special cases.

One way of analyzing the elliptically polarized wave is to consider the wave to be composed of two linear components oriented in the vertical and horizontal planes. This may be expressed as:

$$E_x = E_1 \sin \omega t \quad \text{Horizontal pol. component}$$

$$E_y = E_2 \sin (\omega t + \delta) \quad \text{Vertical pol. component}$$

By eliminating the independent variable  $\omega t$ , it is possible to write the above equations as<sup>1</sup>:

$$a E_x^2 - b E_x E_y + c E_y^2 = 1 \quad (3-1)$$

where

$$a = 1/E_1^2 \sin^2 \delta$$

$$b = 2 \cos \delta / E_1 E_2 \sin^2 \delta$$

$$c = 1/E_2^2 \sin^2 \delta$$

Equation (3-1) may be recognized as the general equation for an ellipse, however, the axes of the ellipse do not necessarily coincide with the x and y axes, see Figure 1.

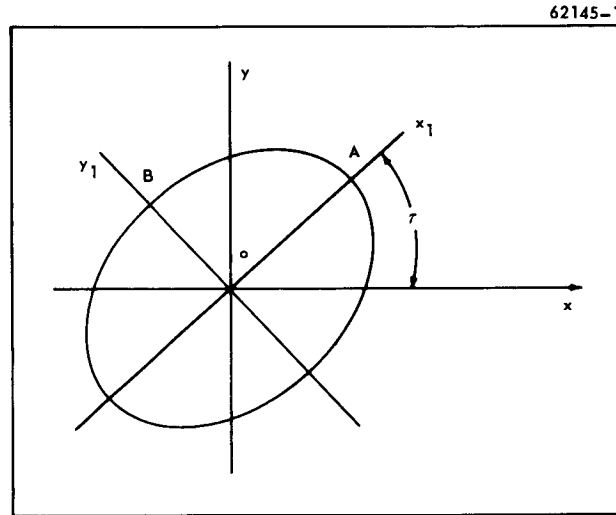


Figure 1. Polarization Ellipse

To determine the voltage axial ratio of the polarization ellipse, it is necessary to know the length of the major and minor axes, OA and OB.

This may be accomplished by rotating the axes such that the new axes coincide with the major and minor axes of the ellipse. The equation of the ellipse in the new coordinate systems ( $x_1$ ,  $y_1$ ) is of the form:

$$\left(\frac{x_1}{A}\right)^2 + \left(\frac{y_1}{B}\right)^2 = 1 \quad (3-2)$$

in which case the axial ratio "R" is merely  $R = \frac{A}{B}$  (or its reciprocal if  $B > A$ ).

Considering equation (3-1) which was of the form  $ax^2 - bxy + cy = 1$  as being represented by Figure 1, it is possible to write the equation of the new axes as

$$x_1 = x \cos \tau + y \sin \tau$$

$$y_1 = y \cos \tau - x \sin \tau$$

Substituting these expressions for  $x_1$  and  $y_1$  into Equation (3-2) and rearranging terms yields:

$$\left(\frac{\cos^2 \tau}{A^2} + \frac{\sin^2 \tau}{B^2}\right) X^2 - 2\left(\frac{\cos \tau \sin \tau}{B^2} - \frac{\cos \tau \sin \tau}{A^2}\right) XY + \left(\frac{\sin^2 \tau}{A^2} + \frac{\cos^2 \tau}{B^2}\right) Y^2 = 1$$

Comparing coefficients with Equation (3-1) re-written as  $aX^2 - bXY + cY = 1$ , it may be seen that

$$a = \cos^2 \tau / A^2 + \sin^2 \tau / B^2$$

$$b = 2 \cos \tau \sin \tau (1/B^2 - 1/A^2) = \sin 2\tau (1/B^2 - 1/A^2) \quad (3-3)$$

$$c = \sin^2 \tau / A^2 + \cos^2 \tau / B^2$$

solving Equation (3-3) for A and B yields:

$$A^2 = \frac{2}{a + c - b/\sin 2\tau}$$

$$B^2 = \frac{2}{a + c + b/\sin 2\tau}$$

Inserting the values for a, b, and c from Equation (3-1) gives:

$$A^2 = \frac{2 \sin^2 \delta}{1/E_1^2 + 1/E_2^2 - 2 \cos \delta / E_1 E_2 \sin 2\tau} \quad (3-4)$$

$$B^2 = \frac{2 \sin^2 \delta}{1/E_1^2 + 1/E_2^2 + 2 \cos \delta / E_1 E_2 \sin 2\tau}$$

from which the axial ratio can now be found:

$$R = B/A$$

Also, Equation (3-3) may be solved for the ellipse tilt angle " $\tau$ ".

$$2\tau = \tan^{-1} \frac{b}{c-a}$$

or

$$2\tau = \tan^{-1} \frac{2 E_1 E_2 \cos \delta}{E_1^2 - E_2^2} \quad (3-5)$$

Solving for the axial ratio from Equation (3-4) and rearranging terms:

$$R^2 = 1 + \frac{4 \cos \delta / P \sin 2\tau}{S - 2 \cos \delta / P \sin 2\tau} \quad (3-6)$$

where

$$P = E_1 E_2$$

$$S = 1/E_1^2 + 1/E_2^2$$

$\delta$  = relative phase between the vertical and horizontal linear polarization components

$\tau$  = ellipse rotation angle [ given by Equation (3-5) ]

A further useful relationship to consider when discussing elliptical polarization is the cross polarization\* component. This may easily be found by using the expression for axial ratio in terms of two orthogonal circularly polarized waves; as given by<sup>1</sup>:

$$R = \frac{E_R + E_L}{E_R - E_L}$$

where

$E_R$  = magnitude of a right circularly polarized wave

---

\* The term "cross polarization" is used here as synonymous to the circularly polarized component of the opposite sense of rotation.

$E_L$  = magnitude of a left circularly polarized wave

This may be rearranged to give the ratio of right to left circular polarization components in terms of the axial ratio:

$$\frac{E_R}{E_L} = \frac{R + 1}{R - 1} \quad (3-7)$$

Equation (3-7) may be used to determine the cross polarization component of a wave.

The results given above in Equations (3-6) and (3-7) may be plotted to give useful reference data. Equation (3-7) results in a single plot as shown in Figure 2. Here the cross polarization is plotted as a function of ellipticity defined as:

$$\text{Ellipticity } e = 20 \log R \text{ (dB)}$$

Equation (3-6) however will result in any number of plots as a function of the amplitude and phase of the two linear components. For example, where

$E_1 = E_2 = 1$ , Equation (3-6) reduces to

$$R^2 = 1 + \frac{2 \cos \delta / \sin 2\tau}{2 - 2 \cos \delta / \sin 2\tau}$$

From equation (3-5),  $\tau = 45^\circ$ ,

therefore

$$R^2 = 1 + \frac{2 \cos \delta}{1 - \cos \delta}$$

Figure 3 is a plot of ellipticity in dB versus the phase angle " $\delta$ " between two linear polarization components. Curves are shown for amplitude ratios of the two linear components of 0 dB (i.e. equal magnitudes), 3 dB, and 6 dB.

For example, if the circularly polarized wave is considered to be made up of a vertical component twice the magnitude of a horizontal component, and the phase between the two components is 120 degrees, the resultant ellipticity from Figure 3 is about 5.9 dB.

The relationship between the linear components, the polarization ellipse, and the measured response of an elliptically polarized wave may be seen by considering the polarization pattern.



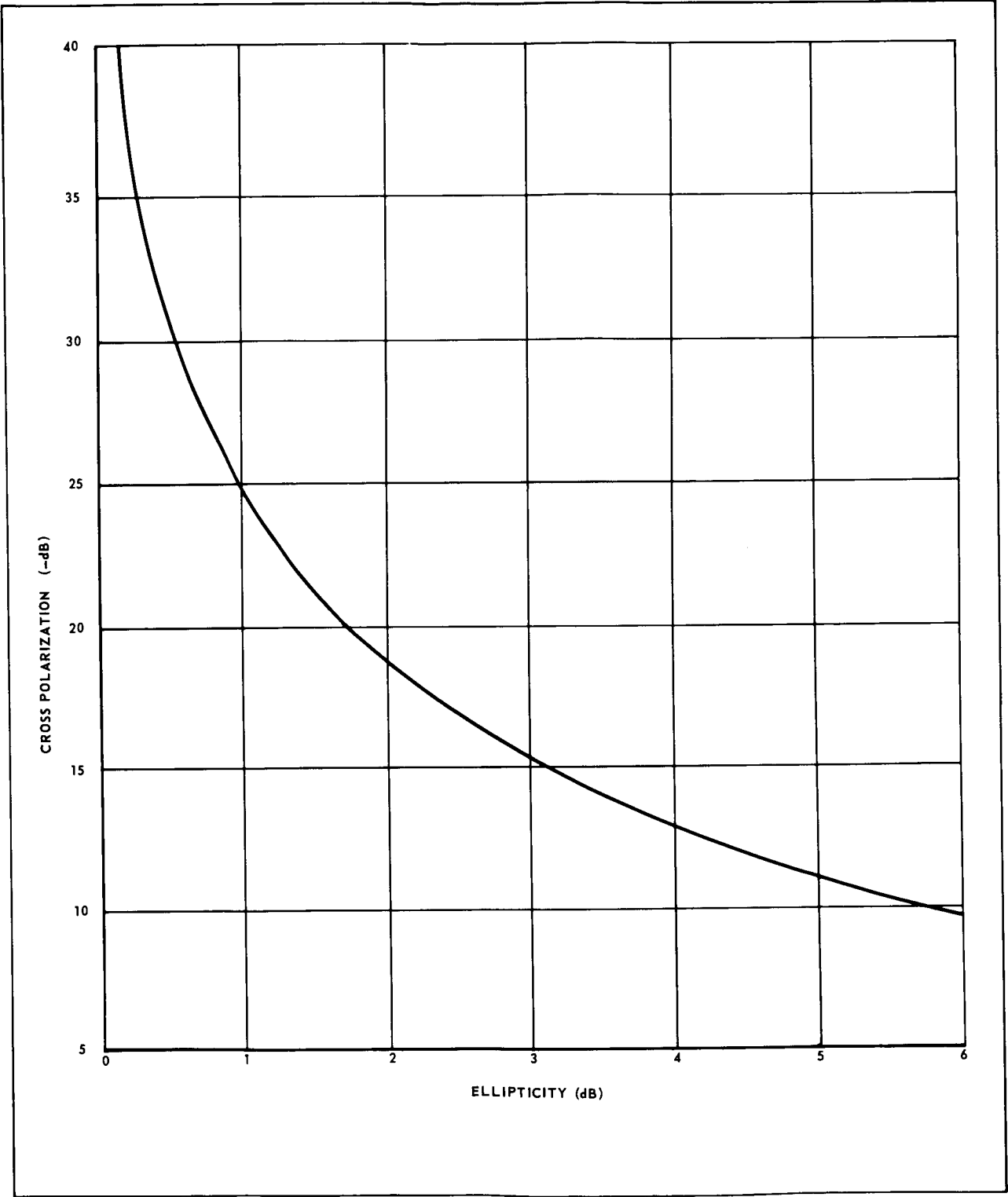


Figure 2. Cross Polarization Versus Ellipticity

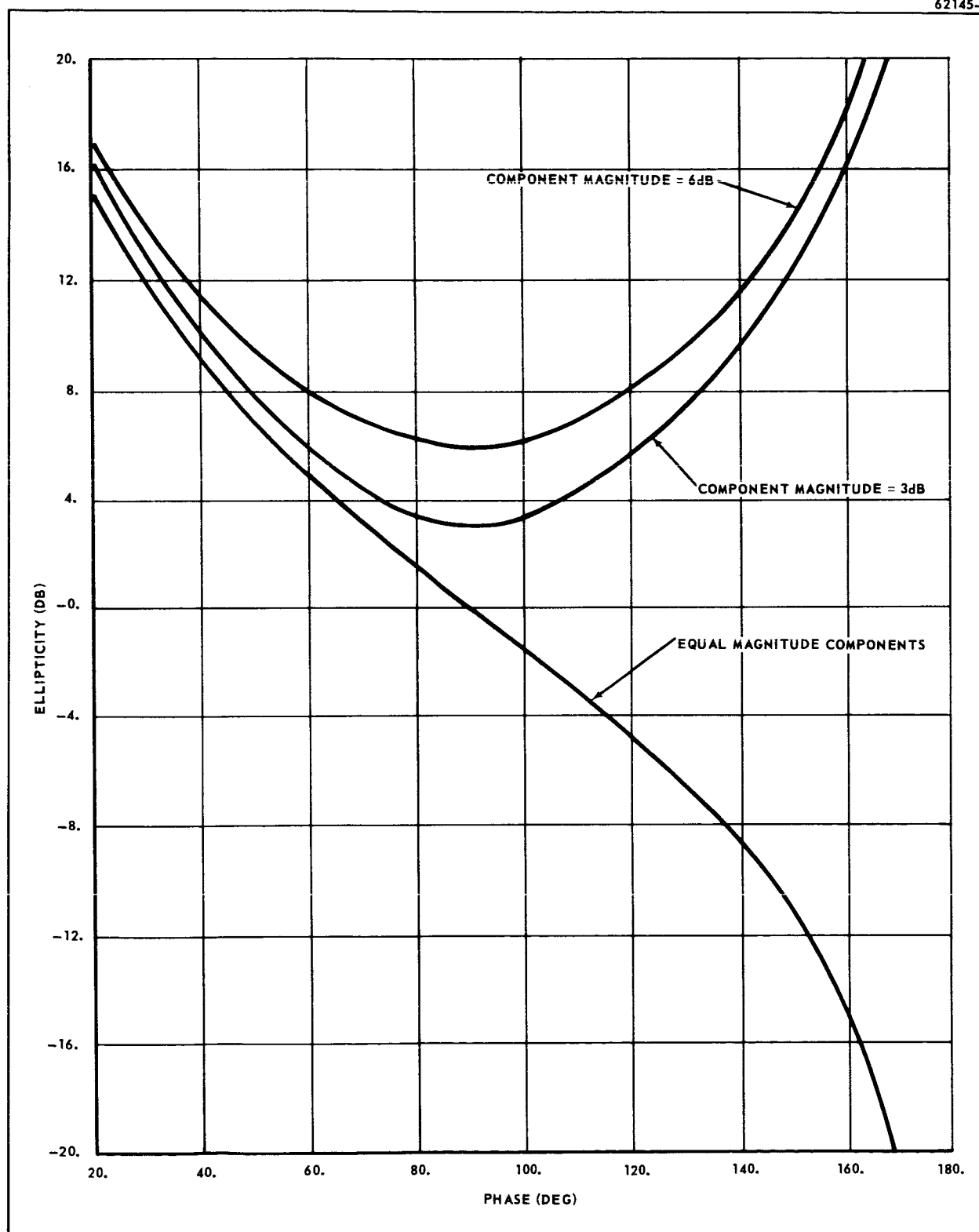


Figure 4(A) shows the familiar donut shaped polarization pattern of a linearly polarized mathematical dipole. Figure 4(B) shows the result of adding two linearly polarized waves whose polarization patterns are oriented  $90^\circ$  apart in space and whose time phase is also  $90^\circ$ . The vectors  $\bar{A}$  and  $\bar{B}$  show the response of a linear probe to each of the dipole fields, and the vector addition of  $\bar{B} + \bar{A}$  to yield  $\bar{C}$  indicates the result of the  $90^\circ$  phase between the components. The response at the angle  $\theta$  would then be  $\bar{C}'$  as indicated. The relationship<sup>1</sup> between the elliptical polarization pattern, (which represents the response of a linearly polarized probe to an elliptically polarized wave) and the polarization ellipse is shown in Figure 4(C). If either the polarization pattern or the polarization ellipse is known, the other can be constructed graphically as shown.

### 3.2 POWER LOSS BETWEEN ARBITRARILY POLARIZED ANTENNAS

In the previous section, the polarization characteristics of a wave radiated from an antenna were considered. The equations for determining the complete polarization characteristics were given. As the wave was broken into two linear components (i. e. : vertical and horizontal polarization), the equations may be used to evaluate the effects of propagation, multipath, etc. on wave polarization characteristics. However, an additional item, the power transfer between two antennas as a function of polarization, is also required to evaluate the overall performance.

This factor has been considered in several sources, one of the most complete in a recent JPL Report.<sup>2</sup> In that report, a general expression is derived for the power loss due to imperfect polarization match between two antennas of arbitrary polarization. This expression is given by:

$$P_1 = 10 \log \frac{(R_1^2 + 1)(R_2^2 + 1)}{(R_1 R_2 \pm 1)^2 \cos^2 \theta + (R_1 \pm R_2)^2 \sin^2 \theta} \quad (3-8)$$

where

$P_1$  = polarization loss between the two antennas (dB)

$R_1$  = voltage axial ratio of one antenna

$R_2$  = voltage axial ratio of second antenna

$\theta$  = angle between the major axes of the polarization ellipses of the two antennas

The plus sign is used when both antennas have the same screw sense; the negative sign is for the cross polarized case.

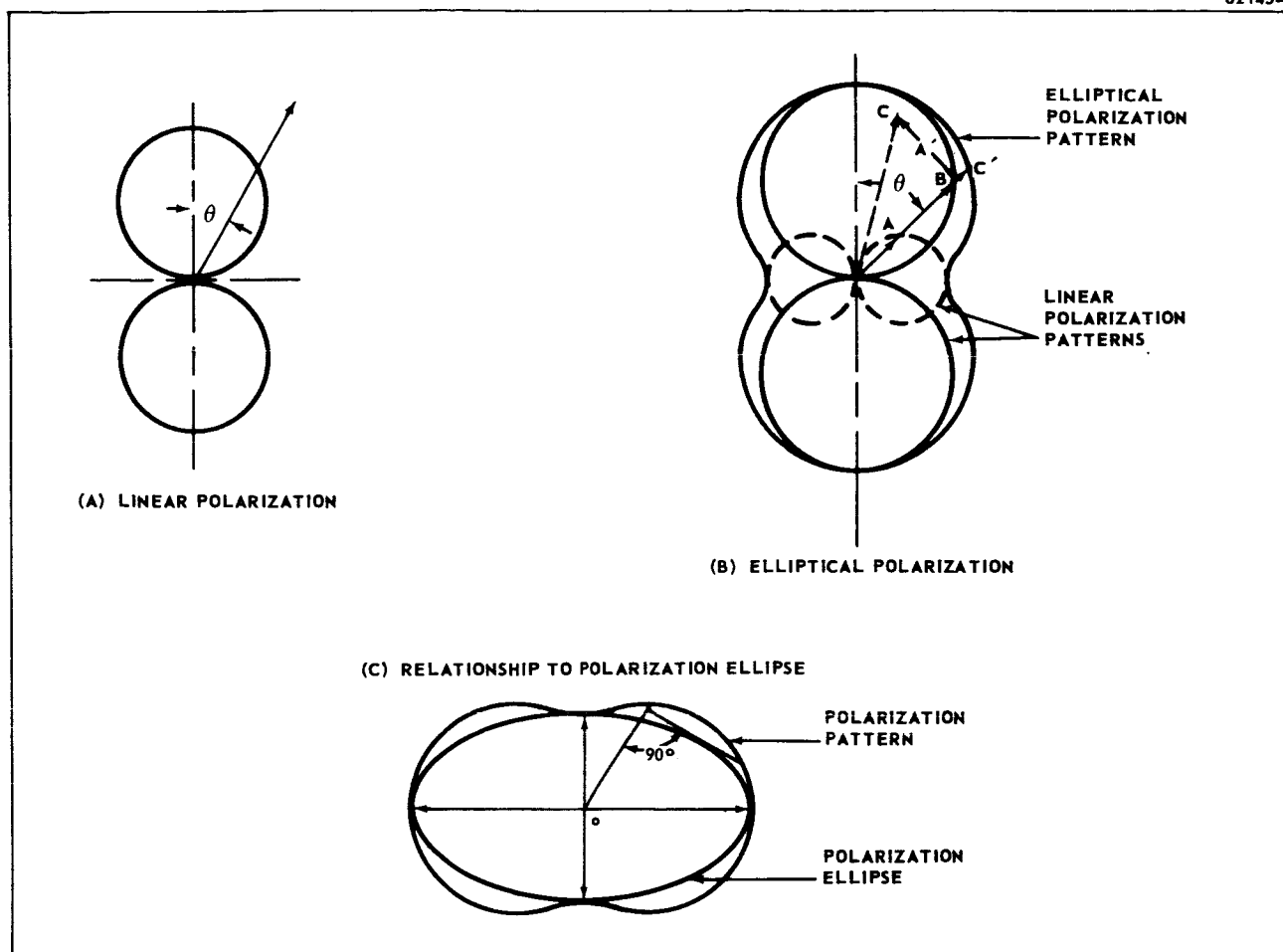


Figure 4. Polarization Patterns

Additional equations are also listed for special cases of interest. For example, when both antennas are linearly polarized, Equation (3-8) reduces to:

$$P_1 = 20 \log \sec \theta$$

and for the case of one antenna radiating perfect circular polarization,

$$P_1 = 10 \log \frac{2(R^2 + 1)}{(R \pm 1)^2}$$

where the definitions are consistent with Equation (3-8).

To generate a set of reference curves, a program was written for the IBM 7094 computer based on the above equations. The program output is a graph of power loss " $P_1$ " (in dB), versus the ellipticity " $E$ " (in dB) of one antenna, for a given

ellipticity value of incident field. A series of curves are shown for each case with the angle between the major axis of the polarization ellipse, " $\theta$ " (in degrees), as a parameter. The angle is shown at the end of each curve. A set of graphs for incident polarizations from 0 dB to 6 dB ellipticity and linear polarization (i. e., infinity dB) are included in Appendix I.

These curves may be used to determine power loss between the spacecraft and the ground stations. For example, if the incoming wave from the spacecraft has an ellipticity of 1.0 dB, and the major axis of the polarization ellipse is orthogonal to that of the ground antenna, (i. e.,  $\theta = 90^\circ$ ), the power loss as a function of the ellipticity of the ground antenna is given by the top curve of Graph I-3. For an ellipticity of 1 dB on the ground antenna, the power transfer loss would be about 0.06 db.

### 3.3 IONOSPHERIC POLARIZATION EFFECTS

#### 3.3.1 Faraday Rotation

When a magnetostatic field is applied to a medium composed of ionized gas (i. e., the ionosphere), the medium becomes anisotropic for electromagnetic waves<sup>3</sup>. That is, the dielectric constant of the medium becomes a tensor. To explain this condition, consider a plane wave propagating in an ionized medium in the  $\bar{n}$  direction as shown in Figure 5. The electric vector has the form  $\bar{E} = \bar{E}_0 e^{j(\omega t - \bar{K} \cdot \bar{r})}$  where  $K$  is the propagation constant and  $\bar{r} = \bar{a}_x x + \bar{a}_y y + \bar{a}_z z$ . The magnetic field ( $B_0$ ) is in the  $z$  direction.

The electrons in the medium are acted upon by the electromagnetic field and their motion can be described by the following equation:

$$m \frac{d\bar{v}}{dt} = e \bar{E} + e \mu_0 \bar{v} \times \bar{H}_0 \quad (3-9)$$

where

$$\bar{B}_0 = \mu_0 \bar{H}_0$$

$\mu_0$  = magnetic permeability

$e$  = electron charge

$m$  = electron mass

$\bar{v}$  = velocity vector

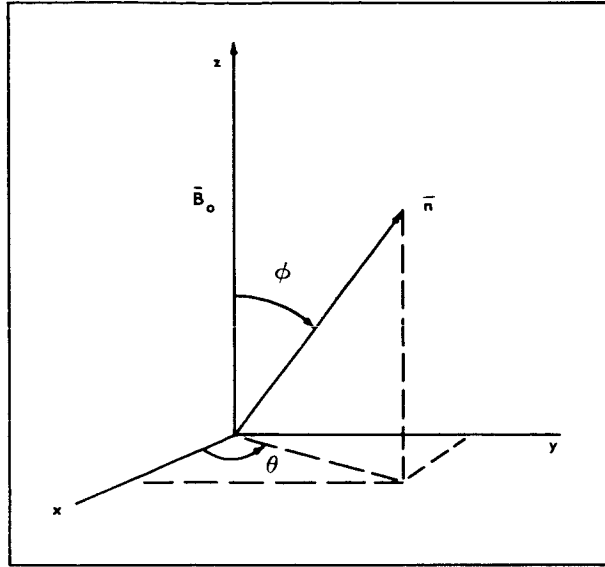


Figure 5. Plane Wave in Ionosphere

Solving equation (3-9) for  $\bar{v}$  and utilizing  $e^{j\omega t}$  time dependence for  $\bar{E}$ :

$$Ne\bar{v} = -j\omega \frac{\epsilon_0 \omega_p^2}{(\bar{\omega}_g \cdot \bar{\omega}_g - \omega^2)} \bar{E} + \frac{\epsilon_0 \omega_p^2}{(\bar{\omega}_g \cdot \bar{\omega}_g - \omega^2)^2} \bar{E} \times \bar{\omega}_g$$

$$- \frac{\epsilon_0}{j\omega(\bar{\omega}_g \cdot \bar{\omega}_g - \omega^2)} (\bar{E} \cdot \bar{\omega}_g) \bar{\omega}_g$$

where:

$$\omega_p = \sqrt{\frac{Ne^2}{m\epsilon_0}} = \text{plasma frequency}$$

$N$  = electron density

$$\bar{\omega}_g = \frac{e}{m} \mu_0 \bar{H}_0 = \text{gyromagnetic frequency}$$

$\epsilon_0$  = dielectric constant

$Ne\bar{v}$  is the convection current to which the displacement current ( $j\omega\epsilon_0\bar{E}$ ) must be added to obtain the total current,  $\bar{J}$ :

$$\bar{J} = Ne\bar{v} + j\omega\epsilon_0\bar{E}$$

It can then be seen that  $\bar{J}$  is generally not parallel to  $\bar{E}$ . If  $\bar{J}$  is expressed in the form  $j \omega(\epsilon) \bar{E}$ , it is clear that  $(\epsilon)$  must be a tensor. The tensor  $(\epsilon)$  can be written in the form:

$$(\epsilon) = \begin{pmatrix} \epsilon_{xx} & -j\epsilon_{xy} & 0 \\ j\epsilon_{yx} & \epsilon_{yy} & 0 \\ 0 & 0 & \epsilon_{zz} \end{pmatrix}$$

where:

$$\epsilon_{xx} = \epsilon_0 \left( 1 - \frac{\omega_p^2}{\omega^2 - \omega_g^2} \right) = \epsilon_{yy}$$

$$\epsilon_{xy} = j\epsilon_0 \left( \frac{\omega_p^2 \omega_g}{\omega(\omega^2 - \omega_g^2)} \right) = -\epsilon_{yx}$$

$$\epsilon_{zz} = \epsilon_0 \left( 1 - \frac{\omega_p^2}{\omega^2} \right)$$

Recalling that the following Maxwell equations must be satisfied for the medium:

$$\nabla \times \bar{H} = j \omega(\epsilon) \bar{E}$$

$$\nabla \times \bar{E} = -j \omega \mu_0 \bar{H}$$

Substitution of the electric field vector expression into these equations, one obtains:

$$\bar{E} - \bar{n} (\bar{n} \cdot \bar{E}_0) = \frac{v^2}{c^2} \frac{(\epsilon) \cdot \bar{E}_0}{\epsilon_0}$$

where

$$v/c = \frac{\omega \sqrt{\mu_0 \epsilon_0}}{k}$$

The components of this vector equation yield three homogeneous simultaneous equations from which the propagation constant (k) can be obtained.

A linearly polarized plane wave can be conveniently represented by two circularly polarized waves of opposite senses of rotation. For the condition when

the direction of propagation of the plane wave is parallel to the magnetic field,  $\theta = \pi/2$  and  $\phi = 0$ , there are two solutions for K:

$$K_O' = \omega \sqrt{\mu_O \epsilon_O} \left[ 1 - \frac{\omega_p^2}{\omega(\omega - \omega_g)} \right]^{1/2}$$

$$K_O'' = \omega \sqrt{\mu_O \epsilon_O} \left[ 1 - \frac{\omega_p^2}{\omega(\omega + \omega_g)} \right]^{1/2}$$

The physical interpretation is that one circularly polarized wave has a propagation constant  $K_O'$  while the other has a propagation constant  $K_O''$ . Because of the different propagation constants, a superposition of the two waves yields a linearly polarized wave whose plane of polarization is continually rotating. The phase difference between the two circularly polarized waves per unit length is then  $(K_O' - K_O'')$ . The Faraday rotation is equal to one half the total phase difference. The same procedure can be carried out for perpendicular propagation ( $\theta = \pi/2$ ,  $\phi = \pi/2$ ). The result is that the Faraday rotation for this condition is less than  $10^{-3}$  that for longitudinal propagation for frequencies above 1 kmc. This concept of Faraday rotation can be extended to the case of elliptical polarization by considering the wave to be composed of two linear components orthogonal to each other in time and space. The effect of Faraday rotation would then be to change the "tilt" angle of the ellipse.

The determination of the amount of Faraday rotation, given a path length in the magneto-ionic medium, is complicated by the fact that  $\omega_p$  (plasma frequency) and  $\omega_g$  (gyromagnetic frequency) are not constant. The plasma frequency depends upon the electron density profile (N) which is quite variable and uncertain. However, the Chapman distribution gives a fairly good approximation to the electron density profile for the F2 layer of the ionosphere and above<sup>5</sup>.

This is given as:

$$N = N_{\max} \exp \left\{ \frac{1}{2} \left[ 1 - \frac{h - h_{\max}}{H} - \exp \left( - \frac{h - h_{\max}}{H} \right) \right] \right\}$$

where:

$N_{\max}$  = maximum electron density

$H$  = scale height which fixes the scale of the electron density profile (100 KM)

$h_{\max}$  = height of maximum electron density (300 KM)



A typical electron density profile is plotted in Figure 6.

62145-6

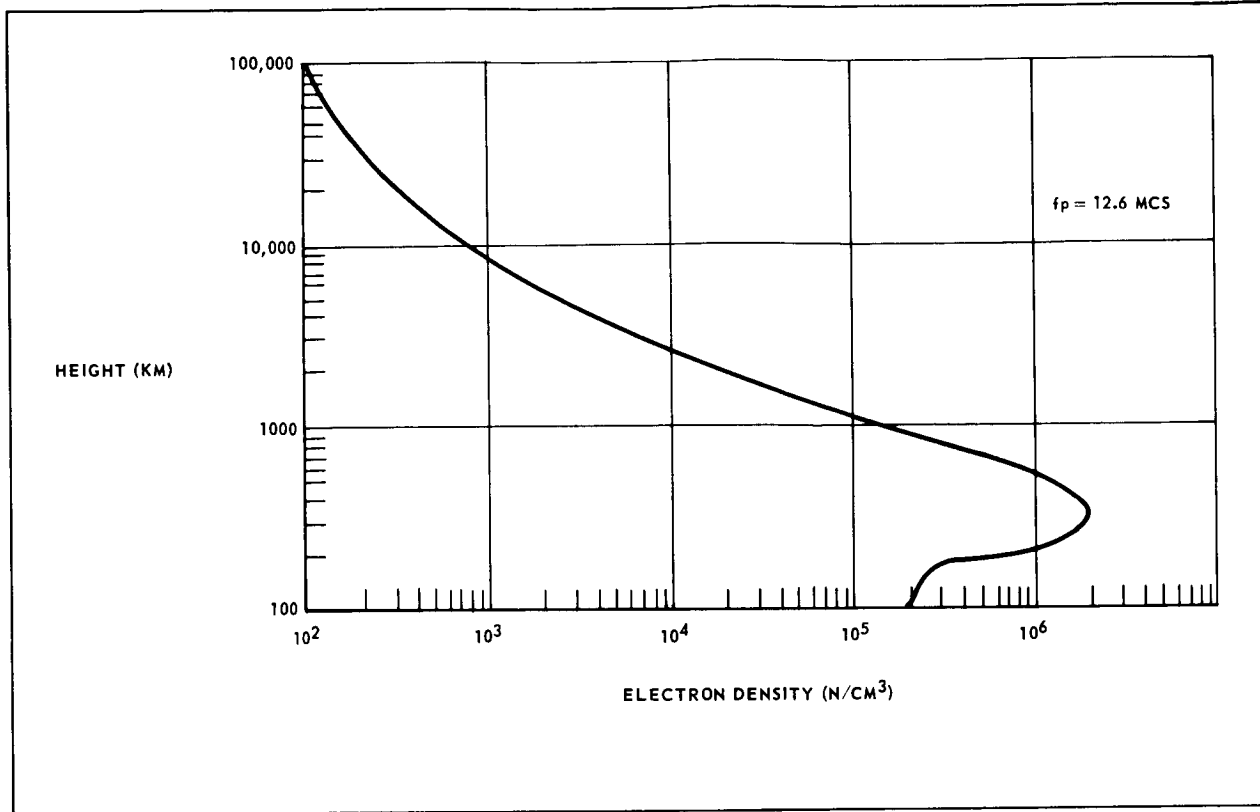


Figure 6. Electron Density vs Height

The gyromagnetic frequency depends upon the magnetic field intensity at some height (h) in the ionosphere. The earth's magnetic field can be approximated by a magnetic dipole<sup>6</sup>, as shown in Figure 7. The magnetic field is as follows<sup>7</sup>:

$$H = \sqrt{H_r^2 + H_\theta^2} = \frac{M}{2\pi r^3} \sqrt{1 - 3/4 \sin^2 \theta'}$$

$$H = \hat{H} \sqrt{1 - 3/4 \cos^2 \theta} \left( \frac{R}{R+h} \right)^3$$

where:

M = magnetic dipole moment

$\hat{H}$  = magnetic field intensity at the magnetic pole at sea level  
(0.7 OERSTEDS)

$\theta$  = magnetic latitude

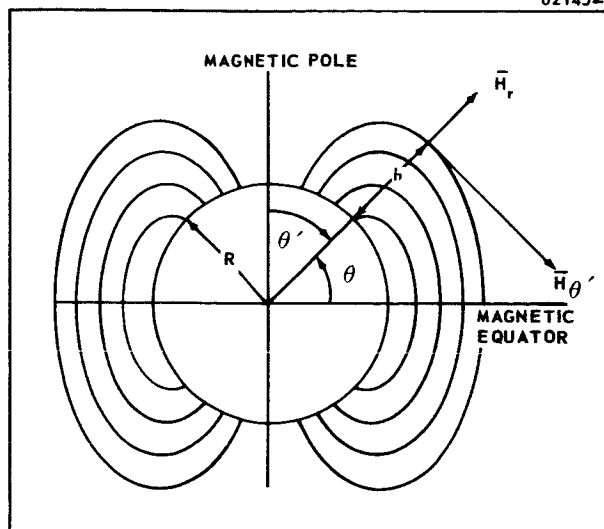


Figure 7. Earth's Magnetic Field

Considering the above discussion, the one way Faraday rotation can be given as:

$$\Omega = \frac{\pi}{c} \frac{f_g f_p^2}{f^2} \int \frac{H}{\hat{H}} \cos \psi \, N \, dr \quad (\text{RADIANS})$$

where:

$\psi$  = angle between earth's magnetic field and direction of propagation.

Radar range ( $r$ ) can be written in terms of height ( $h$ ) and antenna elevation angle ( $\alpha$ ) by: (See Figure 8)

$$(R + h)^2 = R^2 + r^2 - 2 R r \cos (90^\circ + \alpha)$$

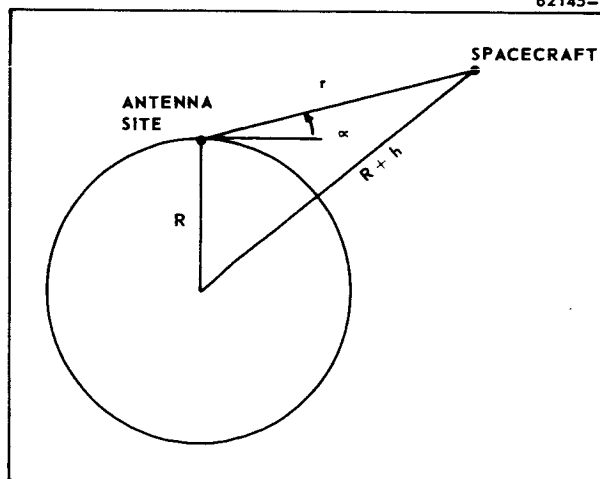


Figure 8. Faraday Rotation Geometry

and the angle  $\psi$  may be expressed as:

$$\psi = \tan^{-1} \left[ 2 \tan \theta \right] - \cos^{-1} \left[ \frac{R \cos \alpha}{R + h} \right]$$

The computed results of one way Faraday rotation (Omega) versus spacecraft height for antenna elevation angles of 0, 30, 60, and 90 degrees are included in Appendix II. The graphs for antennas at 5 degrees latitude apply to the re-entry ship (2 deg. S), the injection ship (6 deg. S), and Ascension Island (7.5 deg. S). 15 degrees latitude applies to the injection ship (18 deg. S), Antigua (17 deg. S), and Guam (13 deg. N). 25 degrees latitude applies to Carnarvon (25 deg. S), Hawaii (20 deg. N), Cape Kennedy (28.5 deg. N), Guaymas (28 deg. N), Canary Islands (28 deg. N), and the re-entry ship (30 deg. N). 35 degrees latitude applies to Bermuda (32 deg. N), Texas (30 deg. N), Goldstone (35 deg. N), Canberra (35 deg. S), Madrid (40.5 deg. N), and the Insertion ship (38 deg. N). Maximum Faraday rotation occurs for a radar beam in the northern hemisphere looking south or a radar beam in the southern hemisphere looking north. The graphs in Appendix II depict the case of maximum Faraday rotation. For each of the four antenna locations considered, there are two graphs, one for the Apollo up-link frequency of 2106 MHz, the other for the Apollo down-link frequency of 2288 MHz. The two way Faraday rotation is the summation of the Faraday rotation of the two links.

It can be seen from the graphs that Faraday rotation is greatest for zero degrees antenna elevation angle and 35 degrees magnetic latitude. Also, there appears to be negligible Faraday rotation for heights above approximately 800 Km.

As was discussed earlier, a radar beam whose direction of propagation is perpendicular to the earth's magnetic field will experience negligible Faraday rotation at the frequencies under consideration. As a result, Faraday rotation will change with antenna azimuth bearing when tracking a spacecraft which is traveling through the ionosphere. The magnitude of change is dependent upon the height and direction of the spacecraft and location of the radar site. The time interval in which the change takes place is dependent upon the height and velocity of the spacecraft. This polarization rotation varies approximately linearly with time for a spacecraft in a relatively circular orbit traveling from west to east or vice-versa<sup>6</sup>. The resulting  $\frac{\Delta \Omega}{\Delta t}$  term will either add to or subtract from the doppler frequency, producing an error in the velocity measurement of the spacecraft. To determine the magnitude of this error, the following worst case condition is examined.

Consider an antenna site (A) located at 35 deg. north latitude tracking a spacecraft (B) 200 Km high traveling at 17,500 mph from north-west to south-east as shown in Figure 9.

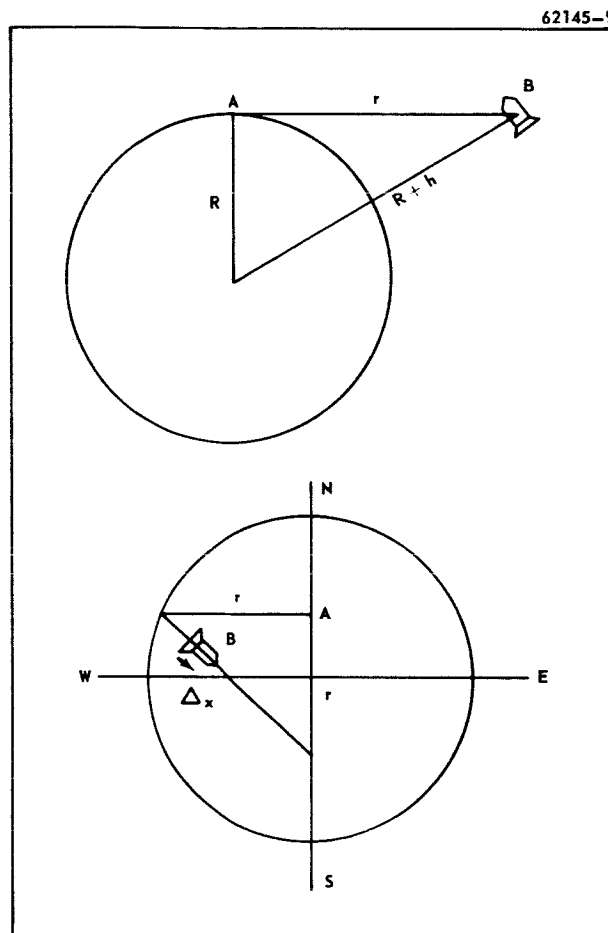


Figure 9. Earth-Orbit Geometry

The antenna elevation angle is zero degrees. From geometric considerations, the range ( $r$ ) is 1609 Km and the path length ( $\Delta x$ ) is 2276 Km. The time required to traverse the path ( $\Delta t$ ) is 293 sec. From Appendix II, the two way Faraday rotation is 7 degrees or 7/360 cycles resulting in a  $\frac{\Delta \Omega}{\Delta t}$  of  $6.65 \times 10^{-5}$  cps. Spacecraft radial velocity is related to doppler frequency by the equation:

$$F_D = F_R \times 2 \frac{v}{c}$$

where:

$F_D$  = doppler frequency

$F_R$  = received carrier frequency

$v$  = spacecraft radial velocity

Using this equation, the radial velocity corresponding to a doppler frequency of  $\frac{\Delta\Omega}{\Delta t}$  is  $4.35 \times 10^{-4}$  cm/sec. This represents the worst case velocity error due to Faraday rotation during earth parking orbit. Since the rms error in velocity at the end of the first parking orbit is  $\pm 4$  cm/sec<sup>8</sup>, it is seen that Faraday rotation error is  $1.09 \times 10^{-4}$  of the tracking system RMS error limits and can therefore be considered negligible.

For the case of trans-lunar injection, the spacecraft undergoes a height change from 197 km to 315 km in 315 seconds and a velocity change from 25,555 ft/sec to 35,631 ft/sec. Referring to the curves on Faraday rotation, the spacecraft's increase in height corresponds to less than 20 degrees rotation in 315 seconds; again, a negligible error contribution to doppler tracking accuracy.

### 3.3.2 Effect on Polarization Ellipticity

It was discussed previously that a plane wave traversing the ionosphere was found to exhibit a maximum rotation of the plane of polarization when propagating parallel, and minimum when traveling perpendicular to the direction of the earth's magnetic field. However, another effect, which takes place when the direction of propagation is perpendicular to the earth's magnetic field, is a change in ellipticity of the wave<sup>3</sup>.

Since a circularly polarized wave can be resolved into two linearly polarized waves in time and space quadrature, any change in ellipticity may be determined by analyzing the effect of the ionosphere upon each of the linearly polarized components.

Consider the two components of the circularly polarized wave oriented as shown in Figure 10 propagating in the  $\bar{n}$  direction.

The propagation constants  $K'$  and  $K''$  of the two waves differ due to their polarization orientation with respect to the direction of the magnetic field ( $\bar{B}_0$ ).

The magnitude of the change in ellipticity for a given path length in the magneto-ionic medium is then dependent upon the difference in propagation constants of the two waves as given by Papas<sup>3</sup>:

$$K' - K'' = \frac{\omega}{c} \left[ \left(1 - \frac{\omega_p^2}{\omega^2}\right)^{1/2} - \left(1 - \frac{\omega_p^2/\omega^2}{1 - \omega_g^2/(\omega^2 - \omega_p^2)}\right)^{1/2} \right]$$

This equation evaluated at the Apollo frequencies for low elevation angles (i.e., a path length through the ionosphere of about 3700 KM) yields a maximum phase difference of 0.068 degrees. This represents a negligible effect on the wave ellipticity.

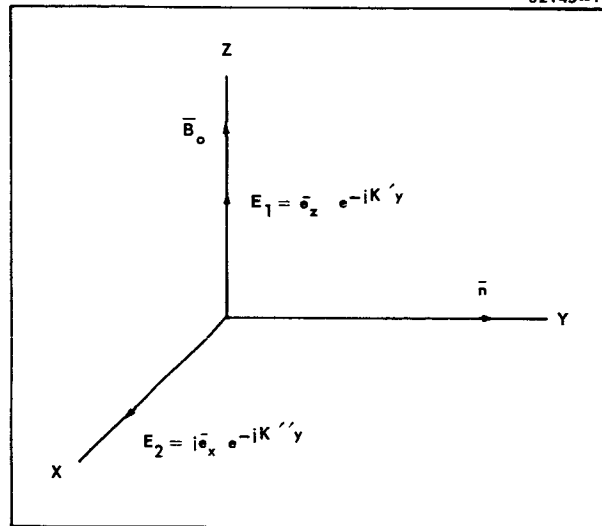


Figure 10. Components of Circularly Polarized Wave

### 3.4 MULTIPATH

One of the major problems encountered in tracking of spacecraft is that of multipath effects near horizon. For the Apollo mission, acquisition of the spacecraft near horizon is limited by multipath, and the acquisition point is expected to be between  $2^{\circ}$  and  $5^{\circ}$  above horizon. To investigate this problem, it is required to know the characteristics of the antenna pattern near horizon for various kinds of terrain. This is a difficult problem as mathematical expressions for reflection coefficients of a surface are limited to uniform ground planes of various conductivity and dielectric constant. Such an idealized ground plane seldom exists, except perhaps on a level desert region or over a smooth sea. Reflections from mountains, rough terrain, etc., are difficult to evaluate, and even in a given case are difficult to measure. However, some knowledge of the effect of various types of ground on antenna patterns will be helpful in developing a "feel" for what may be encountered. For this reason, a detailed analysis was made of this topic.

#### 3.4.1 Pattern Analysis

To analyze the multipath effect, consider an antenna of aperture  $A$ , elevated height  $h$  above a ground plane characterized by the dielectric constant  $\epsilon_r$ , and conductivity  $\sigma$ , see Figure 11. The reflection coefficient  $\rho$  is a function of  $\epsilon_r$ ,  $\sigma$ , and the grazing angle  $\psi$ . At a point in space, the resultant wave is the combination of a direct wave  $E_D$  and a reflected wave  $E_R$ .

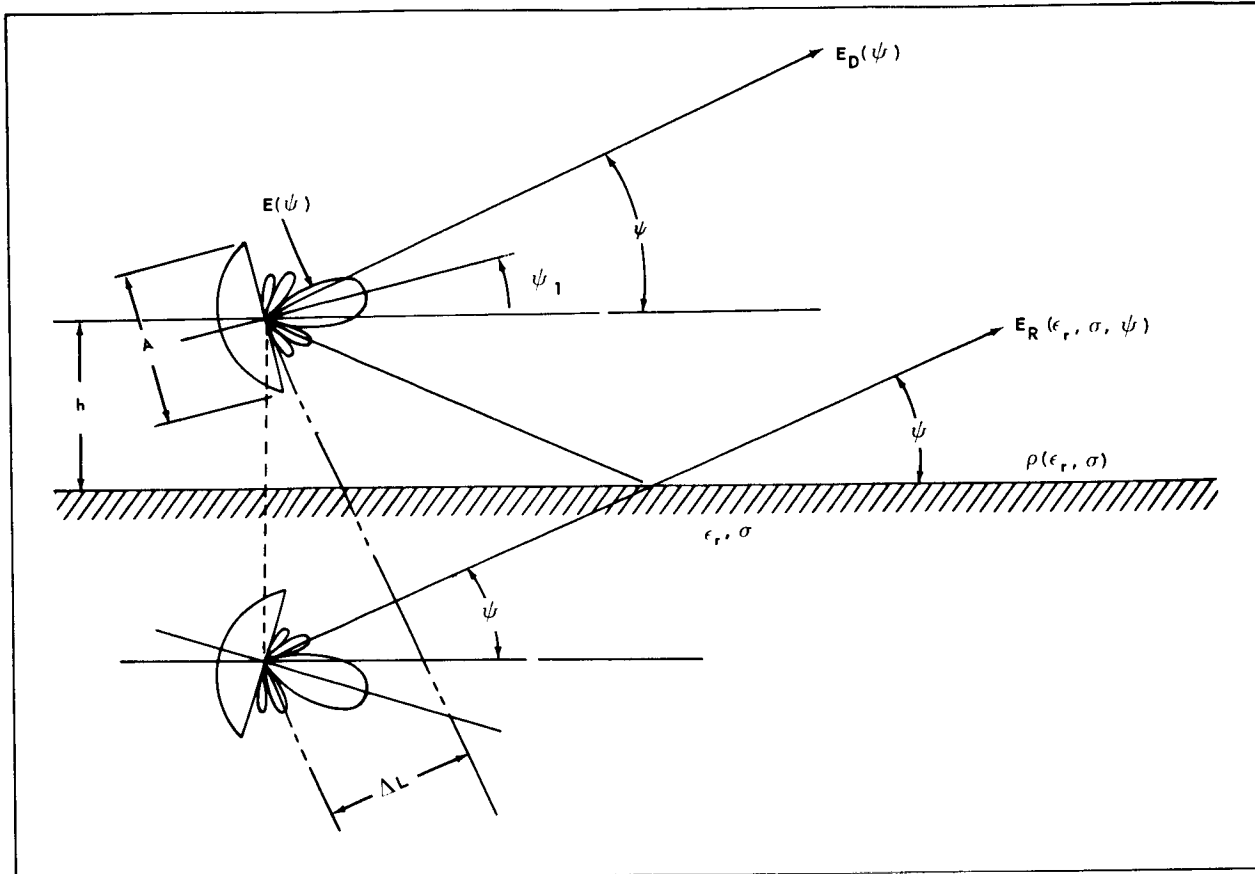


Figure 11. Multipath Image Geometry

The reflected wave may be considered as coming from an image antenna as shown. The reflected wave  $E_R$  may be described in terms of this image antenna, modified by the complex reflection coefficient  $\rho(\epsilon_r, \sigma, \psi) = \rho e^{j\alpha}$ .

Also, assuming the antenna radiation pattern  $E(\psi)$  is symmetrical, the radiation from the image antenna may be described by the same pattern. However, the direction of maximum radiation is reversed, accounting for the fact that as the elevation angle  $\psi_1$  is increased, less energy is directed above the ground plane from the image (i.e., less energy is reflected from the ground).

The phase of the reflected energy is a function of both the reflection coefficient and the path length difference between the direct and reflected rays. The path length difference may be easily evaluated from the image antenna. The difference in path length is given by:

$$\Delta L = 2h \sin \psi$$

Thus the phase term due to path length becomes

$$\phi = \beta \Delta L = 2 \beta h \sin \psi = \frac{4\pi h}{\lambda} \sin \psi$$

The field at a point in space may now be given by:

$$\begin{aligned} E &= E_D + E_R \\ &= E(\psi - \psi_1) + \rho e^{j\phi} E(\psi + \psi_1) \\ &= E(\psi - \psi_1) + \rho e^{j\alpha} e^{j \frac{4\pi h}{\lambda} \sin \psi} E(\psi + \psi_1) \end{aligned}$$

To simplify the problem, it is assumed that the radiation pattern is given by:

$$E(u) = \frac{\sin(u - z)}{(u - z)} \quad (\text{sum pattern})$$

where

$$\begin{aligned} u &= \frac{\pi A}{\lambda} \sin \psi \\ z &= \frac{\pi A}{\lambda} \sin \psi_1 \end{aligned}$$

or for the difference pattern

$$E(u) = \frac{\sin(u + \frac{\pi}{2} - z)}{(u + \frac{\pi}{2} - z)} - \frac{\sin(u - \frac{\pi}{2} - z)}{(u - \frac{\pi}{2} - z)}$$

The expressions for reflection coefficient for vertical and horizontal polarization may be written as:<sup>9</sup>

$$\rho_h = \frac{\sin \psi - \sqrt{(\epsilon_r - jX) - \cos^2 \psi}}{\sin \psi + \sqrt{(\epsilon_r - jX) - \cos^2 \psi}} = \rho e^{j\alpha_h} \quad (3-10)$$

$$\rho_v = \frac{(\epsilon_r - jX) \sin \psi - \sqrt{(\epsilon_r - jX) - \cos^2 \psi}}{(\epsilon_r - jX) \sin \psi + \sqrt{(\epsilon_r - jX) - \cos^2 \psi}} = \rho e^{j\alpha_v}$$

where

$\rho_v$  = reflection coefficient for vertical polarization

$\rho_h$  = reflection coefficient for horizontal polarization

$\epsilon_r$  = relative dielectric constant =  $\frac{\epsilon}{\epsilon_0}$

$\psi$  = grazing angle above horizon

$X = \sigma / w \epsilon_0 = 1.8 \times 10^4 / f_{mc}$



The reflection coefficient for circular polarization may be expressed in terms of  $\rho_v$  and  $\rho_h$ :  $\rho_c = 1/2 (\rho_v + \rho_h)$

The expression which must be evaluated to determine the effect of the ground on the error pattern may now be written:

$$E_D = \frac{\sin(u + \frac{\pi}{2} - z)}{(u + \frac{\pi}{2} - z)} - \frac{\sin(u - \frac{\pi}{2} - z)}{(u - \frac{\pi}{2} - z)} \quad (3-11)$$

$$E_R = \rho e^{j\alpha} e^{j\phi} \left[ \frac{\sin(u + \frac{\pi}{2} + z)}{(u + \frac{\pi}{2} + z)} - \frac{\sin(u - \frac{\pi}{2} + z)}{(u - \frac{\pi}{2} + z)} \right]$$

$$E_{\text{error}} = E_D + E_R$$

where

$E_{\text{error}}$  = error pattern in presence of ground

$E_D$  = direct ray field

$E_R$  = reflected ray field

$\phi = \frac{4\pi h}{\lambda} \sin \psi$

$h$  = antenna height above ground

$\psi$  = angle above horizon

$u = \pi A / \lambda \sin \psi$

$A$  = antenna aperture

$z = \pi A / \lambda \sin \psi_1$

$\psi_1$  = boresight angle above horizon

$\rho e^{j\alpha}$  = complex reflection coefficients (given by Equation (3-10))

A similar expression may be written for the sum pattern.

A program was written for the IBM 7094 computer to calculate the radiation pattern given by Equation (3-11). The program is general enough to calculate both sum and error patterns for any antenna height and elevation look angle. Patterns were calculated for the Apollo 30 ft. antennas over various types of terrain for circular polarization. Parameters varied were the antenna height above the ground, elevation "look" angle, and the conductivity and dielectric

constant of the ground. The program determines the reflection coefficient of the ground for any grazing angle and calculates the resultant far field pattern due to the direct and reflected rays from the antenna. From these patterns the effect of the ground on the boresight characteristics may be determined. A typical set of sum and difference patterns for the Apollo antenna at heights of 30 feet and 45 feet above a good ground are shown in Appendix III. Free space patterns are included for comparison. Patterns were run for a good earth ( $\sigma = .012$ ,  $\epsilon_r = 15$ ,) and for sea water ( $\sigma = 4$ ,  $\epsilon_r = 81$ ). Table 1 summarizes the boresight characteristics of the cases considered.

As may be seen, when the antenna boresight is at  $0^\circ$  elevation, the radiation pattern boresight moves up and the null fills in. This beam tilt or boresight error is a function of the antenna height and elevation angle. From Table 1. it can be seen that the ground still has an effect on the boresight characteristics at a  $2^\circ$  elevation angle, however at  $5^\circ$  the effect appears to be small. Though some distortion and null filling of the patterns is still present, there is no apparent boresight shift. This does not necessarily mean that track could be maintained in this region. Effects of rough terrain, multipath from mountains, and increased noise could result in loss of track.

TABLE 1. MULTIPATH EFFECT

Apollo 30 Foot Antennas  
Circular Polarization

A. Antenna above a good ground ( $\sigma = .012$ ,  $\epsilon_r = 15$ )

Ant. Height (ft)	Elevation Angle (deg)	Null Position (deg)	Null Depth (db)
15	0	0.4	25
15	0.5	0.57	13
15	1.0	1.0	26
30	0	0.2	31
30	0.5	0.6	27
30	1.0	1.0	29
30	2.0	2.0	22
30	3.0	3.0	27
30	4.0	4.0	30
30	5.0	5.0	25
45	0	0.15	25
45	1.0	1.0	29

TABLE 1. MULTIPATH EFFECT (Continued)

Ant. Height (ft)	Elevation Angle (deg)	Null Position (deg)	Null Depth (db)
45	2.0	2.03	29
45	5.0	5.0	26

B. Antenna above sea water ( $\sigma = 4$ ,  $\epsilon_r = 81$ )

15	0	0.46	21
15	0.5	0.57	14
15	1.0	1.0	27
15	2.0	2.06	28
30	0	0.21	32
30	0.5	0.6	23
30	1.0	1.0	30
30	2.0	1.98	23

After observing the effect of the ground on the radiation patterns, it appeared desirable to know the phase characteristics of the antenna patterns in the bore-sight region. The computer program was modified to provide this information and several cases run to include this information. For low elevation angles the results are not good. For some cases it appears that even though a null occurs in the radiation pattern, the antenna might not lock onto the spacecraft, as only  $100^\circ$  phase change is experienced in going through the boresight null. To actually determine the antenna tracking performance at such elevation angles it would be necessary to simulate the tracking receiver output to the antenna servos for these conditions. This could be accomplished by using a monopulse antenna with a monopulse processing circuit to determine the error signal output characteristics. Such an experimental approach could be carried out over various terrain to simulate actual operating conditions. A program of this type would permit correlation with the theoretical calculations, and perhaps enable a modified theory to be established.

#### 3.4.2 Experimental Measurements of Boresight Errors

As the problem of multipath appears to be serious near horizon, and analysis of the problem can only be based on an ideal situation, an experimental approach was also taken. Measurements were made on a monopulse feed over a ground plane, and boresight measurements were also made on a 40 foot diameter tracking antenna. These measurements are described below.

#### 3.4.2.1 Feed Over a Ground Plane

To provide experimental data on boresight shift near the ground, a small monopulse feed was set up over an aluminum ground plane. This assembly was mounted on a pattern range to facilitate taking detailed patterns. As such a model can easily become too large for installing on a mount, a small X-band feed, with a four inch aperture was used. Difference patterns were taken for various elevations above the ground plane. The patterns were then compared with patterns calculated by the computer program. A comparison of the experimental patterns with computed patterns indicate that the position of nulls and peaks of the patterns could be correlated; however, the relative sidelobe levels do not agree. This is probably due to the short ground plane used (about 30 wavelengths). Patterns of the 4 1/4 inch monopulse aperture are shown in Figures 12, 13, 14, 15 for an aperture height above the ground plane of six inches and various elevation angles. The free space patterns are also shown for comparison. As may be seen, the boresight null moves about as a function of elevation angle. Also, the effect of a double null at 10 degrees elevation is seen. At 0 degree elevation, the apparent difference between the free space boresight and the edge of the ground plane is due to the fact that the measurements are made at the ground plane edge, and the height of the aperture above the ground plane results in an angle between the boresight axis and the edge of the ground plane. For an infinite, or very large ground plane, the antenna height could be neglected, and the boresight axis would appear at 0 degrees for both the free space pattern and the pattern above the ground plane. In this case, however, the sum patterns would also have a null at 0 degrees, and the system would have to lock on another null, possibly the first one above the ground plane.

#### 3.4.2.2 Multipath Effect on Boresight of a 40 Foot Antenna

A 40-foot antenna (AN/MS-46) was used to determine the gross effect multipath has on the boresight axis. The antenna has a 3 dB beamwidth of .25 degrees and receives a left hand circular monopulse signal. The antenna was situated atop a hill which is 50 to 100 feet higher than the immediate proximity. A boresight tower was erected at three sites 1,000 to 1,300 feet from the antenna, and the boresight shift was measured by changing the frequency a total of 7 per cent. Although no general conclusions can be made because of the uncontrolled environment, the following may be summarized: (see Table 2).

1. Site I showed no boresight shift.
2. Site II exhibited as much as a beamwidth (.25 degrees) shift in elevation and about 1/4 beamwidth in azimuth. For certain frequencies, two indistinguishable boresight nulls appeared in elevation spaced .25 degrees apart.

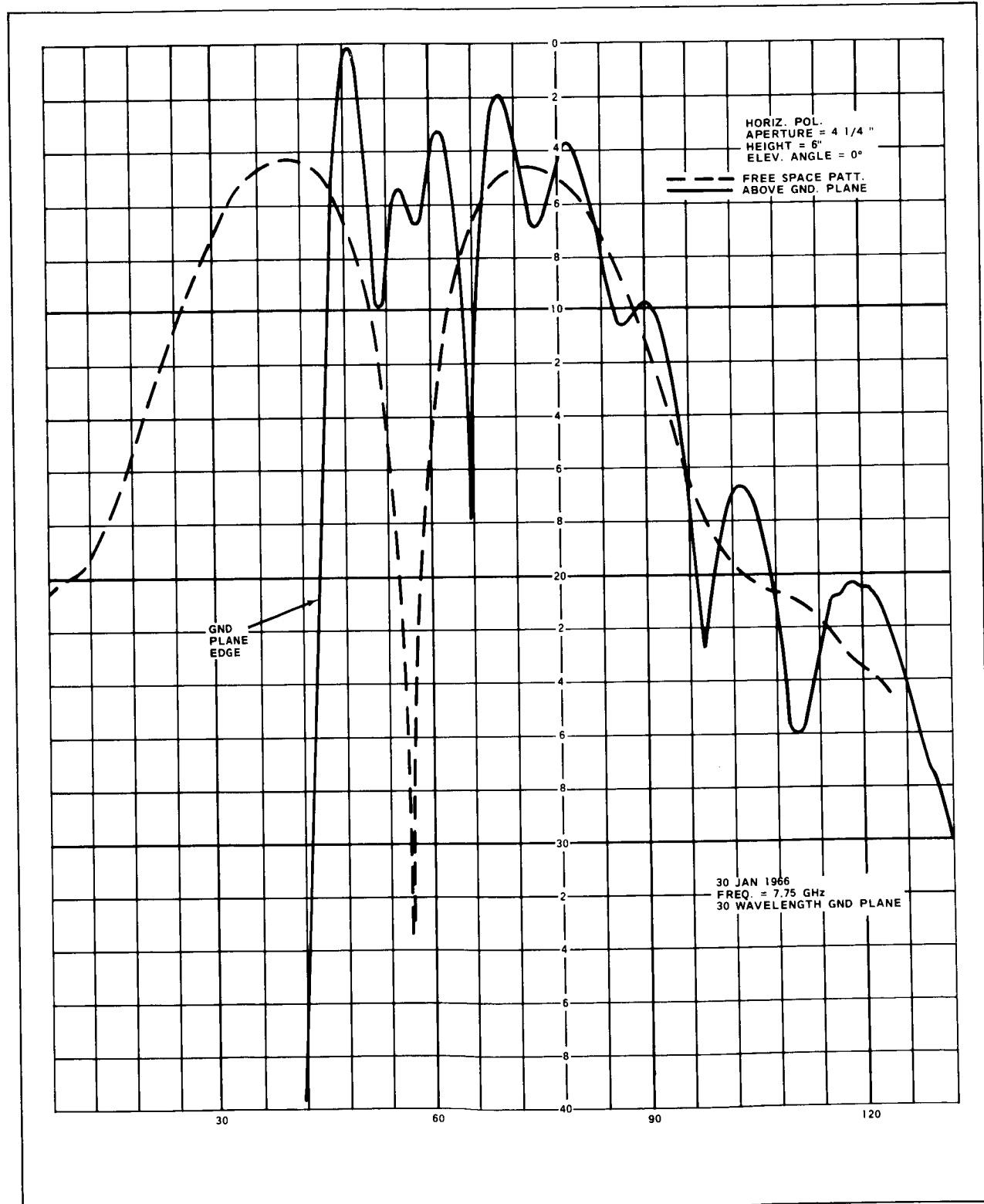


Figure 12. Error Pattern above a Ground Plane Elevation = 0°

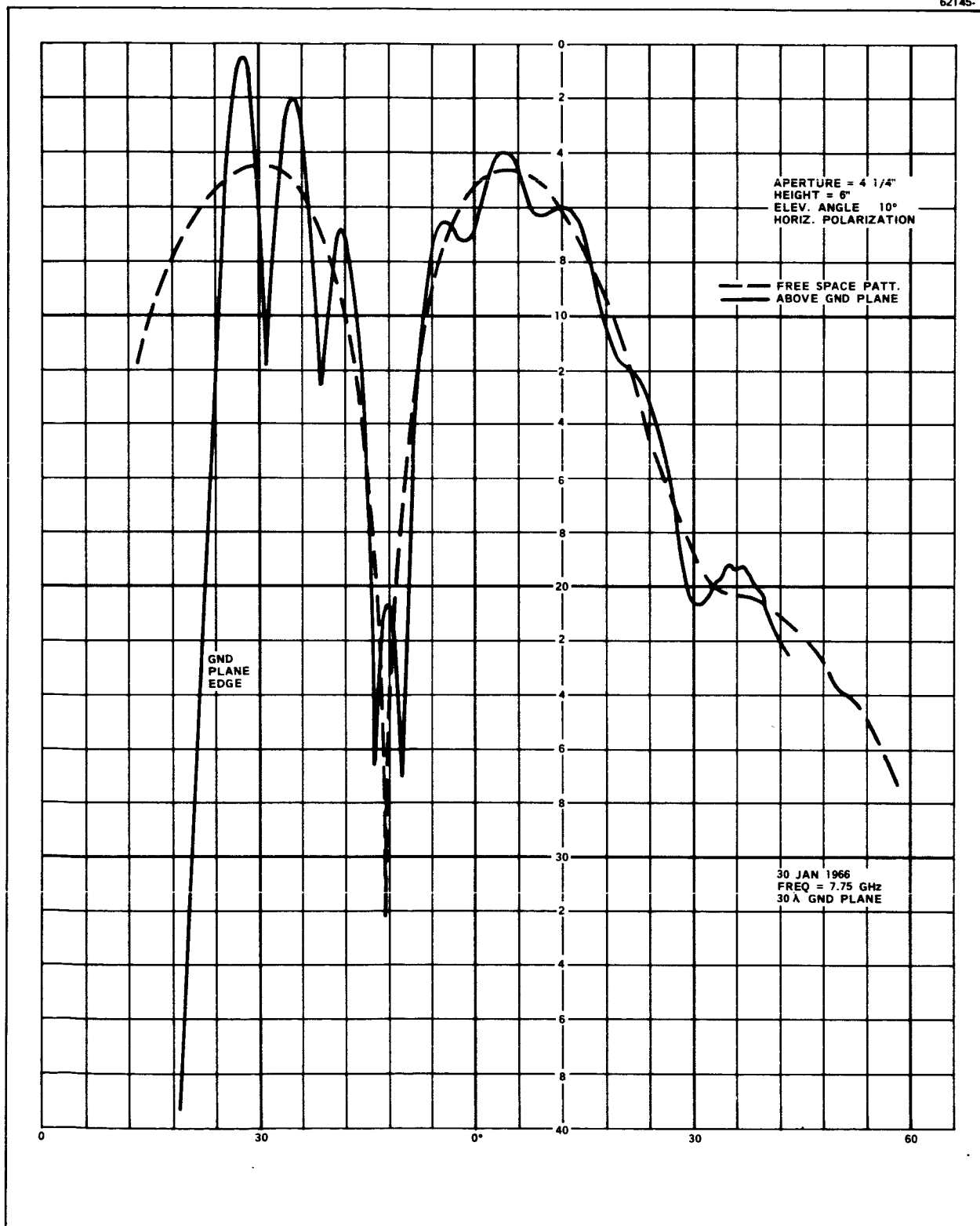


Figure 13. Error Pattern above a ground Plane Elevation =  $10^0$

62145-14

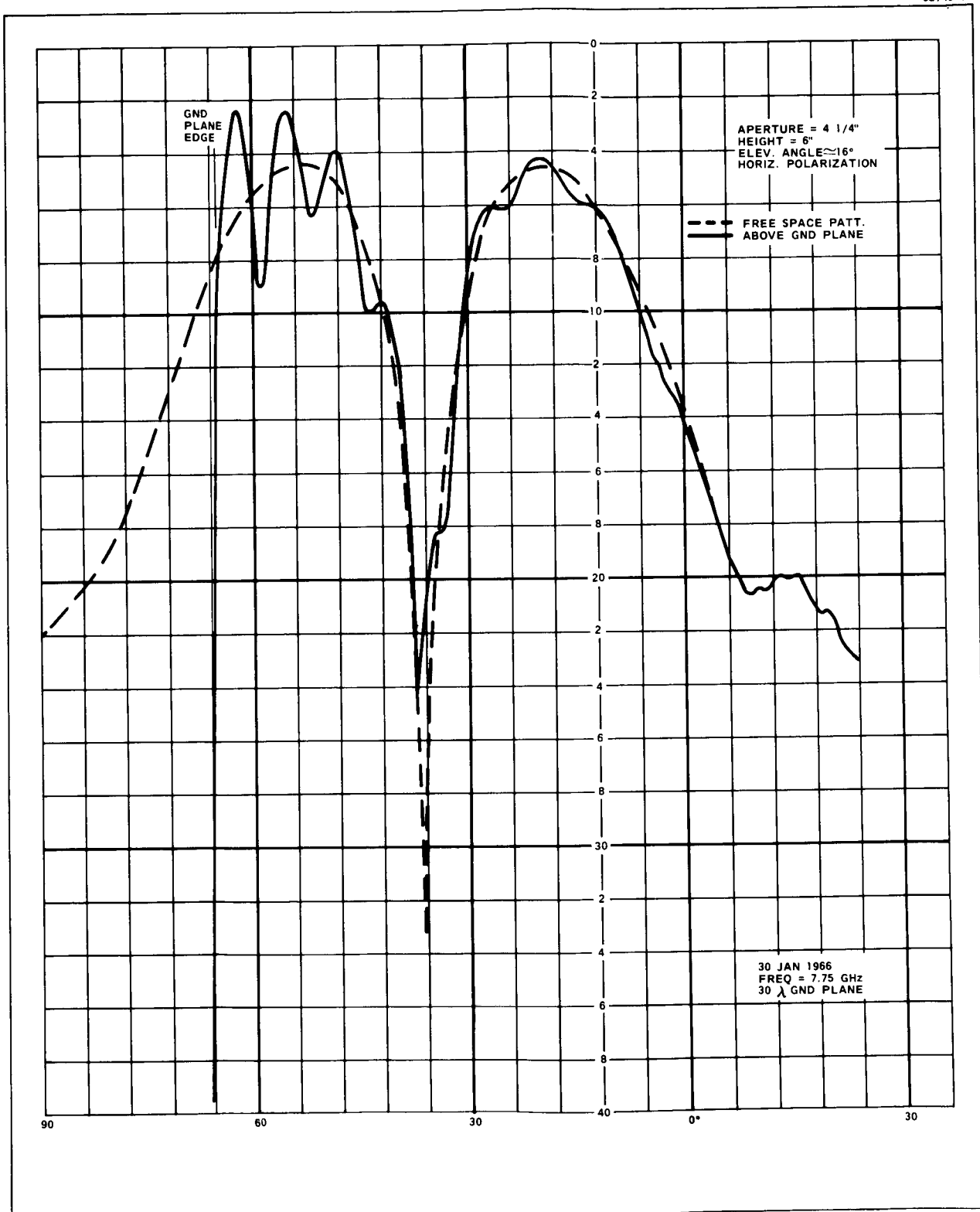


Figure 14. Error Pattern above a Ground Plane Elevation =  $16^\circ$

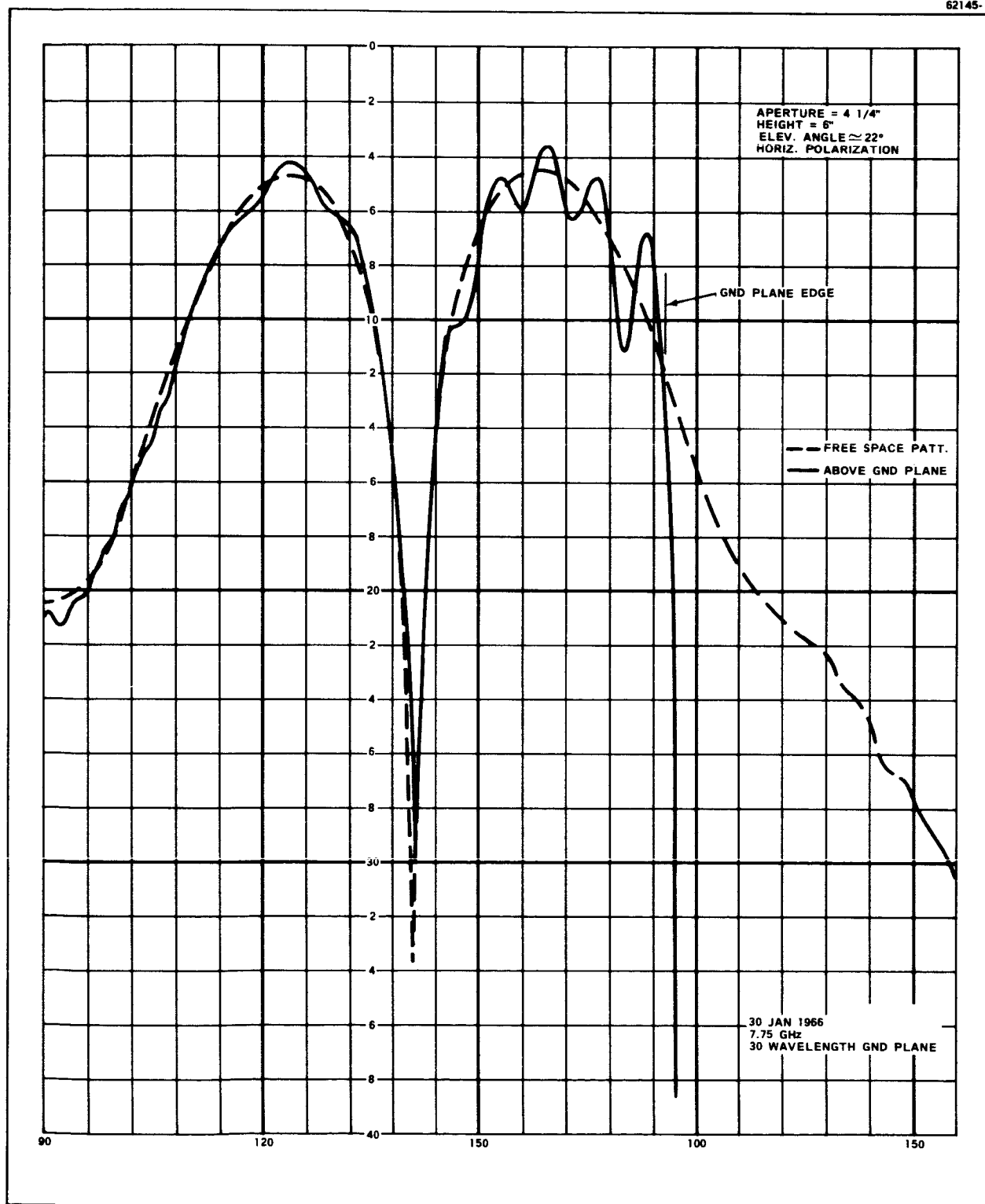


Figure 15. Error Pattern above a Ground Plane Elevation =  $22^\circ$



3. Site III exhibited no azimuth shift but  $1/8$  beamwidth in elevation. The elevation boresight shift occurred primarily over the lower half of the frequency band and negligible amount at the higher frequency band.
4. The boresight tower at Site II was elevated 20 feet higher with no change in magnitude of the boresight shift.
5. The boresight tower at Site III was raised 10 feet higher with no change in magnitude of the boresight shift.

Site I and Site II appear to be very similar in topographical environment with minor differences as noted in Table 2. The six foot high wire mesh fence in the proximity of the antenna may have resulted in cancellation of multipath effect for Site I, and the edge of the building, which was near the line-of-sight for Site II, may be the cause of the large error measured. However, the large effects which multipath may cause near horizon are well illustrated by this data.

TABLE 2. BORESIGHT MEASUREMENTS

	Site I	Site II	Site III
Boresight Shift (Maximum)			
Azimuth	0	.07 degrees	0
Elevation	0	.25	.04 degrees
Tower Height	35 foot tower	20 feet above 35 foot building	30 foot scaffold
Elevation Angle from Antenna	1.5 degrees	2 degrees	1 degree
Environmental Description	Parking lot 50- 100 feet below line of sight. Six foot wire mesh fence near antenna.	Parking lot 50- 100 feet below light of sight. Top edge of of building slightly below and to the side of the line of sight.	Utility wires crossed hori- zontally in line of sight. No buildings in the vicinity.

#### 3.4.3 Signal/Noise Effects

During low angle tracking, an additional problem is encountered which affects both communications and tracking. At low angles (i. e., less than 10 degrees elevation) the noise incident on the antenna increases rapidly. This is due to several effects, two principal ones being atmospheric absorption and sidelobes looking into the "hot" ground. At the same time, the antenna gain is reduced by the atmospheric attenuation at low angles. This factor is also appreciable.

Figure 16 is a graph of atmospheric loss as a function of elevation angle at 2500 MHz, based upon a delta function antenna beam.<sup>10</sup> At the horizon (i. e., 90 degrees in Figure 16) the attenuation is over 2 db with a corresponding noise temperature of about 110° K. This rapidly decreases to about 0.38 db loss and 25° K at an elevation angle of 5 degrees (i. e., 85 degrees from zenith). This effect is in addition to the noise increase due to antenna sidelobes looking into the ground.

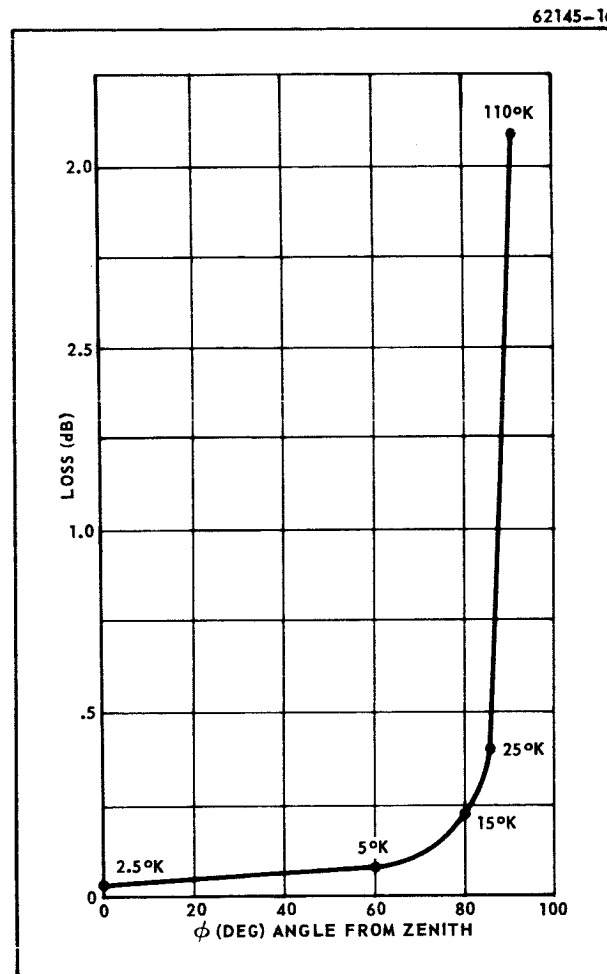


Figure 16 One Way Attenuation Through Atmosphere Due to  $H_2O$  and  $O_2$  at 2500 MHz

Figure 17 illustrates the effect of sidelobe energy incident upon the ground.

For a circular aperture, the antenna radiation pattern null planes may be represented by a set of coaxial cones; thus taking a cut through the boresight axis one would see an energy distribution as represented in Figure 18.

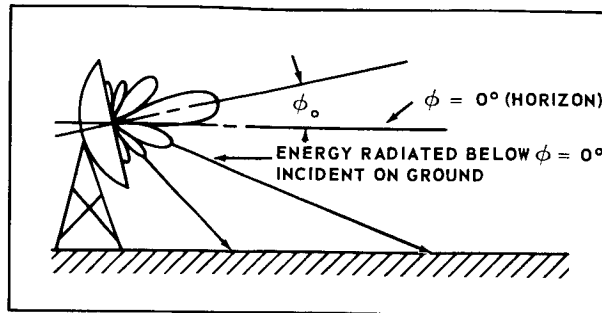


Figure 17. Antenna Sidelobes Radiating Into Ground at Low Elevation Angles

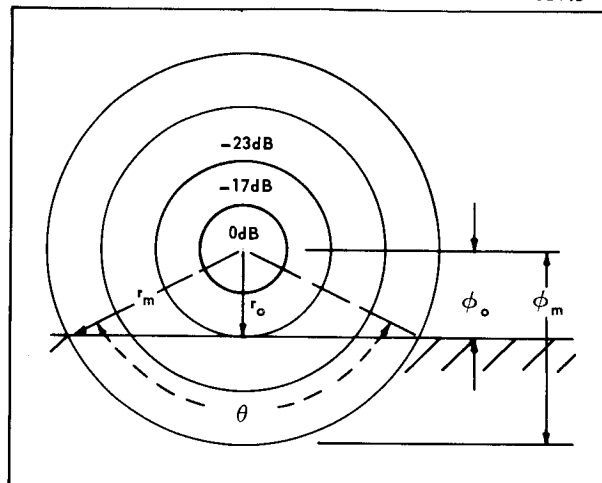


Figure 18. Radiation Pattern - Circular Aperture (Cut Normal to Boresight Axis)

The portion of the area included within the circular null planes which strikes the ground is given by

$$A_{\text{segment}} = (\pi r_m^2 \theta) / 360 - (r_m^2 \sin \theta) / 2 \quad (3-12)$$

If standard graphical integration techniques<sup>11</sup> are used to determine the energy contained within various regions of the antenna beam, that portion lying between  $\phi_o \leq \phi \leq \phi_m$  may be determined. ( $\phi_o$  = elevation angle above boresight,  $\phi_m$  = angle off boresight to where radiated energy is low enough to neglect in graphical integration).

The portion of the energy in this annular region striking the ground is then determined from the ratio

$$P = \frac{A_{\text{segment}}}{A_{\text{ring}}} = \frac{r_m^2 \left[ \pi \theta / 360 - (\sin \theta) / 2 \right]}{\pi (r_m^2 - r_o^2)} \quad (3-13)$$

The distances  $r_m$  and  $r_o$  may be determined approximately from the angles  $\phi_m$  and  $\phi_o$ , i. e.

$$r_m \approx R\phi_m, \quad r_o \approx R\phi_o$$

where  $R$  = range from antenna. Also the segment angle " $\theta$ " may now be found to be:

$$\theta = 2 \cos^{-1} \frac{r_o}{r_m} = 2 \cos^{-1} \frac{\phi_o}{\phi_m}$$

Substituting into Eq. (2) yields:

$$P = \frac{1}{1 - (\phi_o/\phi_m)^2} \left[ \frac{\cos^{-1} \phi_o/\phi_m}{180} - \frac{\sin 2(\cos^{-1} \phi_o/\phi_m)}{2\pi} \right] \quad (3-14)$$

Eq. (3-14) then gives a method of determining the noise temperature increase due to energy striking the ground.

If  $T_g$  = effective noise temperature of the ground,  $E_r$  = energy in the annular region  $\phi_m \leq \phi \leq \phi_o$  determined by pattern integration, then the noise temperature contribution of the energy striking the ground is

$$T_s = PE_r T_g \quad (3-15)$$

Using Eq. (3-15) and the graph, Figure 16, it is possible to approximate the noise temperature of the antenna for any elevation angle near the horizon, for a given ground temperature.

Analytic determination of the increase in noise temperature of the antenna near horizon is difficult, however, because of the various types of terrain encountered. Previous estimates<sup>8</sup> of antenna and system noise temperature have resulted in values of 65°K for zenith and 185°K for the horizon antenna temperature. This results in a system temperature of 233°K at zenith and 353°K at horizon with a 168°K paramp and receiver. If a cooled paramp is used with a temperature of about 35°K, the system temperatures become 100°K (zenith) and 220°K (horizon).

Based on pattern integration of the 30 Foot Apollo antenna patterns, and measurement made on other antennas<sup>12</sup>, the above figures for antenna temperature seem somewhat high. A better figure for zenith temperature would appear to be approximately 35 - 40°K\*. The figure for horizon temperature is probably reasonable. Predicting an exact horizon temperature is difficult as the distribution of energy

---

\*Based on a circuit loss of 0.5 dB, contributing 30°K, a sky temperature of 2.5°K, and about 5 - 10°K due to antenna spillover and reflector absorption.

into the ground, atmosphere, etc. is not explicitly known. Most reasonable estimates of power distribution result in an expected temperature of about 150 - 200°K. Applying the graphical integration technique to the theoretical freespace patterns used to evaluate multipath results in an expected noise temperature at horizon of 165°K. This increases rapidly from 25°K at 5 degrees elevation to 165°K at horizon as would be expected from the increased atmospheric attenuation and sidelobes into the ground at these angles.

### 3.5 Plasma

A space vehicle re-entering the earth's atmosphere at hypersonic velocities acts upon the molecular structure of the surrounding air due to tremendous aerodynamic heating. The effect is thermal ionization of the atmosphere surrounding the vehicle. This action results in liberation of free electrons and ions in the form of a plasma sheath which serves to interfere with electromagnetic propagation. Such interference is characterized by absorption, refraction, and reflection of the electromagnetic energy; at times causing a complete communication blackout. This possible loss in communications poses a serious problem since it occurs during a critical phase of the Apollo mission.

A fundamental requirement for propagation through the plasma is that the signal frequency be above the plasma resonance frequency ( $f_p = 8.9 \times 10^3 \sqrt{N}$ ), where  $N$  is the free electron concentration of the plasma<sup>13</sup>.

Figure 19 shows the relationship between vehicle velocity, electron density, and plasma frequency<sup>13</sup>. Since the Apollo re-entry velocity is 35,000 ft/sec<sup>14</sup>, the operating frequency is far below the plasma frequency and hence; communications will be disrupted. Typical Apollo re-entry trajectories are shown in Figure 20 for ranges of 5000, 3,000, and 1,000 nautical miles at a flight path angle of -6.4 degrees<sup>14</sup>. The communications blackout regions are indicated in cross-hatched areas.

During the periods of re-entry when the velocity of the vehicle is such that the operating frequency is above but near the plasma frequency, degradation in the communication link will be encountered due to the plasma impedance and its close proximity to the spacecraft antenna. The ratio of operating frequency to plasma frequency must, therefore, remain large to insure good re-entry communication. Since it may become impractical to raise the operating frequency well above the plasma frequency, an alternative is to reduce the plasma frequency by reducing the free-electron concentration. Various approaches to this problem are under study<sup>15, 16</sup>, such as adding material to the plasma for de-ionization, aerodynamic shaping of the space vehicle by use of external pods, and introduction of a static magnetic field.

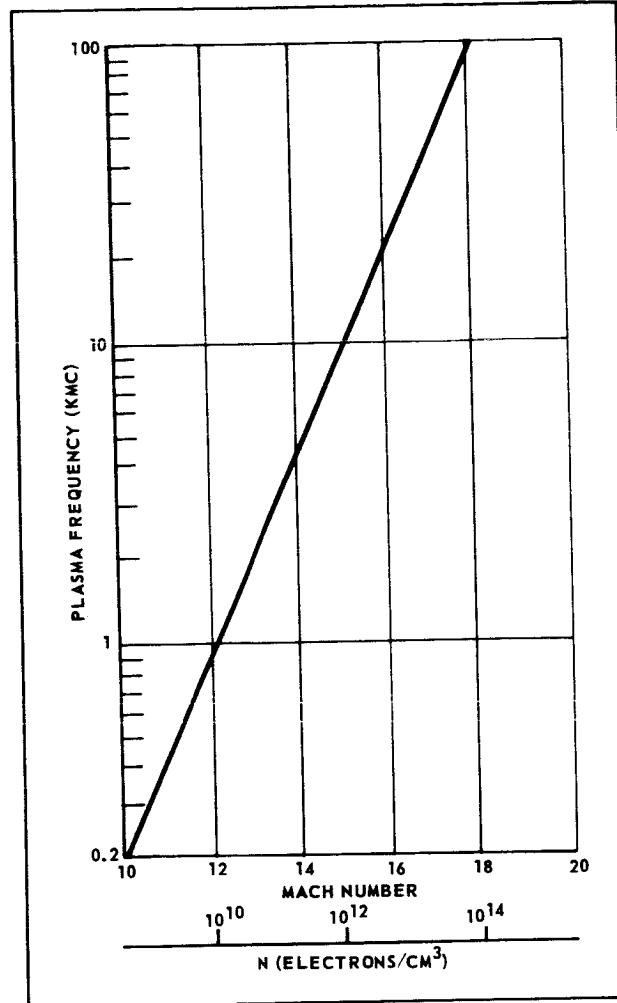


Figure 19. Plasma Frequency Versus Mach Number and Electron Density (N)

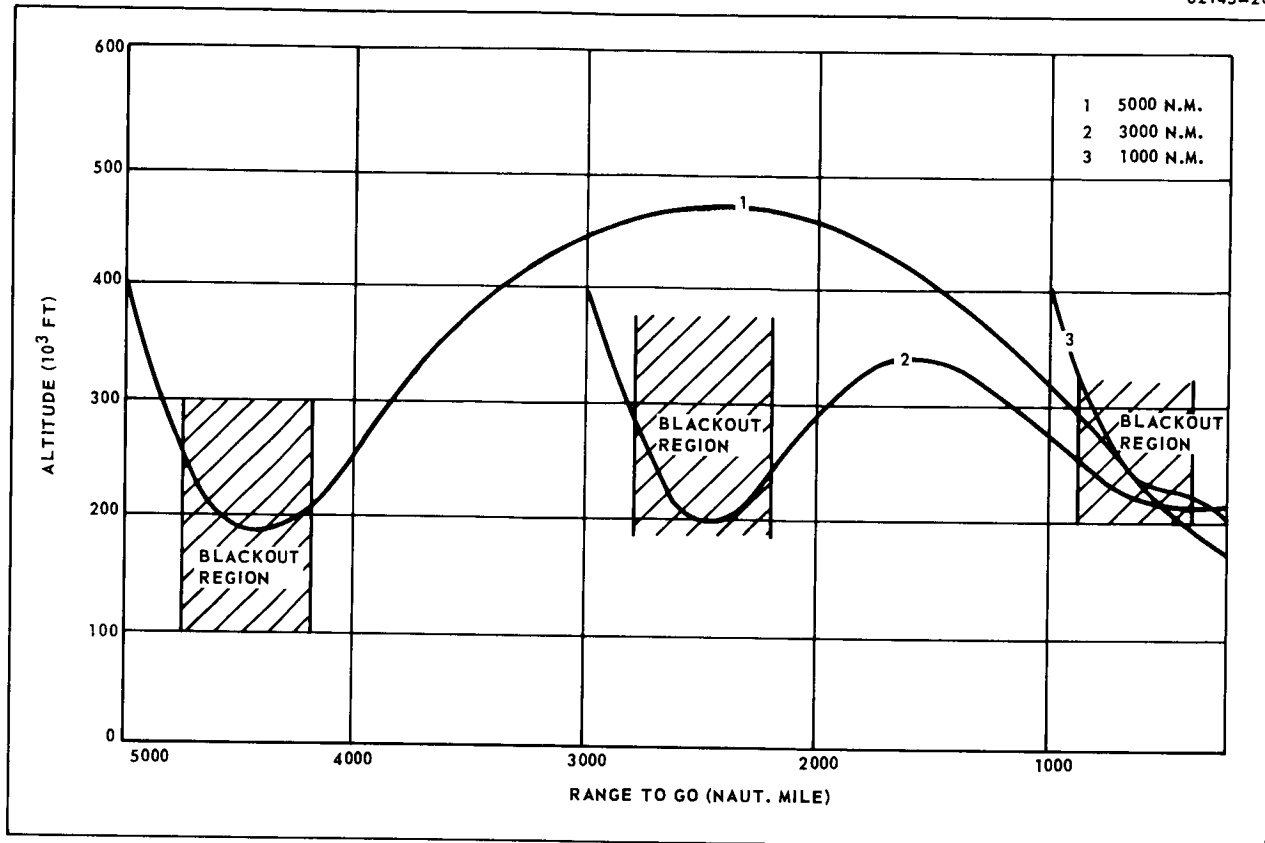


Figure 20. Apollo Re-entry Trajectories

#### **Section Four**

### **SYSTEM PERFORMANCE ANALYSIS**



#### 4. SYSTEM PERFORMANCE ANALYSIS

##### 4.1 EFFECT OF POLARIZATION PARAMETERS ON TRACKING

To determine the tracking performance of the Apollo system, it is first necessary to consider the relative performance of the spacecraft antenna system with respect to the ground stations. The effect of off axis pattern ellipticity may be determined by considering the spacecraft antenna configuration and orientation during various portions of the mission.

Also, the performance of the phase locked loop must be known throughout the mission. Analysis of the phase locked loop performance has been considered in some detail by several authors<sup>17,19,20</sup>, and additional calculations were performed in this study. (See Appendix IV). Using this data, the phase error in the phase lock loop can be related to the angle tracking accuracy and the ranging accuracy.

##### 4.1.1 Mission Geometry

The relative position and movement of the spacecraft antenna system with respect to the ground based antennas in the MSFN plays an important part in ascertaining the overall quality of the Apollo communication and tracking link. In this respect, the off-axis axial ratio characteristics of the spacecraft antennas come into consideration. The investigation of this subject is divided into four specific phases of the mission: (1) lift-off to 2500 nautical miles, (2) 2500 nautical miles to 28,000 nautical miles, (3) 28,000 nautical miles to 115,000 nautical miles, and (4) 115,000 nautical miles to the lunar distance. It will be assumed throughout this analysis that the high gain antenna gimbal will sufficiently compensate for spacecraft yaw and pitch maneuvers.

##### (1) Liftoff to 2500 Nautical Miles

This phase of the mission includes insertion, earth parking orbit, and trans-lunar injection. During these periods, S-band communications and tracking are accomplished by means of the four omnidirectional antennas located at the base of the

command module. In addition, the command and communication system (CCS) located in the SIVB instrument unit (IU) provides a backup for spacecraft ranging as well as up-data command and down-link telemetry.

The omnidirectional antennas are of the helical type with -3 db gain over an 80 percent spherical coverage. This type of antenna normally has a large off axis ellipticity. For the purposes of analysis, it is assumed that the worst case spacecraft axial ratio will approach linear polarization, resulting in a maximum of 3.54 dB additional loss in the communication link (See Graph I-10). Since there are four omni antennas spaced at 90-degree intervals around the perimeter of the command module, coverage is provided by the spacecraft to all ground stations within range, regardless of the spacecraft roll angle.

## (2) 2500 Nautical Miles to 28,000 Nautical Miles

The high gain antenna located on the spacecraft service module is deployed at approximately 2500 nautical miles earth altitude. The high gain antenna transmits and receives RCP with three switchable beamwidths: wide ( $>45^\circ$ ), medium ( $>10.4^\circ$ ), and narrow ( $>4.4^\circ$ ). The wide mode is used both for transmission and reception from 2500 to 30,000 nautical miles. Figures 21, 22, and 23 were obtained from the patterns of the high gain antenna given in reference 21. Axial ratio versus angle off boresight is depicted for the three modes.

Consider the situation at 2500 nautical miles earth altitude as illustrated in Figure 24. The spacecraft is estimated to be at approximately 40 degrees W. long. by 17 degrees N. lat. based upon the lunar transfer trajectory shown in Figure 1, page 14, of reference 8.

During this phase of the mission, the spacecraft is assumed to be tracked by the 30 foot stations at Bermuda and Ascension and the 85 foot station at Madrid. If the spacecraft antenna is boresighted on the Bermuda station, then the Madrid station is approximately 44 degrees off boresight. From Figure 21, the axial ratio of the received signal at Madrid is 7 db. Since the maximum boresight axial ratio of the Madrid antenna is 1 db, then from Graph I-3 (Appendix I), the power loss due to polarization orientation will vary from 0.4 db to 0.8 db. If the maximum roll rate of the spacecraft is 0.5 deg/sec<sup>22</sup> and the spacecraft antenna does not compensate for spacecraft roll, then the signal received at Madrid will be amplitude modulated at 0.00139 cps with a maximum amplitude of 0.4 db.

For the same conditions the Ascension Island tracking station is approximately 66 degrees off boresight corresponding to an axial ratio of at least 10 db. The resulting power loss varies from 0.8 db to 1.3 db which produces a 0.5 db amplitude modulation of the down link signal due to spacecraft roll.

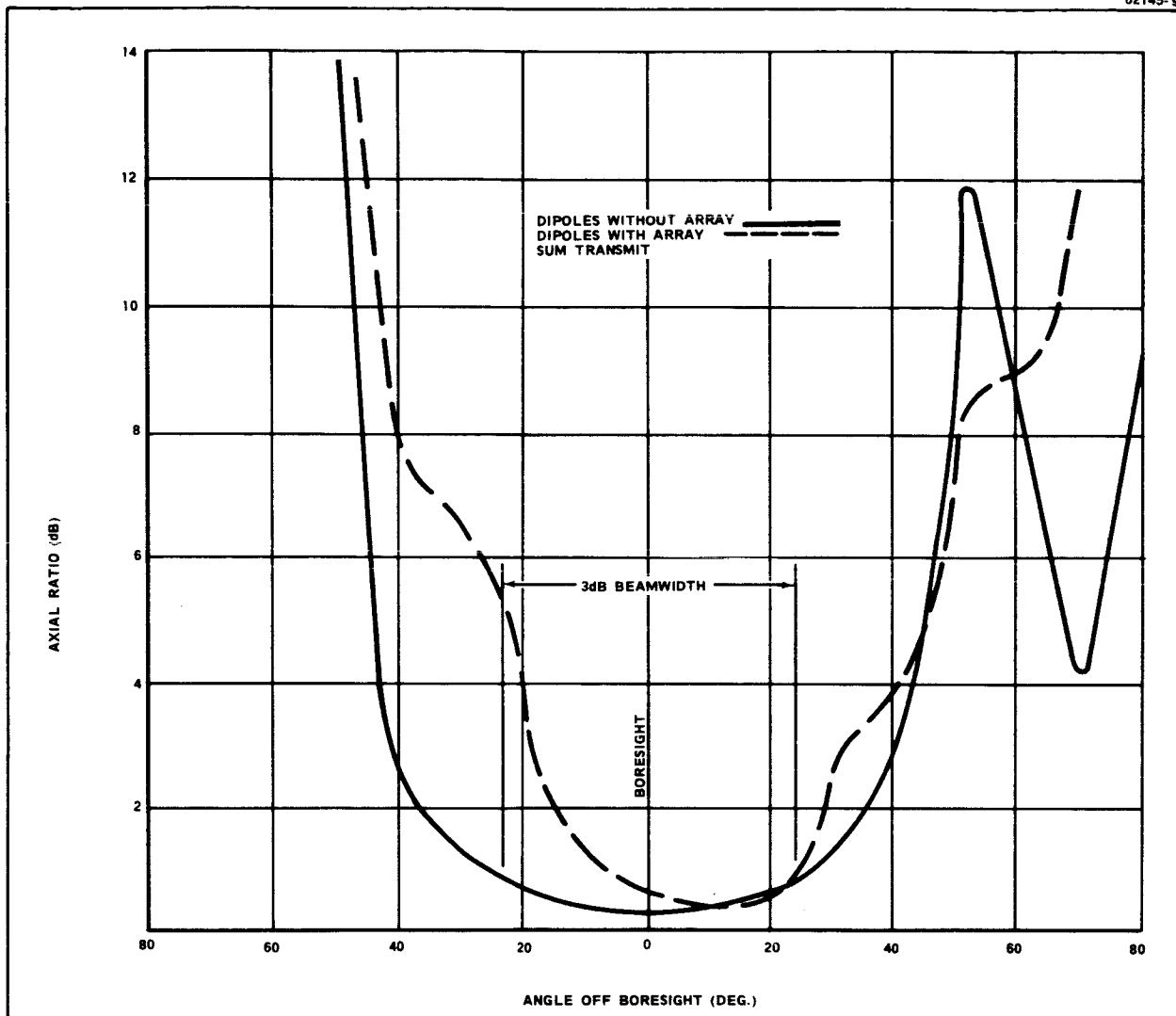


Figure 21 Axial Ratio Versus Angle off Boresight, Wide Mode

62145-92

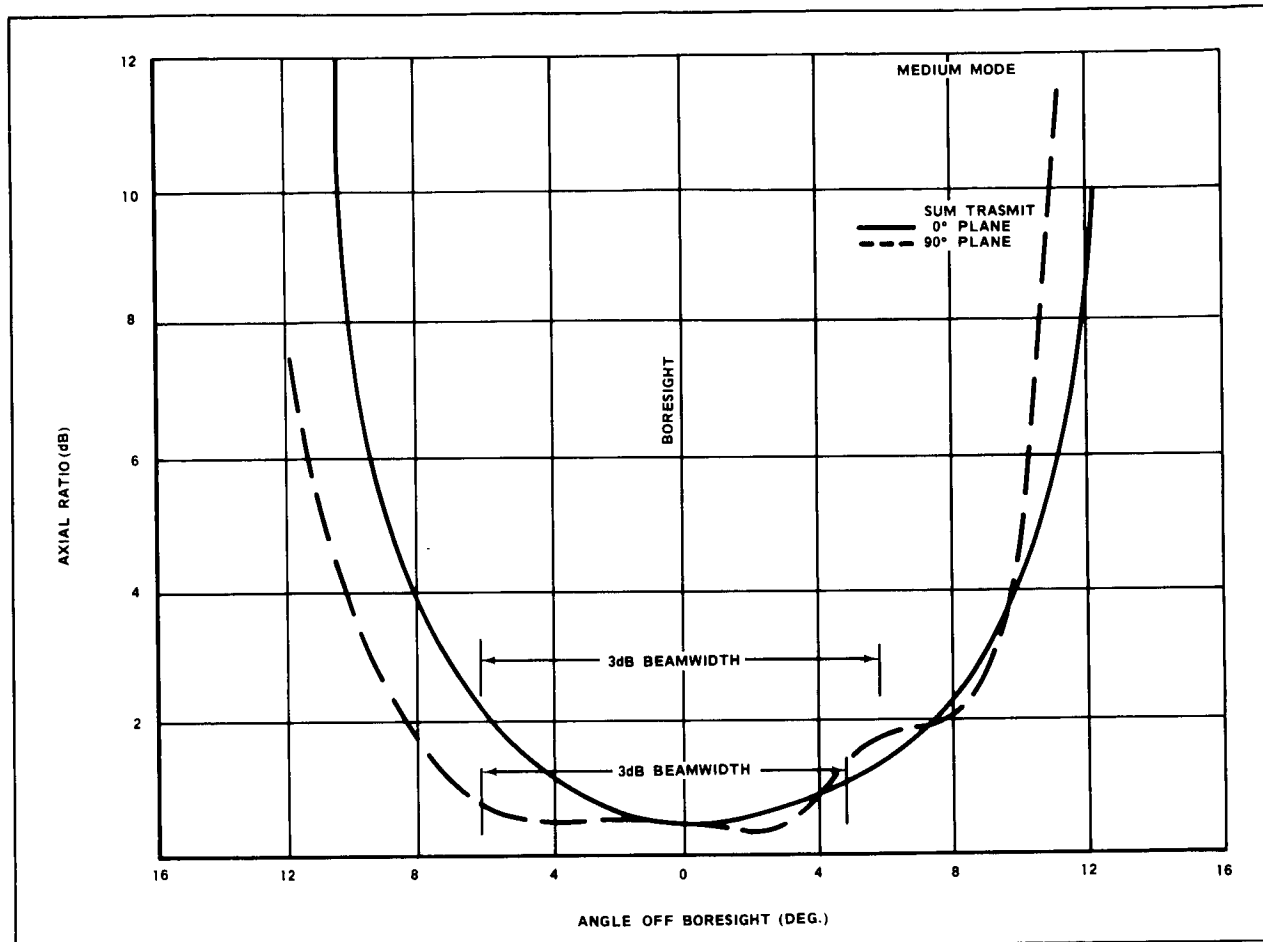


Figure 22 Axial Ratio Versus Angle off Boresight, Medium Mode

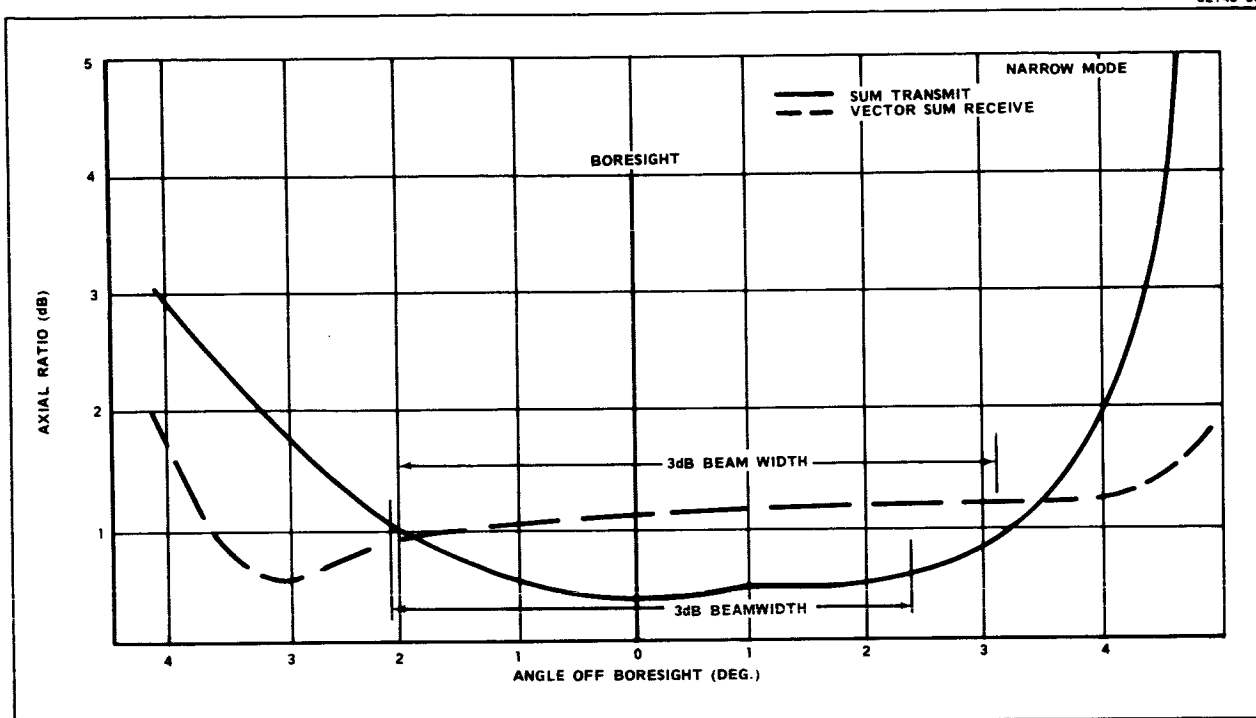


Figure 23 Axial Ratio Versus Angle off Boresight, Narrow Mode

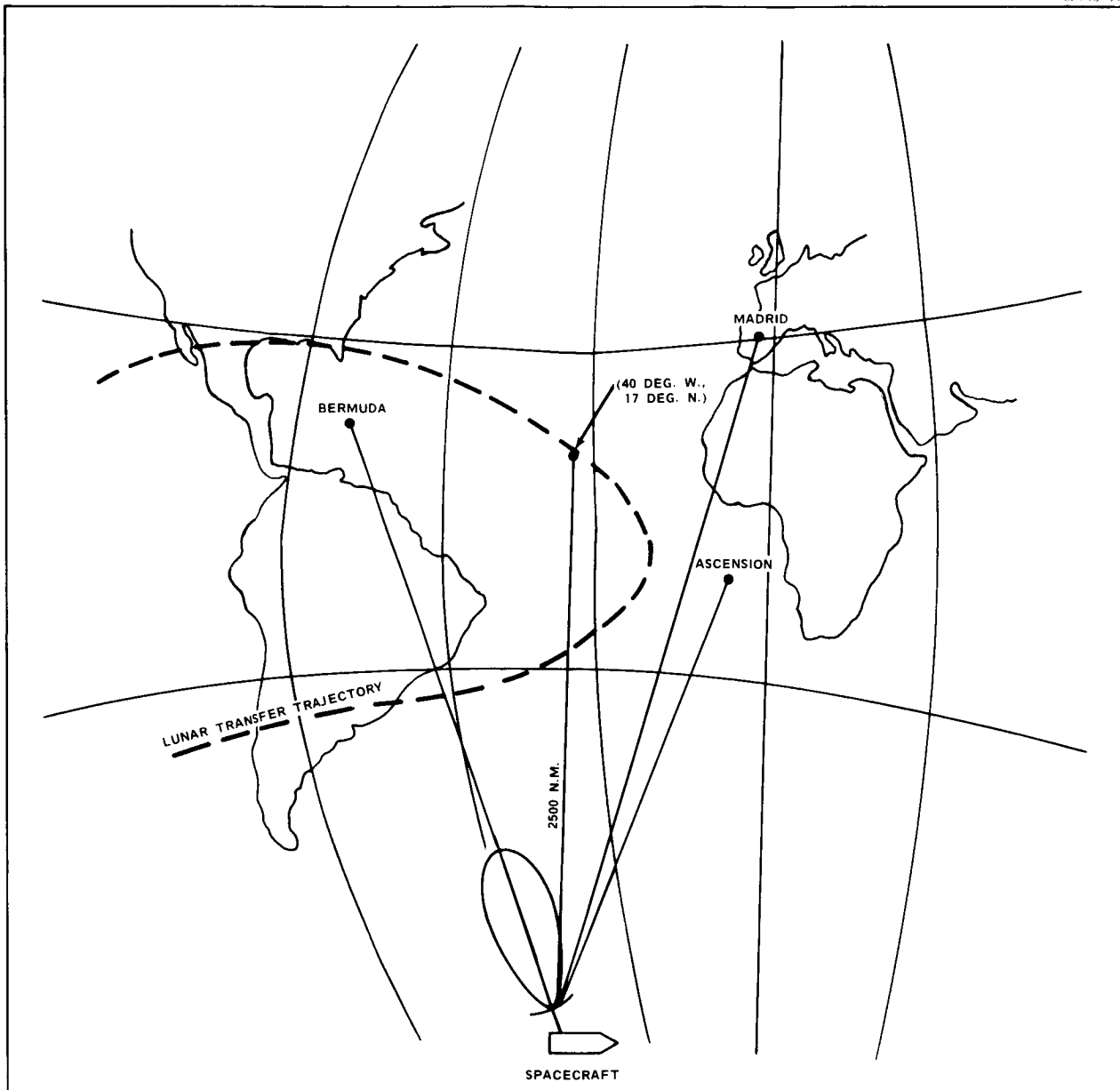


Figure 24. Spacecraft Tracking at 2500 Nautical Miles

Consider now that the spacecraft is boresighted on the Madrid tracking station instead of Bermuda. Ascension Island then lies approximately 37 degrees off boresight corresponding to a received signal axial ratio of 7 db, the same as that received by Bermuda.

These effects decrease as the spacecraft altitude increases because the angle subtended by the earth becomes smaller.

(3) 28,000 to 115,000 Nautical Miles

The medium beam mode of the spacecraft high gain antenna is deployed at an earth distance of approximately 28,000 nautical miles. Worst case conditions for this spacecraft position would occur when the primary tracking station is located at the earth's horizon (zero degrees elevation angle) and the secondary tracking is located at the opposite horizon as shown in Figure 25.

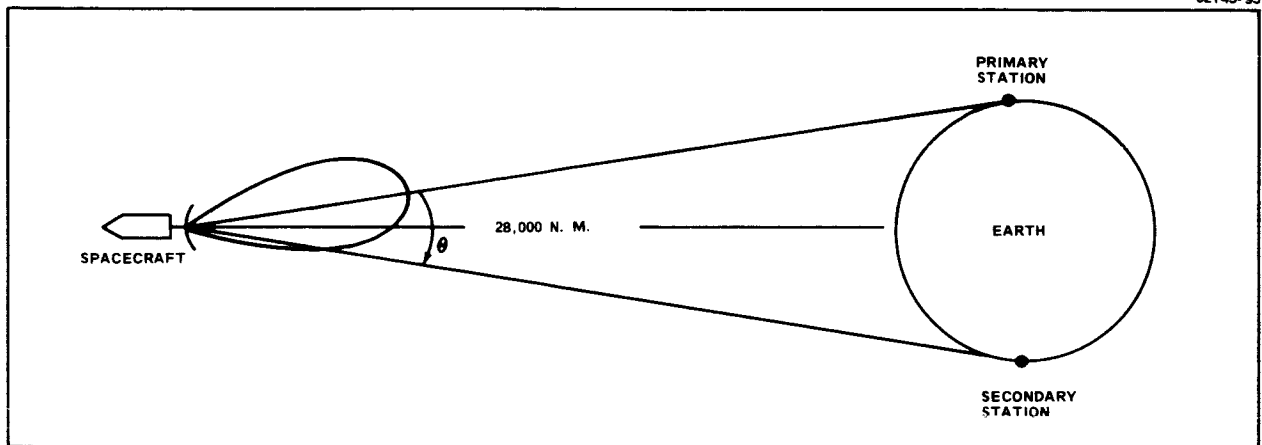


Figure 25. Worst-Case Tracking at 28,000 Nautical Miles

The off boresight angle ( $\theta$ ) of the secondary station is then 12.5 degrees plus 1.05 degrees pointing error. The gain of the antenna (0.2 db) at this angle is sufficient to be above the minimum required gain at 28,000 nautical miles.<sup>21</sup> Referring to Figure 22, the corresponding axial ratio of the signal received at the secondary station becomes extremely large, approaching linear polarization. The polarization loss would then approach 3.54 db maximum and 2.54 db minimum.

(4) 115,000 Nautical Miles to Lunar Distance

The narrow beam mode of the spacecraft high gain antenna is deployed at an earth distance of approximately 115,000 nautical miles. The angle subtended by the earth at this distance is 3.34 degrees and the pointing error for the narrow beam mode is 0.90 degrees. The axial ratio of the signal received by the secondary earth tracking station under worst case conditions would be 3.24 db (Figure 23). The polarization loss is then 0.22 db maximum. The magnitude of amplitude modulation of the carrier due to antenna roll is only 0.12 db.

The angle subtended by the earth at lunar distance is approximately 0.97 degrees, well within the beamwidth of the narrow beam mode. If it is assumed that the command module antenna during lunar orbit remains boresighted on the earth while in line-of-sight of the earth, polarization loss due to axial ratio is then very small, 0.07 db maximum. However, multipath effects due to scattering from the surface of the moon can occur. These effects are most prominent during

the period of lunar orbit when the command module is entering and leaving the occultation period (i.e., spacecraft at moon's horizon as viewed from earth).

The antenna system associated with the LEM consists of a steerable 2 foot parabola which is the primary in-flight antenna, and two omniantennas which serve as a back-up. The steerable antenna and appropriate MSFN stations angle track each other during periods when they are in line-of-sight. Since the ellipticity of the steerable antenna pattern is less than 1 db within  $\pm 4$  degrees of boresight, the maximum polarization loss is 0.07 db. While on the surface of the moon, a 10 foot parabola is erected to maintain communications with the MSFN. The ellipticity of this antenna is less than 1 db within  $\pm 1.3$  degrees of boresight, corresponding to a maximum polarization loss of again 0.07 db.

#### 4.1.2 Phase Lock Loop Performance as a Function of Spacecraft Motion

The accuracy with which the ground station antenna tracks the spacecraft depends to some extent upon the total phase error existing in the phase lock loop. This phase error is most prevalent during the near earth phase of the mission, since the doppler frequency rate is greatest during this period.

The total phase error consists of static phase error ( $\theta_e$ ), phase jitter ( $\theta_r$ ) and velocity error ( $\theta_v$ ). Static phase error is dependent upon doppler frequency rate and can be defined in the following manner (see appendix IV):

$$\theta_e = \frac{\dot{\omega}}{\alpha K}$$

where

$\dot{\omega}$  = rate of change of doppler frequency

$\alpha K$  = loop gain constant

The value of K depends upon the threshold loop noise bandwidth ( $2B_{Lo}$ ) and threshold limiter suppression factor ( $\alpha_o$ ) as follows:

$$K = K_{OPT} = \frac{32}{9} \frac{B_{Lo}^2}{\alpha_o}$$

The values of  $B_{Lo}$  and  $\alpha_o$  used during earth orbit are 350 cps and 0.267 respectively.<sup>8</sup> The value of  $\alpha$  (limiter suppression factor) depends upon the limiter input signal-to-noise ratio. The signal-to-noise ratio for a five watt transmitter during earth orbit is greater than 30 dB. Nelson<sup>17</sup> shows that for this condition;  $\alpha$  equals unity. The value of  $\alpha K$  used in determining static phase error during earth orbit is then  $1.62 \times 10^6$  per sec.<sup>2</sup>



Static phase error in the ground receiver as a function of range for a 100 nautical mile earth orbit is plotted in Figure 26. The phase error is seen to be quite small and reaches a maximum of 1.09 degrees at minimum range.

Figure 27 depicts the two-way doppler frequency versus range during earth orbit.

The equation used in plotting the curve is:

$$f_d = \frac{2 f_c}{c} \dot{R}$$

where

$f_c$  = received carrier frequency

$\dot{R}$  = range rate

It is apparent from the figure that doppler frequency rate is greatest during overhead pass of the spacecraft and rapidly approaches zero with increasing range.

Phase jitter ( $\theta_r$ ) depends upon the phase lock loop input signal-to-noise ratio in the following manner:

$$\theta_r = \sqrt{N/S}$$

where

$N$  = loop input noise power

$S$  = received signal power

The loop input noise power is based upon a horizon noise temperature of 220 degrees Kelvin and a loop input noise bandwidth of 2 KC. The 2 KC bandwidth is derived from unity  $\alpha$  and a  $B_{LO}$  of 350 cps. The received signal power ( $S$ ) is based upon a five watt spacecraft transmitter with 7 dB circuit losses and -3 dB antenna gain. Phase jitter versus range is plotted in Figure 28. The solid curve depicts the case for no atmospheric attenuation, while the dashed curve includes water vapor and oxygen losses (see Figure 16). The effect of a 3.54 dB maximum polarization loss, due to off-axis ellipticity, on phase jitter is also included in Figure 28. An active integrator in the phase lock loop is most probably used in lieu of a passive filter to insure that loss of lock does not occur during the Apollo mission. Under these conditions, the velocity error ( $\theta_v$ ) in the phase lock loop is essentially zero (see Appendix IV).

Figure 29 depicts the total phase error of the phase lock loop in the ground receiver during earth orbit. The cross-hatched area indicates the maximum variance in phase error due to spacecraft roll. (See section 4.1.1).

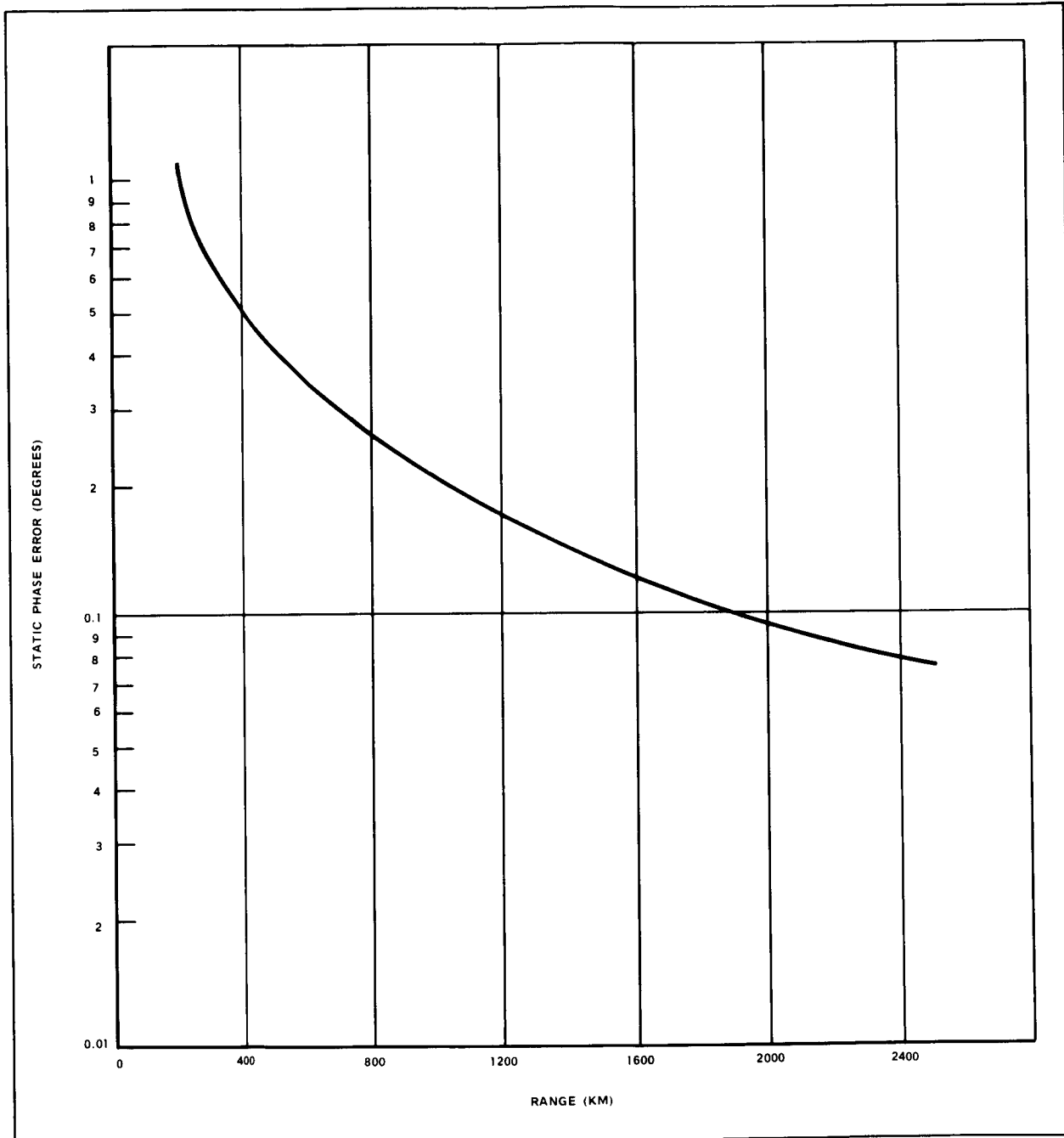


Figure 26 Apollo Ground Receiver Static Phase Error Versus Range

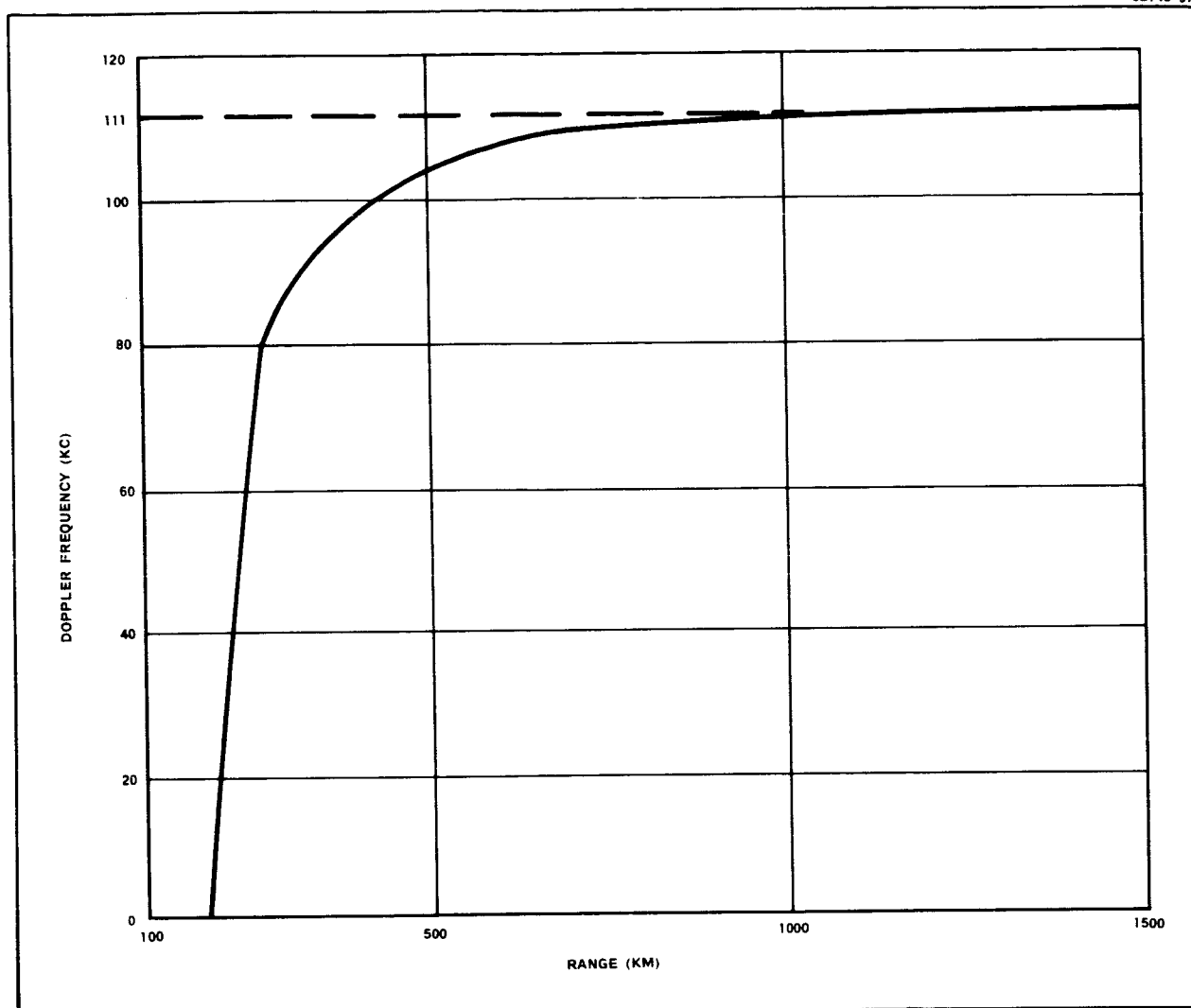


Figure 27 Doppler Frequency Versus Range

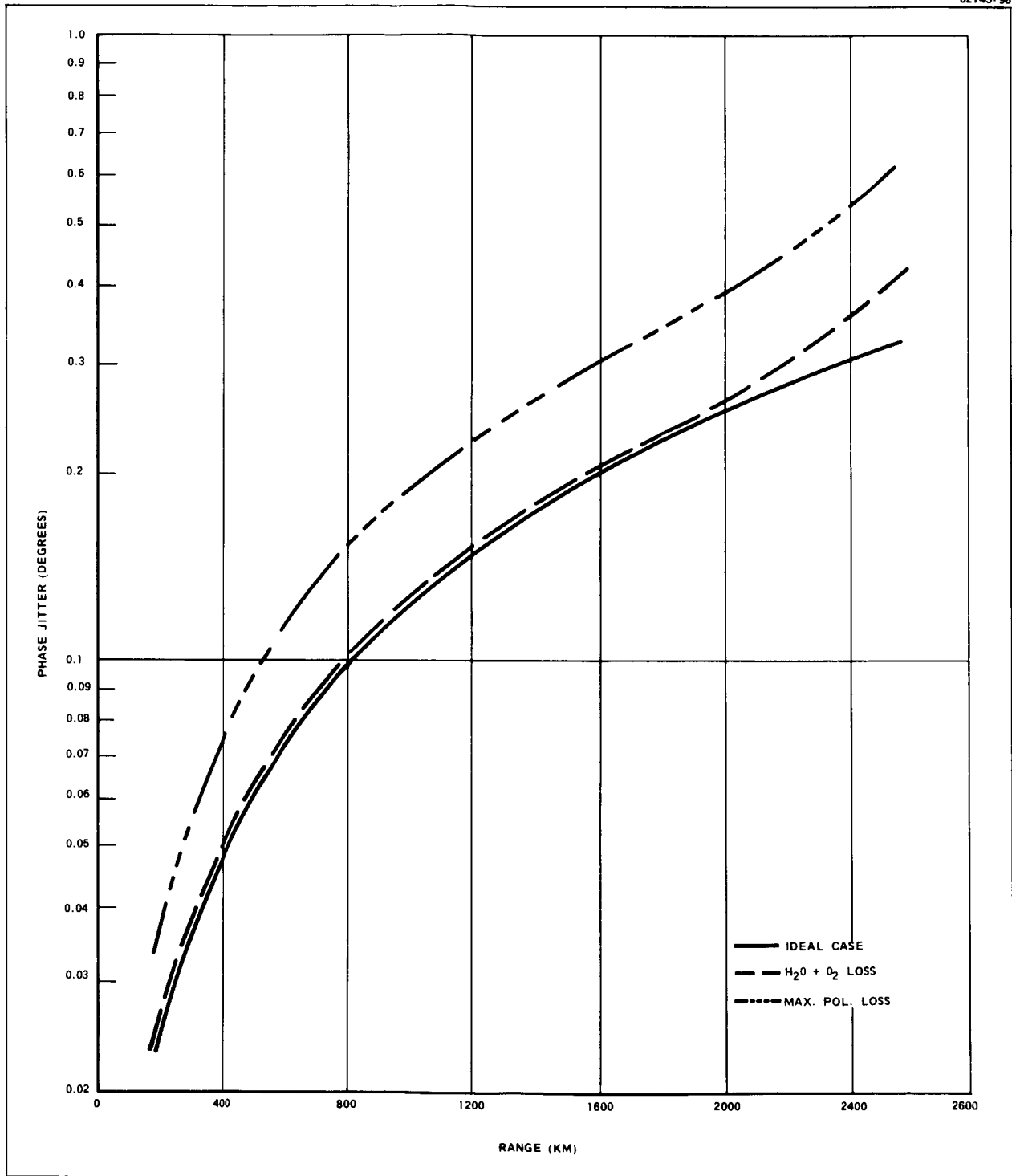


Figure 28 Apollo Ground Receiver Phase Jitter Versus Range

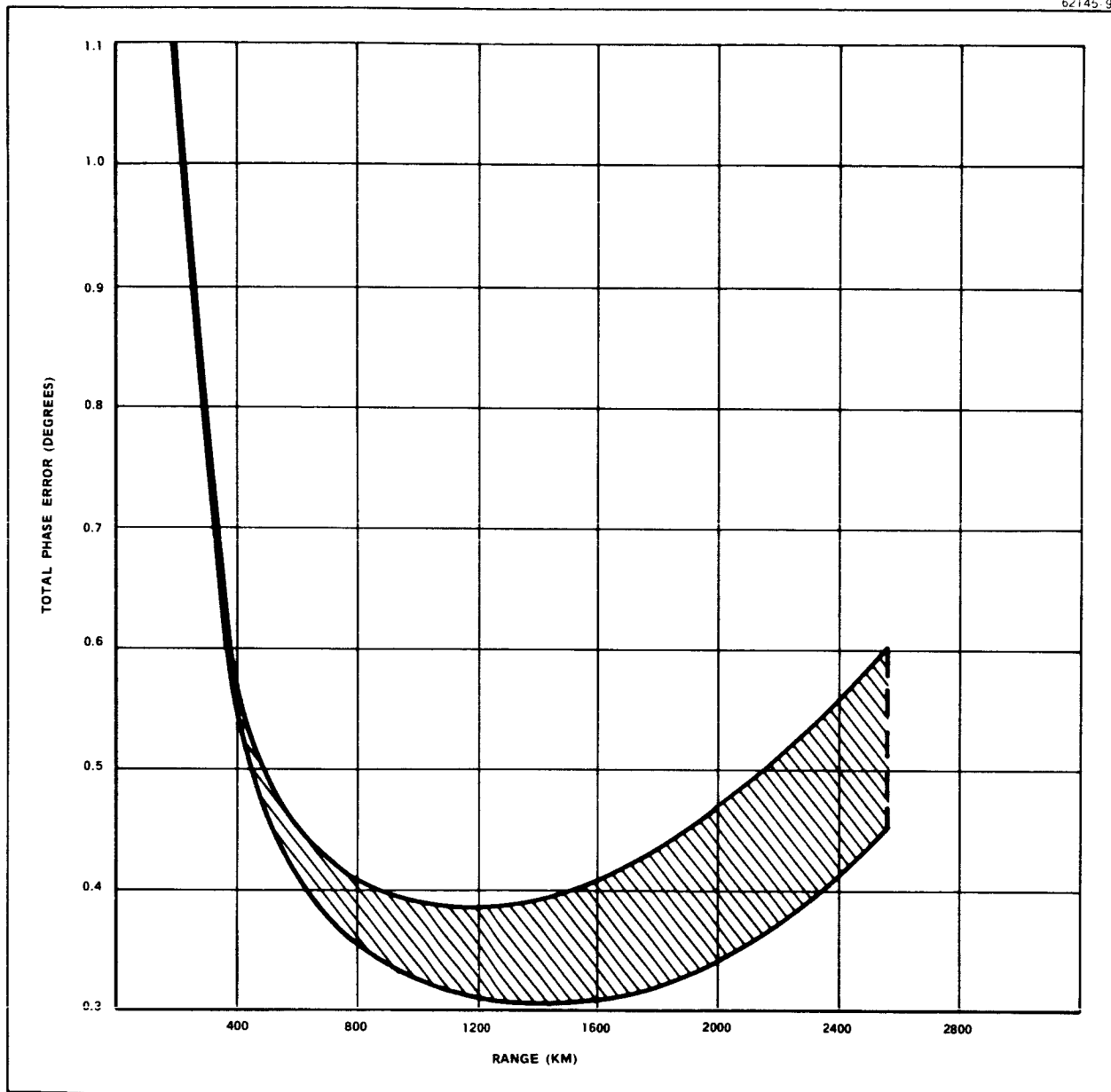


Figure 29 Apollo Ground Receiver Total Phase Error Versus Range

To reduce the likelihood of loss of lock in the phase lock loop due to random perturbation, the condition that  $\alpha K \geq 2 \dot{\omega}$  must hold,<sup>17</sup> which means that the phase error should not exceed 28.6 degrees. Figure 29 indicates that the total phase error is well within this limit; thus, no condition is expected during normal earth orbit which would cause the loop to unlock.

During the remaining phases of the mission, the spacecraft is at a greater distance from earth, resulting in a smaller rate of change in doppler frequency ( $\dot{\omega}$ ); hence, static phase error becomes very small. Since less bandwidth is required because  $\dot{\omega}$  is smaller, the phase lock loop threshold bandwidth is reduced in discrete steps of 200 cps and 50 cps with increasing range. This combination of reduced bandwidth along with the availability of increased spacecraft transmitter power and switchable antenna gains results in a minimization of phase jitter ( $\theta_r$ ) throughout the mission. Thus, no phase errors should exist in the ground station phase lock loop which will present any problems during the remainder of the mission.

#### 4.1.3 Effect of Phase Errors on Angle Tracking

To determine the effect on antenna boresight of phase errors in the phase locked loop which is in the sum channel, it is desirable to consider some general characteristics of monopulse systems.<sup>18</sup> Considering a typical amplitude sensing, Sum and Difference monopulse system as shown in Figure 30, it is convenient to consider the radiation patterns as given by:

$$g_1(u) = \frac{\sin(u - \frac{\pi}{2})}{u - \frac{\pi}{2}}$$

$$g_2(u) = \frac{\sin(u + \frac{\pi}{2})}{u + \frac{\pi}{2}}$$

These patterns result in a monopulse beam crossover level of  $2/\pi$  or - 3.9 dB.

The sum and error signals from the antenna may now be expressed as:

$$\Sigma(u) = \frac{\sin(u + \frac{\pi}{2})}{u + \frac{\pi}{2}} + \frac{\sin(u - \frac{\pi}{2})}{u - \frac{\pi}{2}} = \frac{\pi \cos u}{u^2 - \pi^2/4}$$

$$\Delta(u) = -j \left[ \frac{\sin(u + \frac{\pi}{2})}{u + \frac{\pi}{2}} - \frac{\sin(u - \frac{\pi}{2})}{u - \frac{\pi}{2}} \right] = -j \frac{2u \cos u}{u^2 - \pi^2/4}$$

In an amplitude comparison system such as this, a post comparator (i.e: after the sum and difference signals are formed ) phase shift such as would be caused by

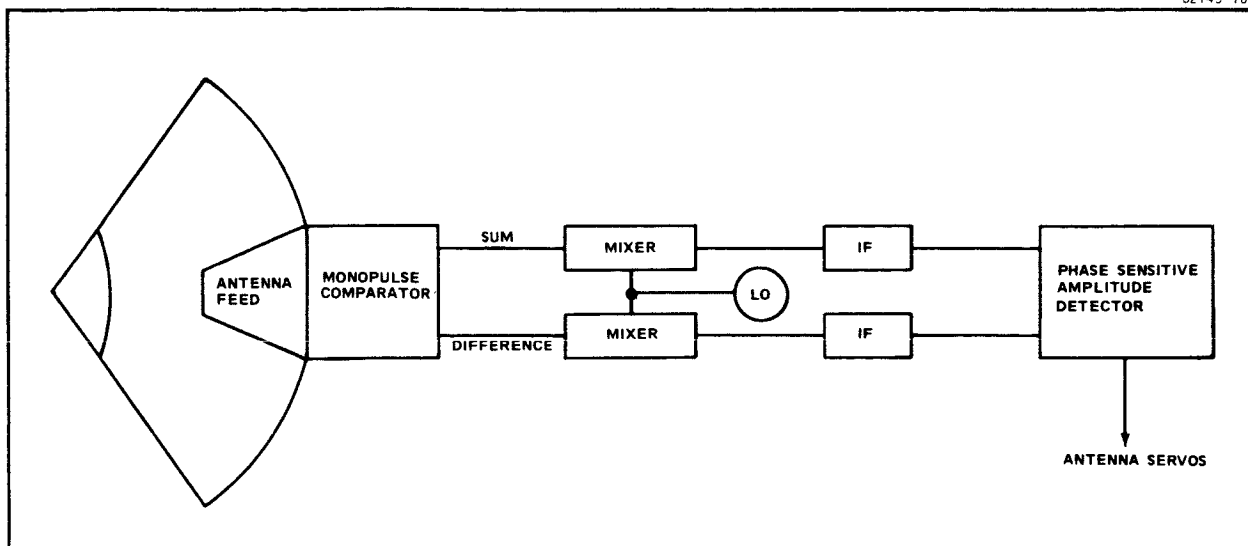


Figure 30. Sum and Difference Monopulse System

the phase locked loop in the sum channel will have no effect on the boresight unless there is null filling caused by precomparator (in the antenna feed) phase shift. Therefore assume a precomparator phase shift exists of magnitude " $\varphi$ " degrees. Then the error pattern can be written

$$E_D = -j \left[ \frac{\sin(u + \frac{\pi}{2})}{u + \frac{\pi}{2}} - \frac{\sin(u - \frac{\pi}{2})}{u - \frac{\pi}{2}} e^{j\varphi} \right]$$

For  $\varphi$  small (less than  $10^\circ$ )

$$E_D \approx -j \left[ \frac{2u \cos u}{u^2 - \pi^2/4} - \frac{j \sin(u - \frac{\pi}{2})}{u - \frac{\pi}{2}} \sin \varphi \right]$$

Near boresight  $u \rightarrow 0$

$$E_D \approx -\frac{2j u \cos u}{u^2 - \pi^2/4} - \frac{2}{\pi} \sin \varphi$$

and the null depth can be seen to be

$$ND = \text{Null depth} = \frac{2}{\pi} \sin \varphi$$

$$\text{but } \sin \varphi \approx \varphi \quad (\varphi \text{ in radians}) \quad (4-1)$$

$$ND = 20 \log \frac{2}{\pi} \varphi \quad (\text{db})$$

The output of the amplitude sensitive phase detector is given by

$$E_o = \sqrt{|E_S| |E_D|} \cos (\alpha_S - \alpha_D + \alpha_K) \quad (4-2)$$

where

$\alpha_S$  = sum phase vs angle

$\alpha_D$  = error phase vs angle

$\alpha_K$  = post comparator phase error

As can be seen from Eq (4-2), if  $E_D$  goes to zero at boresight the post comparator phase shift  $\alpha_K$  could have no effect. However, where a precomparator phase error has caused null filling, and  $E_D$  is not zero on boresight, the indicated boresight will be at the angle where  $\cos (\alpha_S - \alpha_D + \alpha_K)$  changes sign. Again if  $\alpha_K$  is zero, a null filling does not effect the boresight angle, however if  $\alpha_K > 0$ , the phase reversal will occur at some angle other than at  $u = 0$ .

Figure 31 illustrates the effect of a phase error on the phase characteristic.

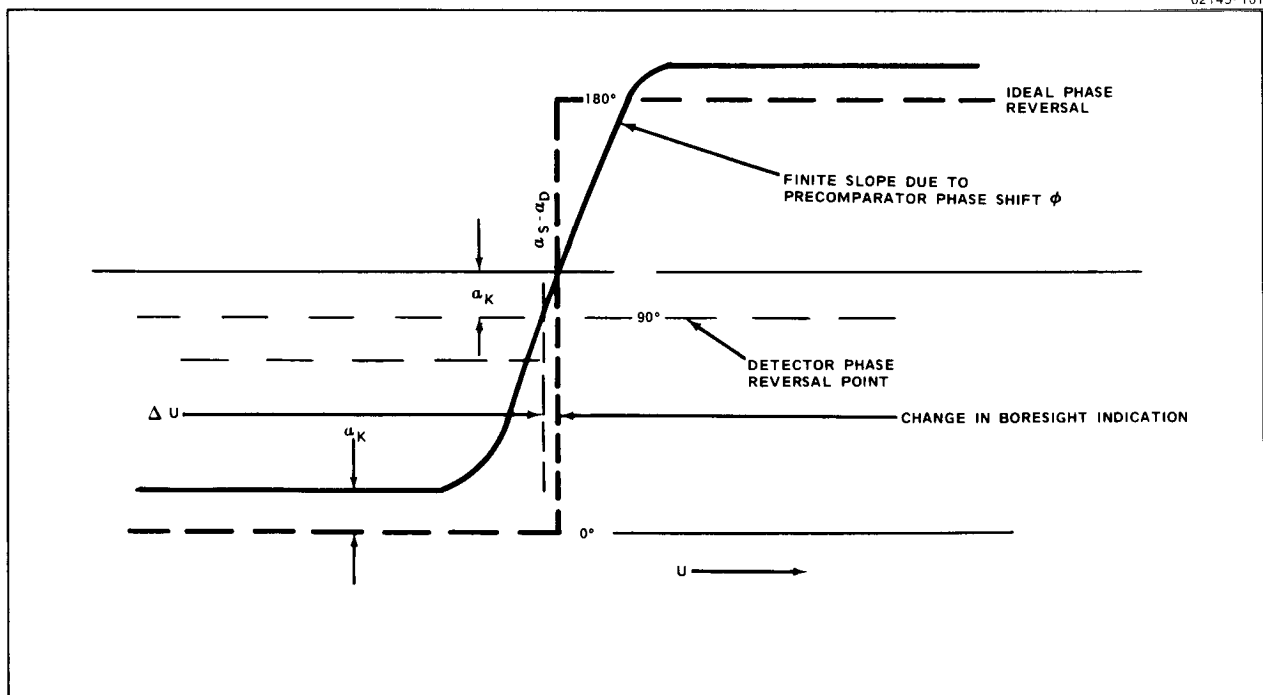


Figure 31. Boresight Shift Due to Pre-Comparator and Post-Comparator Phase Shifts



The expressions for  $\alpha_S$  and  $\alpha_D$  may be easily derived from the individual patterns with the pre-comparator phase shift term included. The resultant expressions are:

$$\alpha_S = -\tan^{-1} \frac{\sin \phi}{\pi} (u + \frac{\pi}{2})$$

$$\alpha_D = -\tan^{-1} \frac{\sin \phi}{2u} (u + \frac{\pi}{2})$$

To determine the magnitude of boresight shift, it is necessary to determine the slope of  $\alpha_S - \alpha_D$  at  $u = 0$ , or more simply the slope of  $\alpha_D$  (as  $\alpha_S$  is essentially constant).

$$\left. \frac{d\alpha_D}{du} \right|_{u=0} = \frac{\frac{\pi}{4} \frac{\sin \phi}{u^2}}{1 + \left( \frac{\pi \sin \phi}{4u} + \frac{\sin \phi}{2} \right)^2} \approx \frac{4}{\pi \sin \phi}$$

The boresight shift may be expressed in terms of  $\alpha_K$  as (see Figure 31)

$$\begin{aligned} \frac{d\alpha_D}{du} &\approx \frac{\alpha_K}{du} = \frac{4}{\pi \sin \phi} \\ \Delta u &\approx du = \frac{\pi \alpha_K \sin \phi}{4} \end{aligned}$$

but

$$\begin{aligned} u &= \frac{\pi A}{\lambda} \sin \theta \\ du &= \frac{\pi A}{\lambda} \cos \theta d\theta \\ d\phi &= \frac{\lambda \alpha_K \sin \phi}{\pi A \cos \theta} \end{aligned}$$

but at  $u = 0$ ,  $\theta = 0$ , and  $\cos \theta = 1$

$$d\theta = \frac{\lambda \alpha_K \sin \phi}{\pi A} \text{ radians}$$

and  $\sin \phi \approx \phi$

$$\therefore \Delta \theta = \frac{\lambda \alpha_K \phi}{57.3 \pi A} \text{ degrees} \quad (4-3)$$

$\lambda$  = free space wavelength (inches)

$\alpha_K$  = post comparator phase shift (degrees)  
(due to phase lock loop)

$\phi$  = pre-comparator phase shift (degrees)

A = antenna aperture (inches)

For the Apollo System, the ground antennas have a specification of difference pattern null depths greater than 35 db. If a worst case null filling of 30 dB is assumed, the corresponding precomparator phase error is approximately 3 degrees. (from Eq (4-1)). In section 4.1.2, it was found that the largest error existing in the phase locked loop during earth orbit was less than 2 degrees.

From Equation (4-3), it can be found that the effect of these errors on bore-sight is an error of only  $4.75 \times 10^{-4}$  degrees, or less than 0.001 mr for the 30 foot antennas at 2300 mc. Even if the phase locked loop phase error approaches 30 degrees, the resulting boresight shift is only about 0.01 mr which is negligible.

Another effect is also caused by the phase error. The output of the phase sensitive detector as given by equation (4-2), may be seen to be proportional to  $\cos(\alpha_S - \alpha_D + \alpha_K)$ . When  $\alpha_K = 0$ , the cosine term will equal  $\pm 1$  when  $(\alpha_S - \alpha_K) = 0$  or  $180^\circ$ . However, for  $\alpha_K \neq 0$ , it can be seen that the cosine term will be smaller than  $\pm 1$ , and the sensitivity of the detector will be reduced which results in the error curve slope being decreased. This desensitization will reduce the signal/noise ratio of the receiver. A curve of desensitization vs phase error " $\alpha_K$ " is plotted in Figure 32. For small phase errors it may be seen that this effect is also negligible; a phase error as large as 20 degrees causing only 0.54 db desensitization.

#### 4.1.4 Range Rate Errors

The roll of the spacecraft about its axis produces a range rate (or velocity) error component in the down-link signal. Since the spacecraft rolls at a maximum rate of 0.5 degrees/sec, the angle between the major axes of the two polarization ellipses (spacecraft antenna and ground antenna) will change at the same rate, resulting in a frequency error of 0.00139 cps. This corresponds to a velocity error of  $9.1 \times 10^{-5}$  meters/sec. Table 3 indicates the relationship of this error to the RMS velocity errors during the mission. The RMS velocity errors are predicted RMS errors in the state vector (a vector composed of the components of the position and velocity vectors) resulting from random errors in measurement, bias errors in measurement, and errors in tracking station location<sup>8</sup>. The minimum value during each phase of the mission is listed in the table. Velocity errors due to spacecraft roll are seen to be greatest during earth orbit; however, the contribution to RMS velocity error is insignificant.

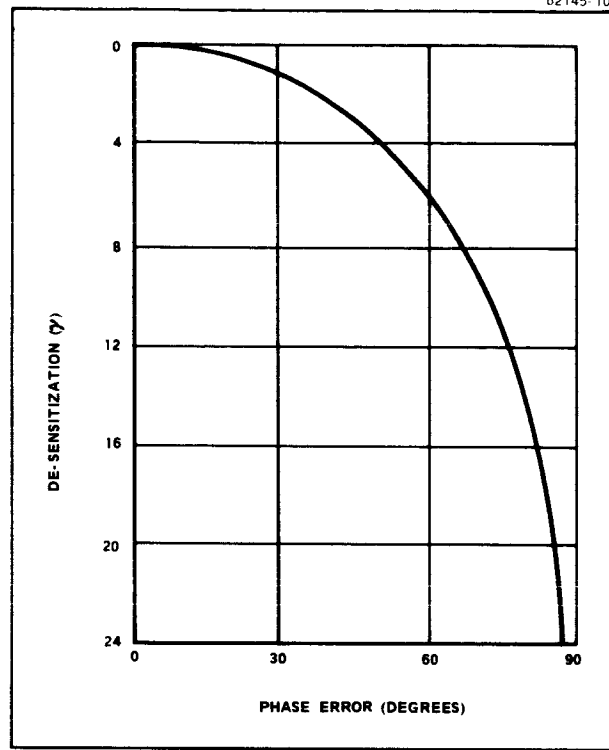


Figure 32 Phase Sensitive Detector Desensitization  
Versus Phase Error

TABLE 3. PREDICTED RMS VELOCITY ERROR AND SPACECRAFT ROLL ERROR CONTRIBUTION

Mission Phase	Minimum RMS Velocity Error (CM/sec)	Spacecraft Roll Error Contribution (percent)
Earth Orbit	$\pm 4$	0.23
Translunar	$\pm 10$	0.091
Lunar Orbit	$\pm 24$	0.038
Transearth Phase (first 20 hours)	$\pm 10$	0.091
Transearth Phase (first 60 hours)	$\pm 5$	0.18
Beginning Re-Entry	$\pm 100$	0.0091

#### 4.2 EFFECT OF POLARIZATION PARAMETERS ON RANGING

The basic method for determining range in the Apollo mission is by use of the pseudo-random code ranging system. This system operates by phase modulation of the transmitted RF carrier with a periodic binary waveform which has the property that the value of the auto correlation function is maximum when compared with a binary waveform of the same phase, and is uniformly low when out of phase. The modulated signal propagates to the spacecraft and is transponded back to earth. The received code is then correlated with a locally generated code, and the time delay between the two codes is a measure of the propagation time to the spacecraft and back; and therefore, is a measure of range.

A phase lock loop is used in the code correlation circuit so that the phase of the received code with respect to the locally generated code can be accurately determined. Hence, phase error in the phase lock loop contributes to range inaccuracies. Any phase shift of the R-F carrier during propagation between spacecraft and ground (i.e., Faraday Rotation) will also result in range inaccuracies since the ranging code is phase coherent with the R-F carrier. In order to determine the magnitude of these range inaccuracies, one must analyze the performance of the spacecraft phase lock loop as well as that of the ground station.

##### 4.2.1 Spacecraft Phase Errors

For the purposes of this study, the spacecraft is assumed to have a phase lock loop identical to that of the ground station. (See section 4.1.) Static phase error and phase jitter may then be calculated for the spacecraft transponder in the same manner as the ground station, and velocity error ( $\theta_v$ ) is again zero.

Figure 33 depicts static phase error versus range for the spacecraft transponder during earth orbit. The phase error is seen to be only half the magnitude as that at the ground station since the doppler frequency rate at the spacecraft is half that at the ground station.

Figure 34 depicts phase jitter versus range for the spacecraft transponder during earth orbit. The curves are based upon a 1KW ground transmitter and 30 foot transmitting antenna, an equivalent noise temperature of 290 degrees Kelvin, and 7 dB circuit losses. A loop bandwidth of 2 KC is again used. The dashed curve includes maximum polarization loss of 3.54 dB and atmospheric loss of 2 dB.

Figure 35 depicts the total phase error in the spacecraft transponder, obtained by addition of static phase error and phase jitter. The cross-hatched area indicates the variation of phase error due to spacecraft roll. Figure 35 is combined with Figure 29 to obtain the total phase error in the communication link during earth orbit. (Figure 36) The maximum phase error (1.62 degrees is seen to occur at minimum range with a maximum possible variation due to spacecraft roll (0.17 degrees) occurring at maximum range.

#### 4.2.2 Ranging Errors

Since the ranging code is phase coherent with the carrier frequency, any carrier phase shift will appear as a range error to the ground receiver. As a result, the two way phase lock loop phase error of 1.62 degrees contributes to range inaccuracy. In addition, a two way Faraday rotation of 4 degrees maximum (see Appendix II) during a 185 KM earth orbit results in a total phase shift of 5.62 degrees to the R-F carrier. The time required by the R-F carrier to change phase by 5.62 degrees is  $6.8 \times 10^{-12}$  sec and the propagation distance of the carrier in this time interval is 0.10 cm. Since the RMS error in position is  $\pm 40$  meters during earth orbit, 0.10 cm represents an insignificant contribution to range inaccuracy.

Referring again to Appendix II, the Faraday rotation can reach a maximum of 44 degrees during the mission at spacecraft altitudes exceeding 700 KM. This represents a range error of 0.820 cm.

It can be concluded from the foregoing that signal polarization variations in the Apollo communication link have an insignificant effect upon the ranging receiver and accuracy with which spacecraft range can be determined.

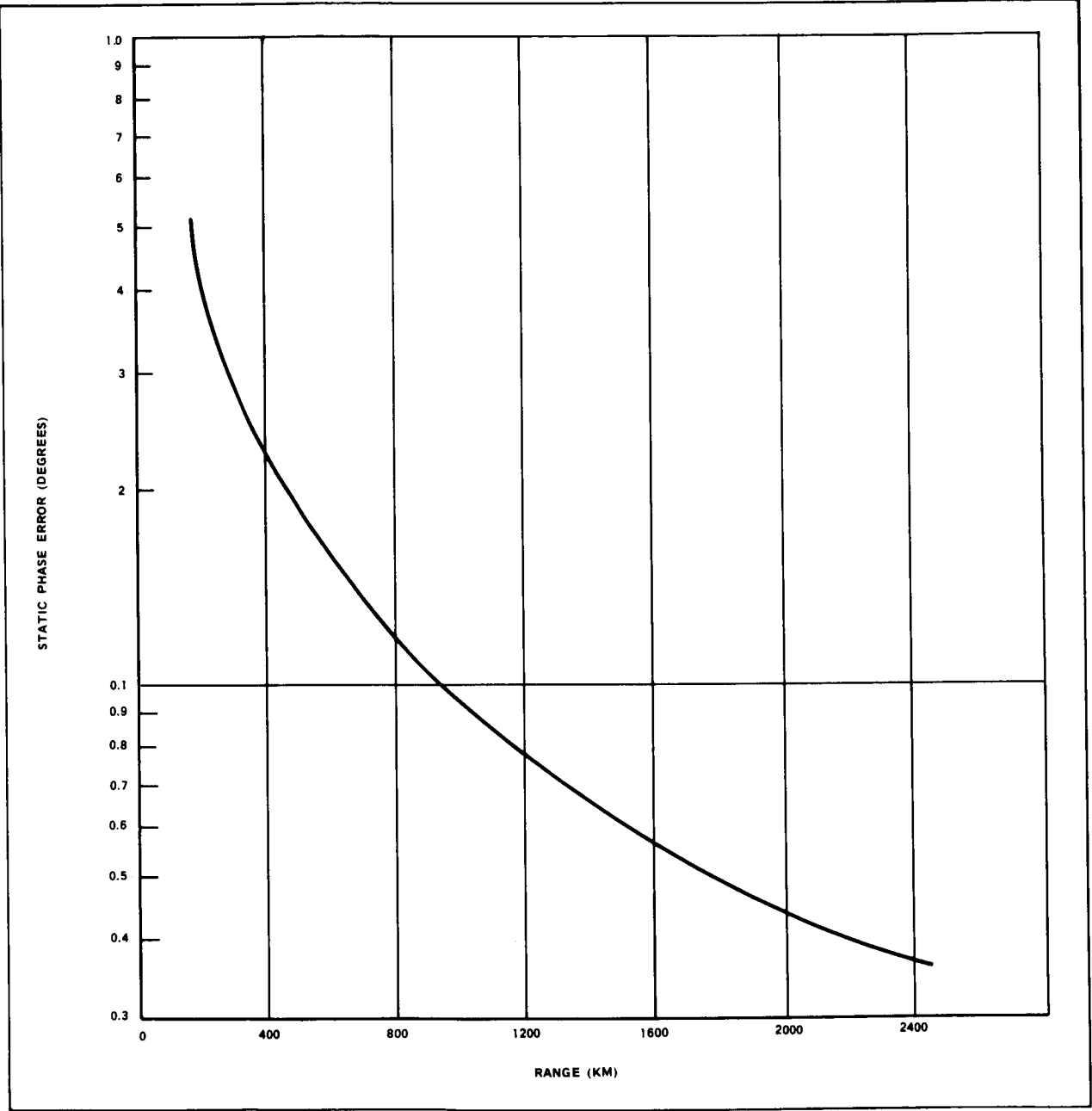


Figure 33 Apollo Spacecraft Static Phase Error Versus Range

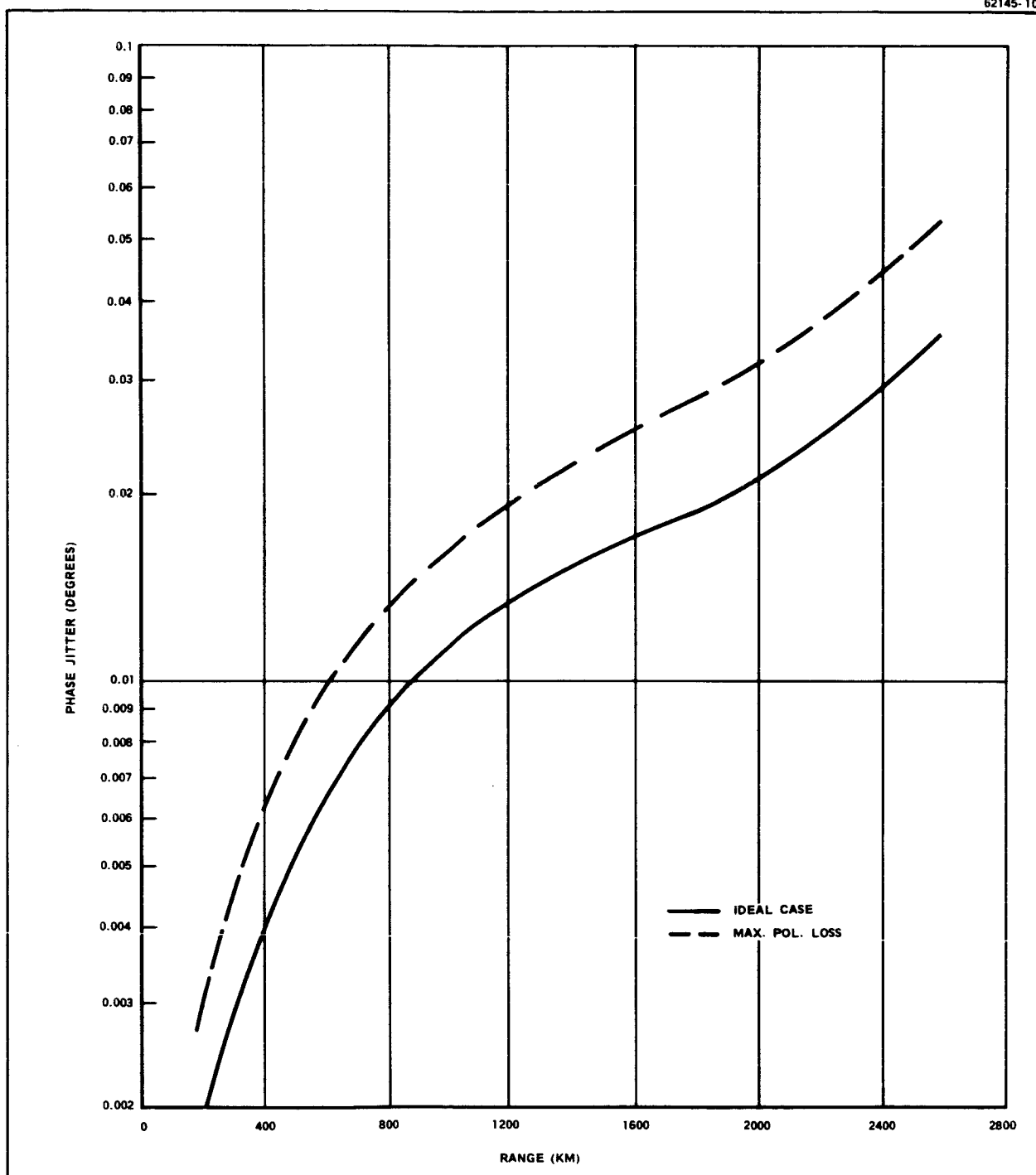


Figure 34 Apollo Spacecraft Phase Jitter Versus Range

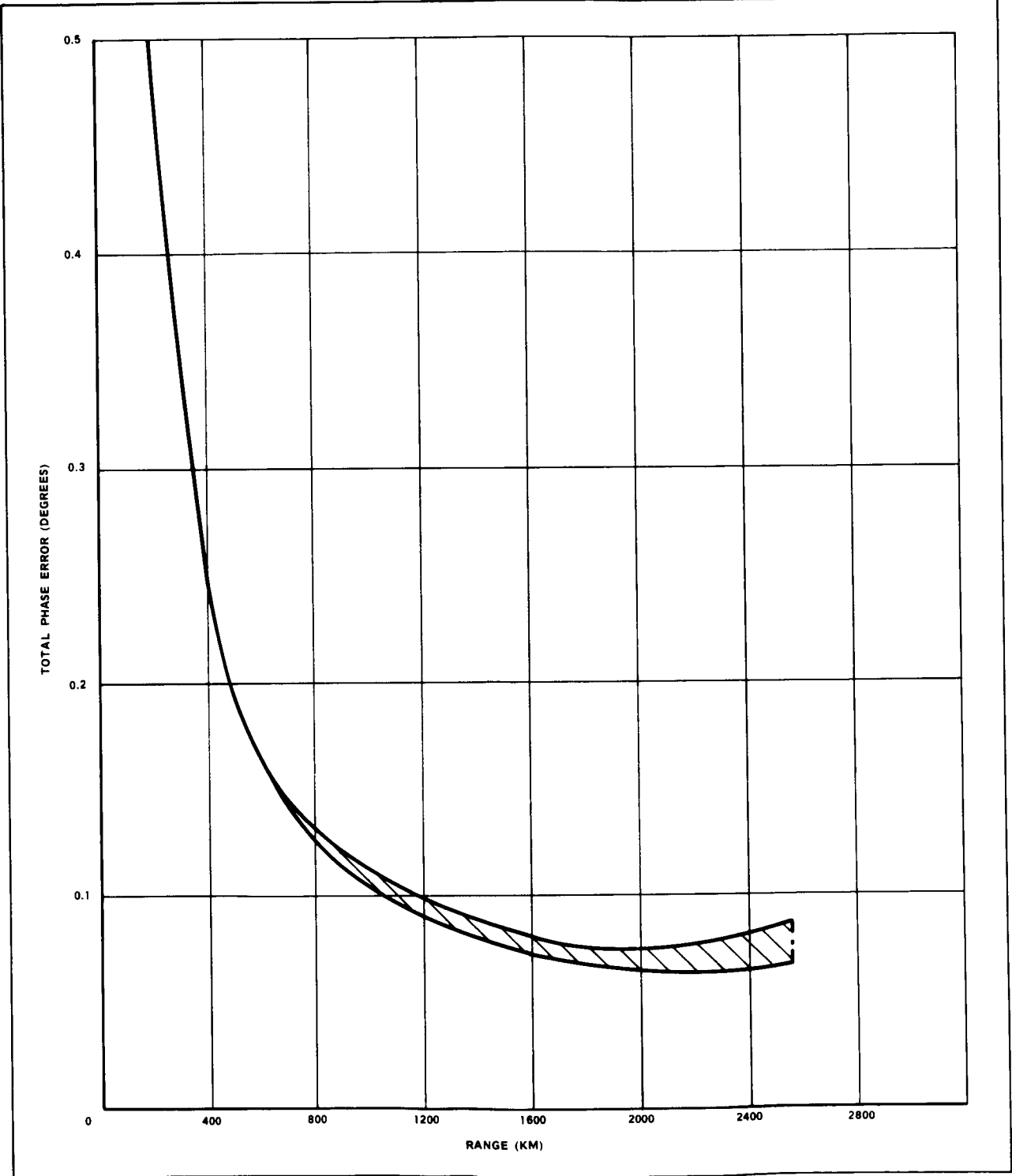


Figure 35 Apollo Spacecraft Total Phase Error Versus Range



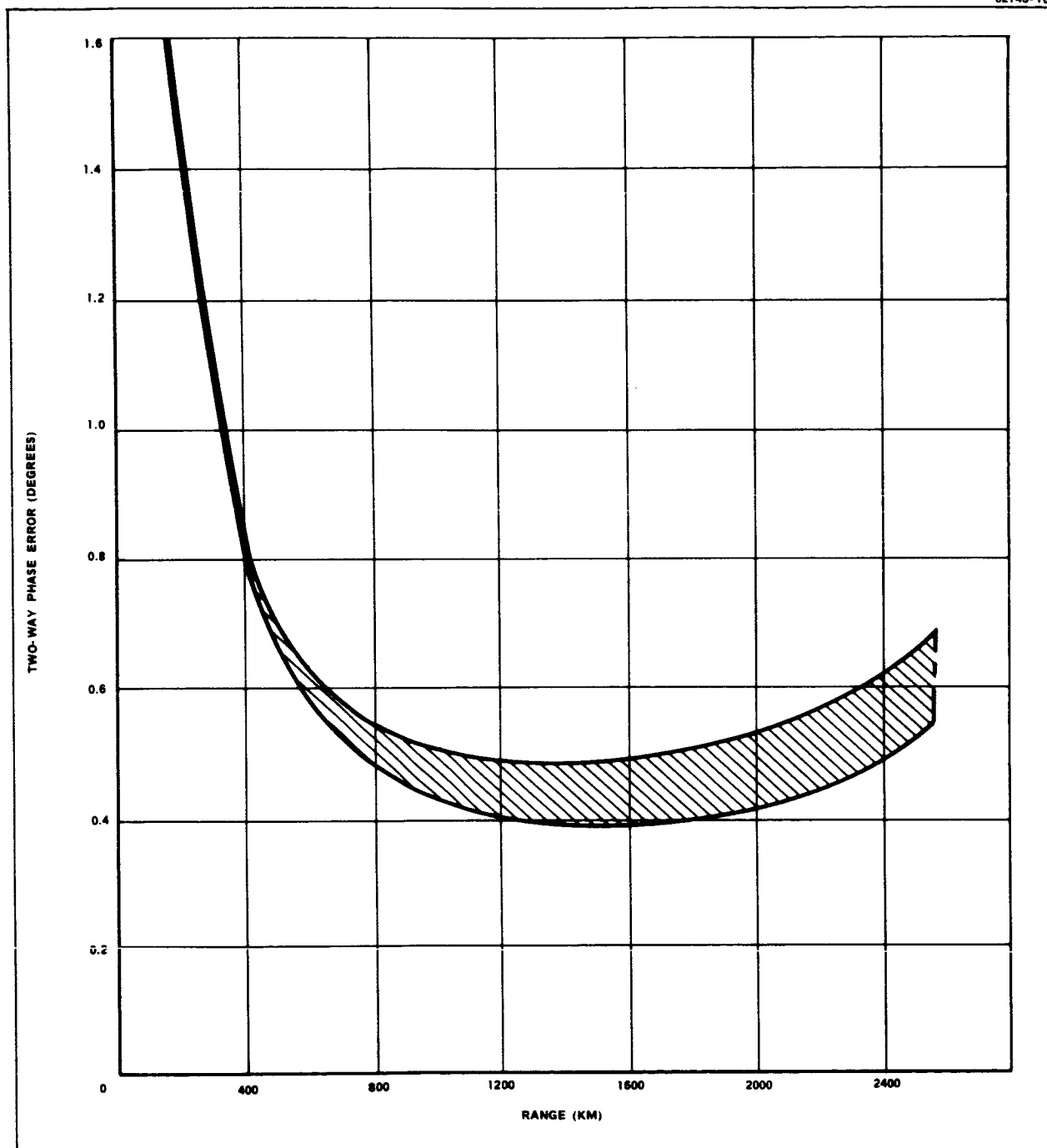


Figure 36 Apollo Communication Link Two-Way Phase Error Versus Range

**Section Five**

**CONCLUSIONS AND RECOMMENDATIONS**

## Section Five

### 5. CONCLUSIONS AND RECOMMENDATIONS

#### 5.1 CONCLUSIONS

From the preceding discussion, it appears that the principal factors resulting in system performance degradation are:

1. Off axis ellipticity resulting in polarization mismatch loss at secondary ground stations.
2. Multipath propagation which causes increased noise temperature and boresight errors at low angles, resulting in loss of tracks and communication.
3. Plasma sheath formation during spacecraft reentry resulting in communication blackout during a critical phase of the mission.

A detailed discussion of the first two factors has been covered in this report. Methods of reducing or eliminating the problem of polarization mismatch loss are considered in section 5.2. The problems arising from multipath propagation require further study, preferably an experimental investigation to determine the magnitude of the boresight errors and noise temperature increase over various types of terrain. Specific recommendations for the type of study required are also considered.

The problem of the plasma sheath, while constituting a major signal transfer problem has not been treated extensively in this study, due to the amount of effort being expended by many others to solve this problem.

Additional factors considered in this study were:

- a) Effect of Faraday rotation on wave polarization and signal transfer.
- b) Effect of spacecraft motion on signal transfer.
- c) Evaluation of the magnitude of phase errors in the phase locked loops during various portions of the mission and the effect of these errors on signal processing including angle track and range information.

- d) Degradation of Doppler information as a function of spacecraft position and the resulting errors in range rate.

The resulting calculations, based upon assumptions which are believed to be reasonable, indicate that the magnitude of these effects are in the most part negligible as applied to the Apollo communications link.

## 5.2. CONSIDERATIONS FOR IMPROVED SYSTEM PERFORMANCE

### 5.2.1. Polarization Matching

To reduce the signal loss caused by the off axis ellipticity of the spacecraft antenna, and any depolarization caused by the transmission path (i. e. Faraday rotation, multipath, etc.), it would be possible to have the ground antenna sense and match the incoming wave from the spacecraft.

Continuous polarization match with an incoming signal may be accomplished in several ways. To be able to match an incoming arbitrarily polarized wave, it is necessary to know the magnitude of the ellipticity and the tilt angle of the major axis with respect to the antenna axes. Two ways of obtaining this data are as follows:

- (a.) By measuring the received signal with two orthogonal circularly polarized antennas, the magnitude of the left circular and right circular components of the field may be determined. The axial ratio may be determined by taking the ratio

$$AR = \frac{R + L}{R - L}$$

AR = axial ratio

R = magnitude of right circular component

L = magnitude of left circular component

A further measurement is necessary to determine the tilt angle of the ellipse. This may be done by either measurement of the maximum field with a rotatable linearly polarized antenna or changing the phase of one of the circularly polarized antennas and adding both the right and left circular components. When the output is minimum, the tilt angle may be determined by the phase setting (with respect to a phase reference).<sup>1</sup>

- (b.) A second method<sup>1</sup> would be to measure the vertical and horizontal components of the incoming waves and the phase between these components. From a knowledge of these three characteristics, the axial ratio and tilt angle may be determined.

Once the characteristics of the incoming field are known, it is necessary to have some scheme for matching the ground antenna polarization characteristics to those of the incoming wave. One possible technique of polarization matching is shown in Figure 37. This method consists of a rotating half wave plate which effectively rotates the plane of a linearly polarized wave, and a rotatable quarter wave plate which forms the elliptically polarized wave.

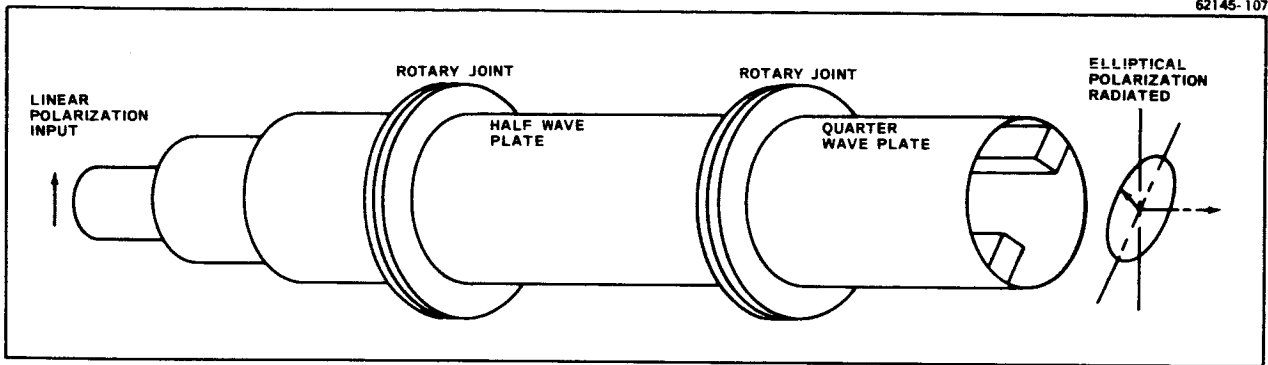


Figure 37 Polarization Control Circuitry

By rotating the quarter wave plate with respect to the half wave plate, any elliptical polarization from linear to left or right circular may be generated.

Then the quarter wave plate may be locked to the half wave plate and the combination of the quarter and half wave plates rotated with respect to the linear polarized feed signal. This will rotate the polarization ellipse axis.

#### 5.2.1.1 Implementation

Implementation of these functions of sensing and control into a tracking system may be done in a manner as shown below.

a. Linear Polarization Sensing — A pair of orthogonal linearly polarized sensing elements are mounted separately from the antenna feed. (See Figure 38.) The amplitude of each linear signal and the relative phase between the two signals are fed into a computer which calculates the incoming signal axial ratio and tilt angle of the polarization ellipse. Commands are then generated which are sent to the antenna feed system which will rotate the quarter wave plates ( $\lambda/4$ ) and half wave plates ( $\lambda/2$ ) in the antenna feed. For a monopulse system, four polarization control elements are normally required, as a typical monopulse circuit consists basically of a four horn feed.

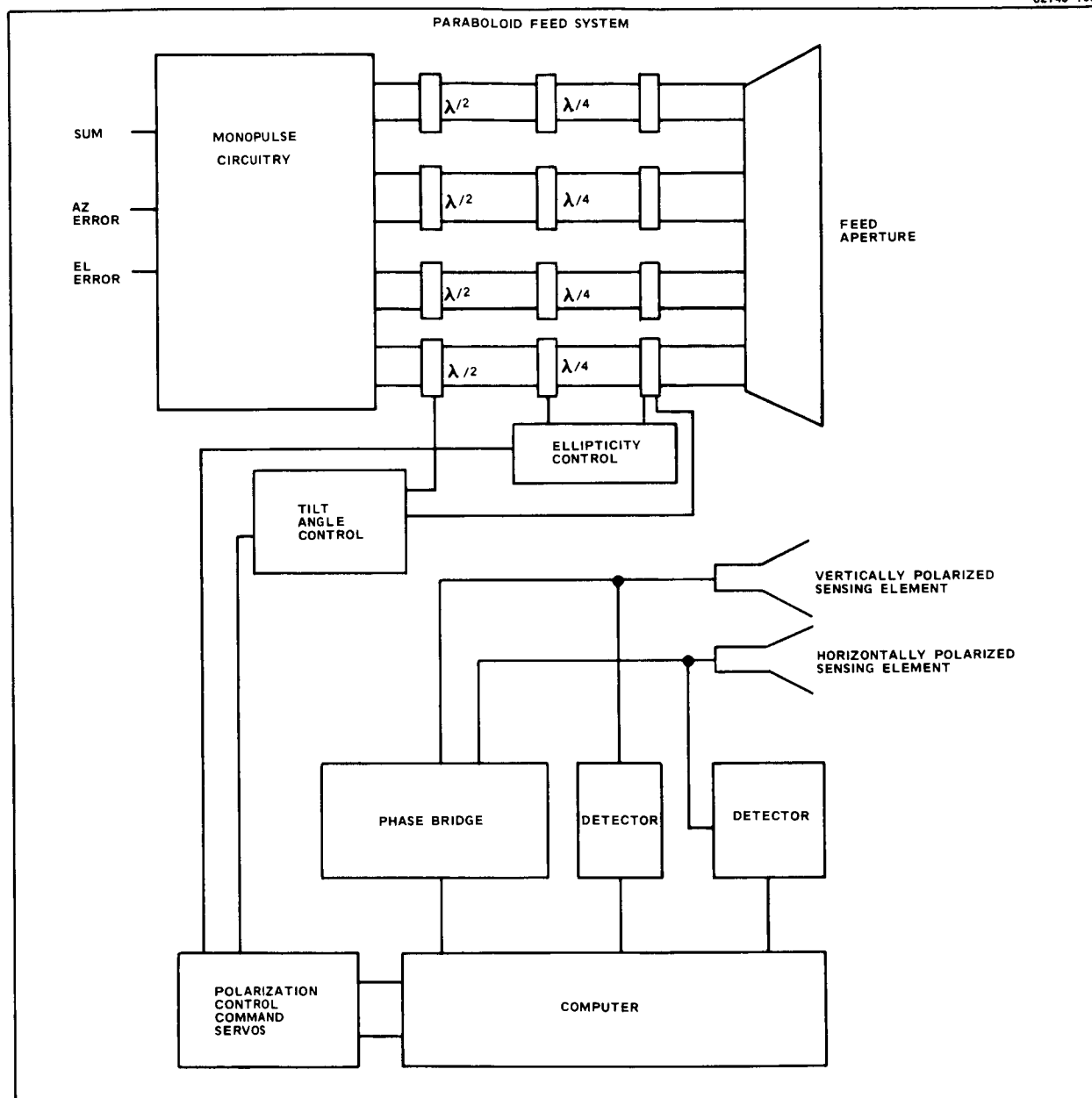


Figure 38 Linear Polarization Sensing and Polarization Control Scheme

This system has the disadvantage of requiring a computer to determine the characteristics of the incoming wave.

b. Circular Polarization Sensing — Implementation of the circular sensing method is shown in Figure 39. Here the axial ratio is determined easily by the ratio detector, however, the ellipse tilt angle must be determined by a minimum on a detector. Automatically determining the tilt angle may again require a computer, unless the detector were set to respond to a preset minimum level. However,

for slow polarization variation, a human operator could read out the axial ratio and tilt angle and set up the necessary polarization control settings.

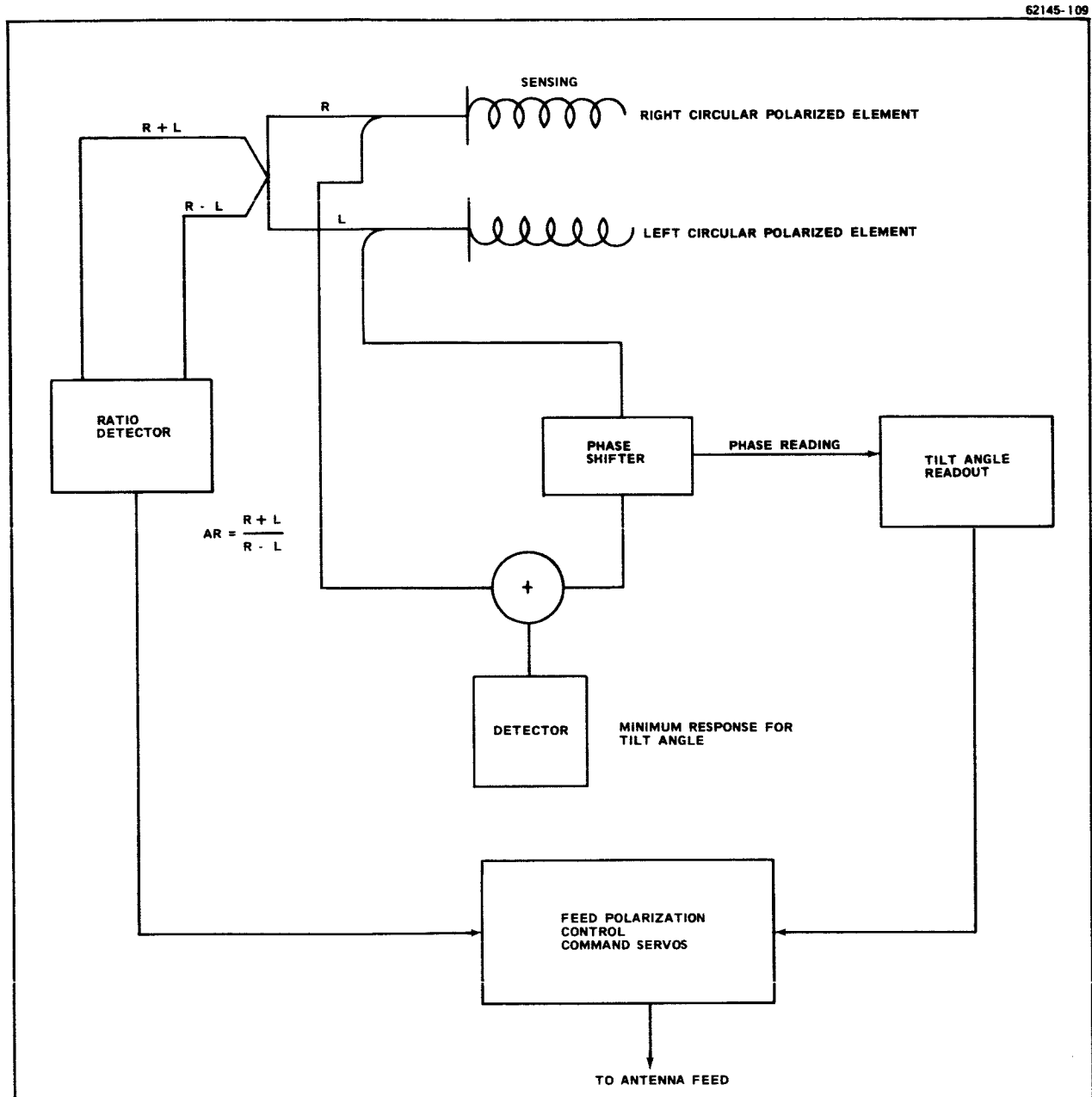


Figure 39 Circular Component Sensing

Another way of utilizing the circular polarization sensing is shown in Figure 40. This may be the most practical method of implementation. The incoming wave axial ratio is determined as before from the circular polarization components. The antenna feed axial ratio is then set to match that of the incoming wave. Then the polarization ellipse is rotated by the tilt angle control servos until a null is obtained on the orthogonal linear component of incoming signal at the input to the

monopulse bridge. This ensures that maximum power is being received. This method also has the advantage of a closed loop feedback control when aligning the ellipse axis. This could further be refined by incorporating an additional feedback loop on the axial ratio control servos after the tilt is aligned.

62145-110

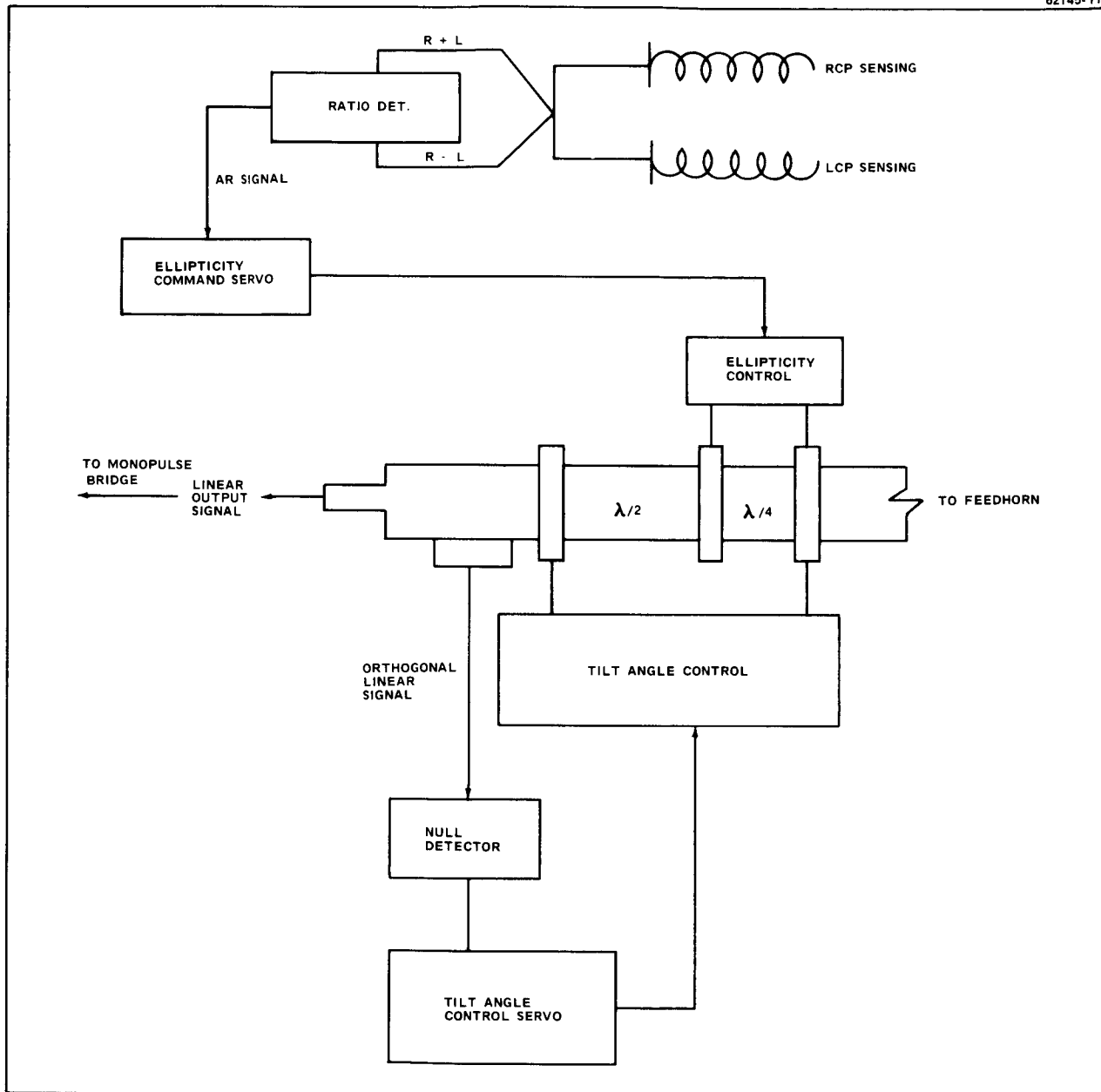


Figure 40 Circular Component Sensing Utilizing Antenna Feed for Tilt Angle Control



#### 5.2.1.2 Cost Consideration

The technique considered above may require extensive modification of the existing equipment. As polarization matching is principally only a problem for a secondary ground station (i.e.: The station on which the spacecraft is locked experiences no off axis polarization loss) it may not be economically feasible.

If such a scheme is desirable, the method illustrated in Figure 40 would appear to be the most feasible. Although it requires replacement of the ground antenna feed systems, with the resulting development of the required hardware, it does not require the facilities of a computer for polarization sensing.

However, it may be feasible to utilize one of the other schemes if a human operator is used to match polarization for maximum signal response. This technique has the advantage of requiring less hardware in that no closed loop servos are required.

#### 5.2.2 Reducing Multipath

Reducing the effects of multipath propagation may be approached in two ways. One would be to use polarization diversity to receive the returned signals and attempt to perform a correlation technique to reduce the ambiguities arising from each of the returned signals. Some scheme may be possible to take advantage of the fact that the reflection coefficients for vertical and horizontal polarization are different in the near grazing angles encountered near horizon. See Figure 41.

The most straightforward approach to reducing multipath effects would be to utilize vertical polarization for tracking at angles less than approximately 12 degrees, and circular polarization for angles greater than 12 degrees. This would take advantage of the lowest ground reflection coefficients in each region as may be seen from Figure 41.

Another approach would be to eliminate or minimize the energy radiated into the ground. This may be feasible for particular applications. By shaping the antenna subreflector, and using low spillover feeds, it should be possible to reduce the sidelobes on one side of the antenna pattern. (See Figure 42.) Techniques for accomplishing this are at present under study at Hughes for application to deep space tracking antennas which must track near the sun, an extremely noisy source. It is possible to achieve such an effect by an antenna distribution shaped to cancel specific sidelobes. Adaptation of this technique to steerable paraboloids would be an area in which to concentrate further study efforts.

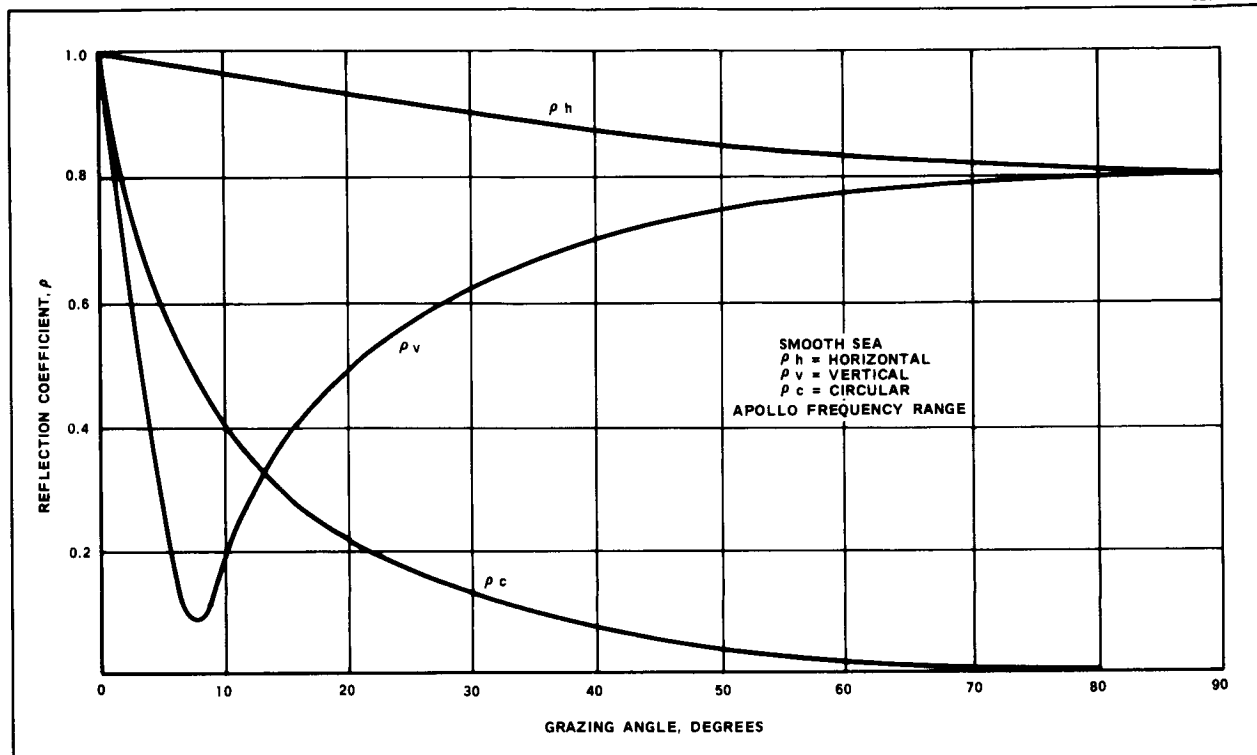


Figure 41 Reflection Coefficient Versus Grazing Angle for Smooth Sea

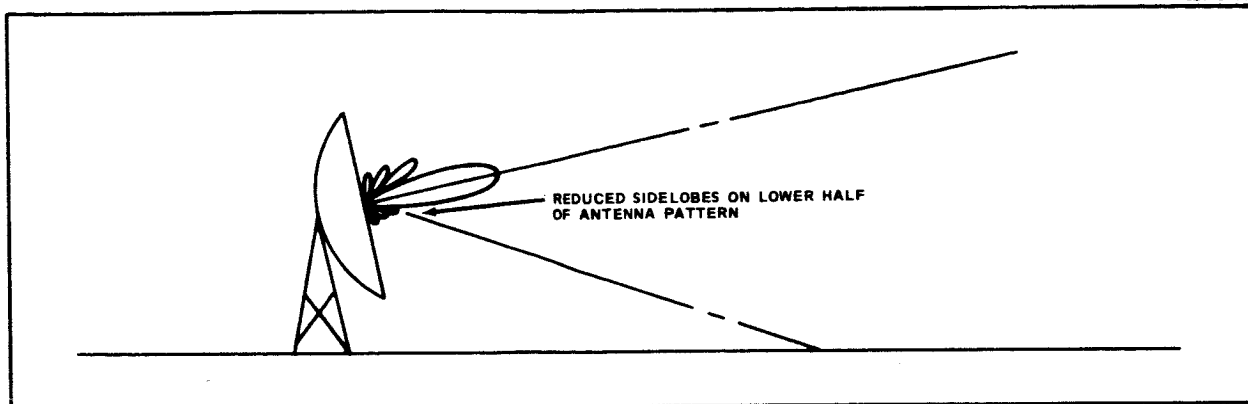


Figure 42 Reducing Lower Sidelobes to Reduce Multipath Effects

### 5.3 RECOMMENDATIONS

Section 5.2 discusses some considerations for polarization match schemes. If such an approach seems justified on a cost/performance judgement, the development of hardware to accomplish accurate polarization sensing and tracking would be required. Possibly further consideration could be given to methods of implementation of polarization matching, from the standpoint of detailed price and performance comparisons.

The problem of multipath would appear complex enough to warrant a further experimental study to measure the magnitude of the boresight errors and noise contribution over various types of terrain. Actual measurement with a tracking system to determine the systems data processing response at low angles would be informative. Study of specific techniques such as antenna beam shaping, low spillover feeds, etc., may be warranted to determine to what extent tracking and communications can be improved over existing systems. Measurements on existing Apollo stations should be available in such a study.

As mentioned in Section 5.2.2, the most economical method of reducing multipath would be the use of vertical polarization for tracking the spacecraft at angles below 12 degrees to take advantage of the lower ground reflection coefficient. Above 12 degrees, circular polarization will yield the best performance with respect to multipath reflections.

## **Section Six**

### **REFERENCES**

## Section Six

### 6. REFERENCES

1. John D. Krauss, Antennas, McGraw Hill, New York, 1950.
2. R. W. Hartop, Power Loss Between Arbitrarily Polarized Antenna, JPL Technical Report No. 32-457, JPL, CIT, Pasadena, California, Sept 1, 1964.
3. Papas, Theory of Electromagnetic Wave Propagation, McGraw Hill Book Co, New York, 1965.
4. Daniels and Bauer, "The Ionospheric Faraday Effect and its Applications," Journal of the Franklin Institute, Vol. 267, March 1959.
5. Wright, "A Model of the F Region above  $N_{\max} F_2$ ," Journal of Geophysical Research, Vol. 65, Jan 1960.
6. Millman, "The Geometry of the Earths Magnetic Field at Ionospheric Heights," Journal of Geophysical Research, July 1959.
7. D. M. Joe, Faraday Rotation in the Ionosphere, Hughes ID 63-11-20, Hughes Aircraft Co., Fullerton, California, March 11, 1963.
8. Proceedings of the Apollo Unified S-Band Technical Conference, Goddard Space Flight Center, NASA SP-87, July, 1965.
9. E. C. Jordan, Electromagnetic Waves and Radiating Systems, Prentice Hall, Englewood Cliffs, N.J., 1950.
10. D. C. Hogg, "Effective Antenna Temperatures Due to Oxygen and Water Vapor in the Atmosphere," Journal Applied Physics, Vol. 30, No. 9, September 1959.
11. P. D. Potter, The Aperture Efficiency of Large Paraboloid Antennas as a Function of their Feed-System Radiation Characteristics, JPL Technical Report No. 32-149, JPL-CIT, Pasadena, California, 25 Sept 1961.

12. Ground Terminal Noise Minimization Study, Final Report, Philco WDL-TR 1972, Palo Alto, California, Jan 18, 1963, Contract AF041695)-113.
13. Dirsra, "The Telemetry and Communication Problem of Re-Entrant Space Vehicles, " Proceedings of the IRE, April, 1960, p705.
14. Lehnert and Rosenbaum, Plasma Effects on Apollo Re'Entry Communication, NASA Technical Note TN D-2732, March, 1965.
15. Cudeliyh, Beckivith, Sehraeder, RAM B2 Flight Test of a Method for Reducing Radio Attenuation during Hypersonic Re-entry, NASA TMX-902, 1963.
16. Evans, "Reduction of Free Electron Concentration in a Re-entry Plasma by Injection of Liquids, "NASA paper presented at the Third Symposium on the Plasma Sheath, September 21-23, 1965, Boston, Mass.
17. W. L. Nelson, "Phase Lock Loop Design for Coherent Angle-Error Detection in the Telstar Satellite Tracking System, " Bell System Technical Journal, September 1, 1963, p. 1967.
18. Cohen and Steinmetz, "Amplitude and Phase Sensing Monopulse System Parameters, " Microwave Journal, November 1959, p. 37.
19. R. C. Tausworthe, Theory and Practical Design of Phase-Locked Receivers, Vol 1, Technical Report No. 32-819, Jet Propulsion Laboratory, Pasadena, Calif, 15 Feb 1966.
20. Kline and Moore, Concepts and Computational Techniques Used in the Design of Phase Lock Circuits, Motorola, Inc, Military Electronics Division, Scottsdale, Arizona.
21. R. F. Earth Sensor 60 Day Study Final Report for Apollo CSM High Gain Antenna, Dalmo Victor Report R-3028-3953, 14 Oct 1965 (and excerpts from Dalmo Victor Report R-3028-3944).
22. "Design and Reference Mission, " Volume I, Mission Description, Contract #NAS 9-1100, Report #LED-540-12, 30 October, 1964.

**Section Seven**  
**BIBLIOGRAPHY**

## Section Seven

### 7. BIBLIOGRAPHY

#### 7.1 SPACECRAFT

1. G. Tyras, An Experimental Study of Plasma Sheath Effects on Antennas, University of Arizona, AFCRL - 65-53, December 1964.
2. D. Jacavano, Electromagnetic Properties of a Plasma Covered Antenna, Cambridge Research Laboratories, AFCRL - 65-323, May, 1965.
3. V. L. Granatstein, "The Open Plasmaguide In Extremes of Magnetic Field," IRE Transactions, PGAP, July 1963.
4. K. Golden, A Study of Artificial Dielectrics, Aerospace Corporation, TDR-269, May 1964.
5. E. Dirs, "The Telemetry and Communication Problem of Re-Entrant Space Vehicles," Proc. IEEE, April 1960.
6. RF Earth Sensor 60-Day Final Report for Apollo CSM High Gain Antenna, Dalmo Victor Report, R-3028-3953, 14 October 1965.
7. LEM-MSFN S-Band System Signal Performance and Interface Specification, Grumman Aircraft, LSP-380-17, June 7, 1965.
8. D. Spencer, An Evaluation of the Communication Blackout Problem for a Blunt Mars-Entry Capsule and a Potential Method for the Elimination of Blackout, Technical Report No. 32-594, Jet Propulsion Laboratory, Pasadena, California, April 15, 1964.
9. Lehnert and Rosenbaum, Plasma Effects on Apollo Re-Entry Communication, National Aeronautics and Space Administration, Washington, D. C., NASA TN D-2732, March 1965.



## 7.2 GROUND SYSTEM

1. Final Report for Shipboard Unified S-Band Feed System - Hughes Aircraft Company, Fullerton, California, Contract NAS-5-9767, Reeves, P. O. C-63429, September, 1965.
2. Specification for a Cassegrain Feed System for a 30-Foot Antenna, Collins Radio, Dallas, Texas, August 1964.
3. Block II Performance and Interface Specifications, North American Aviation, Downey, California, (SID 64-1613), February 22, 1965.
4. Design and Error Analysis and Performance Prediction, Rantec, Calabassas, California, Project No. 40314, September 22, 1964.
5. Space Programs Summary No. 3724, Vol. III, Jet Propulsion Laboratory, Pasadena, Calif., November 30, 1963.
6. Space Programs Summary, No. 37-26, Vol. III, Jet Propulsion Laboratory, Pasadena, California, March 31, 1964.
7. Space Programs Summary, No. 37-28, Vol. IV, Jet Propulsion Laboratory, Pasadena, California, August 31, 1964.
8. M. Easterling, Methods for Obtaining Velocity and Range Information from CW Radars Technical Report No. 32-657, Jet Propulsion Laboratory, Pasadena, Calif., 1 September 1964.
9. R. P. Mathison, Tracking Techniques for Interplanetary Spacecraft, Technical Report No. 32-284, Jet Propulsion Laboratory, Pasadena, California, 1 August 1962.
10. M. Easterling, A Long Range Precision Ranging System, Jet Propulsion Laboratory, Pasadena, California, Technical Report No. 32-80, July 10, 1961.
11. Apollo Entry Tracking: A shipboard Unified S-Band Interferometer System, National Aeronautics and Space Administration, Washington, D. C., NASA - N65-31143, August, 1965.
12. Apollo Digital Up-Data Link Description, National Aeronautics and Space Administration, Washington, D. C., NASA - NC5-34241, October, 1964.
13. Cutler, C. C., "Parabolic Antenna Design for Microwaves," Proceedings of IRE, pp. 1284-1294, November 1947.
14. P. A. Jensen, "A Low Noise Multimode Cassegrain Monopulse Feed with Polarization Diversity," NEREM, November, 1963.

15. Final Report for Low Noise, High Efficiency Cassegrain Antenna Studies, Contract No. NAS 5-3282, Hughes Aircraft, Fullerton, California, Report No. FR 65-14-8, December 31, 1963.

### 7.3 MEDIUM

1. R. F. Whitmer, "Principles of Microwave Interactions with Ionized Media," Microwave Journal, February, 1959.
2. M. Bonnet, "Study of the Faraday Effect in a Plasma at 10 KMC," N62-11789, Annales Des Telecommunications 10, 150-158, 1955, France, Translated and Reissued, December 1961.
3. J. P. Ruina, "Antenna Resolution as Limited by Atmospheric Turbulence," IRE Transactions, PGAP, March 1963.
4. S. Basu, Study of the Earth's Ionosphere by Reception of Radio Waves from Satellites, Air Force Cambridge Research Laboratories, AFCRL-64-831, October 1964.
5. M. Katzin, Studies in Ionospheric Propagation, Electromagnetic Research Corporation, GRC-7233-1, 15 April, 1962.
6. B. Katsenelenbaum, On the Question of Propagation of Electromagnetic Waves Between the Earth and Ionosphere, National Aeronautics and Space Administration, Washington, D. C., N65-14602, 1 December 1964.
7. Space Surveillance Techniques, Massachusetts Institute of Technology, AD 324-655, April 1961 (Confidential).
8. M. Barasch, et al, The Physics of Radio Communication Via the Moon, University of Michigan, Ann Arbor, Contract AF-30(602) - 1725, March 1958.
9. J. Scheibner, Research on Various Phenomena for the Performance of Circuit Functions, Georgia Institute of Technology, AD 257-864, October 1959.
10. R. Silverstein, High Frequency Anti-Multipath Investigation, National Bureau of Standards, Boulder, Colorado, NBS-502-0-38, March 1959.
11. R. Bates, Troposcatter Investigation by Rake Techniques, National Company, Inc., Malden, Mass., AF-30(602)-2195, January, 1961.
12. G. Millman, "Atmospheric Effects on VHF and UHF Propagation," Proc. IRE, August 1958.

13. R. Hill, "Some Observations of Ionospheric Faraday Rotation on 106.1 Mc/s, J. Geo. Res., Vol. 65, January, 1960.
14. Daniels and Bauer, "Ionospheric Faraday Effect and Its Applications," J. Franklin Institute, Vol. 207, March, 1959.
15. Ratcliffe, "Physics of the Upper Atmosphere, Academic Press, 1960.
16. Ionospheric Radio Propagation, National Bureau of Standards, Boulder, Colorado, NBS Report, June 1948.
17. J. Pope, "An Estimate of Electron Densities in the Exosphere by Means of Nose Whistlers," J. Geo. Res., Vol. 66, January 1961.
18. D. M. Joe, Faraday Rotation in the Ionosphere, Hughes Aircraft Company, Fullerton, California, ID 63-11-20, March 1963.
19. C. I. Beard, "Coherent and Incoherent Scattering of Microwaves from the Ocean," IRE Transactions, PGAP, September 1961.
20. J. Katz, "Radar Reflectivity of the Ocean Surface for Circular Polarization," IRE Transactions, PGAP, July, 1965.
21. M. Harrison, "The Receiving Antenna in a Plane-Polarized Field of Arbitrary Orientation," Proc. IRE, January, 1944.
22. H. R. Reed and C. M. Russell, Ultra-High Frequency Propagation, Wiley and Sons, New York, 1953.
23. Walsh, et al, "Subtle Differences in System Noise Temperature Measuring Techniques," Proceedings 1963 PGMTT Meeting, Boulder, Colorado.
24. G. Millman, "The Geometry of the Earth's Magnetic Field at Ionospheric Heights," Journal of Geophysical Research, July, 1959.
25. J. Wright, "A Model of the F Region above  $h_{\max}$  F2," Journal of Geophysical Research, January 1960.
26. Papas, Theory of Electromagnetic Wave Propagation, McGraw-Hill, 1965.
27. M. Easterling, R. Goldstein, The Effect of the Interplanetary Medium on S-Band Telecommunication, Technical Report No. 32-825, Jet Propulsion Laboratory, Pasadena, California, 1 September 1965.
28. D. C. Hogg, "Effective Antenna Temperatures due to Oxygen and Water Vapor in the Atmosphere," Journal Applied Physics, Vol. 30, No. 9 September 1959, p. 1417.

#### 7.4 COMMUNICATIONS SYSTEM

1. V. Rumsey, "Techniques for Handling Elliptically Polarized Waves with Special Reference to Antennas," Proc. IRE, May 1951.
2. H. E. King, Research and Experimentation on Space Applications of Millimeter Waves - Aerospace Corp, TDR-269, October 1964.
3. S. Fordyce, Communications and Tracking on the Apollo Lunar Exploration Mission, National Aeronautics and Space Administration, Washington, D. C., NASA N64-16176.
4. Watson, Apollo Telecommunications System, National Aeronautics and Space Administration, Washington, D. C., N64-16177.
5. Brennan, et al, Some Aspects of Space Communication, Lincoln Laboratory, N63-13858, 21 March 1962.
6. R. Choate, Design Techniques for Low Power Telemetry, Technical Report No. 32-153, Jet Propulsion Laboratory, Pasadena, California, 5 March 1962.
7. I. Olin, Power Transfer Between Arbitrarily Polarized Antennas From Experimentally Measurable Parameters, U. S. Naval Research Laboratory, Washington, D. C., NRL No. 6212, March 1965.
8. R. Hartop, Power Loss Between Arbitrarily Polarized Antennas, Technical Report No. 32-457, Jet Propulsion Laboratory, Pasadena, California, September 1964.
9. G. Sinclair, "The Transmission and Reception of Elliptically Polarized Waves," Proc. IRE, February 1950.
10. J. Painter, et al, Unified S-Band Telecommunications Techniques for Apollo, National Aeronautics and Space Administration, Washington, D. C., TND-2208, March 1965.
11. Basic Operating Limits on Communication Links with Spacecraft, National Aeronautics and Space Administration, Washington, D. C., N65-33959, September 1965.
12. R. Mathison, Mariner March 1964 Telemetry and Command System, Jet Propulsion Laboratory, Pasadena, California, Technical Report No. 32-684, June 1, 1965.

13. Proceedings of the Apollo Unified S-Band Technical Conference, Goddard Space Flight Center, NASA SP-87, July 1965.
14. Syncom C System Summary - NAS5-1560, Hughes Aircraft Company, Culver City, California, April, 1964.
15. Proceedings of the IRE - Space Electronics Issue, April 1960.
16. R. Mathison, Tracking Techniques for Interplanetary Spacecraft, Jet Propulsion Laboratory, Pasadena, California, Report No. 32-284, 1 August 1962.
17. Cohen and Steinmetz, "Amplitude and Phase Sensing Monopulse System Parameters," Microwave Journal, November, 1959.
18. M. Easterling, Methods for Obtaining Velocity and Range Information from CW Radars, Jet Propulsion Laboratory, Pasadena, California, Technical Report 32-657, 1 September 1964.
19. M. Easterling, A Long Range Precision Ranging System, Jet Propulsion Laboratory, Pasadena, California, Technical Report No. 32-80, 10 July 1961.

## SECTION EIGHT

### APPENDICES

Appendix I. Graphs of Power Loss Between Two Arbitrarily Polarized Antennas Versus Axial Ratio

Appendix II. One Way Faraday Rotation Versus Spacecraft Height

Appendix III. Theoretical Pattern of a Thirty Foot Antenna Above a Good Earth

Appendix IV. Phase Lock Loop Analysis

Introduction

Response for a Frequency Step Input

Response for a Frequency Ramp Input

**Appendix I**

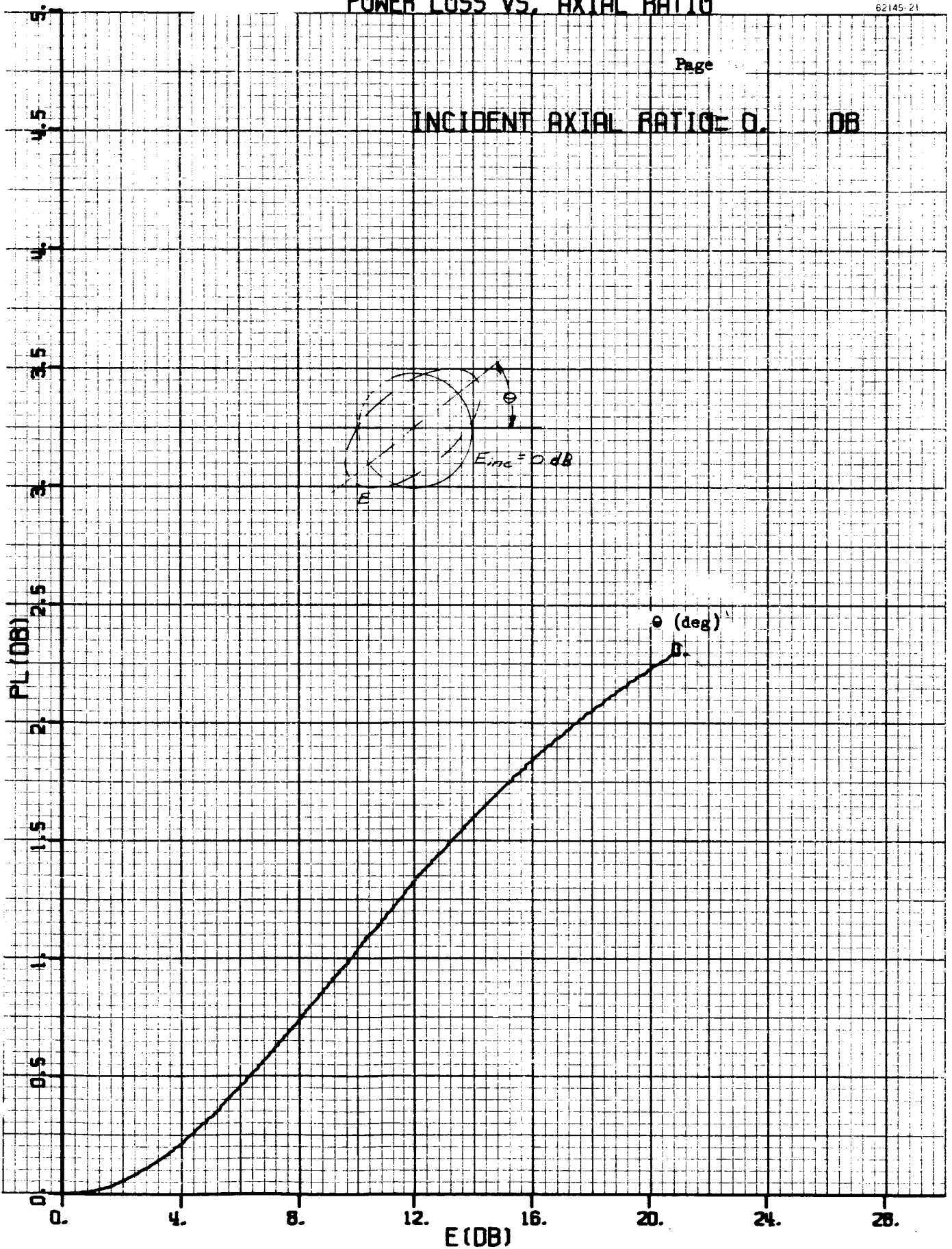
**GRAPHS OF POWER LOSS BETWEEN TWO ARBITRARILY POLARIZED  
ANTENNAS VERSUS AXIAL RATIO**

# POWER LOSS VS. AXIAL RATIO

62145-21

Page

INCIDENT AXIAL RATIO = 0. DB



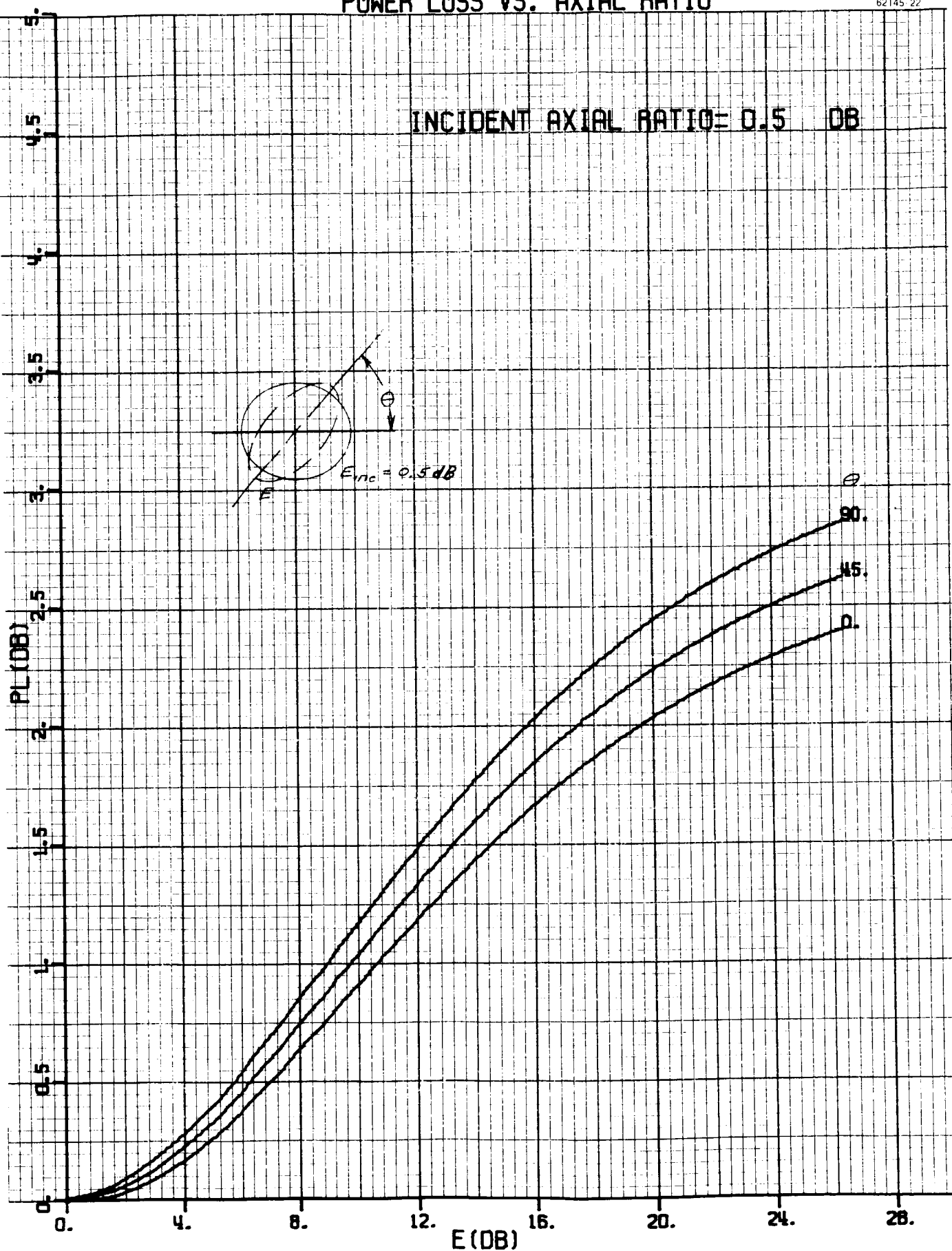
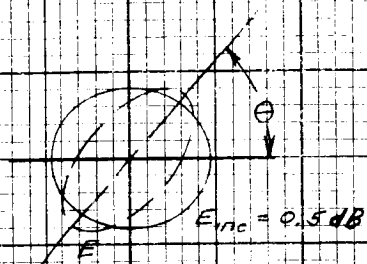
Graph I-1. Power Loss Versus Axial Ratio



# POWER LOSS VS. AXIAL RATIO

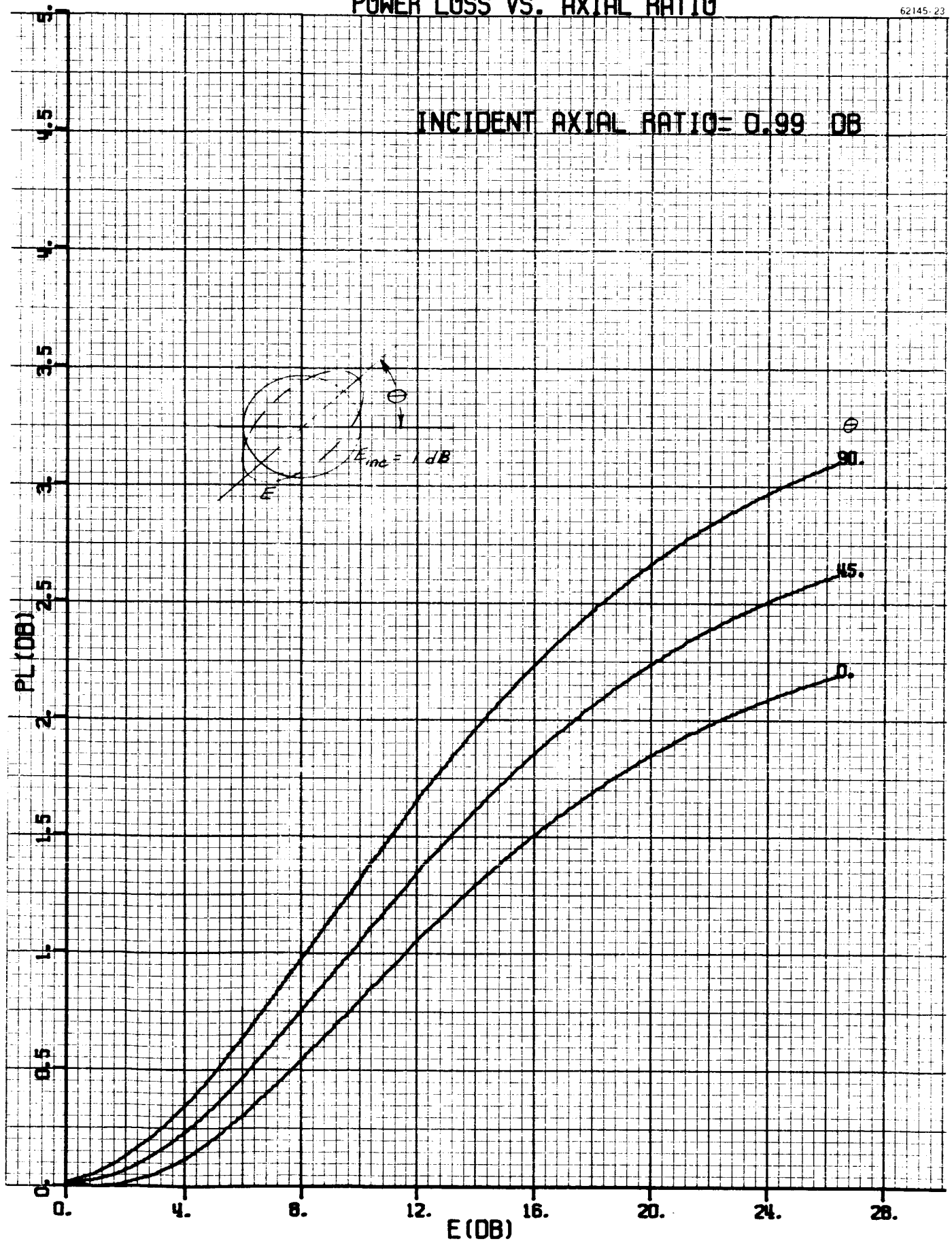
62145-22

INCIDENT AXIAL RATIO = 0.5 DB



# POWER LOSS VS. AXIAL RATIO

62145-23

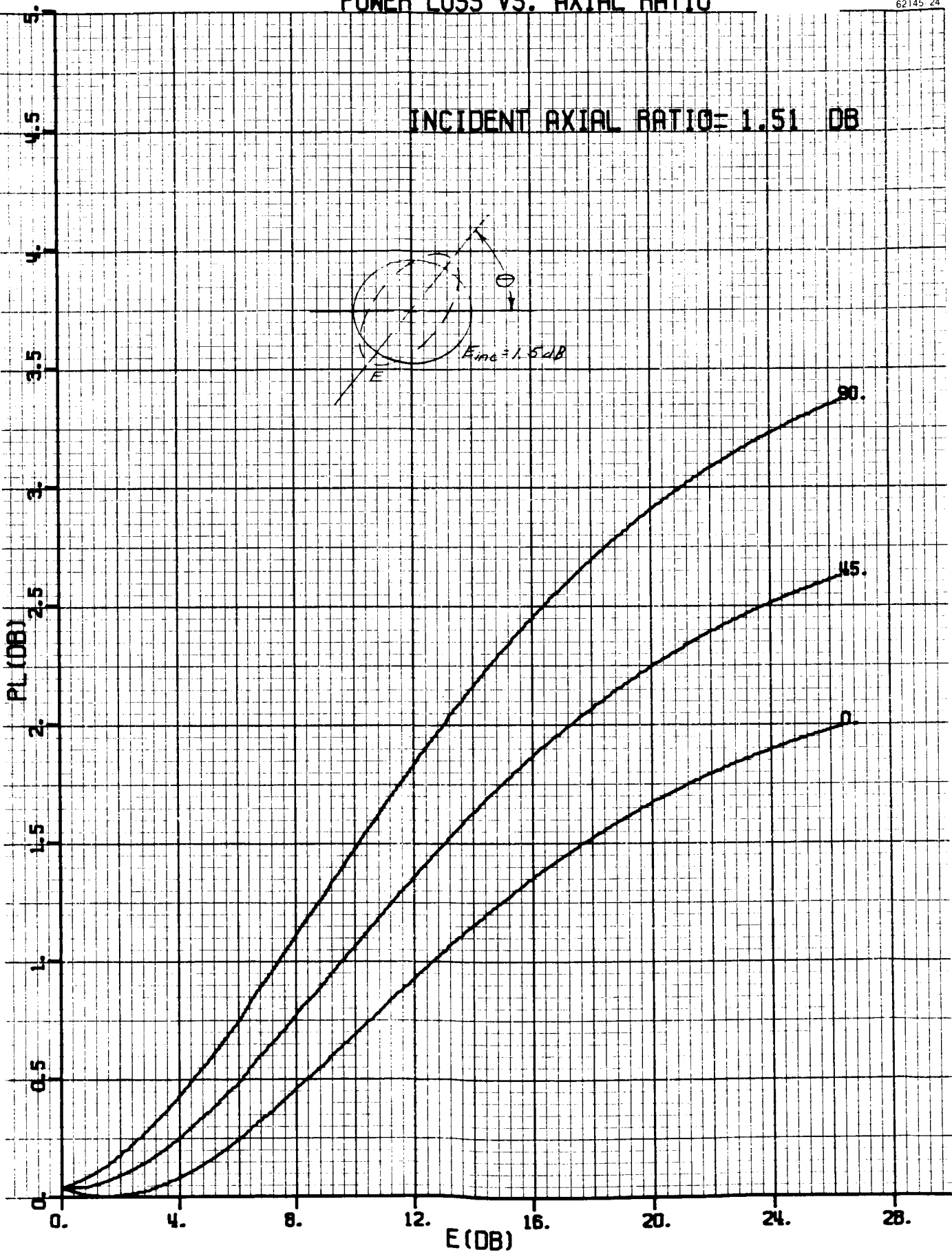
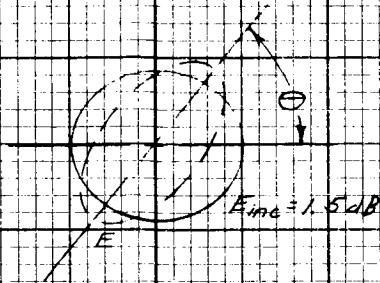


Graph I-3. Power Loss Versus Axial Ratio

# POWER LOSS VS. AXIAL RATIO

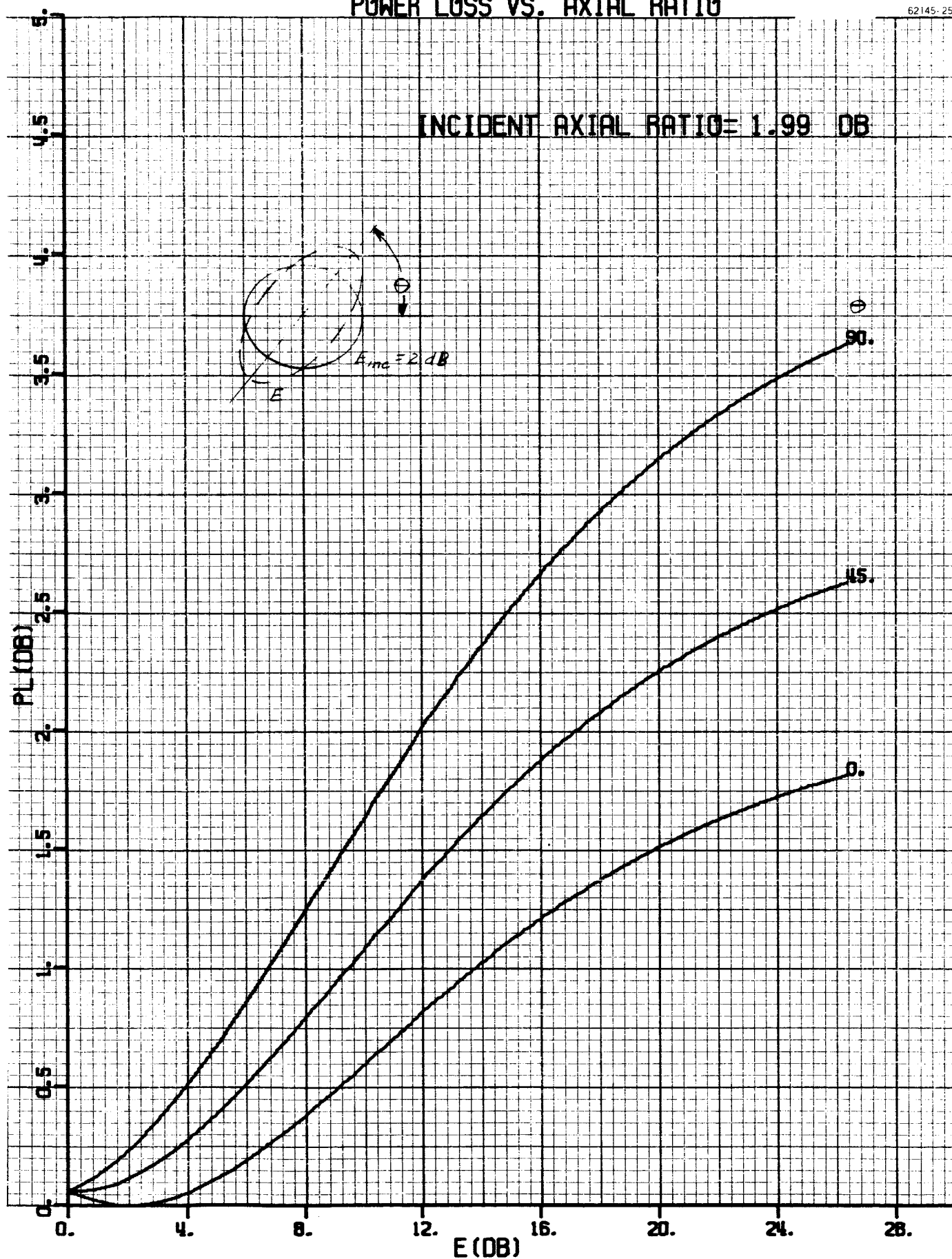
62145 24

INCIDENT AXIAL RATIO = 1.51 DB



# POWER LOSS VS. AXIAL RATIO

62145-25

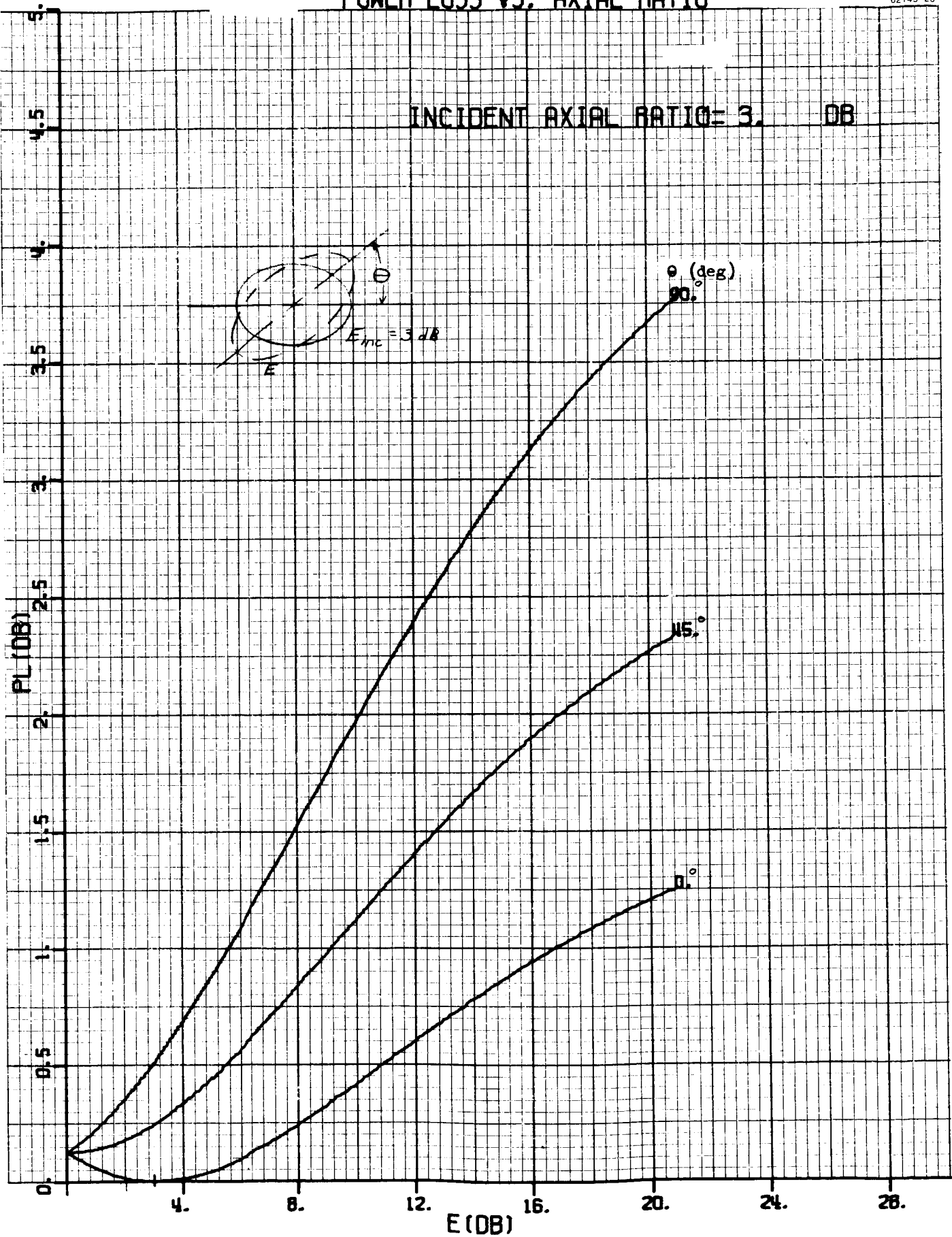


Graph I-5. Power Loss Versus Axial Ratio

# POWER LOSS VS. AXIAL RATIO

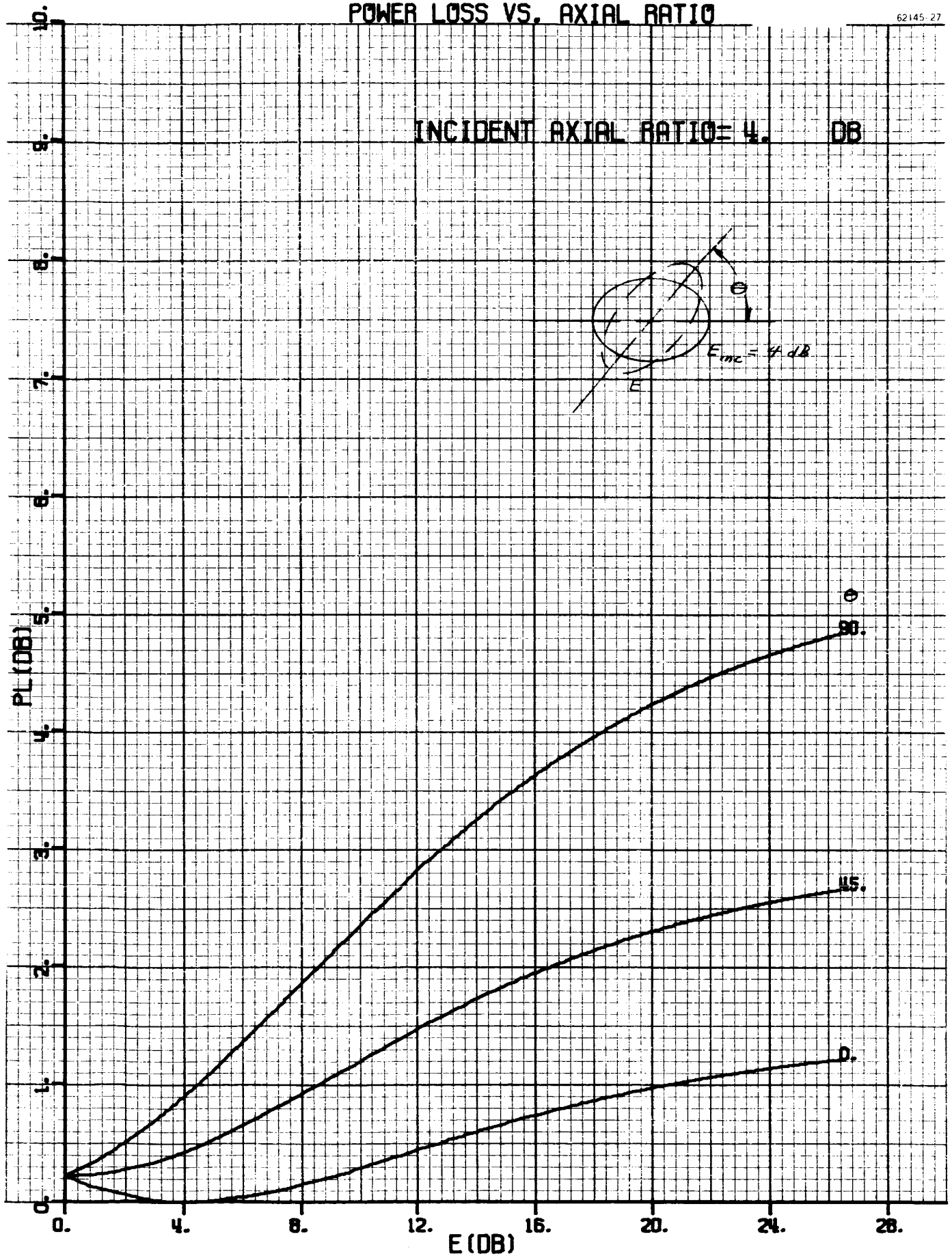
62145-26

INCIDENT AXIAL RATIO = 3.00 DB



# POWER LOSS VS. AXIAL RATIO

62145-27

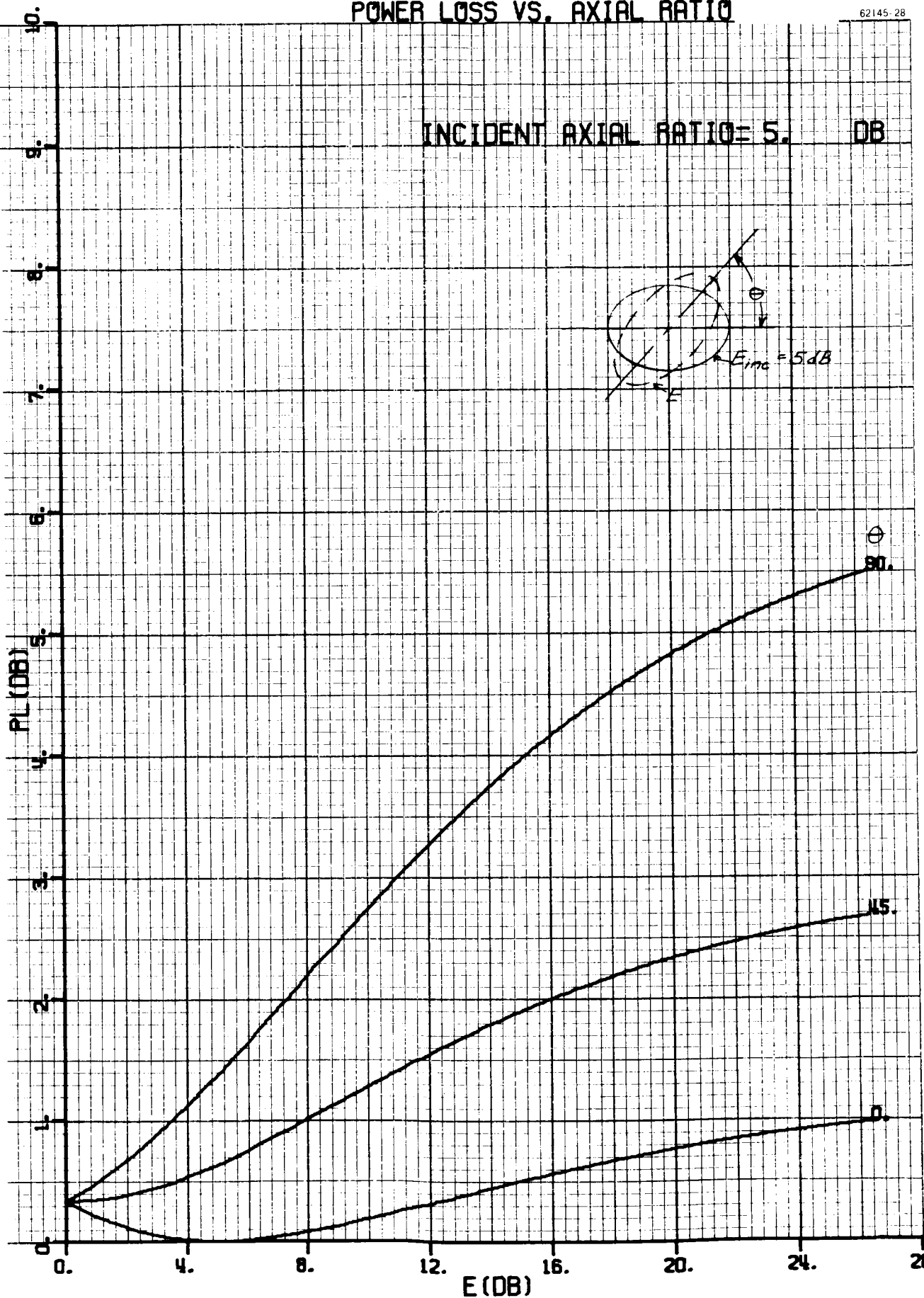
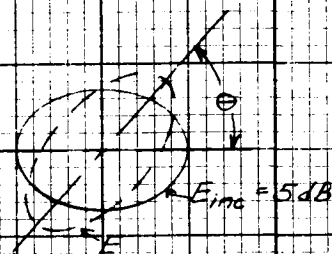


Graph I-7. Power Loss Versus Axial Ratio

# POWER LOSS VS. AXIAL RATIO

62145-28

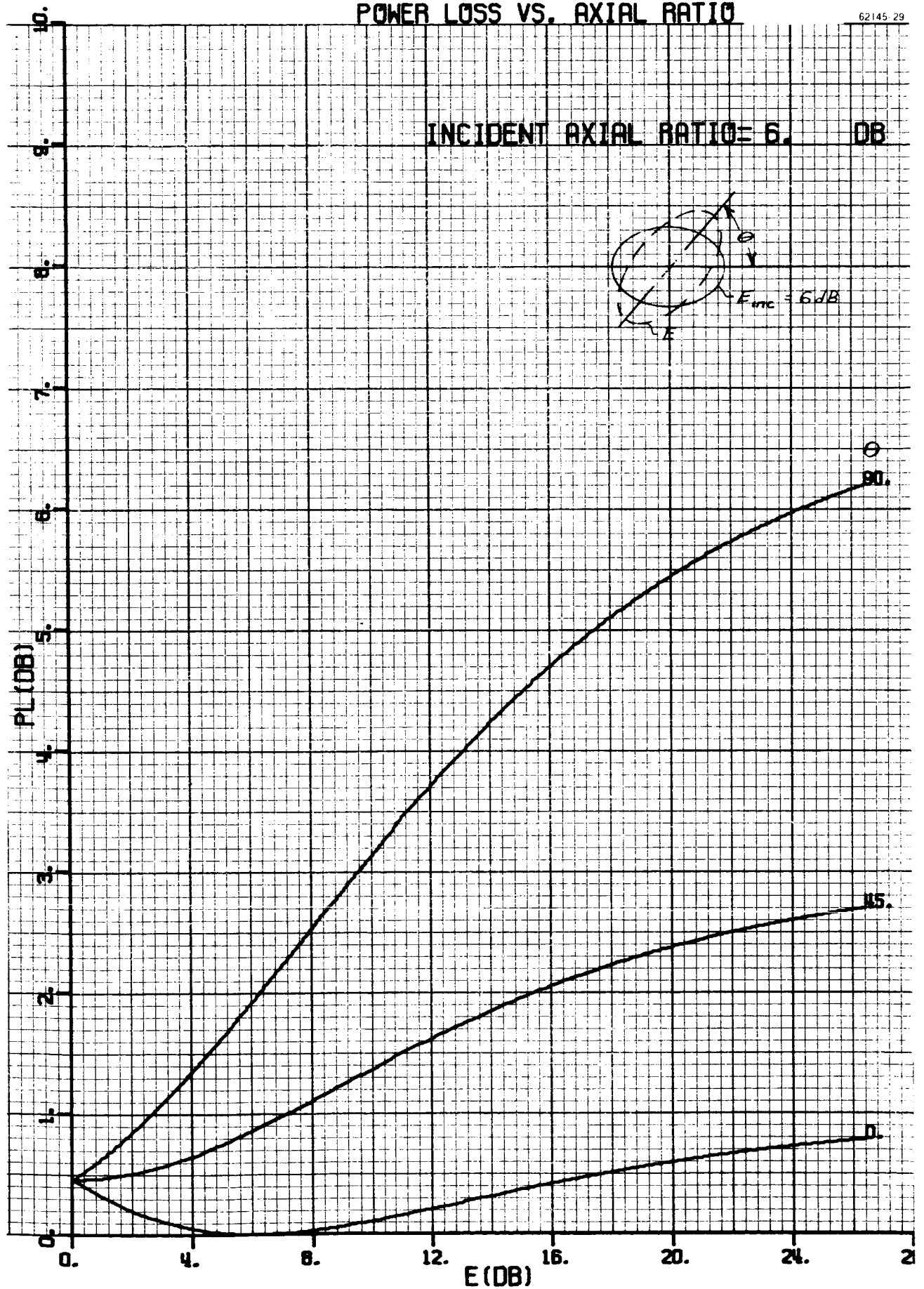
INCIDENT AXIAL RATIO = 5. DB





# POWER LOSS VS. AXIAL RATIO

62145 29



Graph I-9. Power Loss Versus Axial Ratio

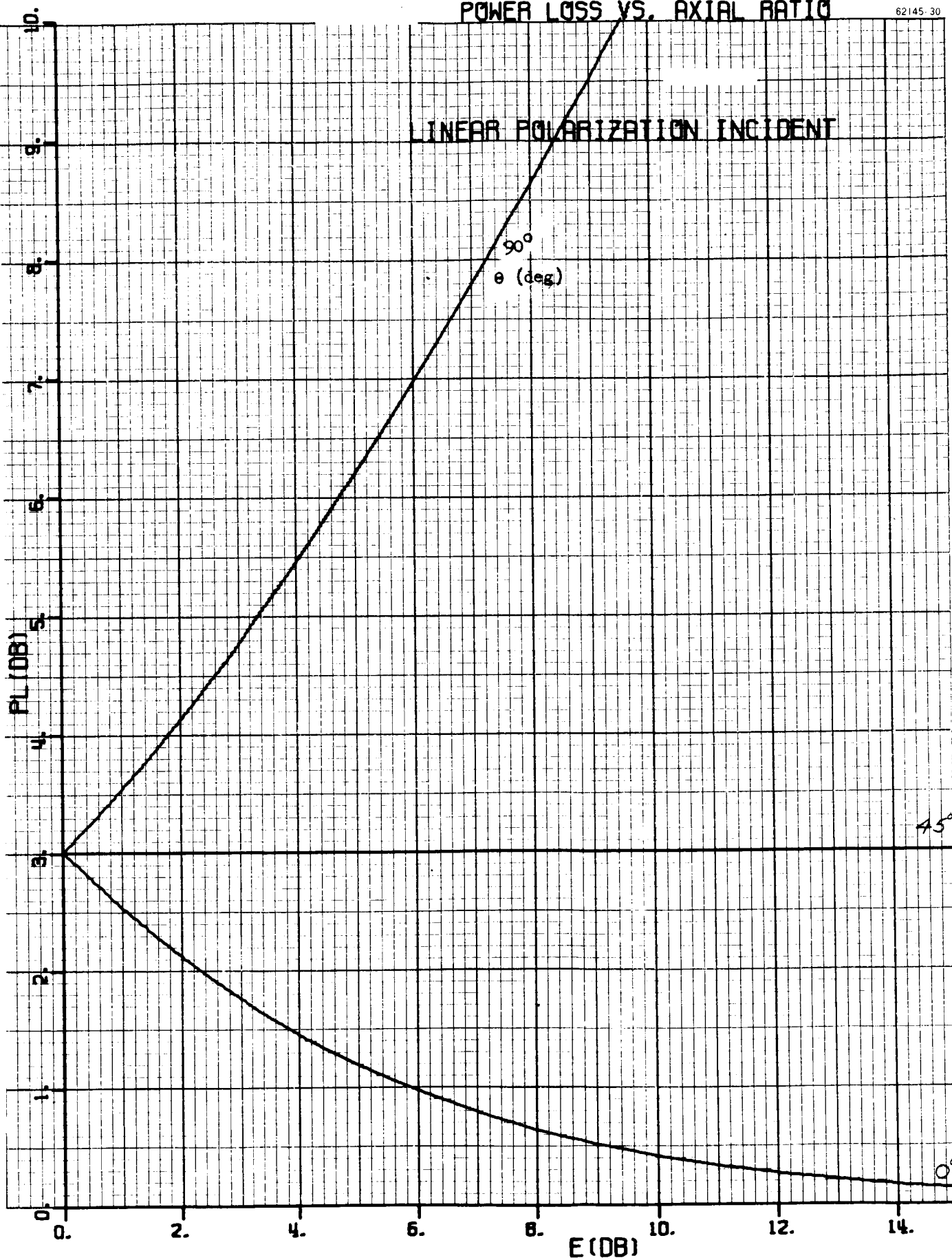


# POWER LOSS VS. AXIAL RATIO

62145-30

LINEAR POLARIZATION INCIDENT

90°  
θ (deg)

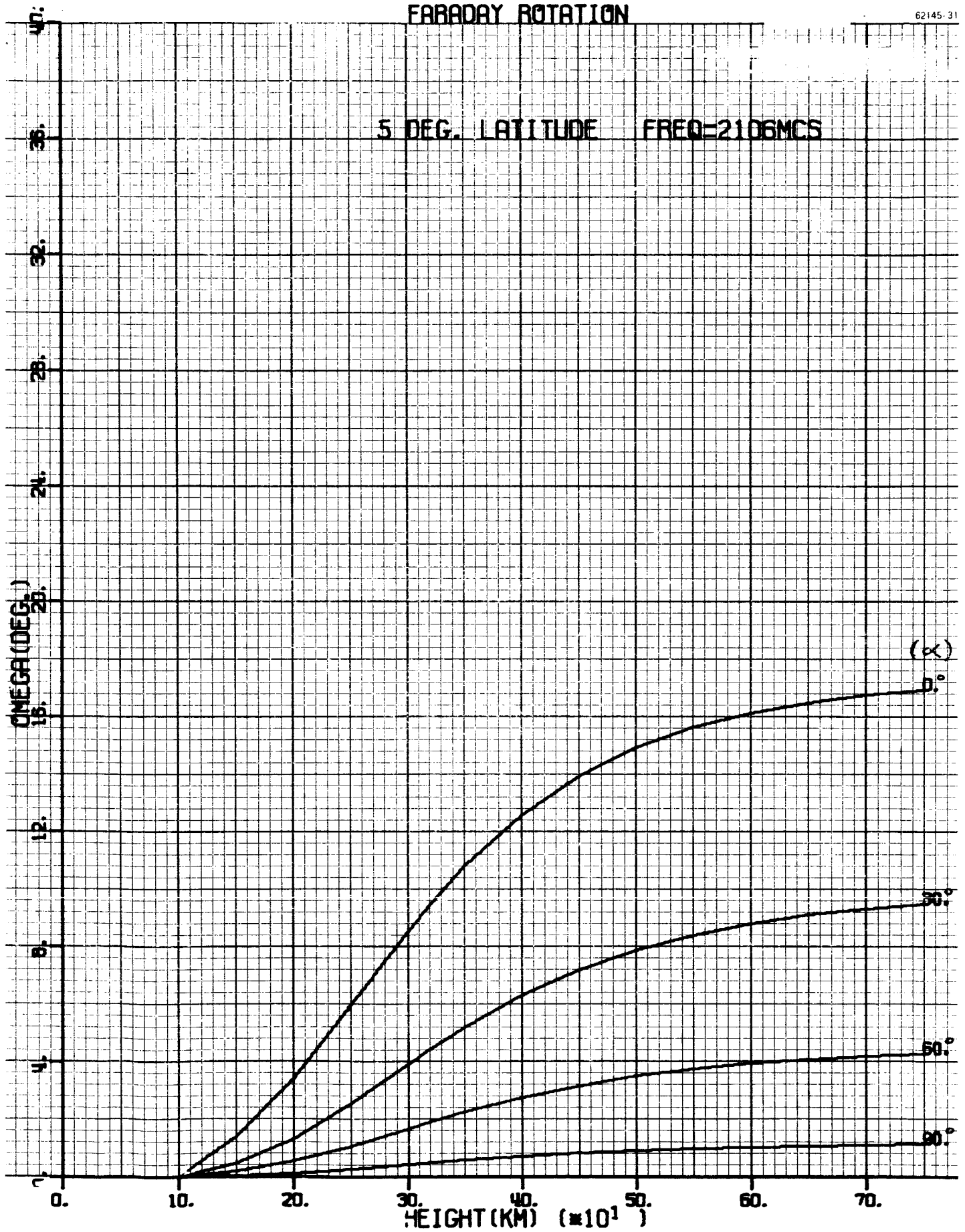


**Appendix II**

**ONE WAY FARADAY ROTATION VERSUS SPACECRAFT HEIGHT**

# FARADAY ROTATION

62145-31



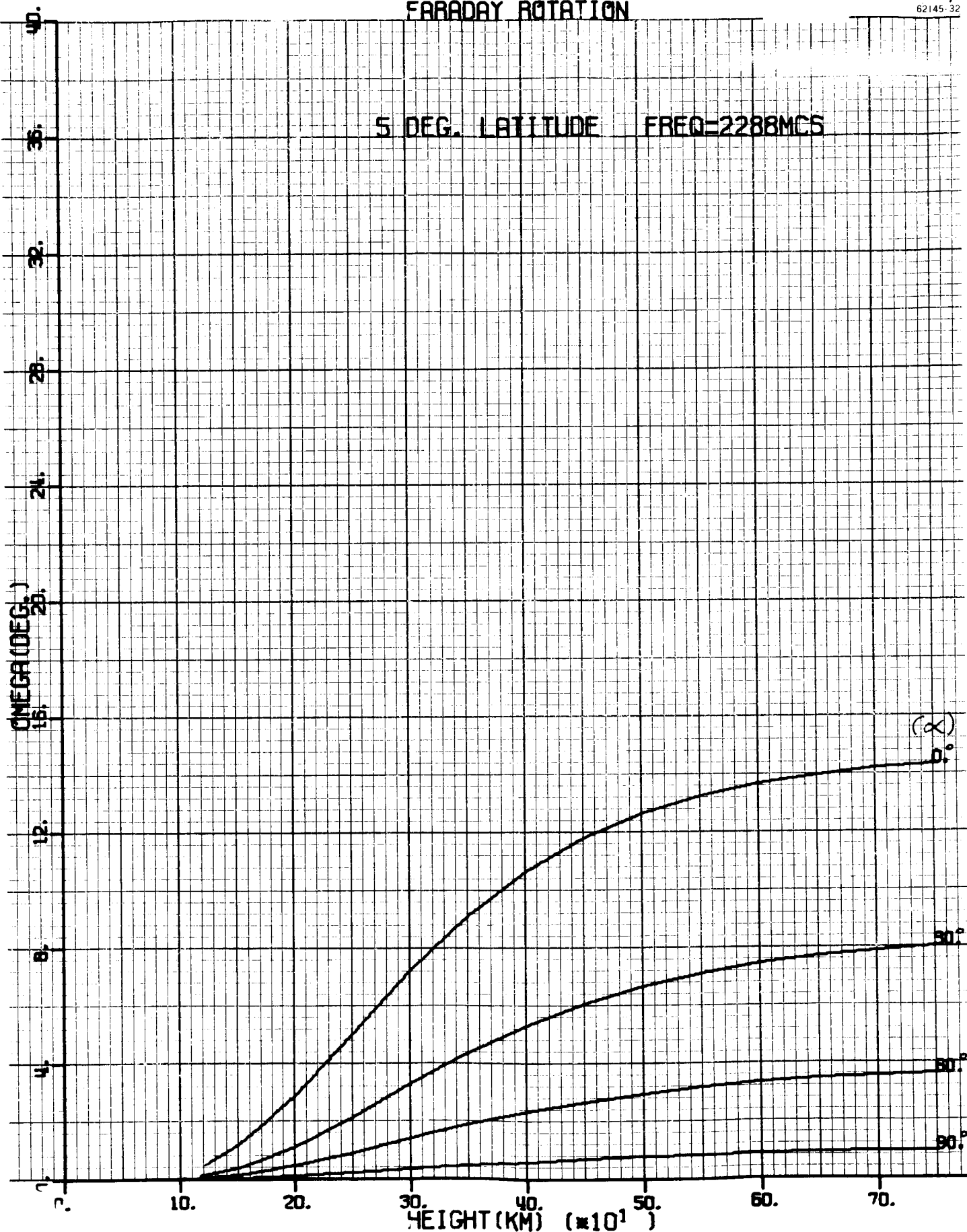
Graph II-1.

# FARADAY ROTATION

62145-32

5 DEG. LATITUDE

FREQ=2288MCS



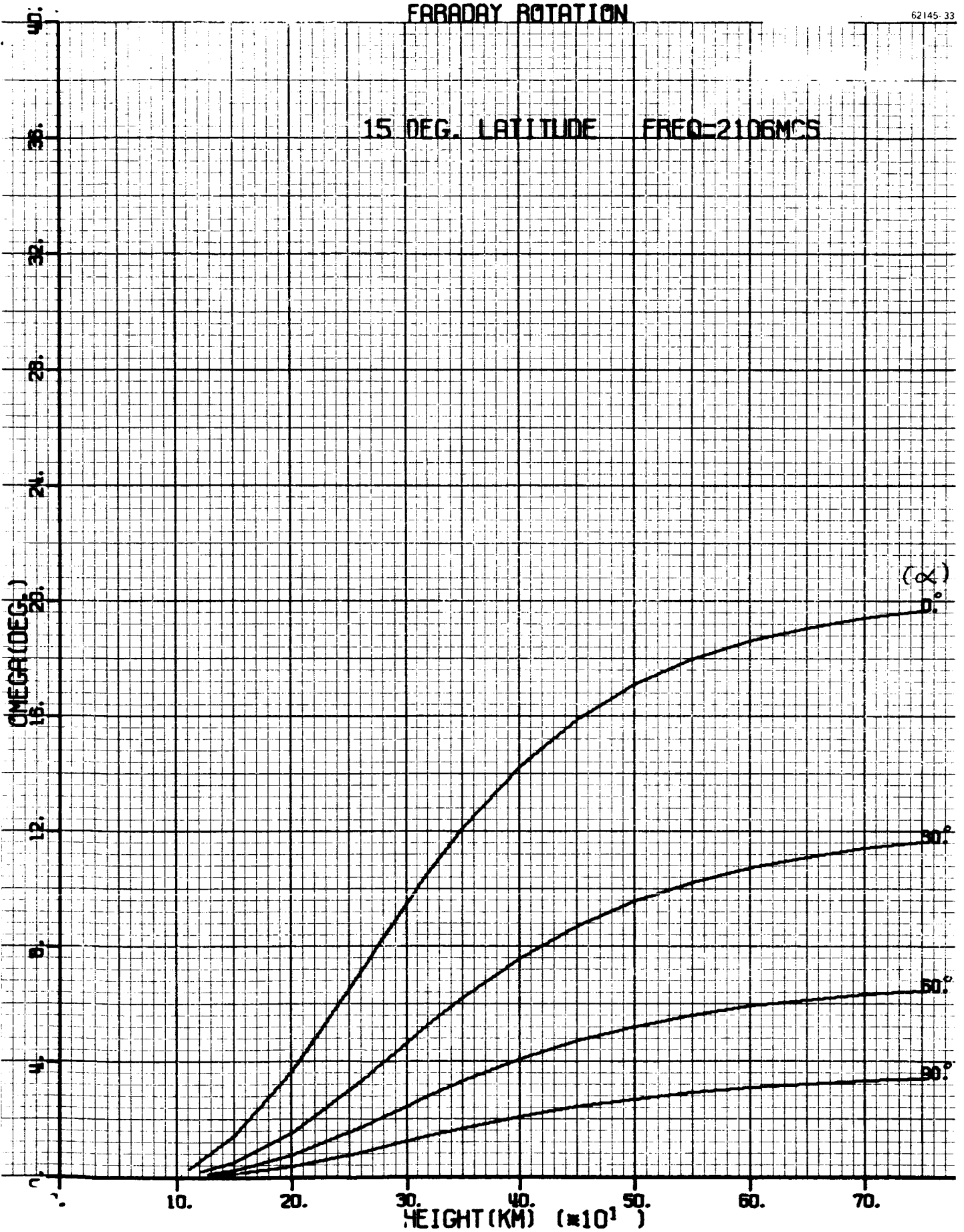
Graph II-2.

# FARADAY ROTATION

62145-33

15 DEG. LATITUDE

FREQ=2106MCS

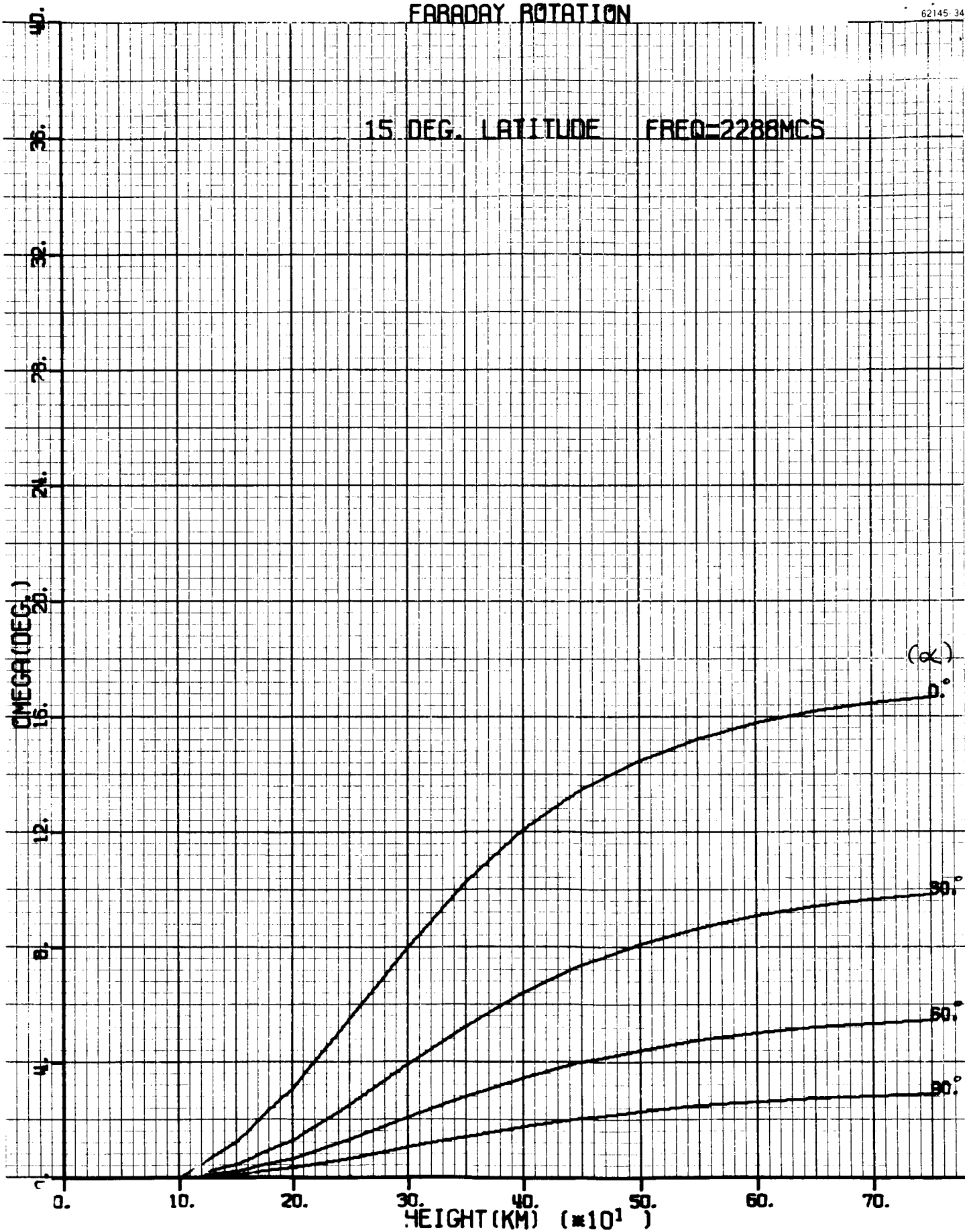


Graph II-3.

# FARADAY ROTATION

62145 34

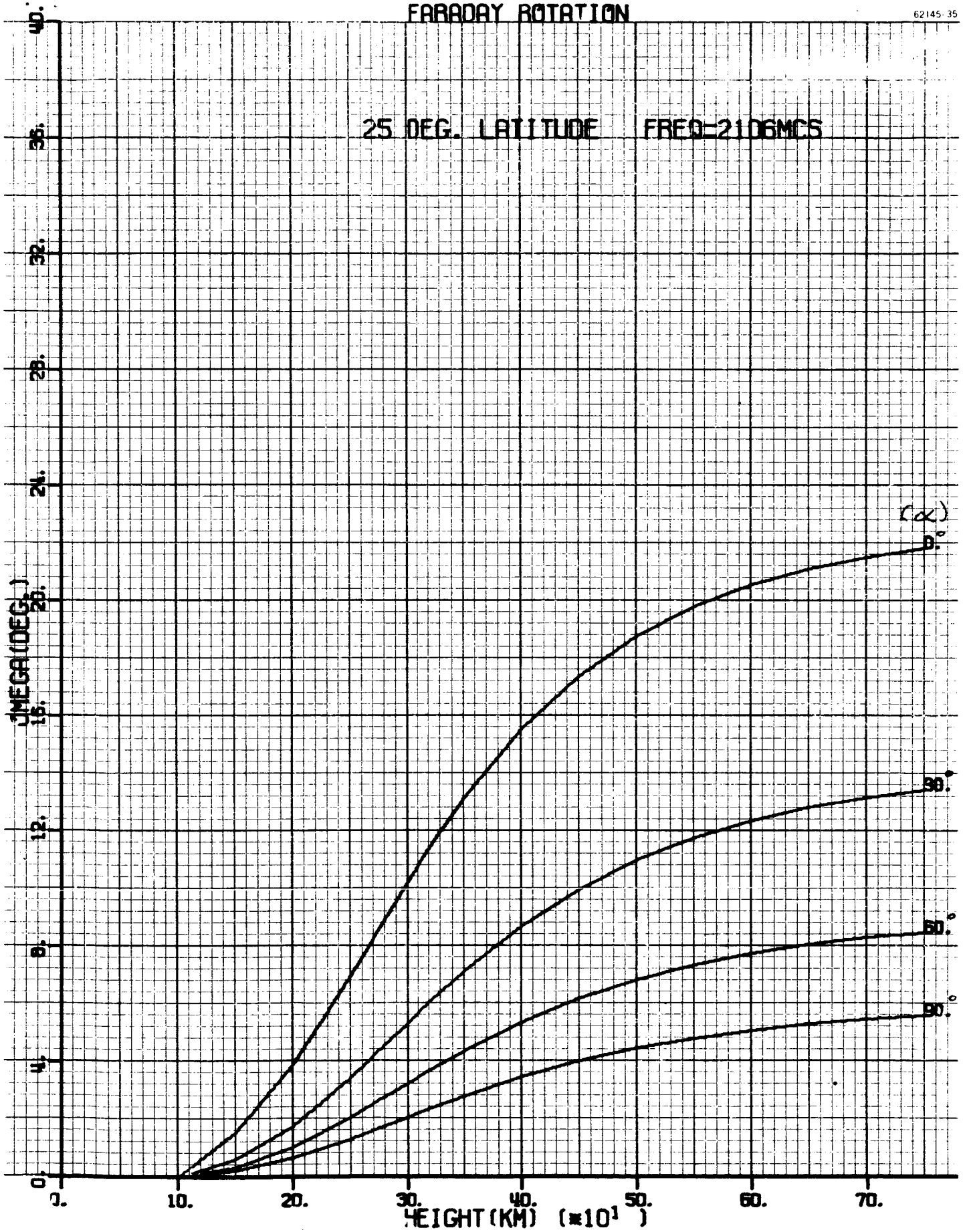
15 DEG. LATITUDE FREQ=2288MCS



Graph II-4.

# FARADAY ROTATION

62145-35



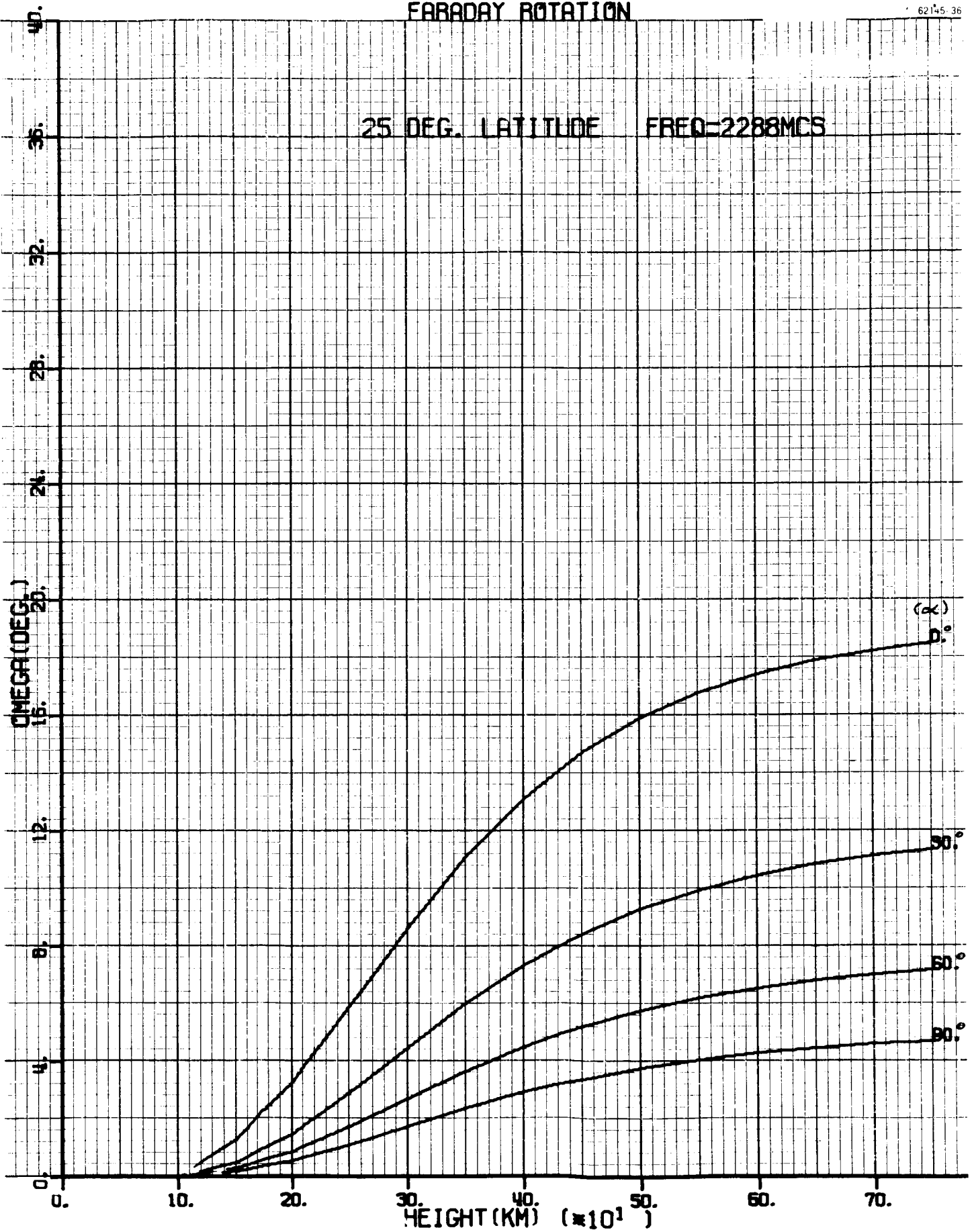
Graph II-5.

# FARADAY ROTATION

62145-36

25 DEG. LATITUDE

FREQ=2288MCS



Graph II-6.

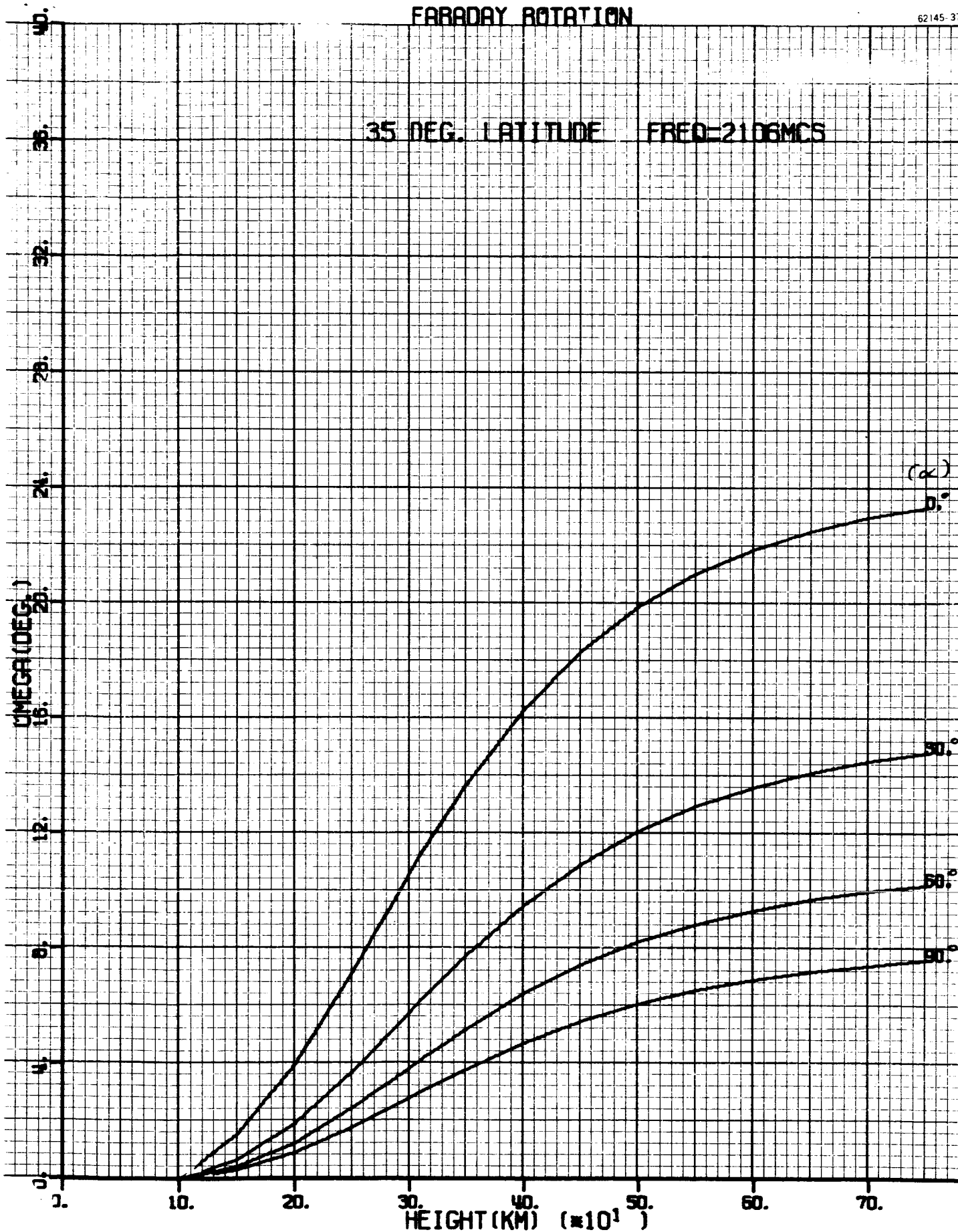


# FARADAY ROTATION

62145-37

35 DEG. LATITUDE

FREQ=2106MCS



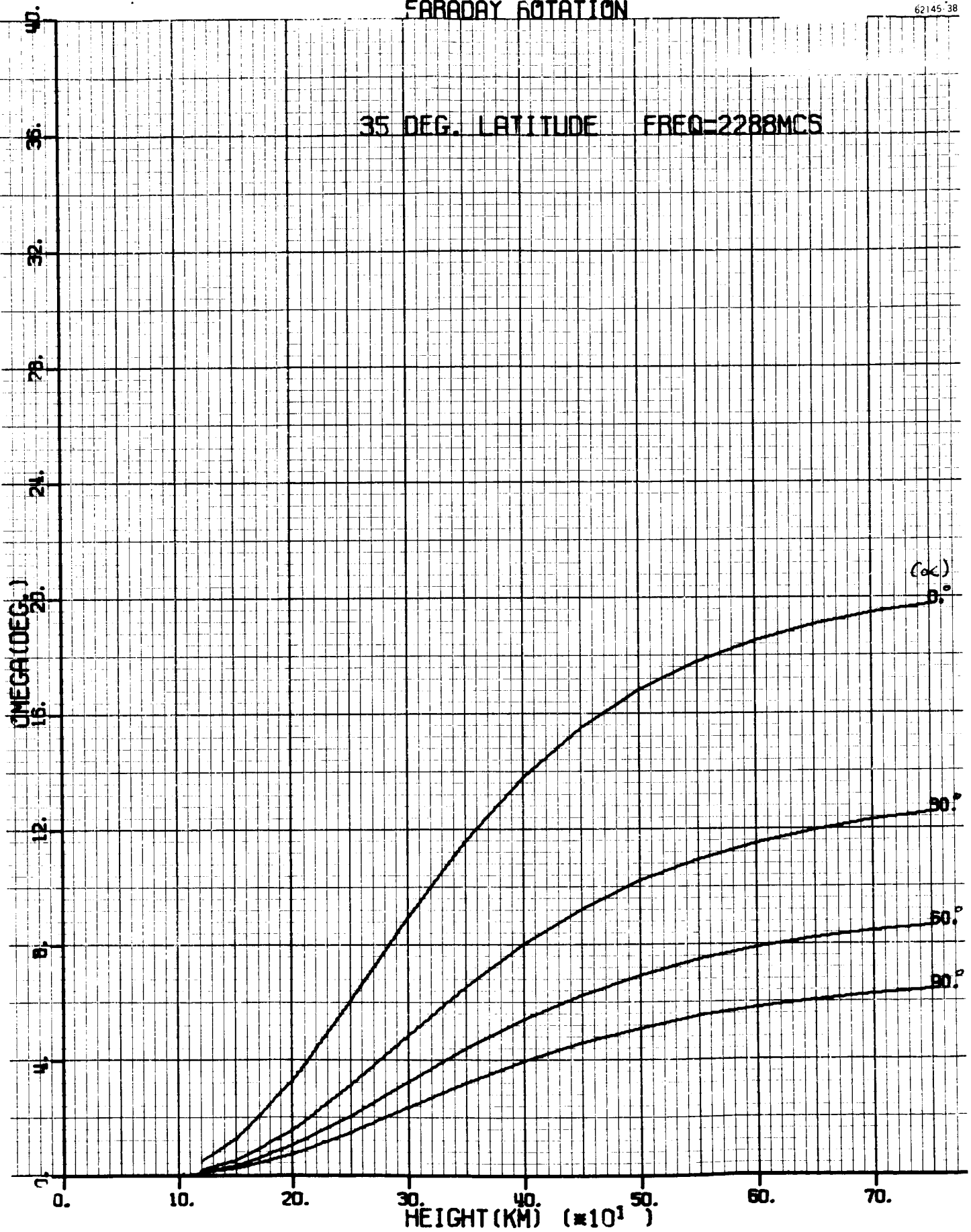
Graph II-7.

# FARADAY ROTATION

62145-38

35 DEG. LATITUDE

FREQ=2288MCS



Graph II-8.

**Appendix III**

**THEORETICAL PATTERNS OF A THIRTY FOOT ANTENNA ABOVE A GOOD  
EARTH ( $\sigma = 0.012$ ,  $\epsilon_r = 15$ )**

# PATTERN IN FREE SPACE

62145-39

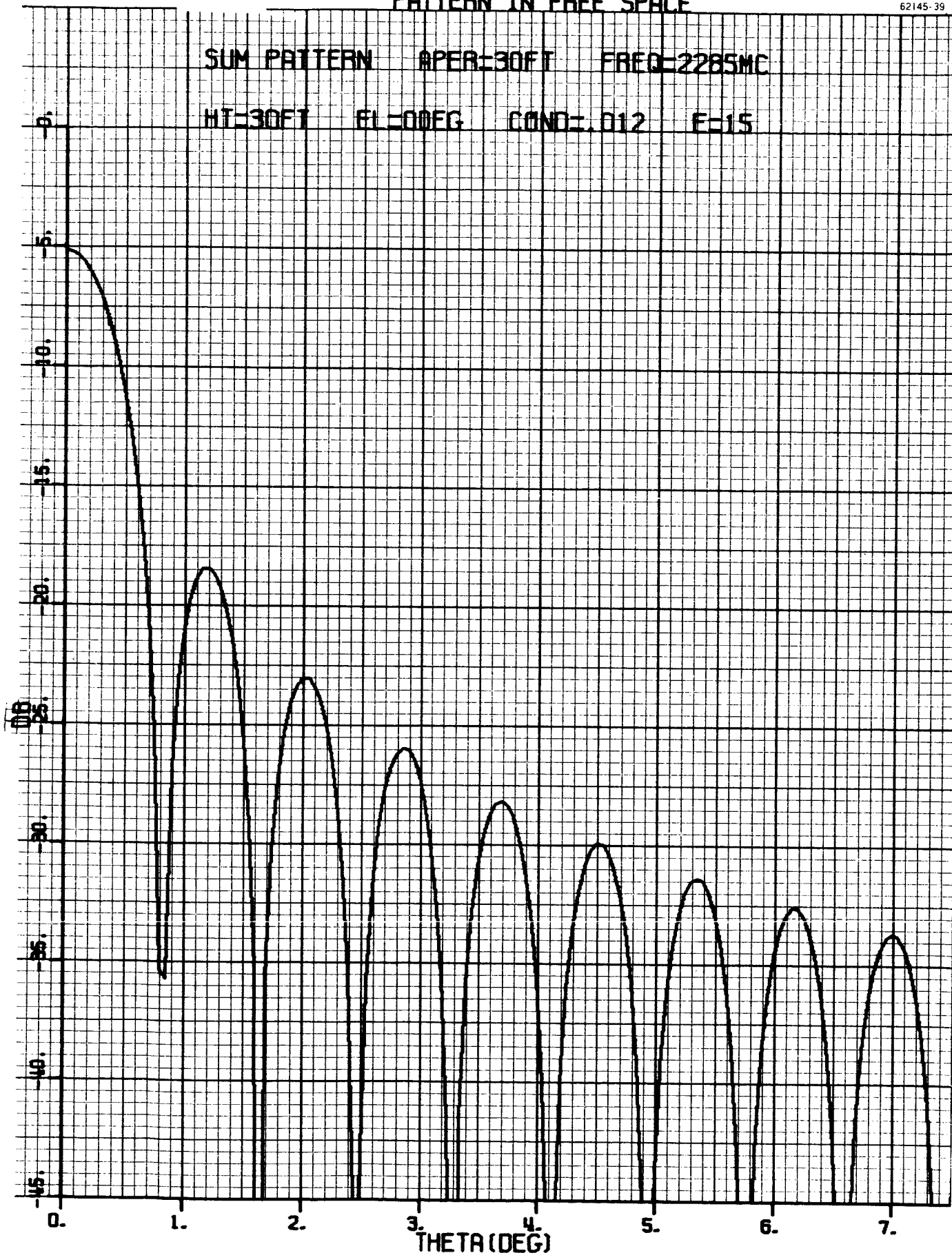


Figure III-1.

# PATTERN IN FREE SPACE

62145-40

ERROR PATTERN

APER=30FT

FREQ=2285MC

HT=30FT

EL=0DEG

COND=.012

E=15

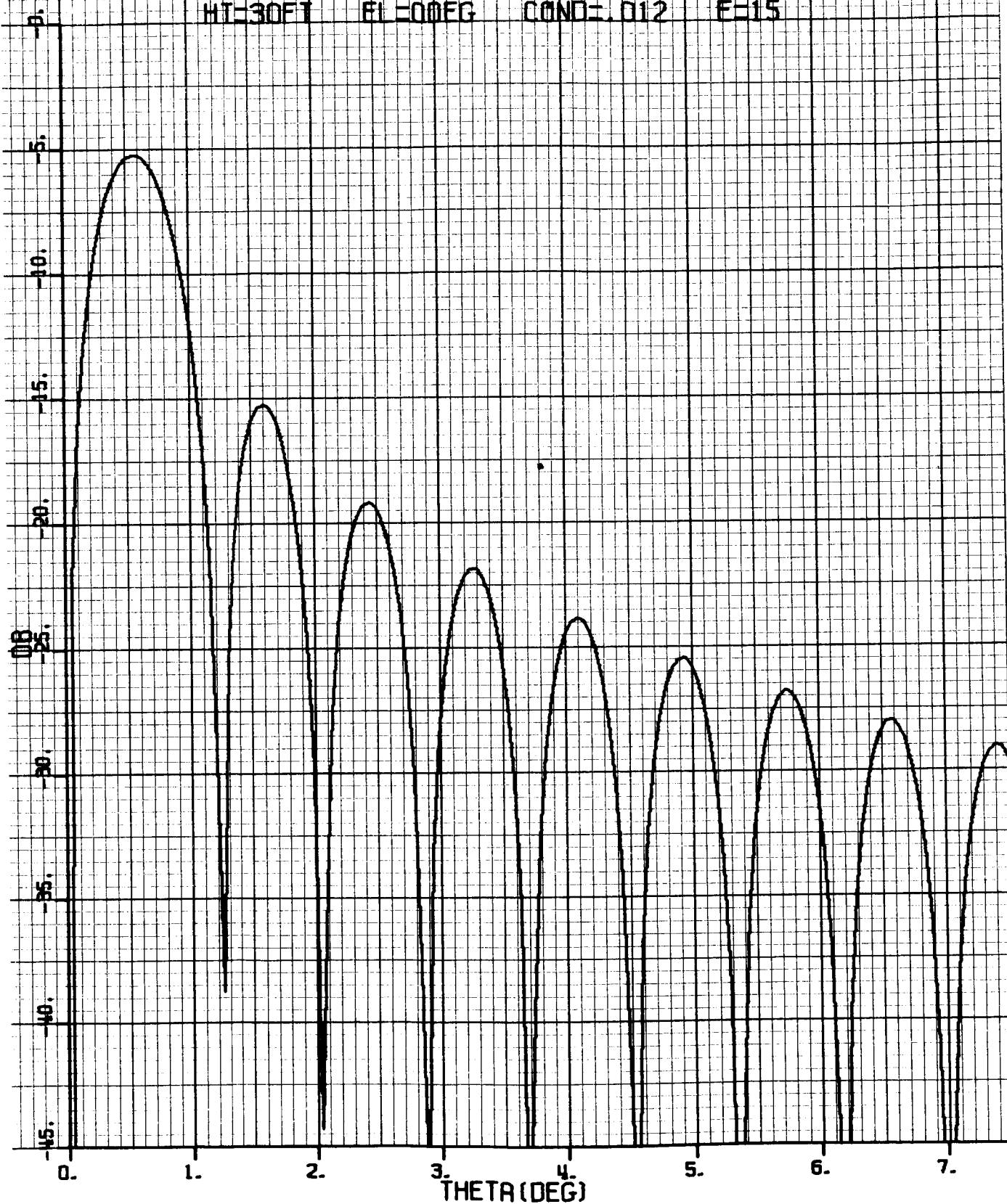


Figure III-2.

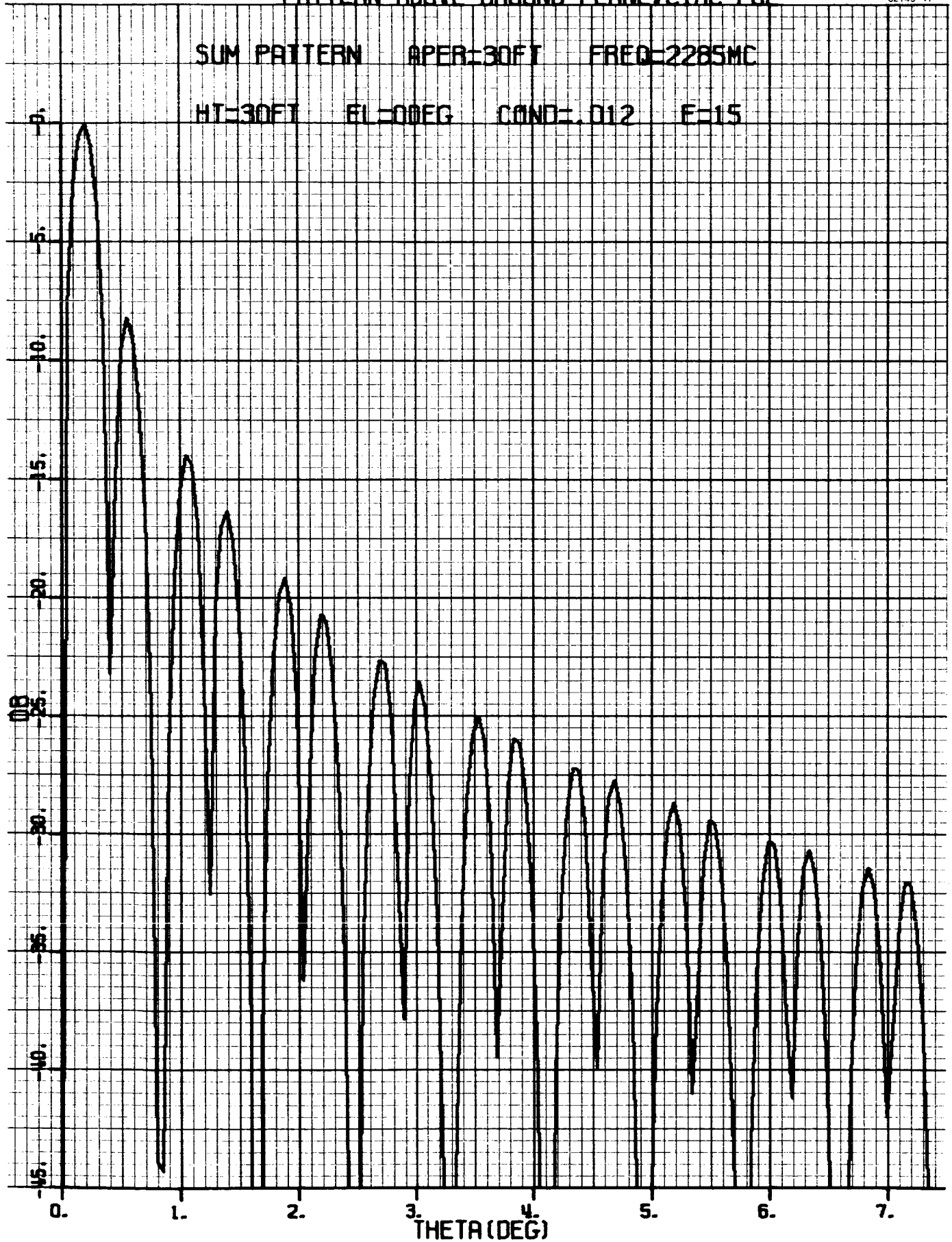


Figure III-3.

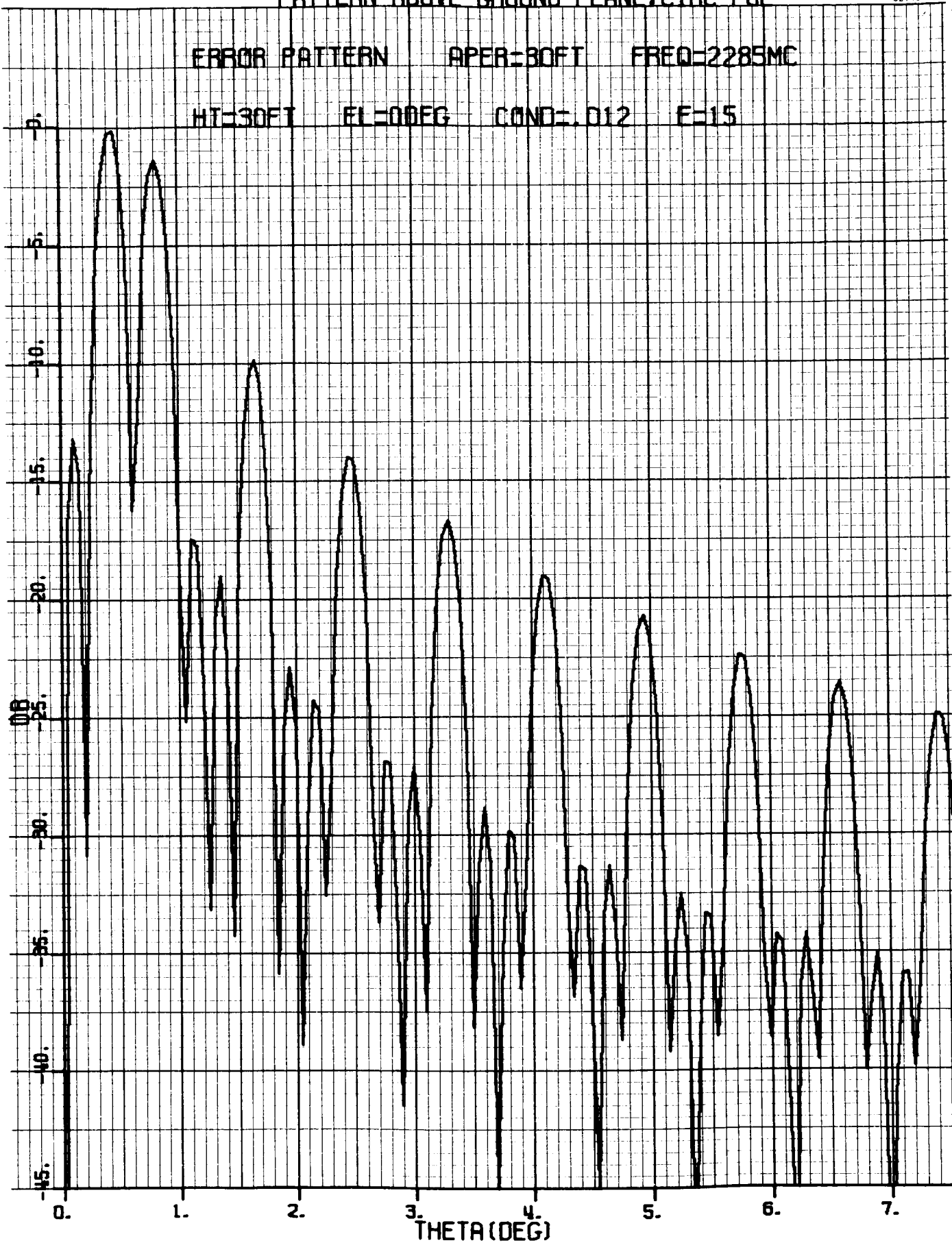


Figure III-4.

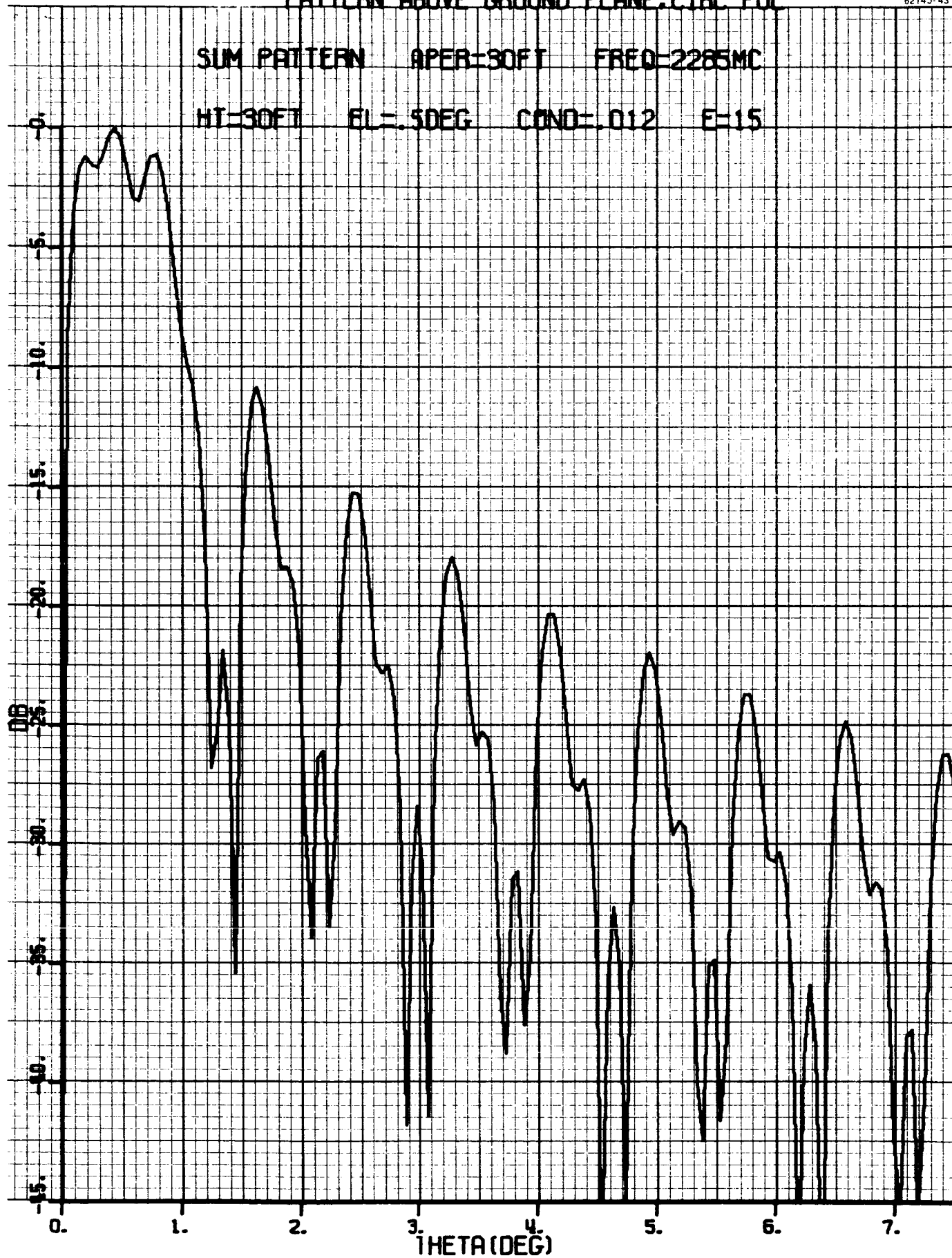


Figure III-5.



ERROR PATTERN APER=30FT FREQ=2285MC

HT=30FT EL=.50EG COND=.012 E=15

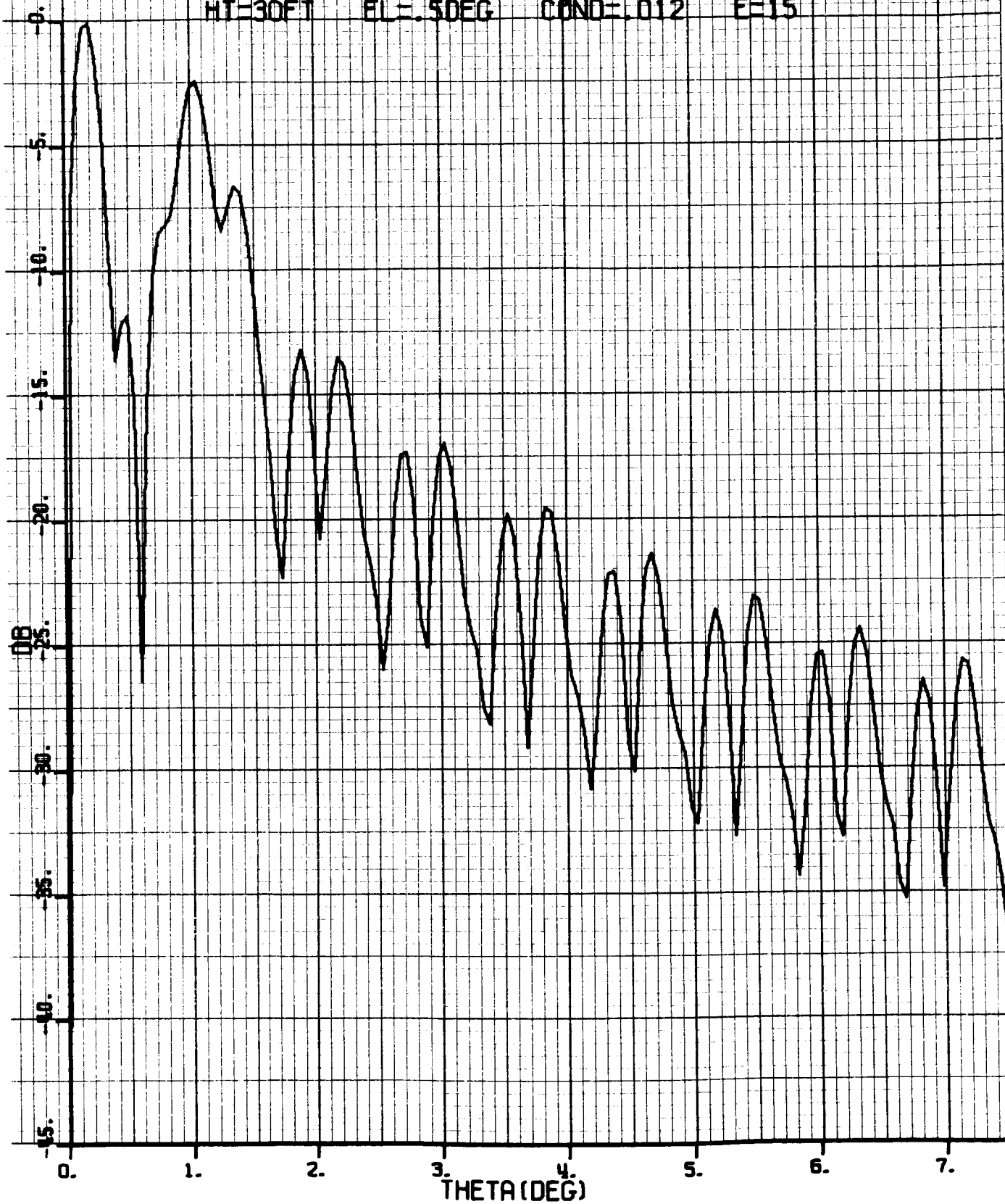


Figure III-6.

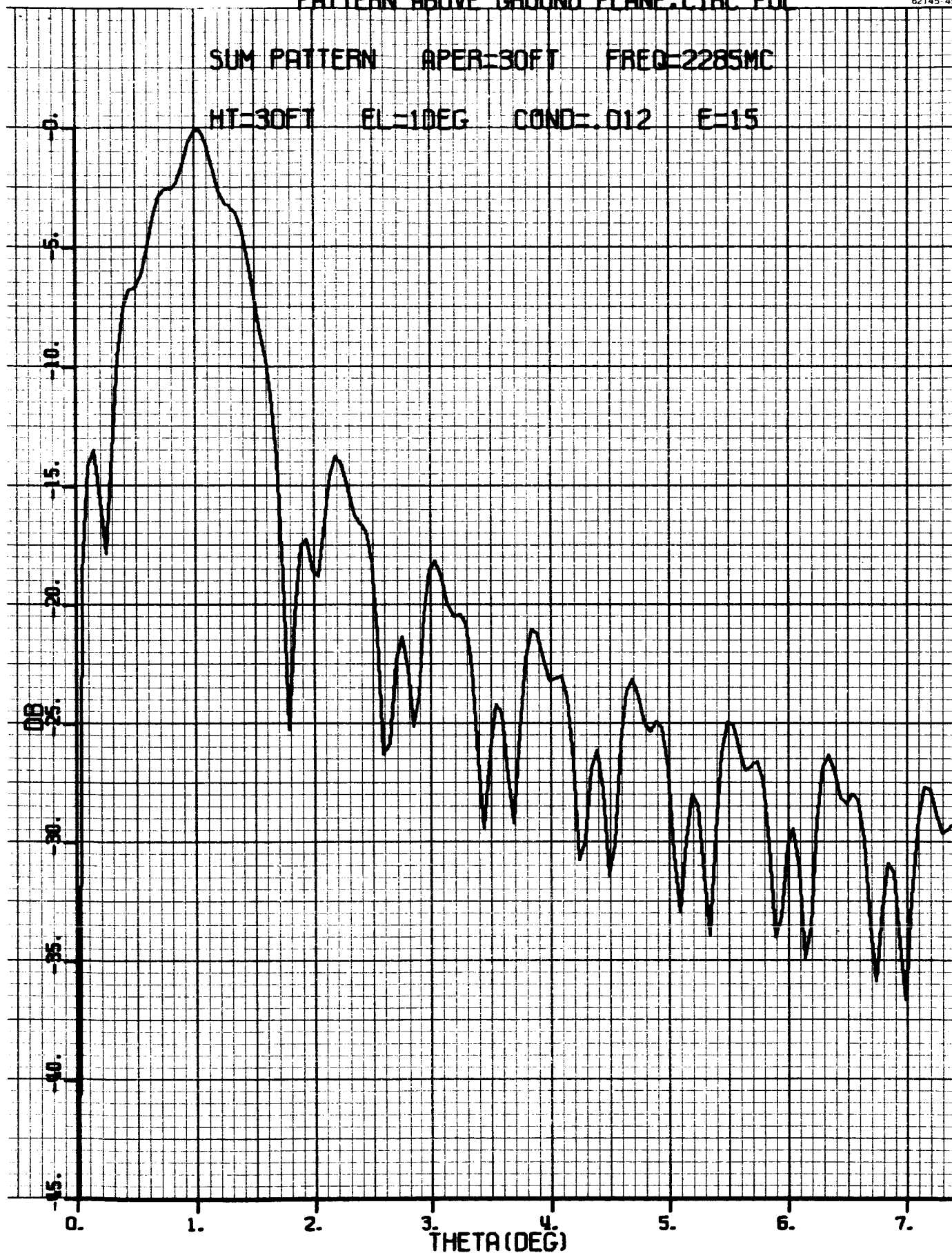


Figure III-7.

# PATTERN ABOVE GROUND PLANE, CIRC POL

62145-46

ERROR PATTERN APER=30FT FREQ=2285MC

HT=30FT EL=10DEG COND=.012 E=15

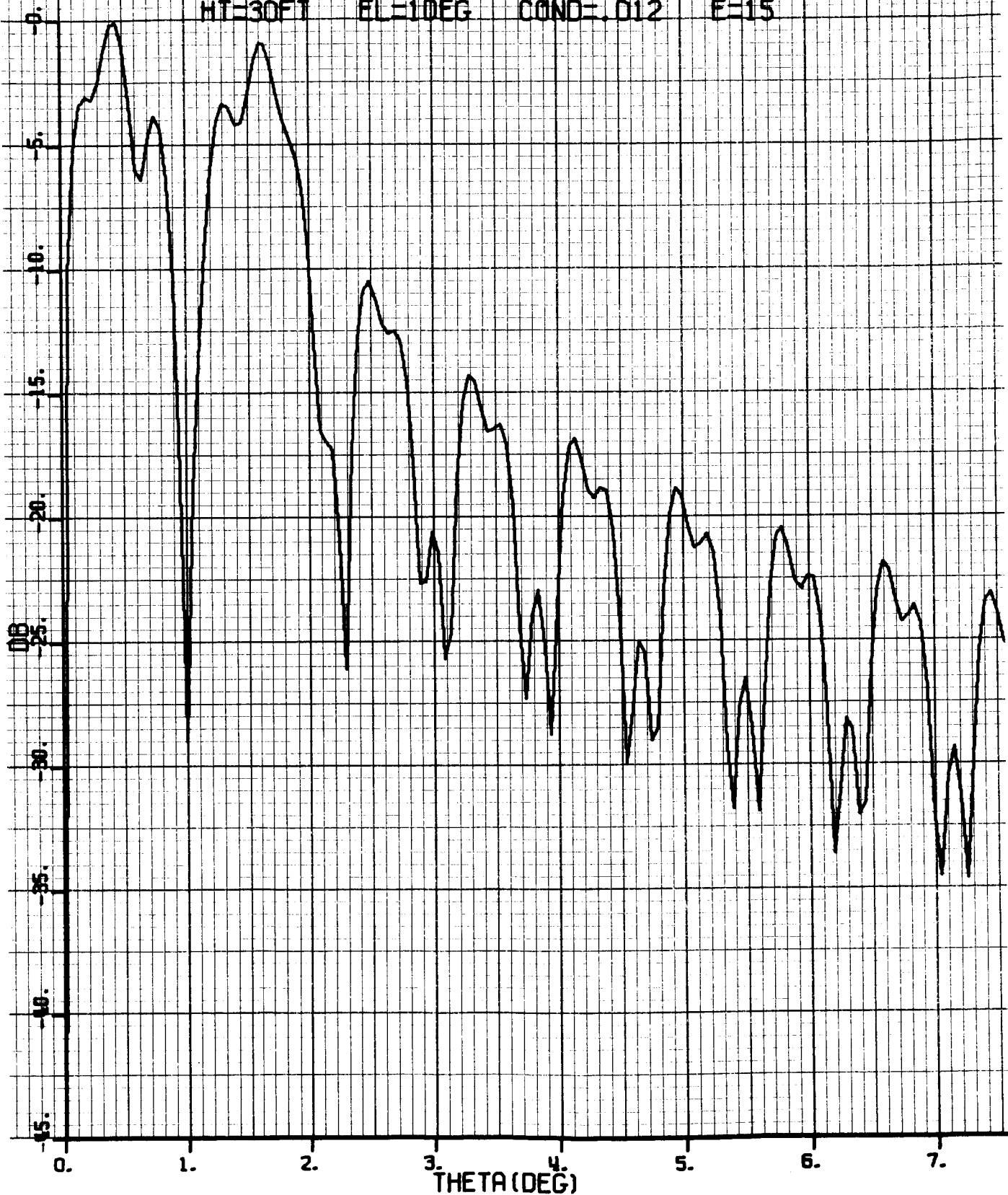


Figure III-8.

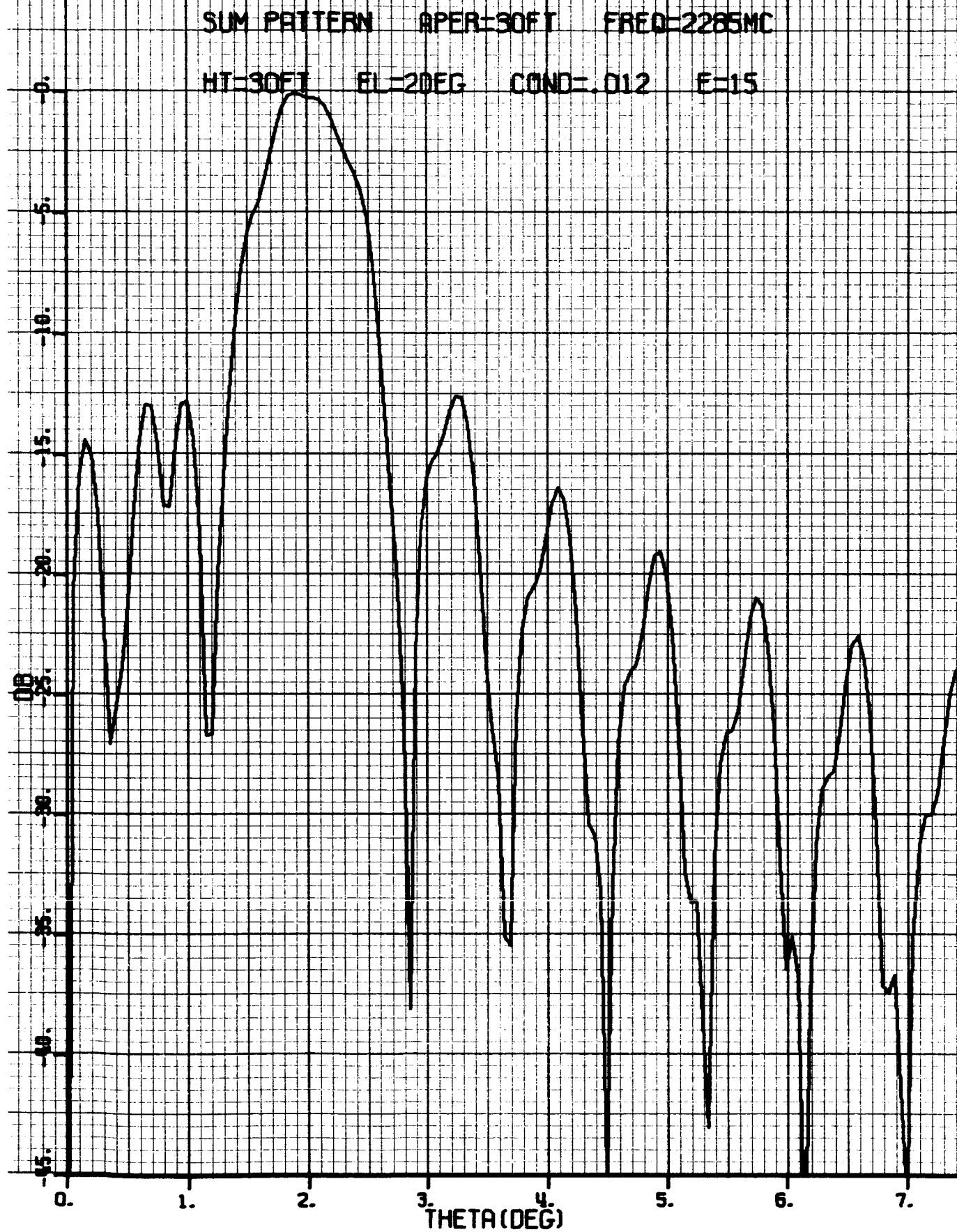


Figure III-9.

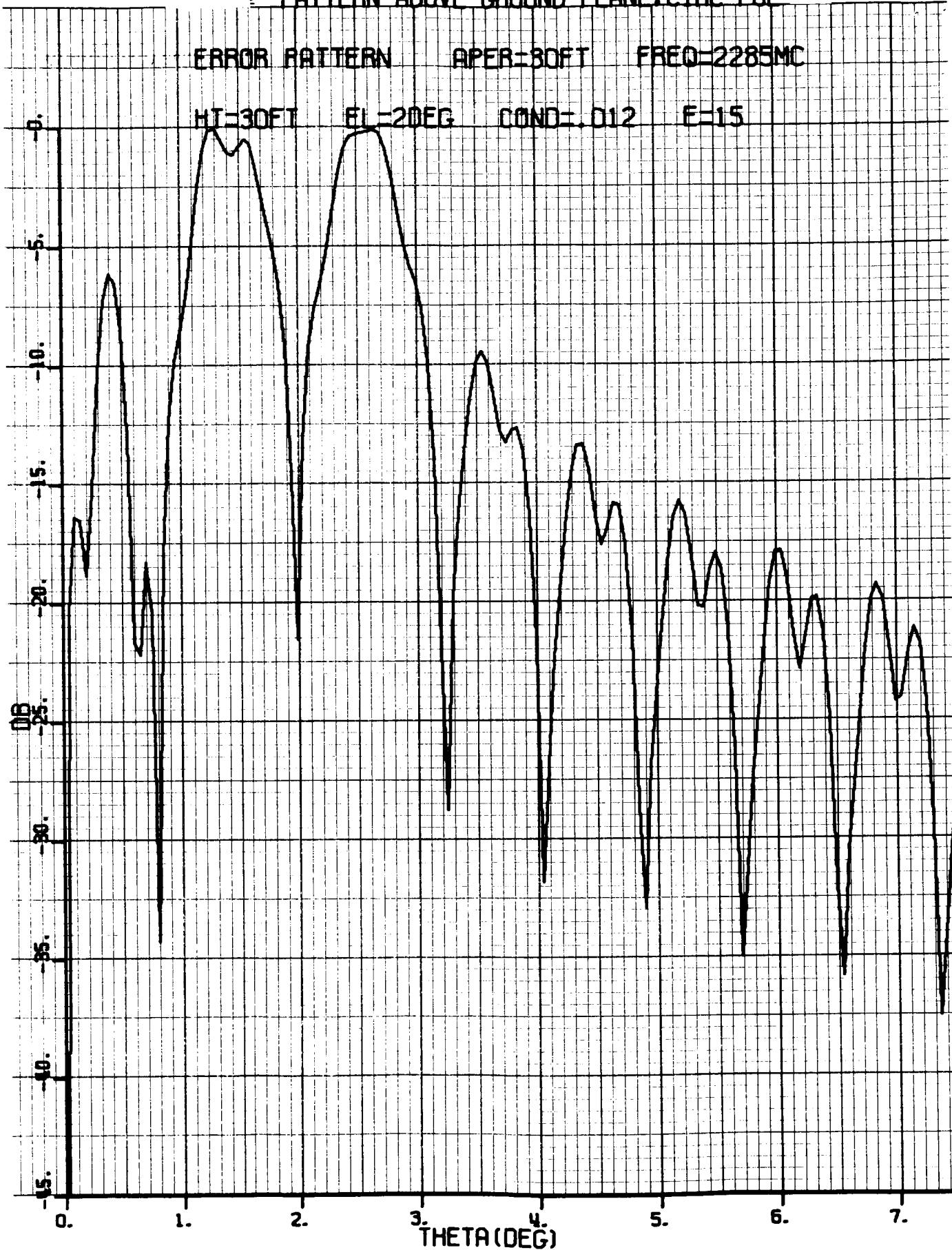


Figure III-10.

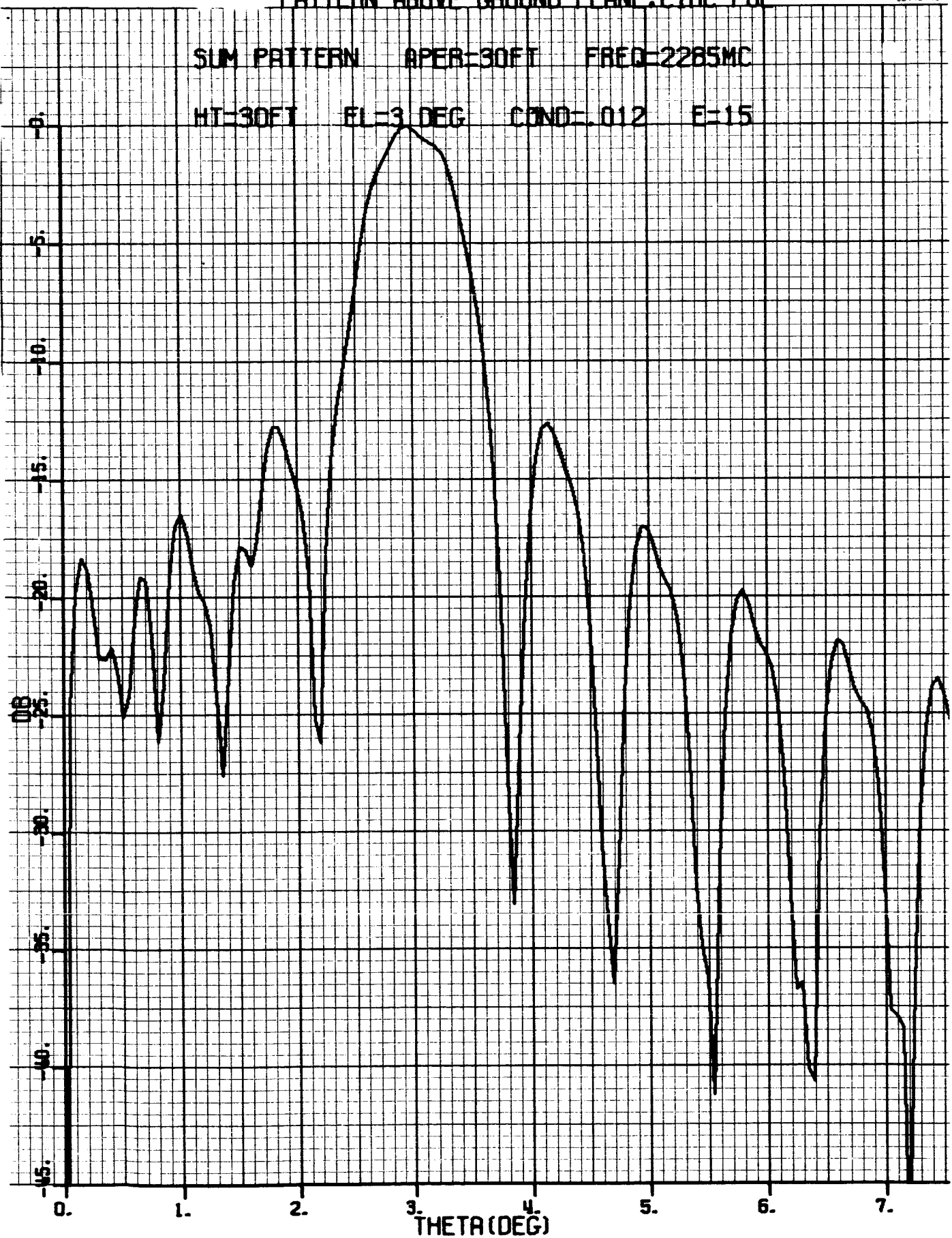


Figure III-11.

# PATTERN ABOVE GROUND PLANE. CIRC POL

62145-50

ERROR PATTERN APER=30FT FREQ=2285MC

HT=30FT EL=3 DEG COND=.012 E=15

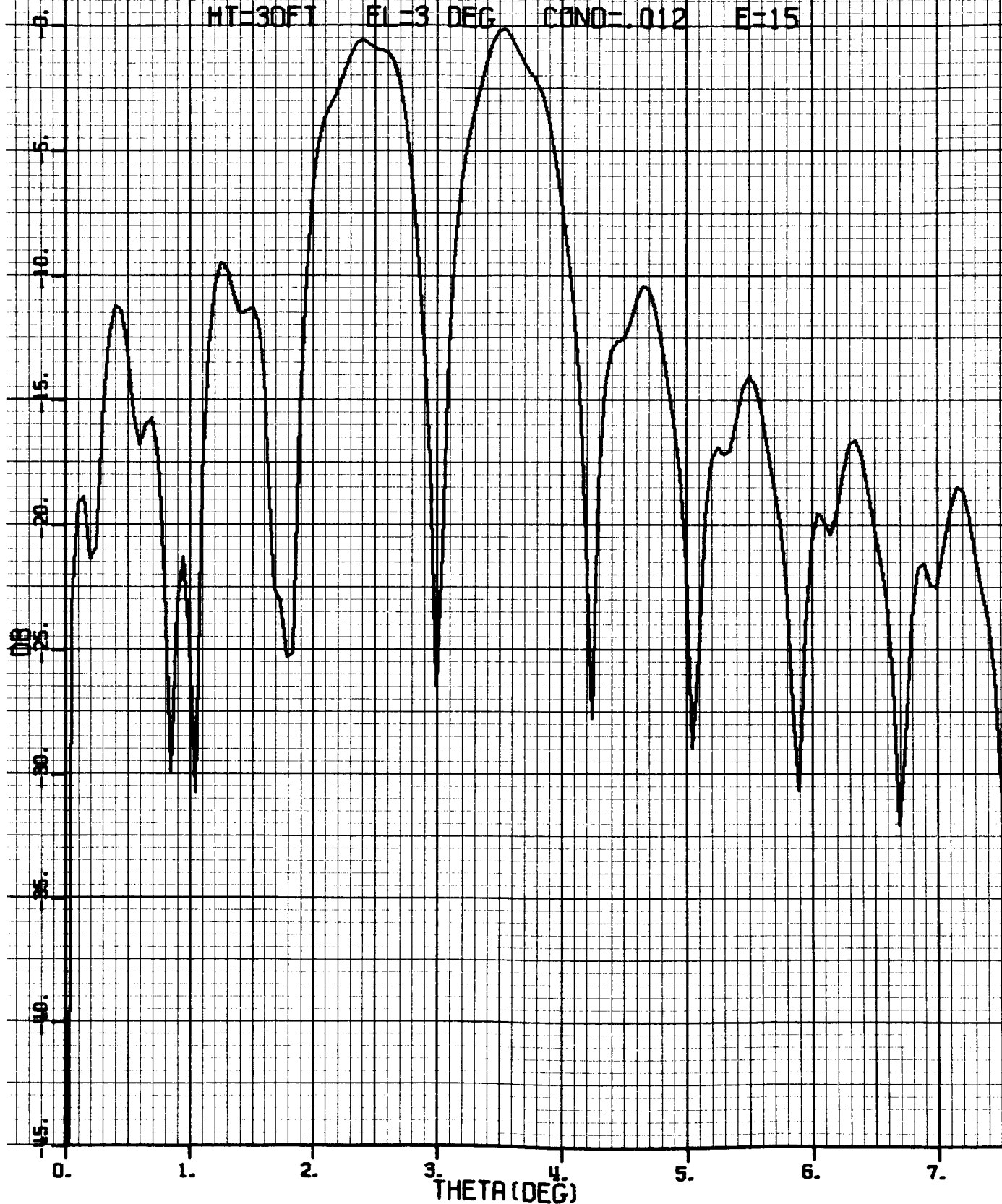


Figure III-12.



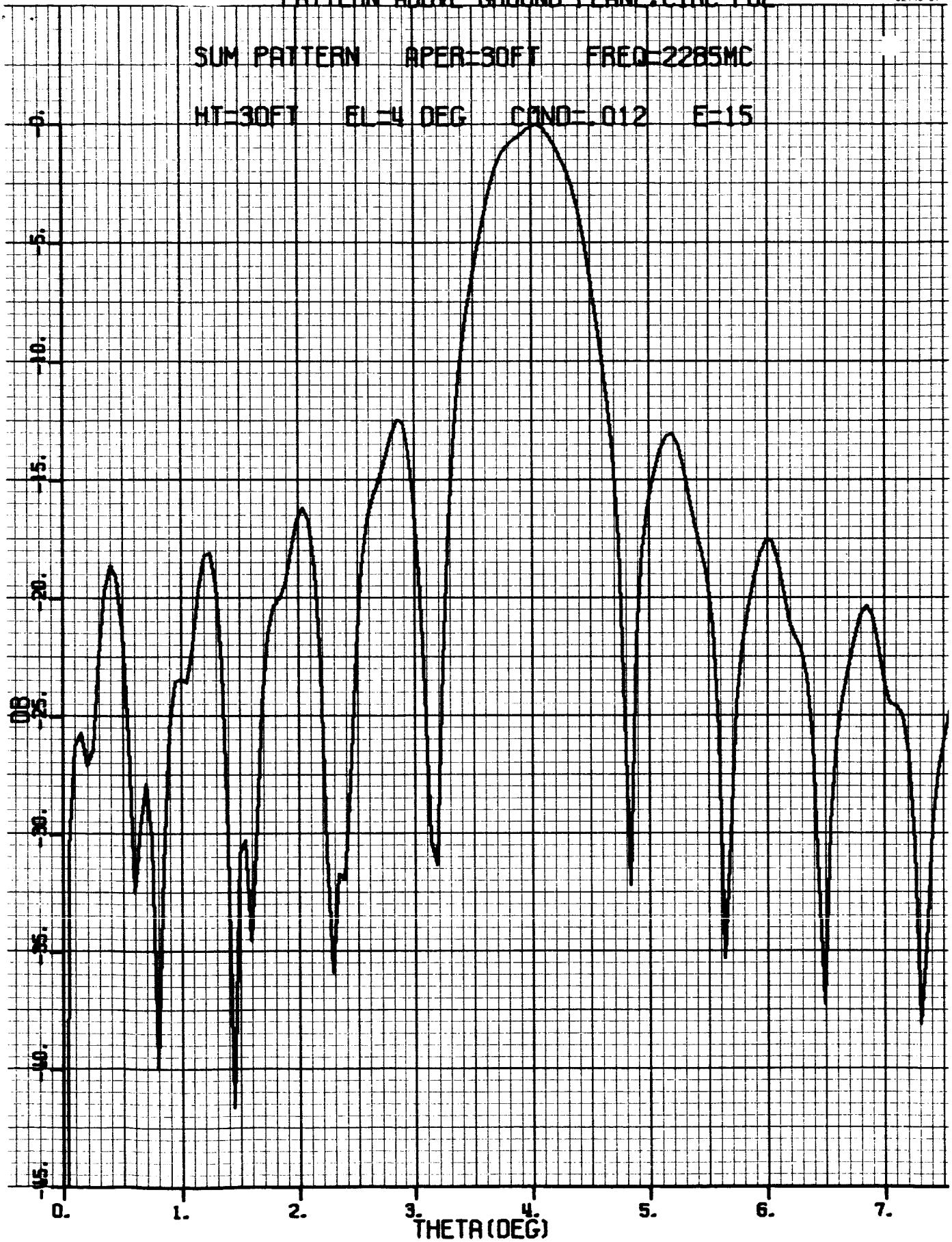


Figure III-13.



# PATTERN ABOVE GROUND PLANE, CIRC POL

62145-52

ERROR PATTERN APER=30FT FREQ=2285MC

HT=30FT EL=4 DEG COND=.012 E=15

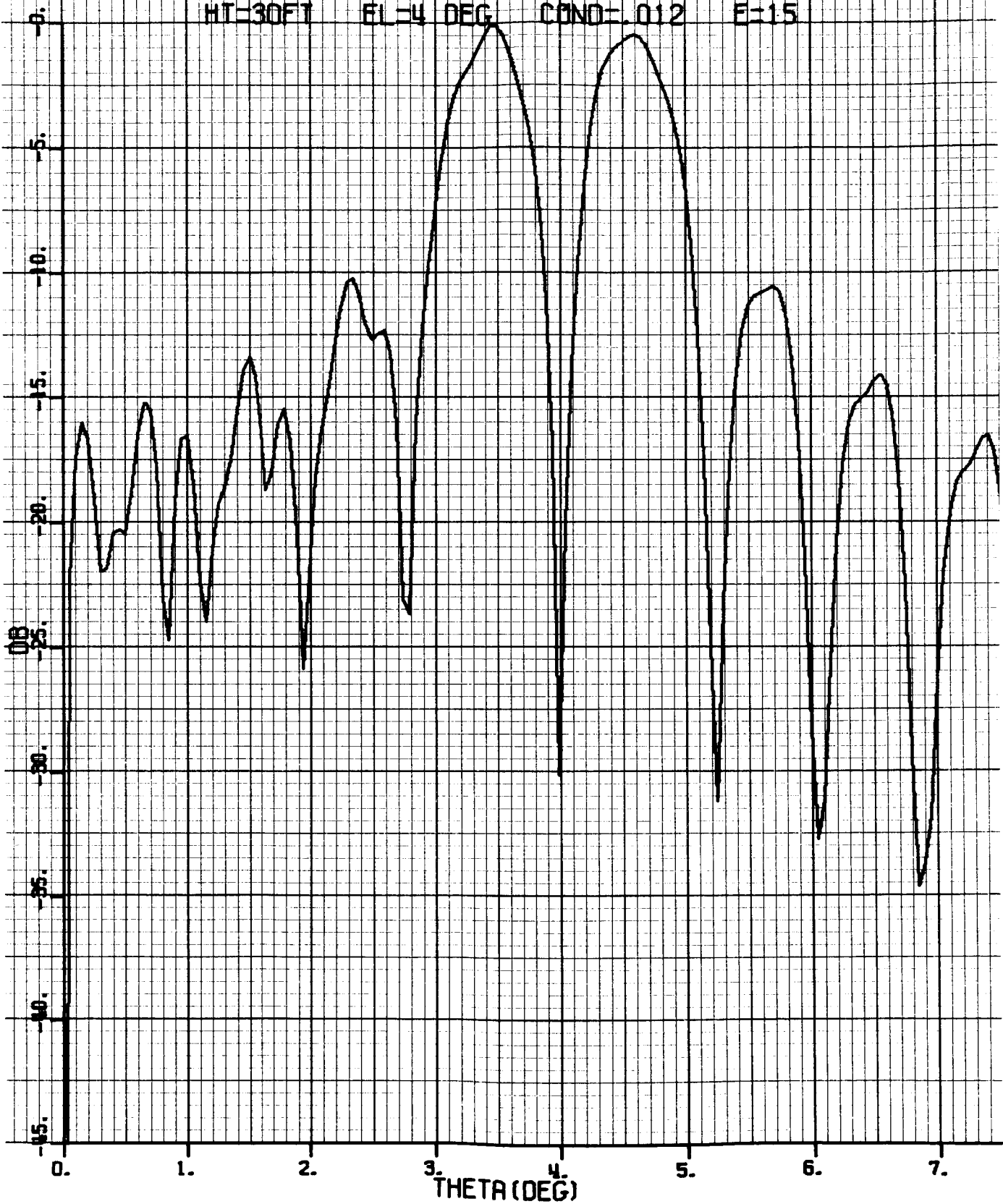


Figure III-14.

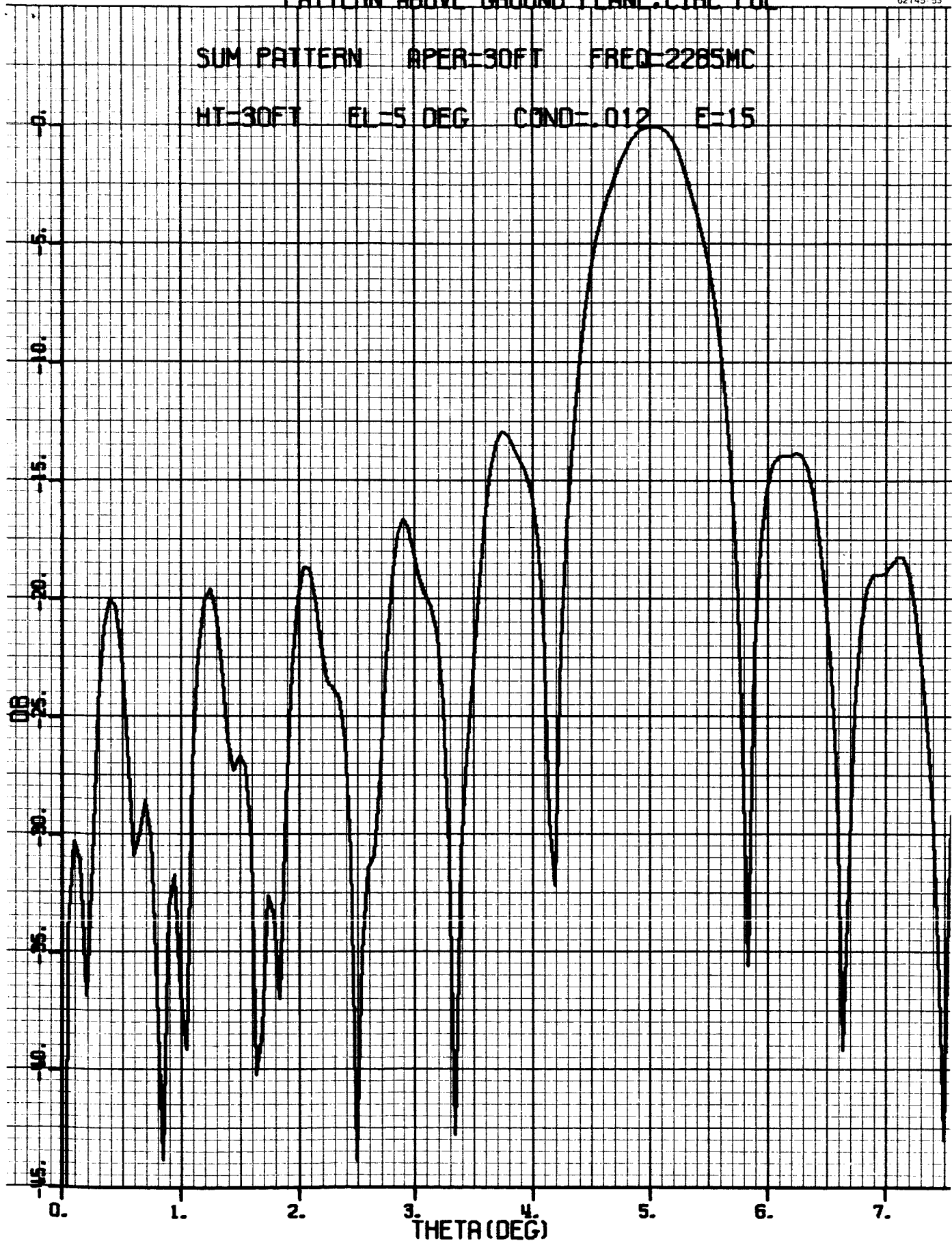


Figure III-15.

# PATTERN ABOVE GROUND PLANE, CIRC POL

62145-54

ERROR PATTERN

APER-30FT

FREQ-2285MC

HT-30FT

EL-5 DEG

COND-.012

E-15

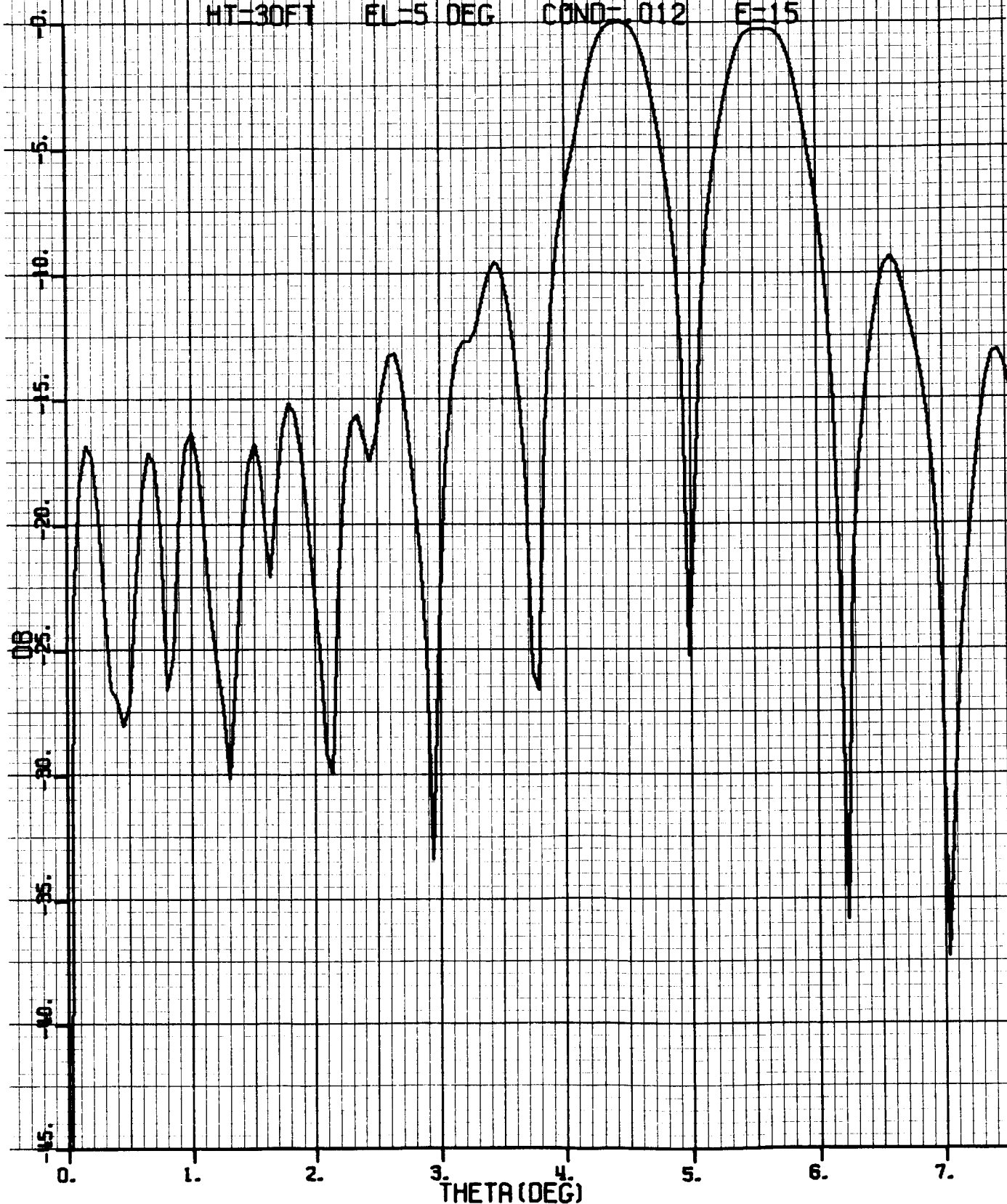


Figure III-16.

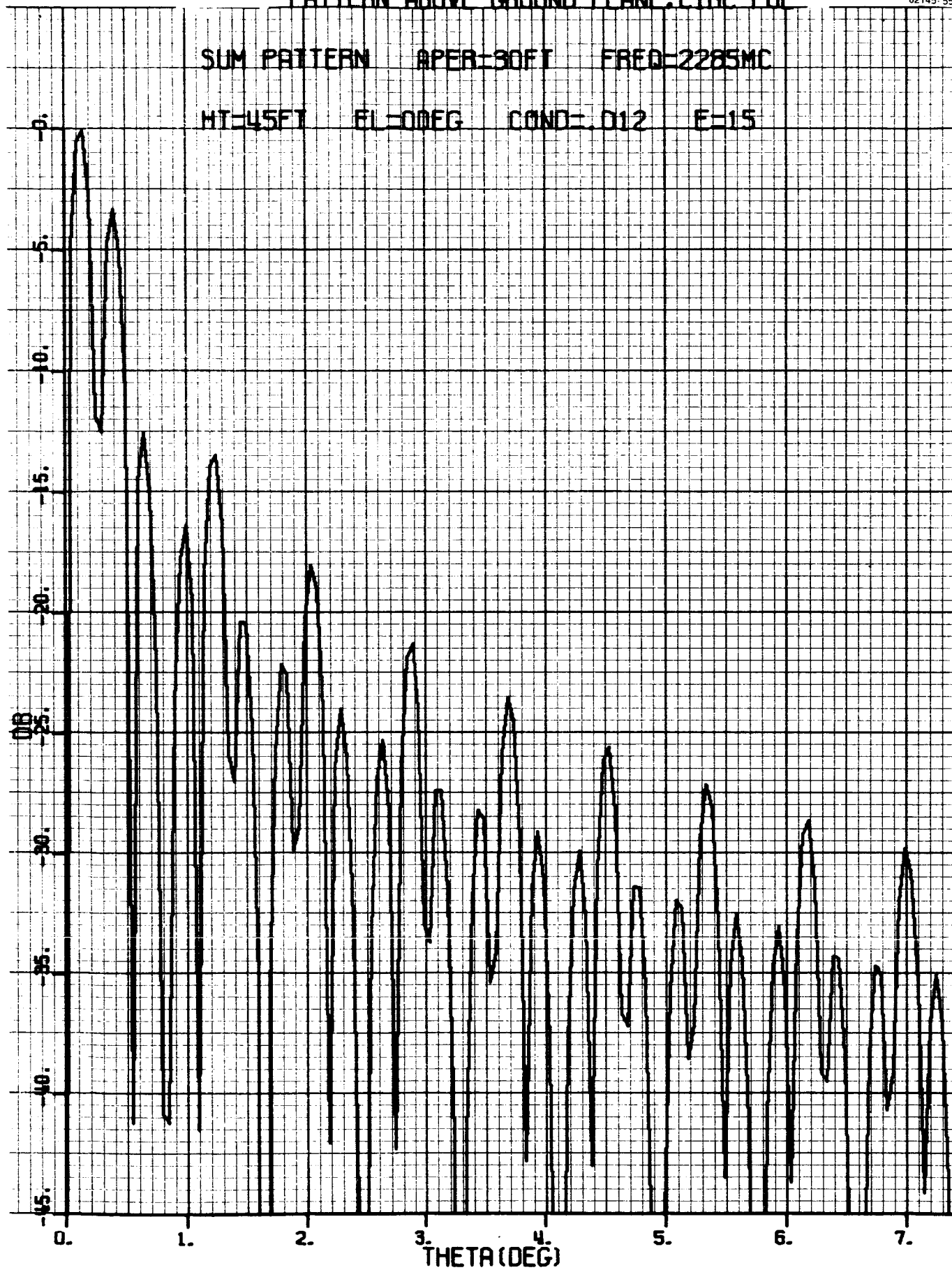


Figure III-17.

ERROR PATTERN APER=30FT FREQ=2285MC

HT=45FT EL=0DEG COND=.012 E=15

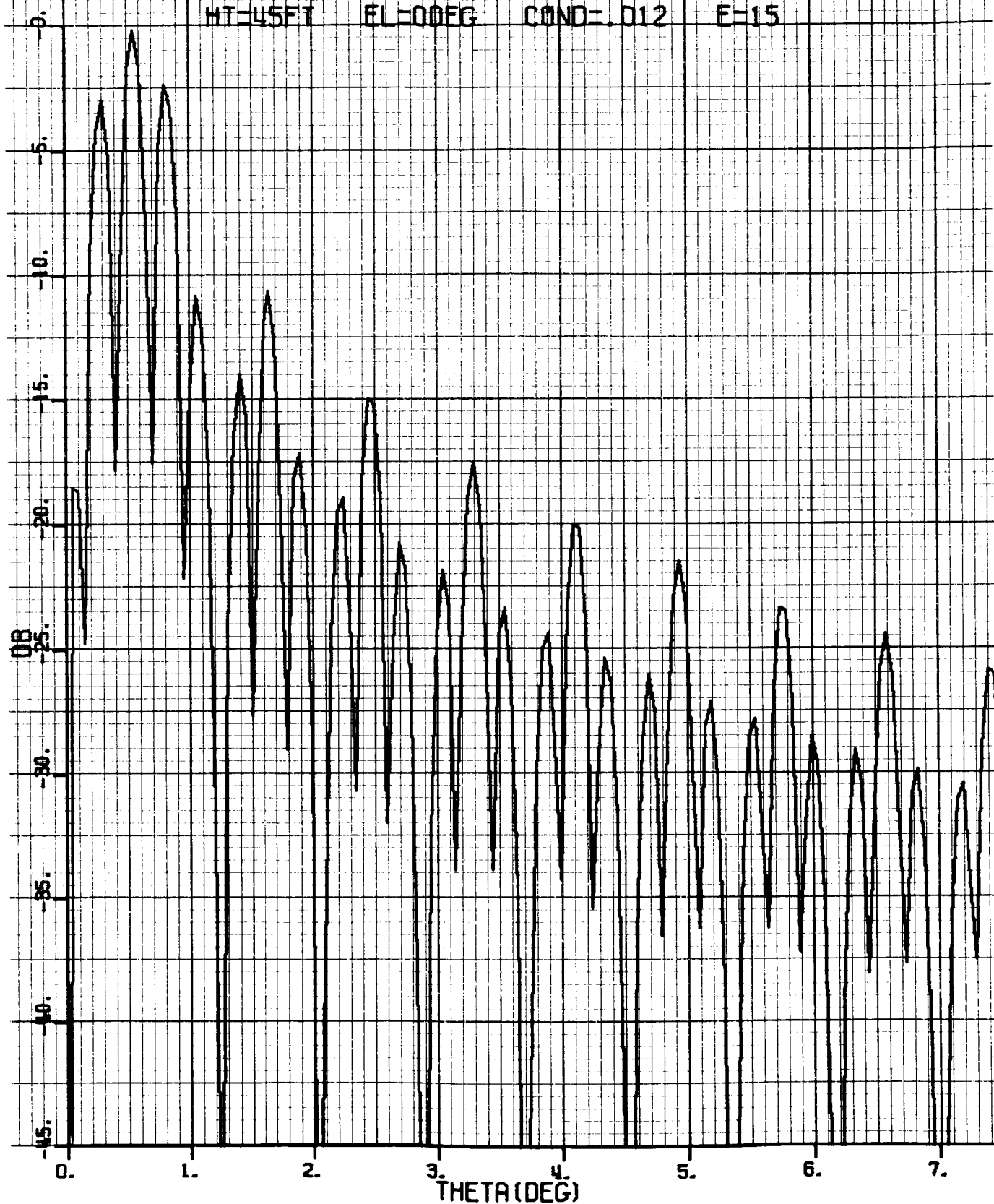


Figure III-18.

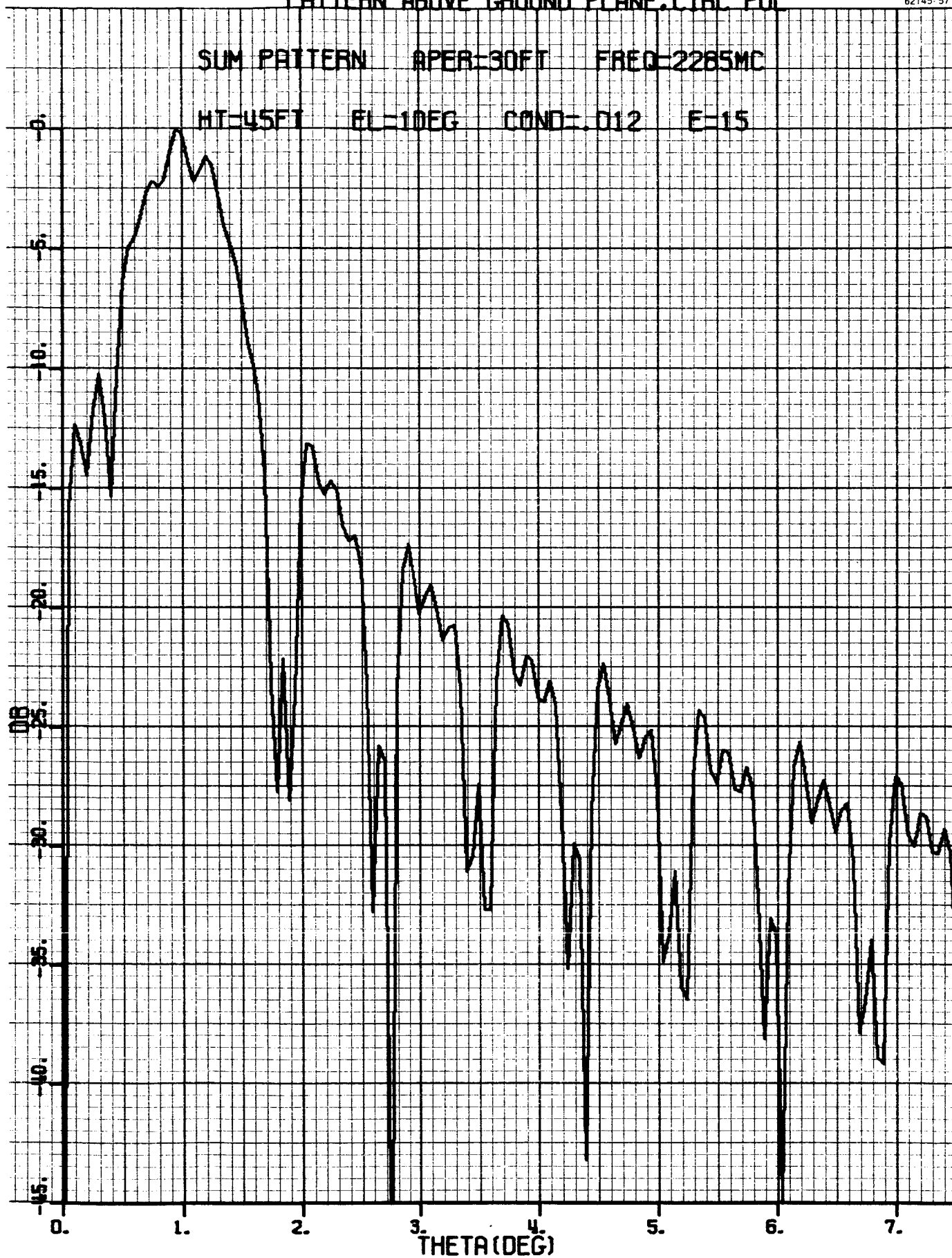


Figure III-19.

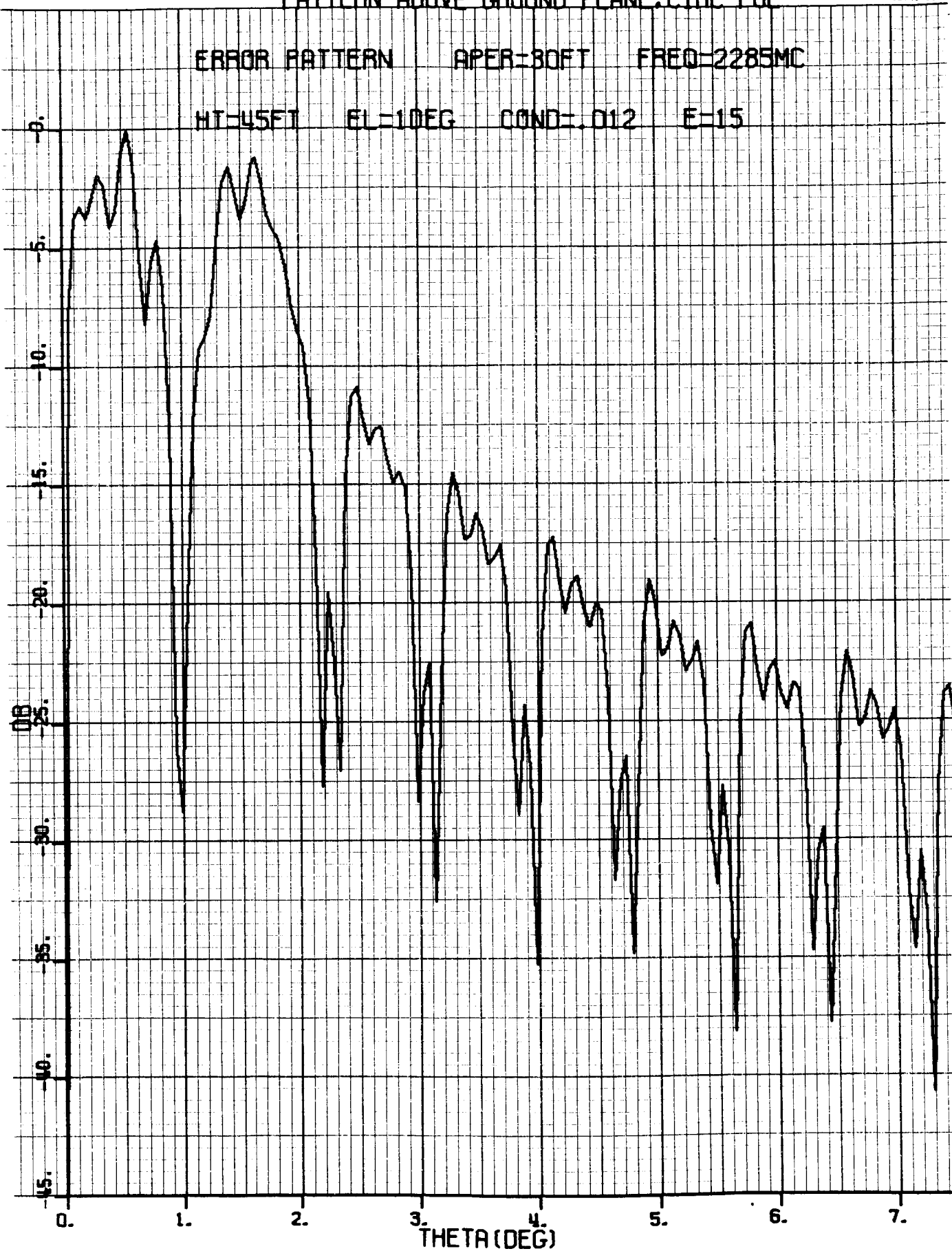


Figure III-20.



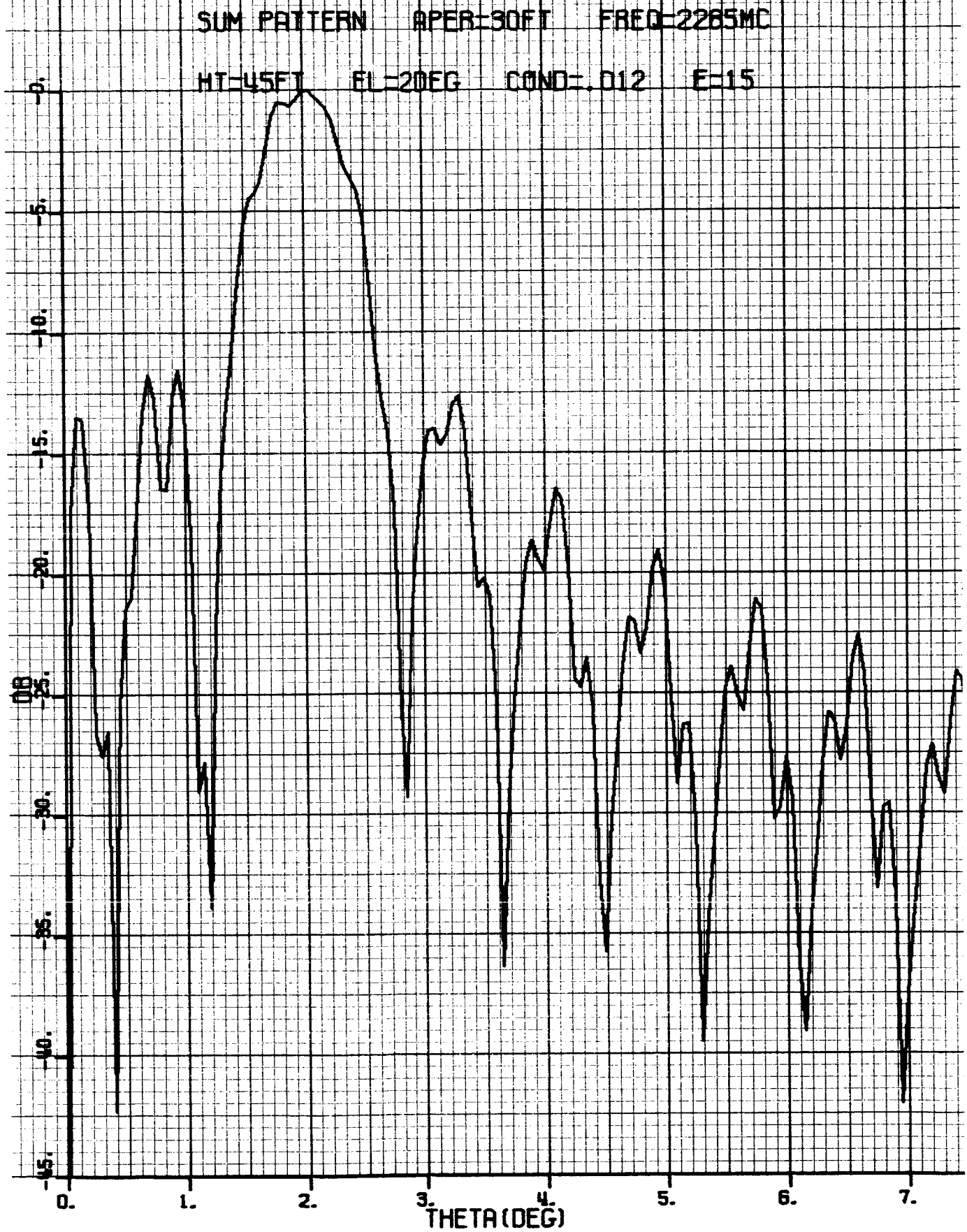


Figure III-21.



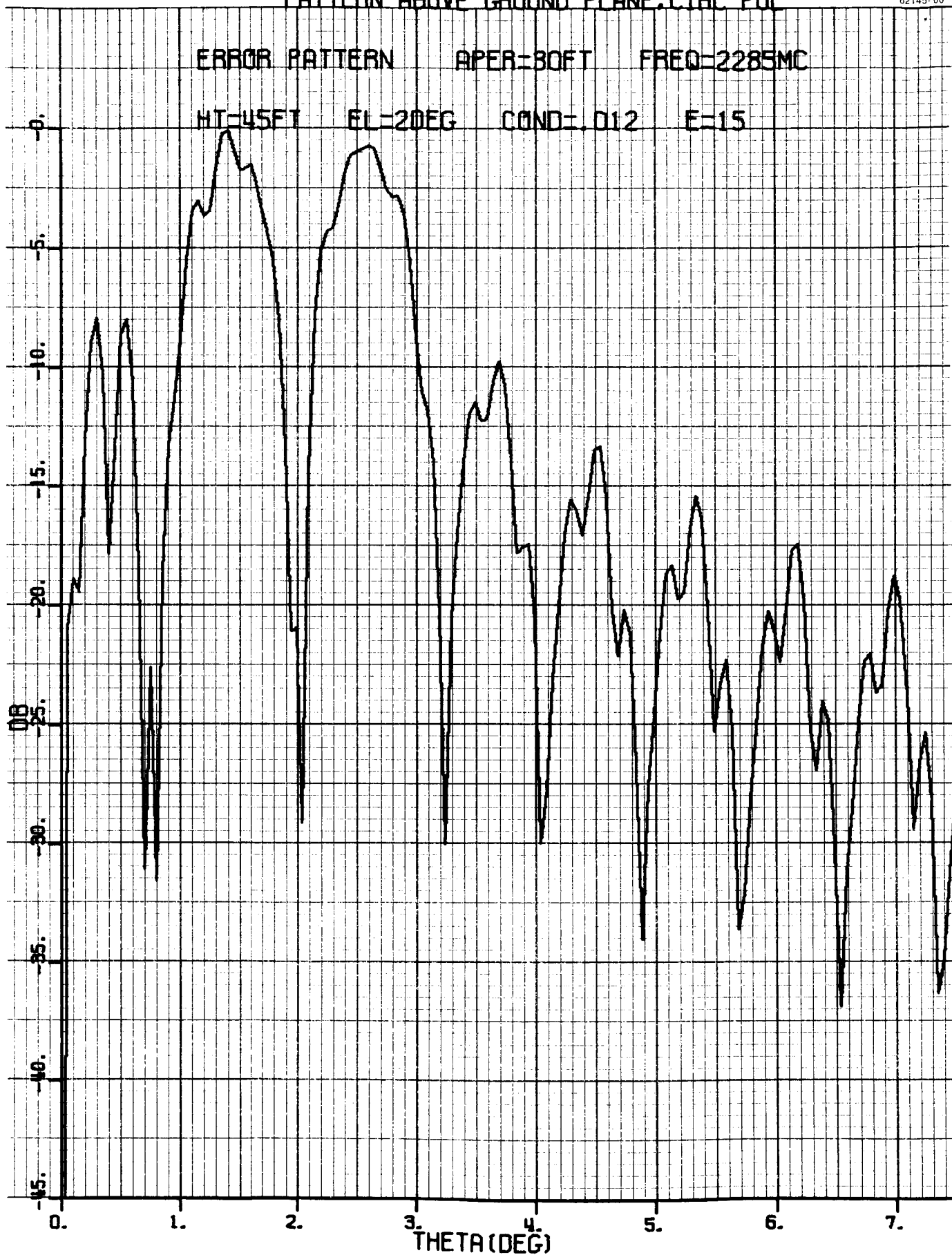


Figure III-22.

## Appendix IV

### PHASE LOCK LOOP ANALYSIS

## Appendix IV

### PHASE LOCK LOOP ANALYSIS

#### 1.0 INTRODUCTION

A typical second order phase locked loop circuit is shown in Figure IV-1. The object of the phase locked loop is to voltage control the VCO so that its output will track coherently the phase of the input signal  $E_s$ . The input signal is represented as  $\sqrt{2} E_s \sin (\omega_s t + \theta_1)$  and is fed into one input arm of the first mixer. The output from the VCO is represented as  $\sqrt{2} E_o \cos (\omega_s t - \omega_1 t + \theta_2)$  and is fed into the other input arm of the first mixer. The output of the first mixer is simply the product of the inputs and is  $K_m E_o E_s \sin (\omega_1 t + \theta_1 - \theta_2)$  where  $\omega_1$  is the angular frequency of the first i.f. and  $K_m$  is a constant associated with the first mixer. Only the low frequency component has been retained since the circuit is designed to respond only to these frequencies. Double mixing system is shown here, since in general the incoming signal contains subcarriers which are coupled off after the first mixer.

The output of the first mixer is fed into a second mixer to generate a second i.f. frequency. Although a reference oscillator is shown here, the reference signal for this second mixer can be derived from the VCO output. The output of the second mixer is  $K'_m E_o E_s \sin (\omega_2 t + \theta_1 - \theta_2)$  where  $K'_m$  is a constant associated with the first and second mixers and  $\omega_2$  is the angular frequency of the second i.f.

The output of the second mixer is fed through a bandpass limiter and onto the phase detector. Again the reference signal for the phase detector can be derived from the output of the VCO. The bandpass limiter contains a suppression factor  $\alpha$  which varies with the magnitude of the input signal level (see Reference 1).

The bandpass limiter provides narrow loop bandwidths at low signal levels and wider bandwidths at high signal levels. The signal suppression factor,  $\alpha$ , is given approximately by,

$$\alpha = \frac{1}{\sqrt{1 + \frac{4}{\pi} \left( \frac{N}{S} \right)}} \quad (1)$$

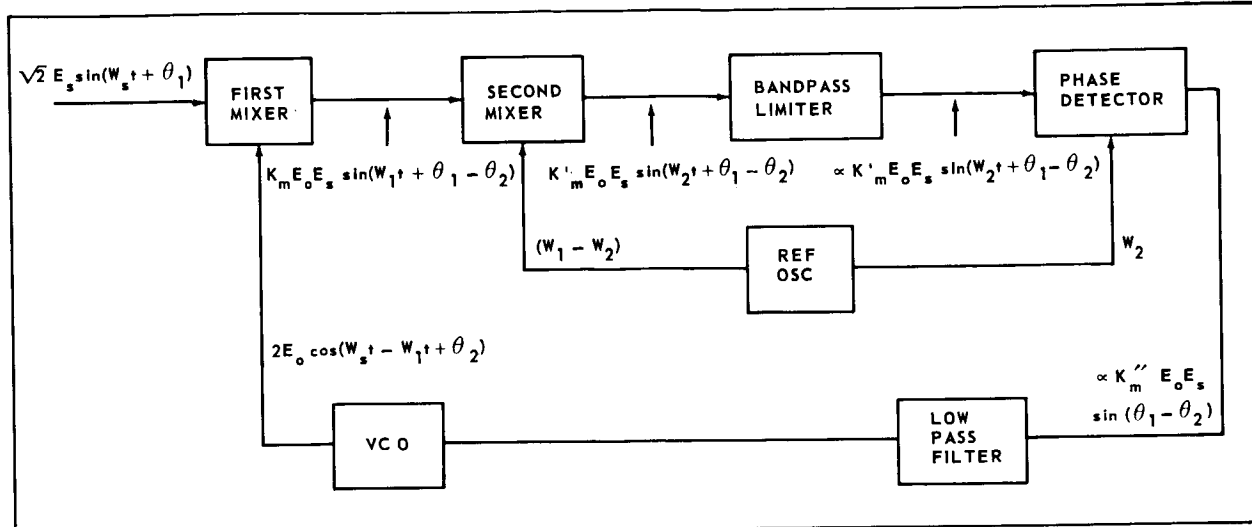


Figure IV-1. Typical Phase-Locked Loop

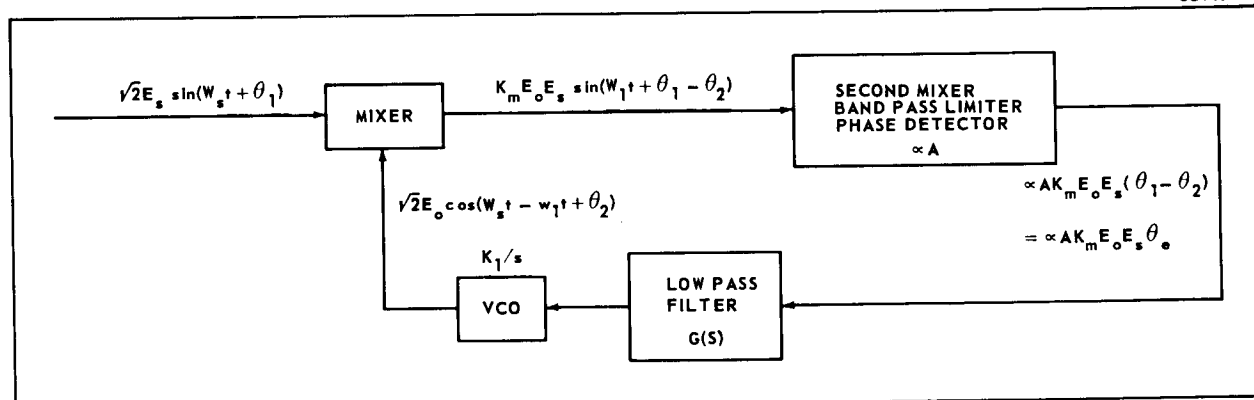


Figure IV-2. The Linearized Phase-Locked Loop

where

$N$  = noise power contained in the pre-detection i.f. bandwidth

$S$  = input signal power level

In the above equation the approximation occurs because the factor  $\frac{4}{\pi}$  varies with  $\frac{S}{N}$ . This factor varies from  $\frac{4}{\pi}$  to  $1/2$  as the  $\frac{S}{N}$  varies from 0 to  $\infty$  (see Reference 2).

The output of the phase detector which modifies the constant  $K'_m$  to  $K''_m$  is transmitted through a low pass filter. The output of the low pass filter is applied to the VCO which is the component to be controlled.

## 2.0 ANALYSIS OF THE CIRCUIT

Figure IV-2 shows a simplification of the circuit shown in Figure IV-1. Several of the components have been combined and  $\sin(\theta_1 - \theta_2)$  has been set equal to  $\theta_1 - \theta_2 = \theta_e$ . The open loop gain  $H(s)$  is,

$$H(s) = \alpha A K_m E_o E_s \frac{K_1}{s} G(s)$$

where  $G(s)$  is the transfer function which determines the order of the loop and for the second order loop it is a low pass filter.  $K_1/s$  is the transfer function of the VCO.

Letting  $K = A K_m E_o E_s K_1$

$$H(s) = \alpha K \frac{G(s)}{s} \quad (2)$$

The low pass filter in most cases is either an active network or a passive network. An active circuit is shown in Figure IV-3 and a passive network is shown in Figure IV-4.

For the active network  $G(s)$  is given by,

$$G(s) = \frac{1 + R_2 Cs}{1 + \mu R_1 Cs}$$

with  $R_1 C$  set equal to 1 and letting  $R_2 C = \tau$ ,

$$G(s) = \frac{1 + \tau s}{\frac{1}{\mu} + s} \quad (3)$$

For the passive network of Figure 4,

$$G(s) = \frac{1 + R_2 Cs}{1 + R_1 Cs}$$

62145-63

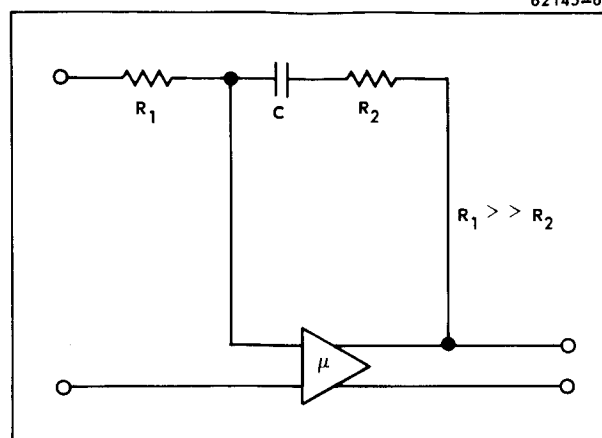


Figure IV-3. Active Low Pass Filter

62145-64

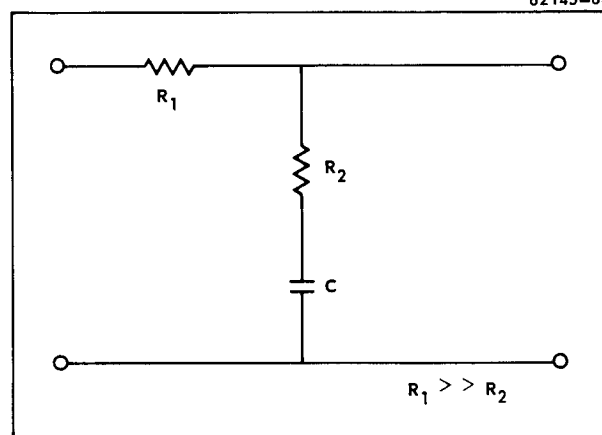


Figure IV-4. Passive Low Pass Filter

Again with  $R_1 C$  set equal to 1 and letting  $R_2 C = \tau$ ,

$$G(s) = \frac{1 + \tau s}{1 + s} \quad (4)$$

Hence, the active network reduces to the passive network when  $\mu = 1$ .

Now, substitute (3) into Equation (2) to obtain

$$H(s) = \alpha K \frac{1 + \tau s}{\left(\frac{1}{\mu} + s\right) s} \quad (5)$$

If  $R_1 C \neq 1$ , then,

$$H(s) = \frac{\alpha K}{R_1 C} \frac{1 + \tau s}{\left(\frac{1}{\mu R_1 C} + s\right) s} \quad (6)$$

Substituting Equation (5) into the transfer error function;

$$\frac{\theta_e(s)}{\theta_1(s)} = \frac{1}{1 + H(s)},$$

one obtains:

$$\frac{\theta_e(s)}{\theta_1(s)} = \frac{s^2 + \frac{s}{\mu}}{s^2 + \left(\tau \alpha K + \frac{1}{\mu}\right) s + \alpha K}$$

For  $\frac{1}{\mu} \ll \tau \alpha K$ ,

$$\frac{\theta_e(s)}{\theta_1(s)} = \frac{s \left(s + \frac{1}{\mu}\right)}{s^2 + (\tau \alpha K) s + \alpha K} \quad (7)$$

Even when  $\mu = 1$  (passive network) and for loop noise bandwidths greater than 50 cps,  $1 \ll \tau \alpha K$ . When the loop noise bandwidths approach 20 cps,  $\tau \alpha K$  is an order of magnitude greater than one. Hence, Equation (7) even at these low bandwidths is a fairly good approximation.

By using Equation (7) one wishes to obtain the time response when  $\theta_1(t)$  is equal to a frequency step and when  $\theta_1(t)$  is equal to a frequency ramp, since these are the principal driving functions for phase-locked loops employed for tracking satellites and space vehicles. Derivations are given in the following two sections for these inputs.

### 3.0 FREQUENCY STEP INPUTS

For  $\theta_1(t) = (\Delta\omega)t$ ,  $\theta_1(s) = \frac{\Delta\omega}{s^2}$

Substituting into Equation (7),

$$\theta_e(s) = \frac{\Delta \omega (s + \frac{1}{\mu})}{s(s^2 + \tau \alpha K s + \alpha K)} \quad (8)$$

Using the inverse transform given on page 342, No. 1.305, of Reference 3, one obtains

$$\frac{\theta_e(t) \sqrt{\alpha K}}{\Delta \omega} = \frac{1}{\mu \sqrt{\alpha K}} + \frac{\left[ \left( \frac{1}{\mu} - \frac{\tau \alpha K}{2} \right)^2 + \beta^2 \right]^{1/2}}{\beta} e^{-\frac{\tau \alpha K}{2} t} \sin(\beta t + \psi) \quad (9)$$

where

$$\beta^2 = \alpha K \left[ 1 - \frac{\tau^2 \alpha K}{4} \right]$$

and

$$\psi = \tan^{-1} \frac{\beta}{\frac{1}{\mu} - \frac{\tau \alpha K}{2}} - \tan^{-1} \frac{\beta}{-\frac{\tau \alpha K}{2}}.$$

Equation (9) applies to the under damped case where  $\tau \sqrt{\alpha K} < 2$ .

For the critically damped case where  $\tau \sqrt{\alpha K} = 2$ :

$$\theta_e(t) \frac{\sqrt{\alpha K}}{\Delta \omega} = \frac{1}{\mu \sqrt{\alpha K}} + e^{-\sqrt{\alpha K} t} \left( \sqrt{\alpha K} t - \frac{1}{\mu \sqrt{\alpha K}} \right) \quad (10)$$

For the overdamped case, where  $\tau \sqrt{\alpha K} > 2$ ,

$$\frac{\theta_e(t) \sqrt{\alpha K}}{\Delta \omega} = \frac{1}{\mu \sqrt{\alpha K}} + \frac{\left[ \left( \frac{1}{\mu} - \frac{\tau \alpha K}{2} \right)^2 - \beta'^2 \right]^{1/2}}{\beta'} e^{-\frac{\tau \alpha K}{2} t} \sinh(\beta' t - \phi) \quad (11)$$

where

$$\beta' = \sqrt{\left( \frac{\tau \alpha K}{2} \right)^2 - \alpha K}$$

and

$$\phi = \tanh^{-1} \frac{-\beta'}{\frac{1}{\mu} - \frac{\tau \alpha K}{2}} - \tanh^{-1} \frac{\beta'}{\frac{\tau \alpha K}{2}}$$



#### 4.0 FREQUENCY RAMP INPUT

For  $\theta_1(t) = \frac{\dot{\omega} t^2}{2}$ ,  $\theta_1(s) = \frac{\dot{\omega}}{s^3}$

Substituting into Equation (7):

$$\theta_e(s) = \frac{\dot{\omega} (s + \frac{1}{\mu})}{s^2 (s^2 + \tau \alpha K s + \alpha K)} \quad (12)$$

Using the inverse transform given on page 347, No. 2.245 of Reference 3, one obtains,

$$\frac{\theta_e(t) \alpha K}{\dot{\omega}} = \frac{t}{\mu} + 1 - \frac{\sqrt{\alpha K}}{y} e^{-xt} \sin(yt + \psi) \quad (13)$$

where

$$x = \frac{\tau \alpha K}{2}$$

$$y = 1/2 \sqrt{4 \alpha K - (\tau \alpha K)^2}$$

$$\psi = \tan^{-1} \frac{y}{x}$$

Equation (13) applies to the underdamped condition where  $\tau \sqrt{\alpha K} < 2$ .

For the critically damped case, where  $\tau \sqrt{\alpha K} = 2$ ,

$$\frac{\theta_e(t) \alpha K}{\dot{\omega}} = \frac{t}{\mu} + 1 - e^{-\sqrt{\alpha K} t} (t \sqrt{\alpha K} + 1) \quad (14)$$

For the overdamped case when  $\tau \sqrt{\alpha K} > 2$

$$\frac{\theta_e(t) \alpha K}{\dot{\omega}} = \frac{t}{\mu} + 1 - e^{-xt} \left( \frac{x}{y} \sinh yt + \cosh yt \right) \quad (15)$$

where

$$x = \frac{\tau \alpha K}{2}$$

$$y = 1/2 \sqrt{(\tau \alpha K)^2 - 4 \alpha K}$$

#### 5.0 RESULTS OF COMPUTATION FOR FREQUENCY STEP INPUT

Equations (9), (10), and (11) were programmed for the IBM 7094 computer and the results are shown in Graphs IV-1 through IV-11. A brief description of what is plotted on the graphs will first be given.

All the graphs for the frequency step input shows

$$\frac{\theta_e \sqrt{\alpha K}}{\Delta \omega}$$

as a function of  $\sqrt{\alpha K} t$  for either varying  $\tau \sqrt{\alpha K}$  with  $\mu$  and  $\sqrt{\alpha K}$  fixed or varying  $\sqrt{\alpha K}$  with  $\mu$  and  $\tau \sqrt{\alpha K}$  fixed. The quantity  $\tau \sqrt{\alpha K}$  is equal to twice the damping ratio assigned conventionally to circuits employing feedback controls. The quantity  $\sqrt{\alpha K}$  is equal to the undamped natural frequency of the system. Whenever  $\mu = \infty$ , it is not necessary to assign values to  $\sqrt{\alpha K}$  to obtain the curves, since it is obvious from Equations (9), (10), and (11) that values of

$$\frac{\theta_e \sqrt{\alpha K}}{\Delta \omega}$$

can be calculated without numerical values assigned to  $\sqrt{\alpha K}$ . The value for  $\tau \sqrt{\alpha K}$  depends on the loop bandwidth and the input signal strength. Hence, knowing these values,  $\tau \sqrt{\alpha K}$  can be determined and the transient responses can be observed by referring to the corresponding graph. The case when  $\mu$  is very large ( $\mu = \infty$  or  $10^6$ ), the static phase error is zero and only the transient error is of interest.

Graph IV-1 shows the transient responses for various values of  $\tau \sqrt{\alpha K}$  with  $\mu = \infty$ . The error is zero at  $t = 0$  and approaches zero as  $t$  approaches  $\infty$ . The critically damped curve is obtained when  $\tau \sqrt{\alpha K} = 2$ . Below this value, the peak transient error gets larger and above this value the peak transient value is lower but the settling time is longer.

The next set of curves, Graphs IV-2 to IV-11 are responses for frequency step input when the value of  $\mu$  is finite. For these curves, numerical values must be assigned to  $\sqrt{\alpha K}$ . The values assigned (50 to 1000) are for the conditions where the threshold loop noise bandwidth varies between 50 and 700 cps. To further clarify the curves, a more detailed explanation will be given by referring to Graph IV-2 and IV-3. Figure IV-2 gives the response for  $\tau \sqrt{\alpha K} = 2.0$  and  $\mu = 1.0$  (passive filter). Only two curves are given, since the curves for other values of  $\sqrt{\alpha K}$ , between 50 and 1000, lie within the curves shown. The curve for  $\sqrt{\alpha K} = 50$  as  $t$  approaches  $\infty$ , approaches

$$\frac{1}{\mu \sqrt{\alpha K}} = .02.$$

The curve for  $\sqrt{\alpha K} = 1000$  as  $t$  approaches  $\infty$ , approaches 0.001. Graph IV-3 shows the response for  $\tau \sqrt{\alpha K} = 2.0$  with  $\mu = 10^6$  (active filter). Only one curve is shown since for values of  $\sqrt{\alpha K} = 50$  to 1000 the transient response is very nearly the same. As  $t$  approaches  $\infty$ , the curves approach  $1/(\mu \sqrt{\alpha K})$ .

## 6.0 RESULTS OF COMPUTATION FOR FREQUENCY RAMP INPUT

Equations (13), (14), and (15) were programmed for the IBM 7094 Computer and the results are shown in Graphs IV-12 through IV-26. Before getting into a detailed discussion of the various graphs, a brief explanation of what is plotted on the figures will be given.

As in the case for the frequency step input, all graphs are plotted for the error function,  $\theta_e \alpha K / \dot{\omega}$ , as a function of  $\sqrt{\alpha K} t$ . Again when  $\mu = \infty$ , it is not necessary to assign values to  $\sqrt{\alpha K}$  to obtain the curves presented. Unlike the response for the frequency step input, after the initial transient there exists either a fixed error ( $\mu = \infty$ ) or a linearly increasing error function of  $t/\mu$  (See Graph IV-14).

Graphs IV-12 and IV-13 show the response for  $\mu = \infty$  for  $\tau \sqrt{\alpha K}$  varied from 1.0 to 4.8. The critically damped curve is obtained when  $\tau \sqrt{\alpha K} = 2.0$ . All the curves approach  $\theta_e \alpha K / \dot{\omega} = 1.0$  for  $t$  approaching  $\infty$ .

Graphs IV-14 to IV-26 give the responses for finite values of  $\mu$ . An explanation of the curve will be given by referring to Graph IV-14 and IV-15. Similar discussions apply to the remaining curves. Graph IV-14 shows the response for  $\tau \sqrt{\alpha K} = 1.0$  and  $\mu = 1.0$  with  $\sqrt{\alpha K}$  varied from 50 to 1000. After the initial transient peak, all the curves increase linearly with  $\sqrt{\alpha K} t$ . The rate of increase is  $1/(\mu \sqrt{\alpha K})$ . Graph IV-15 represents the response for  $\tau \sqrt{\alpha K} = 1.0$  and  $\mu = 10^6$  with  $\sqrt{\alpha K}$  varied from 50 to 1000. There is only one curve shown since for these values of  $\sqrt{\alpha K}$ , the response is essentially the same.

As an example of the use of the graphs, suppose one wishes to find the time and the amount of overshoot and when the steady state value equals the overshoot value for  $\tau \sqrt{\alpha K} = 1.0$ ,  $\mu = 1.0$ , and  $\sqrt{\alpha K} = 100$ . From Graph IV-14 the overshoot value is 1.2 at  $\sqrt{\alpha K} t = 3.7$  ( $t = 3.7/100 = 0.037$  sec). For this value of the error function  $\theta_e = \dot{\omega} \times 1.2 \times 10^{-4}$ . From the same Graph, the error function again equals 1.2 at  $\sqrt{\alpha K} t = 20$  ( $t = 0.2$  sec).

## 7.0 USEFUL FORMULAS APPLICABLE TO PHASE LOCKED LOOPS

### Loops

The loop bandwidth is given in Reference 1 as:

$$B_L = \frac{\alpha K \tau}{4} + \frac{1}{4 \tau} \quad (16)$$

Let  $\alpha_o$  be the threshold value of  $\alpha$  when the noise power contained in the threshold loop noise bandwidth is substituted for S in Equation (1). Replacing  $\alpha$  by  $\alpha_o$ , Equation (16), becomes:

$$B_{Lo} = \frac{\alpha_o K \tau}{4} + \frac{1}{4\tau} \quad (17)$$

where  $B_{Lo}$  is defined as the threshold loop bandwidth.

At threshold,  $\tau \sqrt{\alpha_o K} = \sqrt{2}$ . When this equality is substituted into (17), the following expression can be derived:

$$K = \frac{32}{9} \frac{B_{Lo}^2}{\alpha_o} \quad (18)$$

The units are:  $B_{Lo}$  in (cps)<sup>2</sup> and K in (sec)<sup>-2</sup>. When

$$\tau = \sqrt{\frac{2}{\alpha_o K}}$$

is substituted into Equation (16), the following expression can be derived:

$$B_L = B_{Lo} \left( \frac{2}{3} \frac{\alpha}{\alpha_o} + \frac{1}{3} \right) \quad (19)$$

When Equation (18) is substituted into

$$\tau = \sqrt{\frac{2}{\alpha_o K}}$$

one obtains,

$$\tau = \frac{3}{4 B_{Lo}} \quad (20)$$

When  $B_{Lo}$  is in cps,  $\tau$  is in seconds.

The static phase error for frequency ramp input is given by:

$$\theta_e = \frac{\dot{\omega}}{\alpha K} \text{ radians}$$

when  $\dot{\omega}$  is in radians/sec<sup>2</sup> and  $\alpha K$  is in (sec)<sup>-2</sup>.

The static phase error for frequency step input is given by

$$\theta_e = \frac{\Delta\omega}{\mu \alpha K} \text{ radians.}$$

and the phase jitter is given by:

$$\sigma_e = \sqrt{\frac{2 k T B_L}{S}} \text{ radians} \quad (22)$$

where

$k$  = Boltzmann's constant,  $1.38 \times 10^{-23} \frac{\text{watts} \cdot \text{sec}}{\text{K}^\circ}$

$T$  = Equivalent excess noise temperature of the antenna plus receiver, in degrees K.

$S$  = Signal power into receiver.

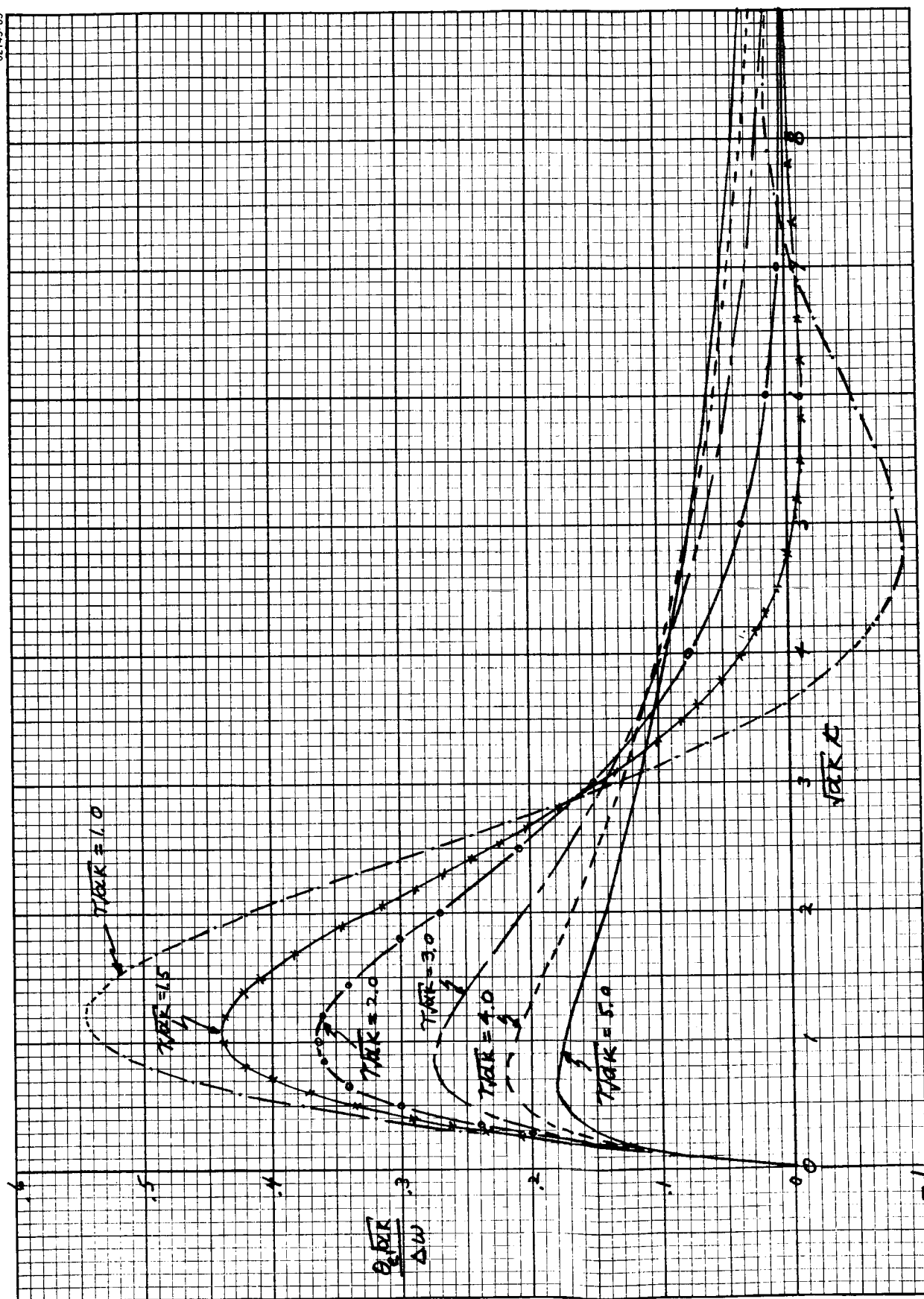
#### References

1. Nelson, W. L., "Phase Lock Loop Design for Coherent Angle-Error Detection in the Telstar Satellite Tracking System", The Bell System Technical Journal, Volume XLII, Sept. 1963, No. 5, pp. 1941 - 1975.
2. Davenport, W. B., "Signal-to-Noise Ratios in Band-Pass Limiters", Journal of Applied Physics, Volume 24, No. 6, June 1953, pp. 720-727.
3. Gardner, M. F., and Barnes, J. L., Transients in Linear Systems, John Wiley and Sons, New York, 1945.

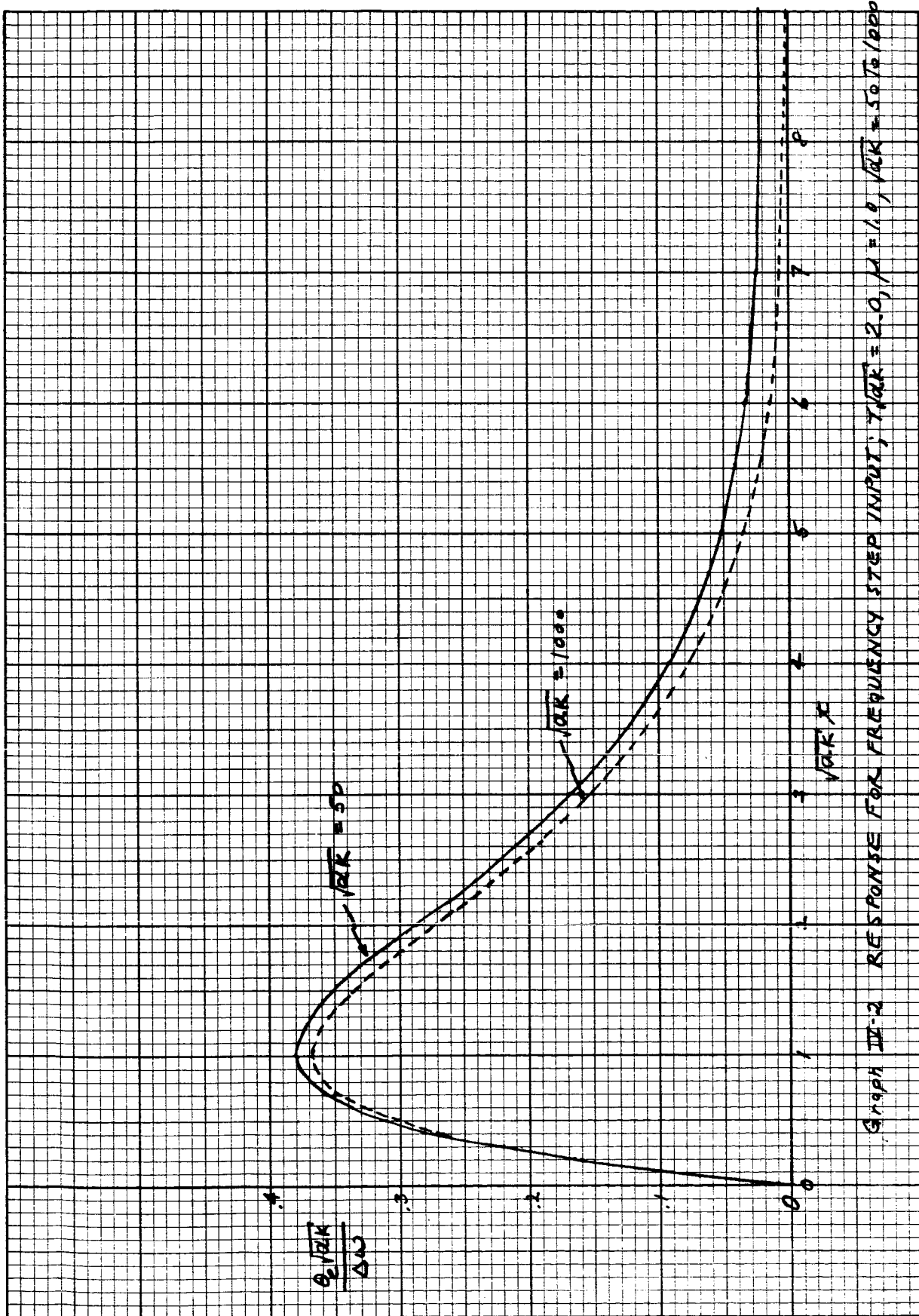
**Appendix IV**

**RESPONSE FOR A FREQUENCY STEP INPUT**

62145-65

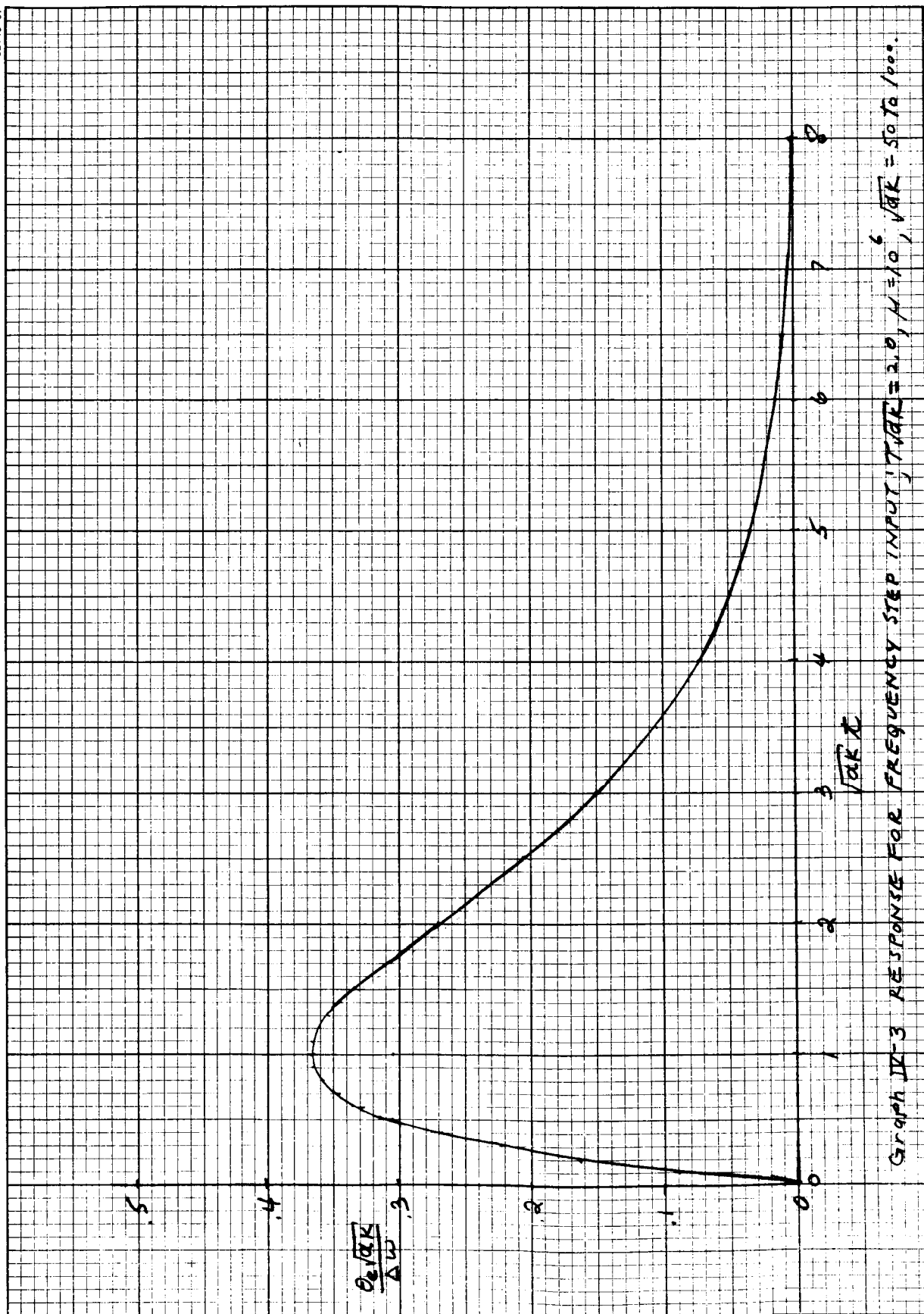


Graph II-1 RESPONSE FOR FREQUENCY STEP INPUT;  $\gamma_k/k = 1.0$  TO  $5.0$  WITH  $M = \infty$ .

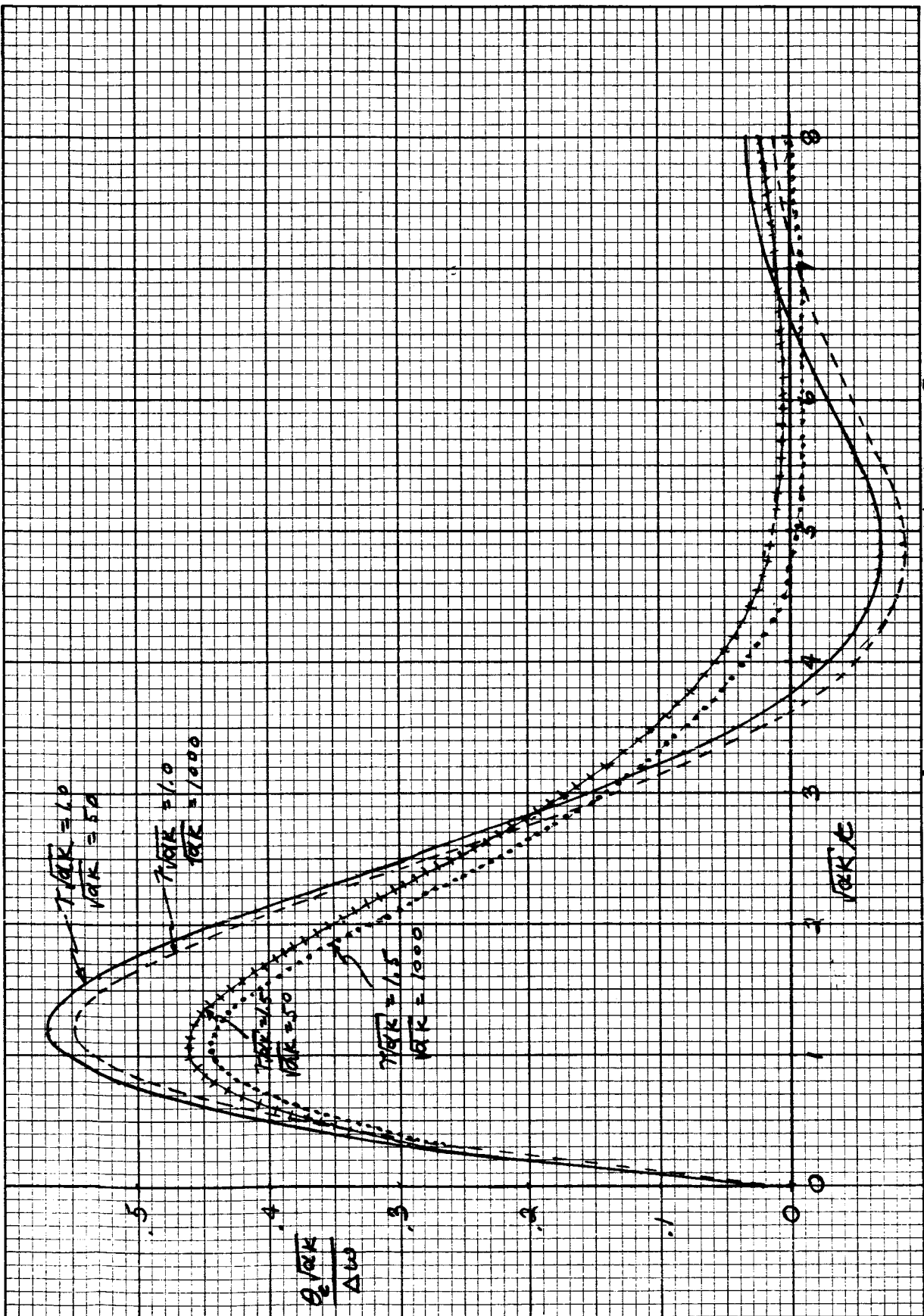




62145-67

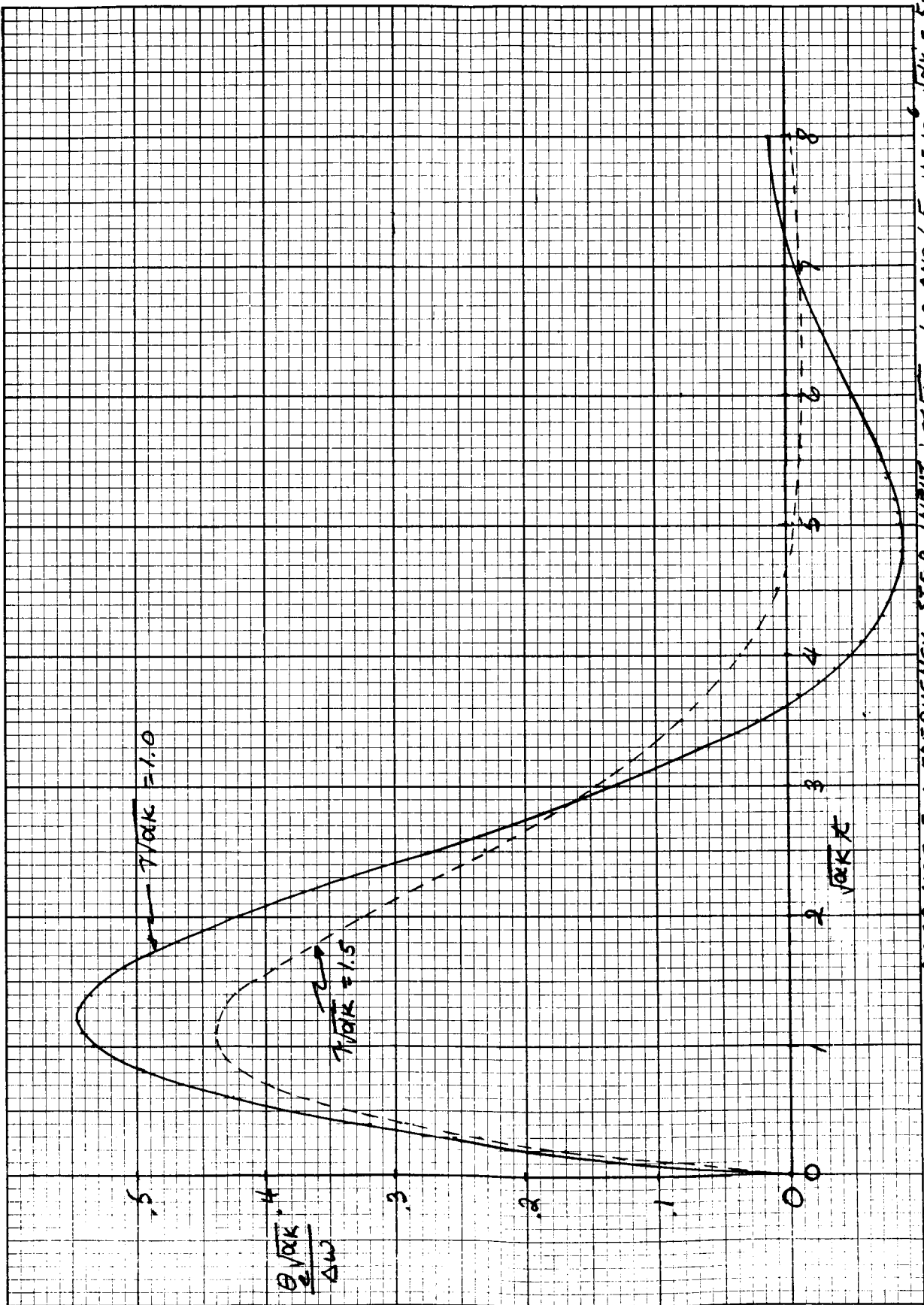


Graph IV-3 RESPONSE FOR FREQUENCY STEP INPUT,  $\eta = 10^6$ ,  $\sqrt{K} = 50 \text{ Ta} / 100^\circ$ .

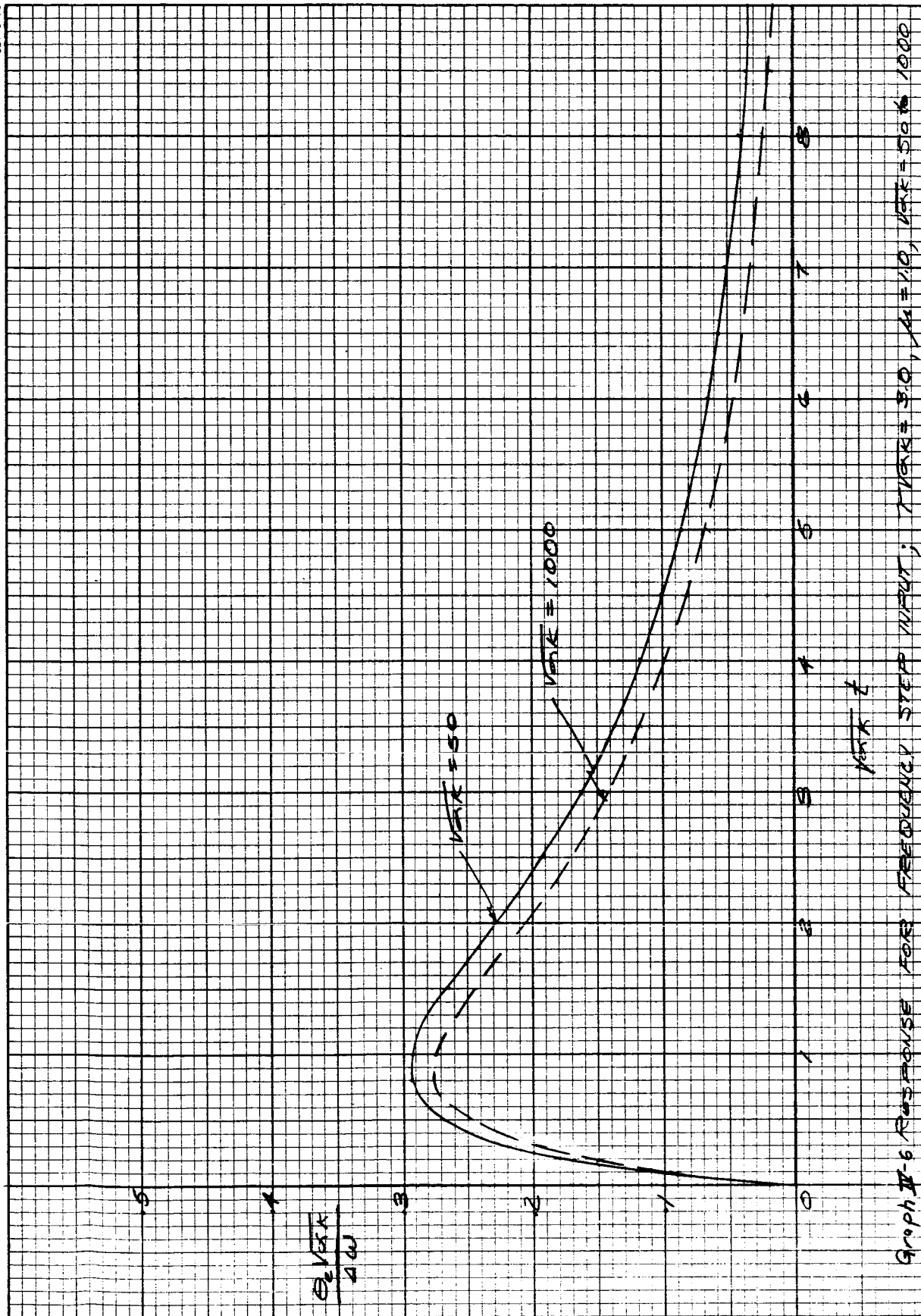


Graph II-4 RESPONSE FOR FREQUENCY STEP INPUT;  $\gamma \sqrt{K} = 1.0$  AND  $1.5$ ;  $\mu = 1.0$ ,  $\sqrt{K} = 50$  TO  $1000$ .

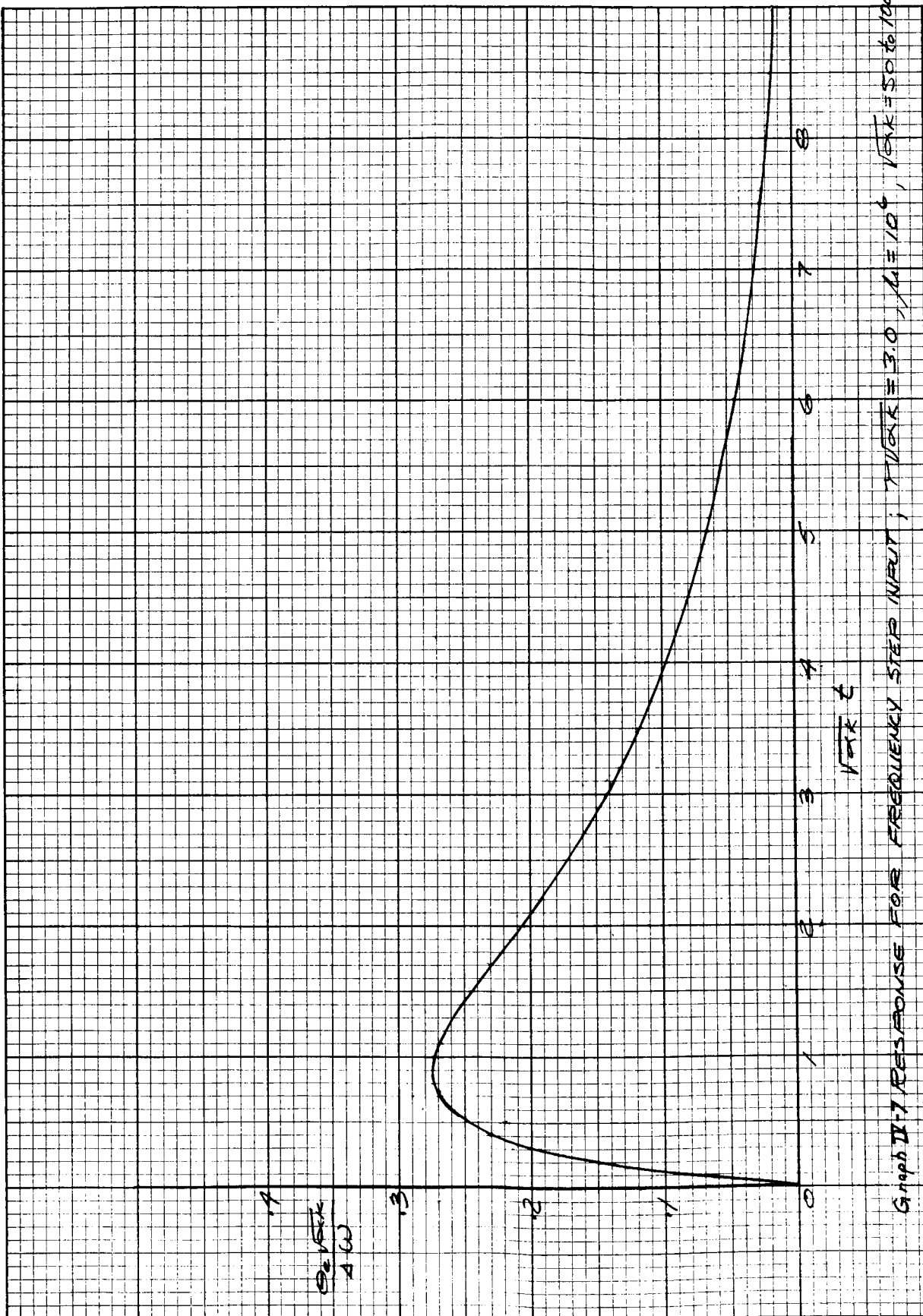
62145-69



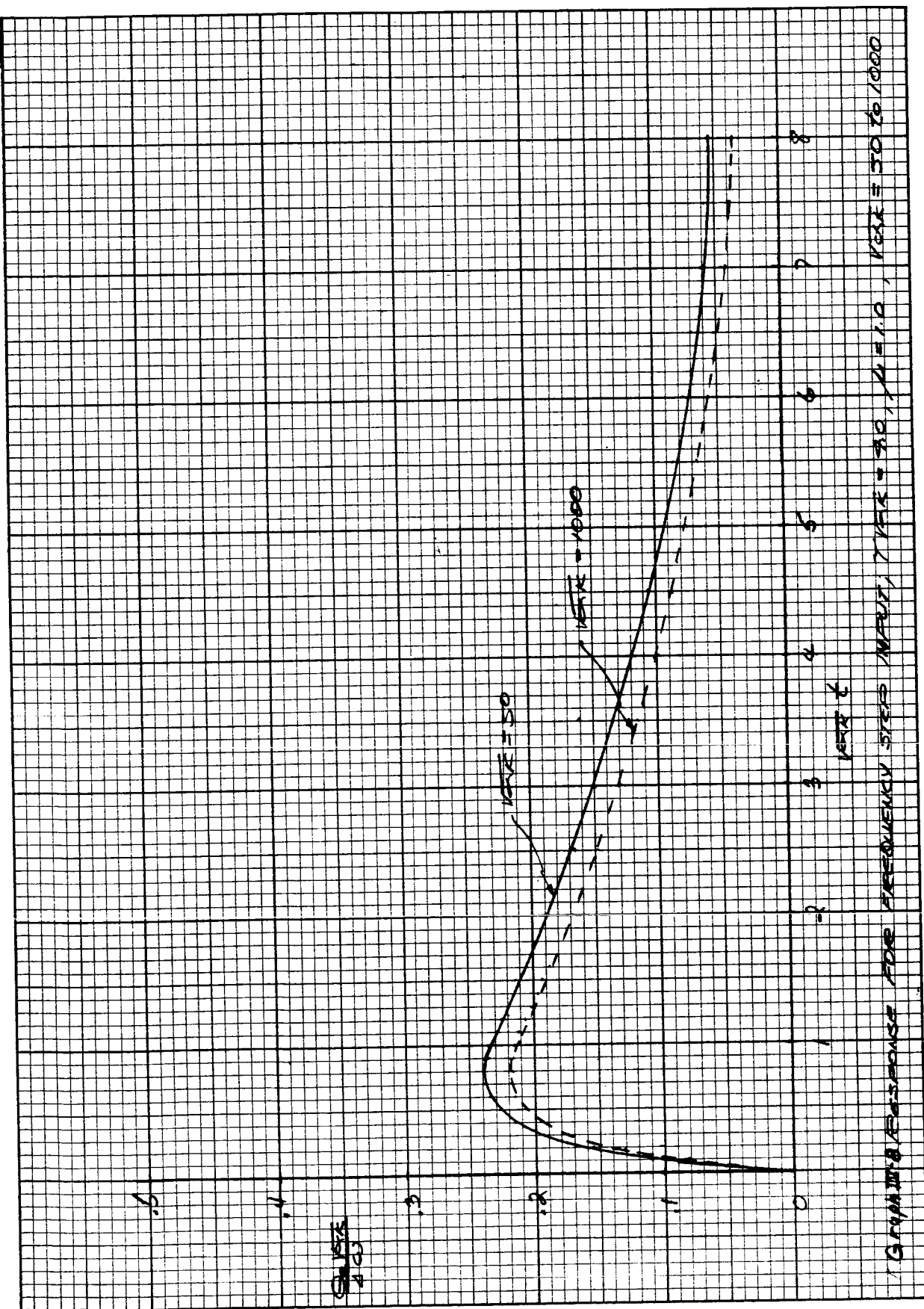
Graph II-5 RESPONSE FOR FREQUENCY STEP INPUT,  $T\sqrt{\omega K} = 1.0$  AND  $1.5$ ,  $M = 10$ ,  $\sqrt{\omega K} = 50$  To 1000.

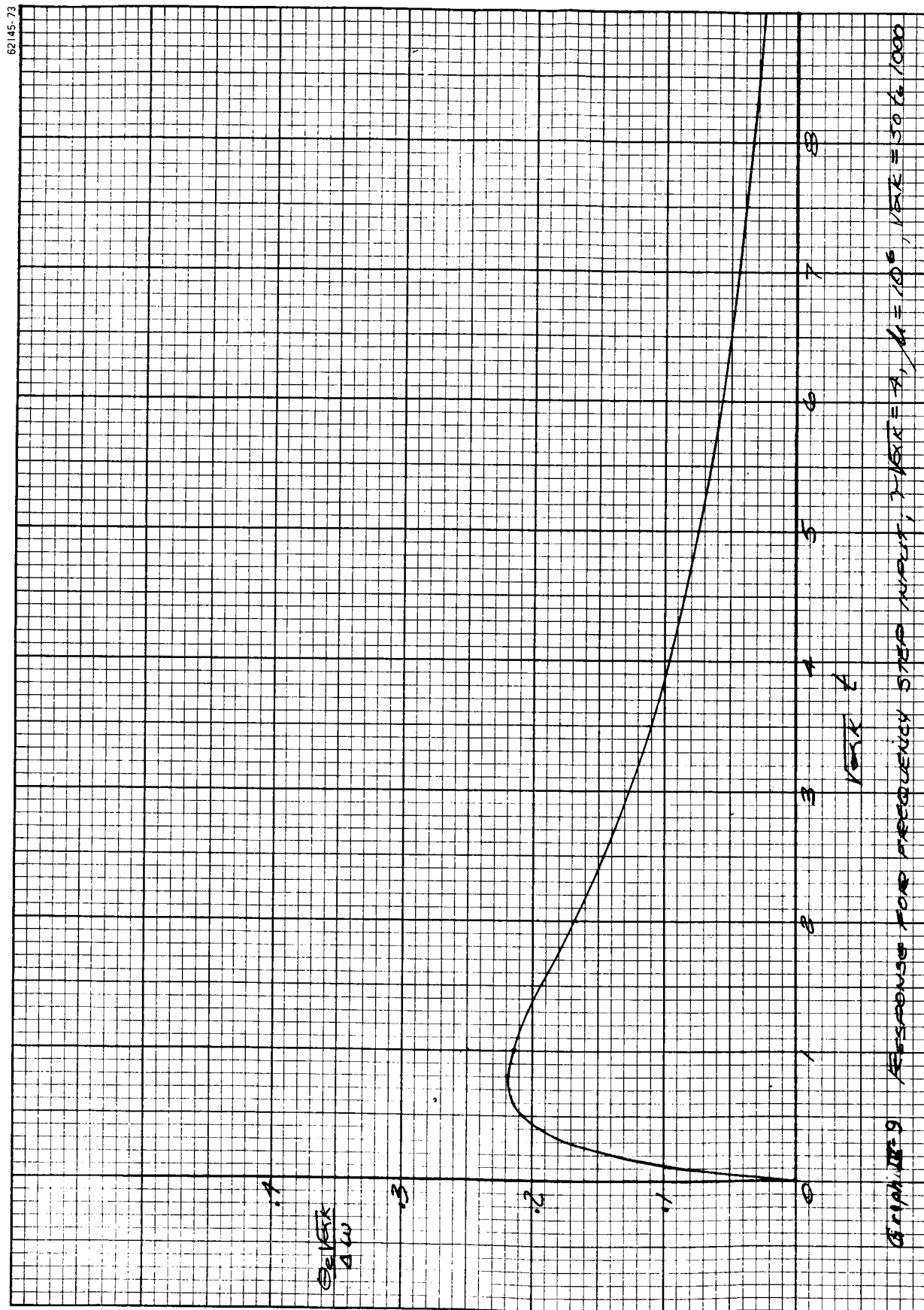


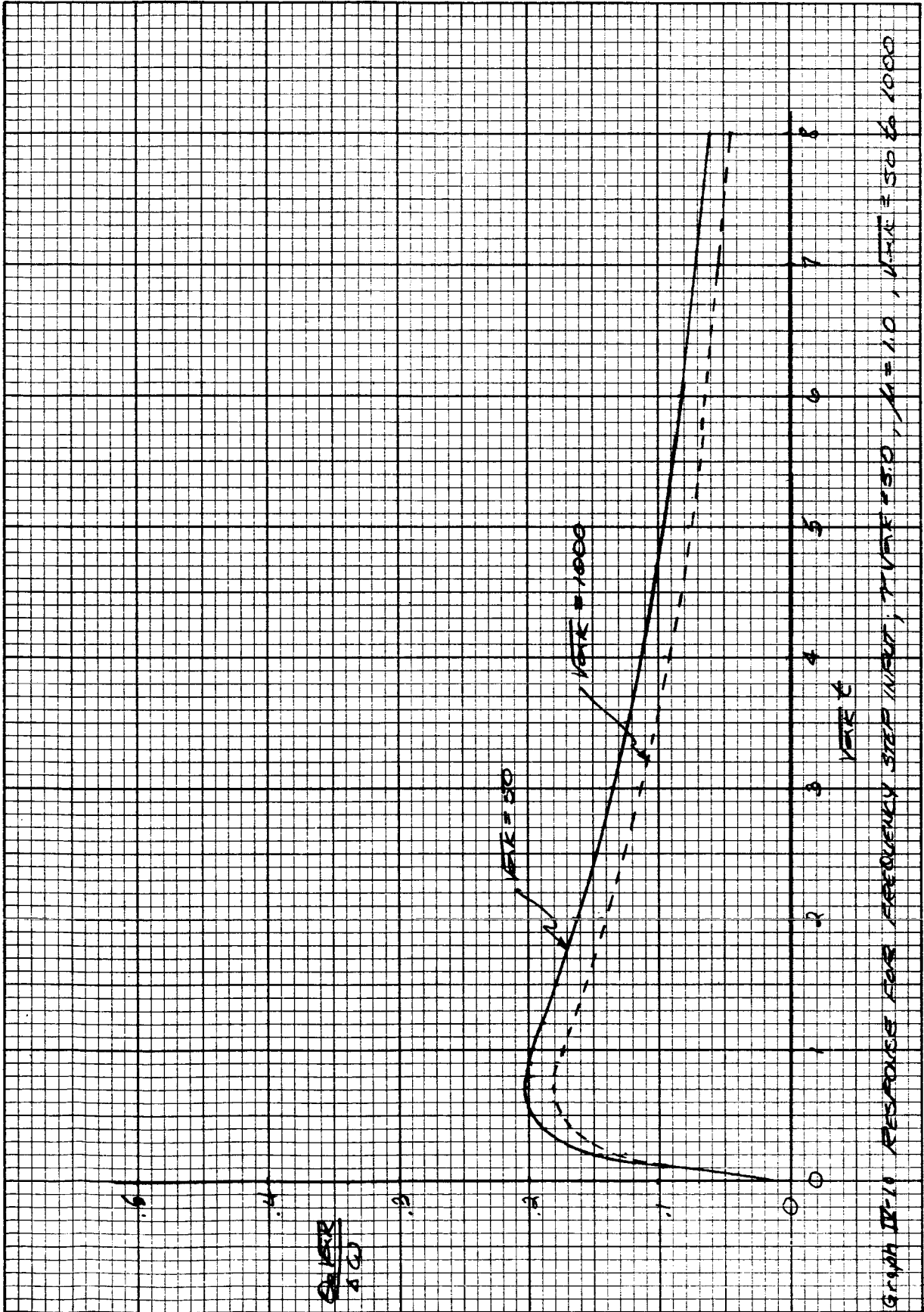
62145-71



Graph II-7 RESPONSE FOR FREQUENCY STEP INPUT;  $7/10K = 3.0$ ,  $11 = 10^4$ ,  $10K = 50$  to  $1000$

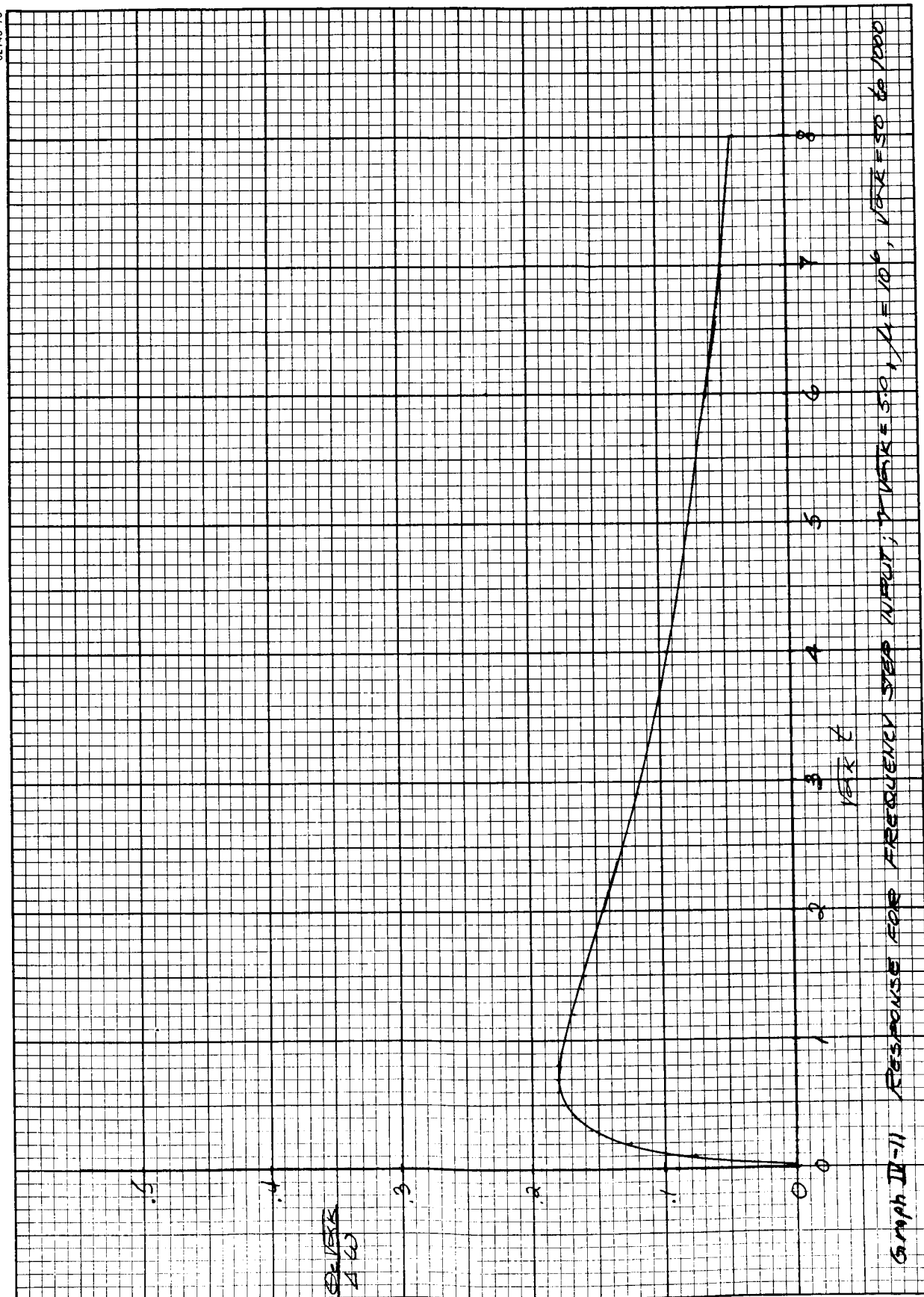






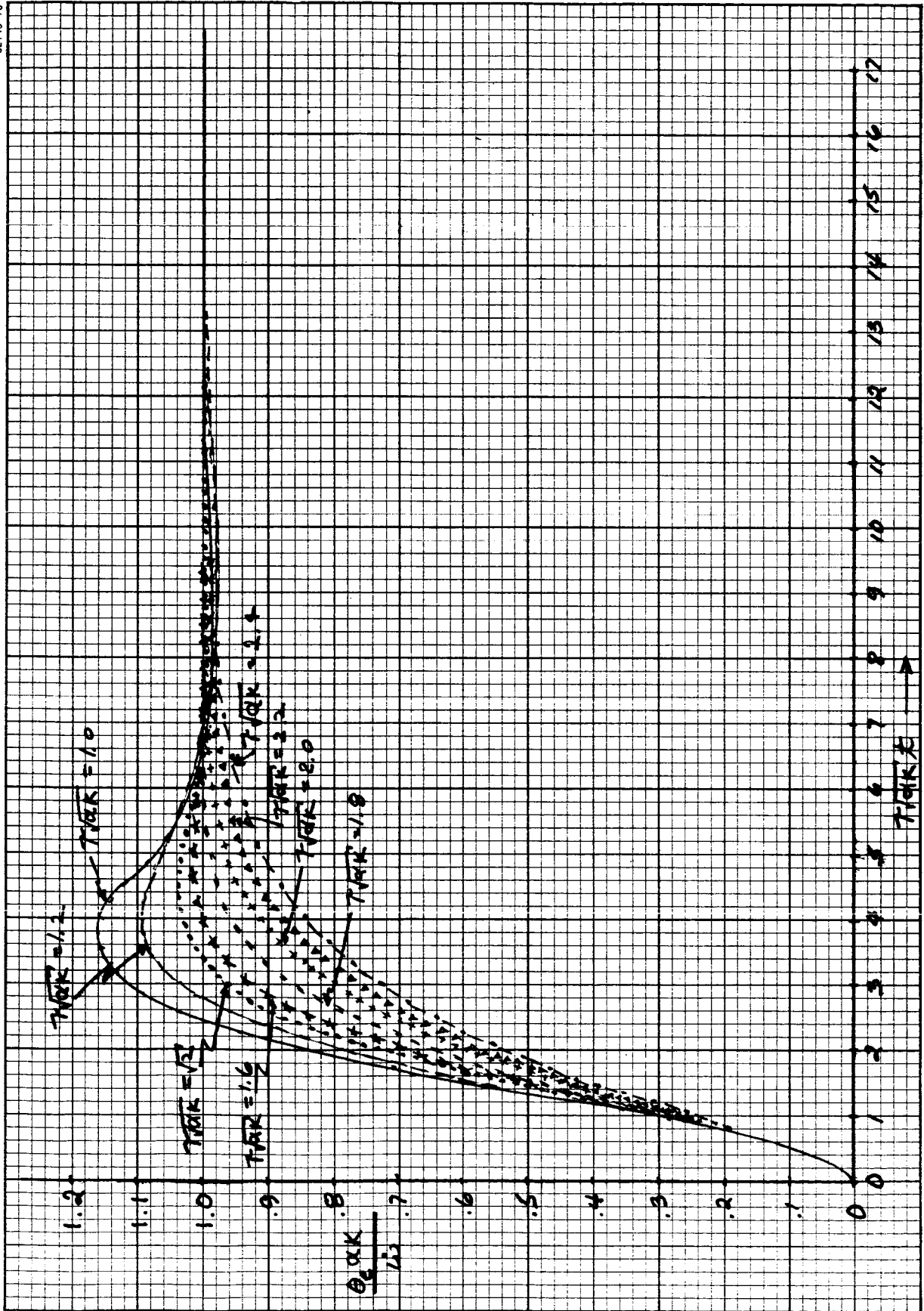


62145-75

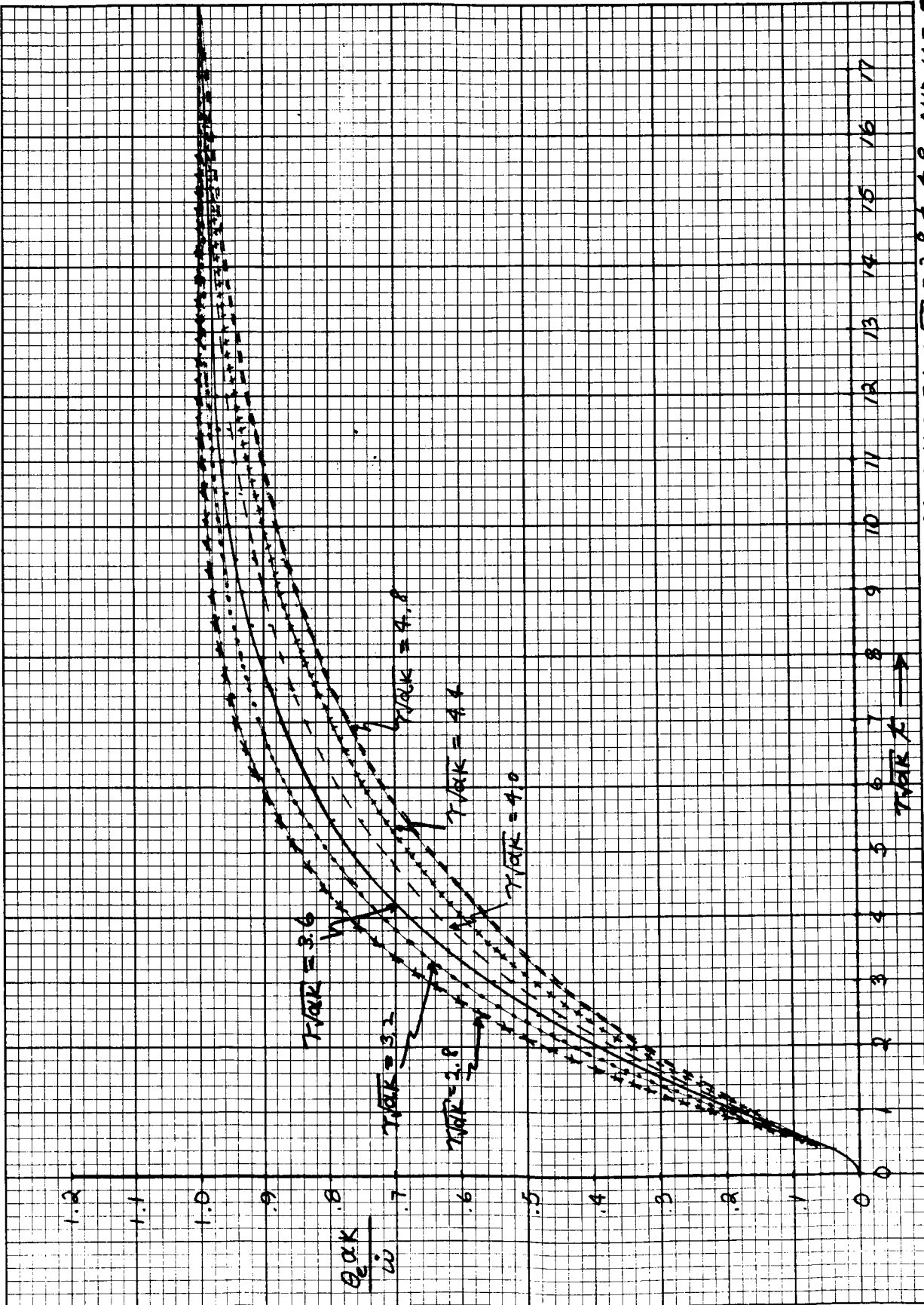


**Appendix IV**

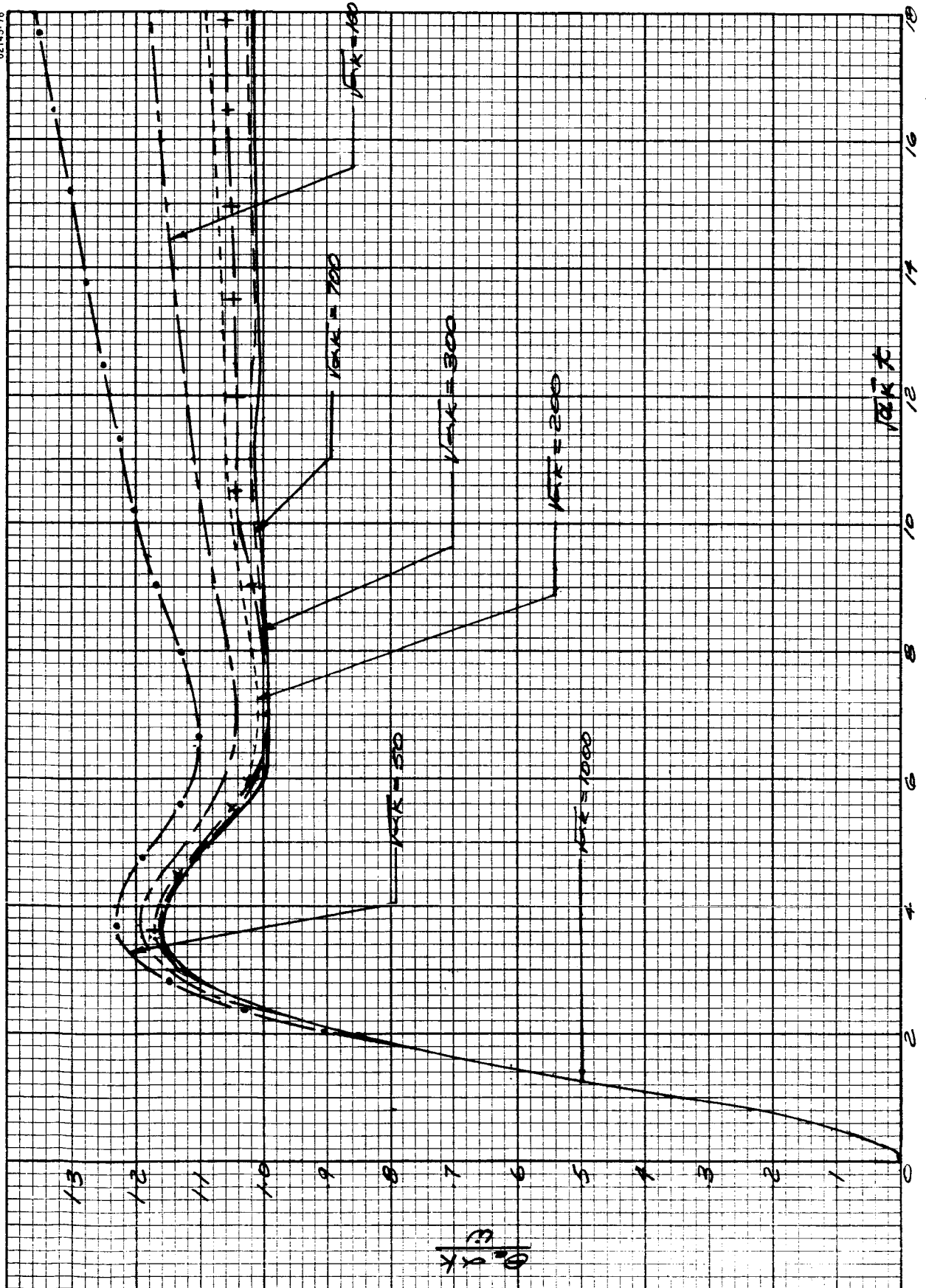
**RESPONSE FOR A FREQUENCY RAMP INPUT**



62145-77

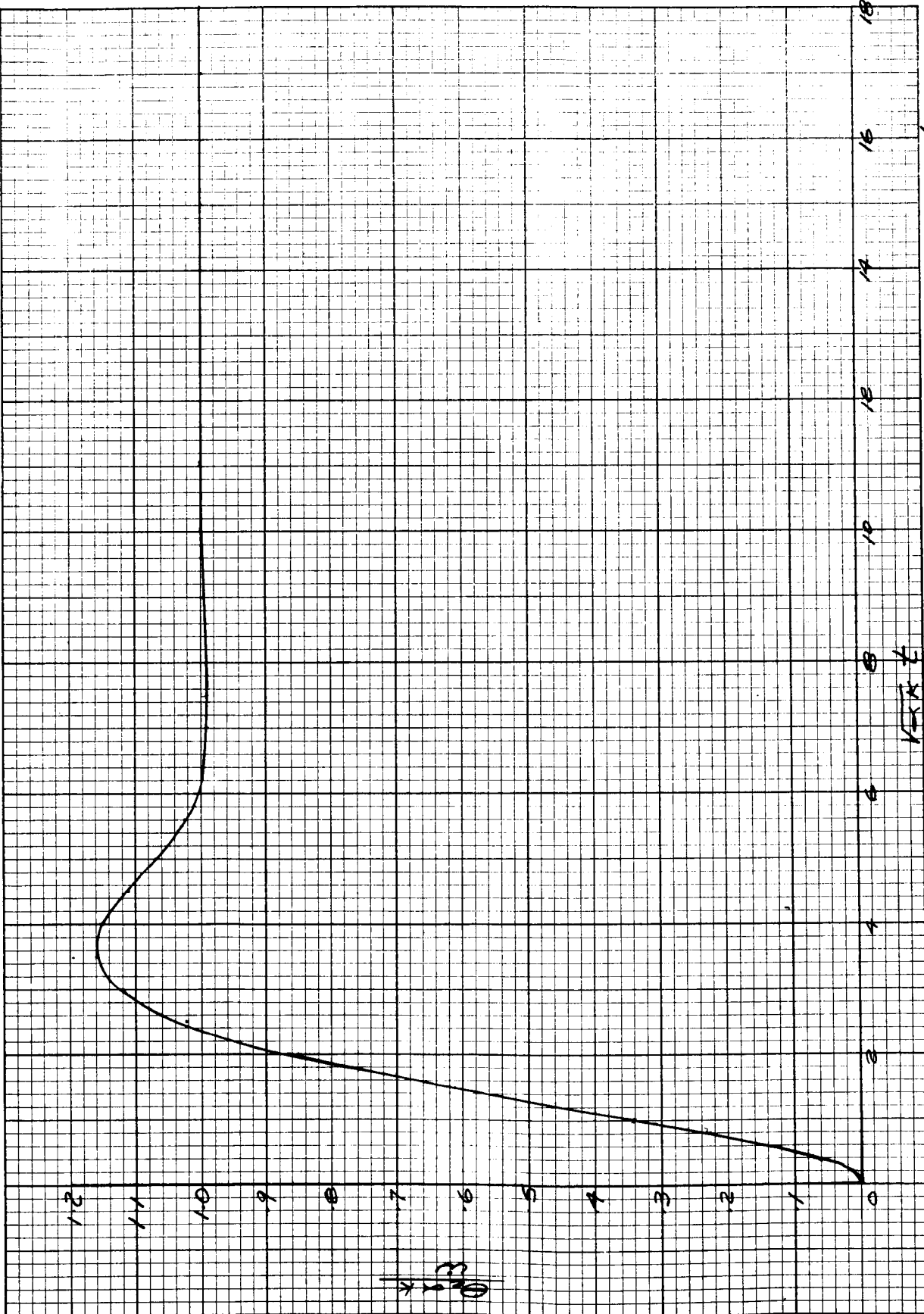


Graph IV-13 RESPONSE FOR FREQUENCY RAMP INPUT;  $\gamma/\omega_n = 2.8$  TO  $4.8$  AND  $\mu = \infty$ .

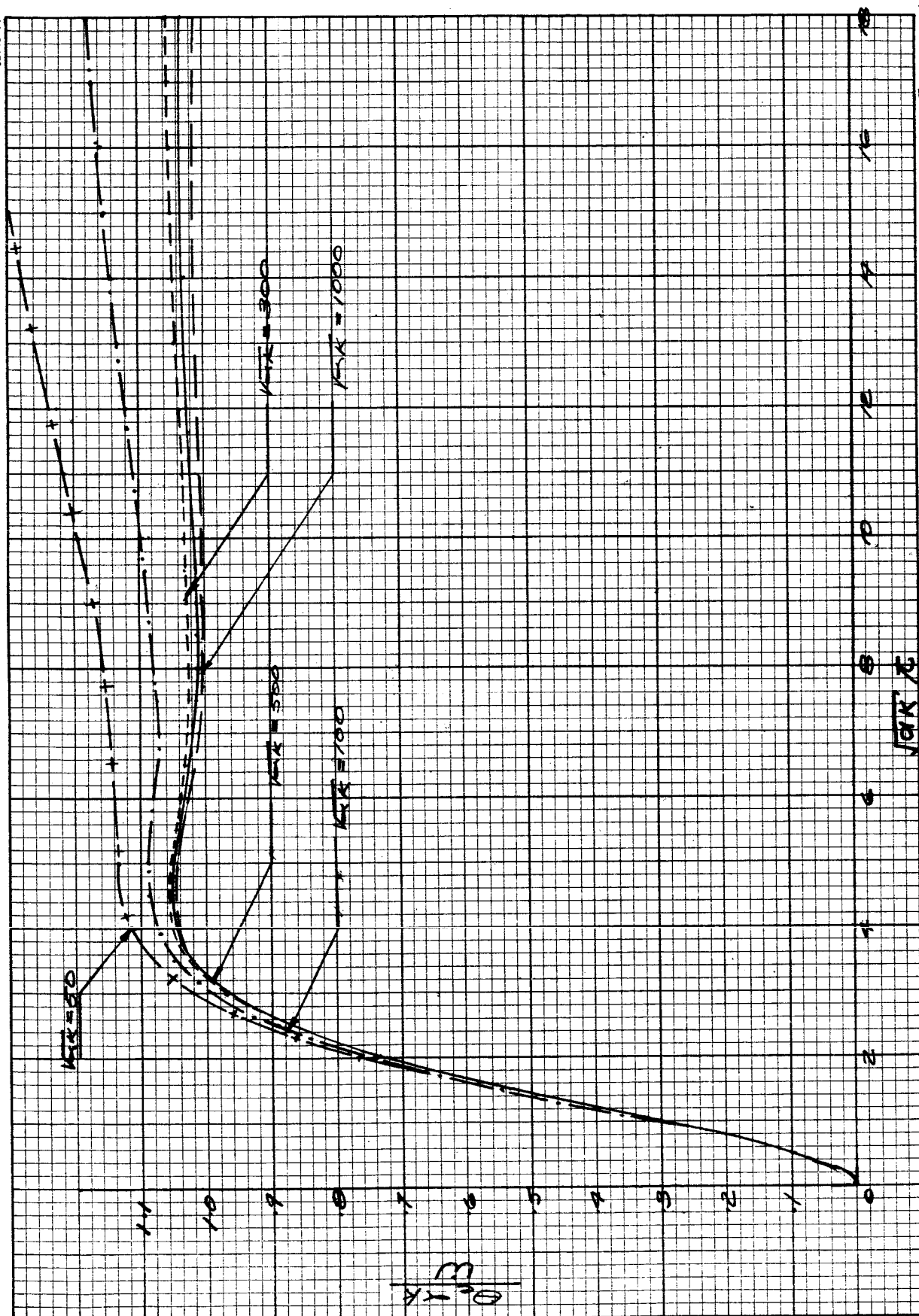


Graph III-14 RESPONSE FOR FREQUENCY RAMP INPUT;  $\gamma/\omega_n K = 1.0$ ,  $\mu = 1.0$ ,  $\sqrt{\omega_n K} = 50$  to  $1000$ .

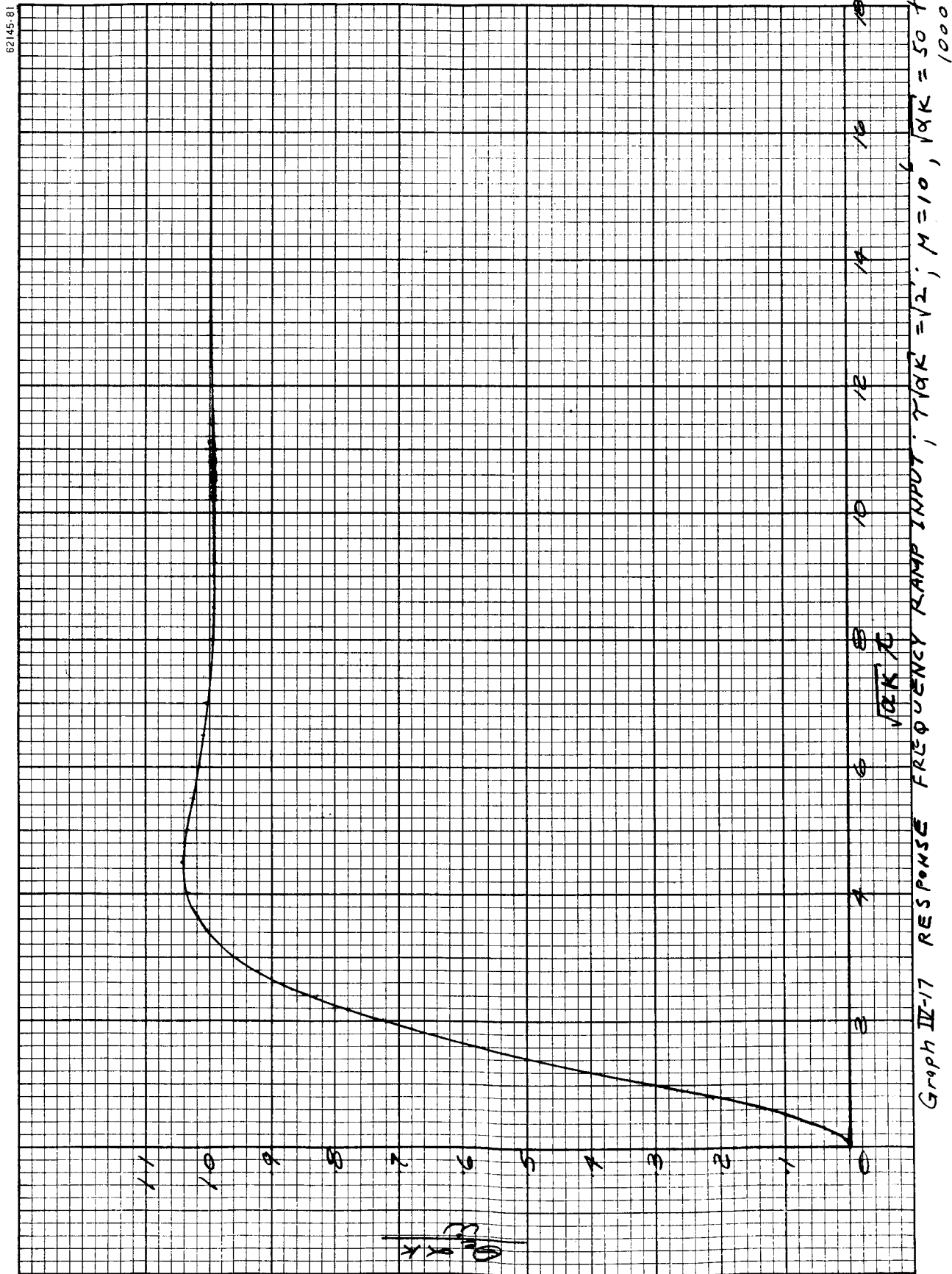
62145-79



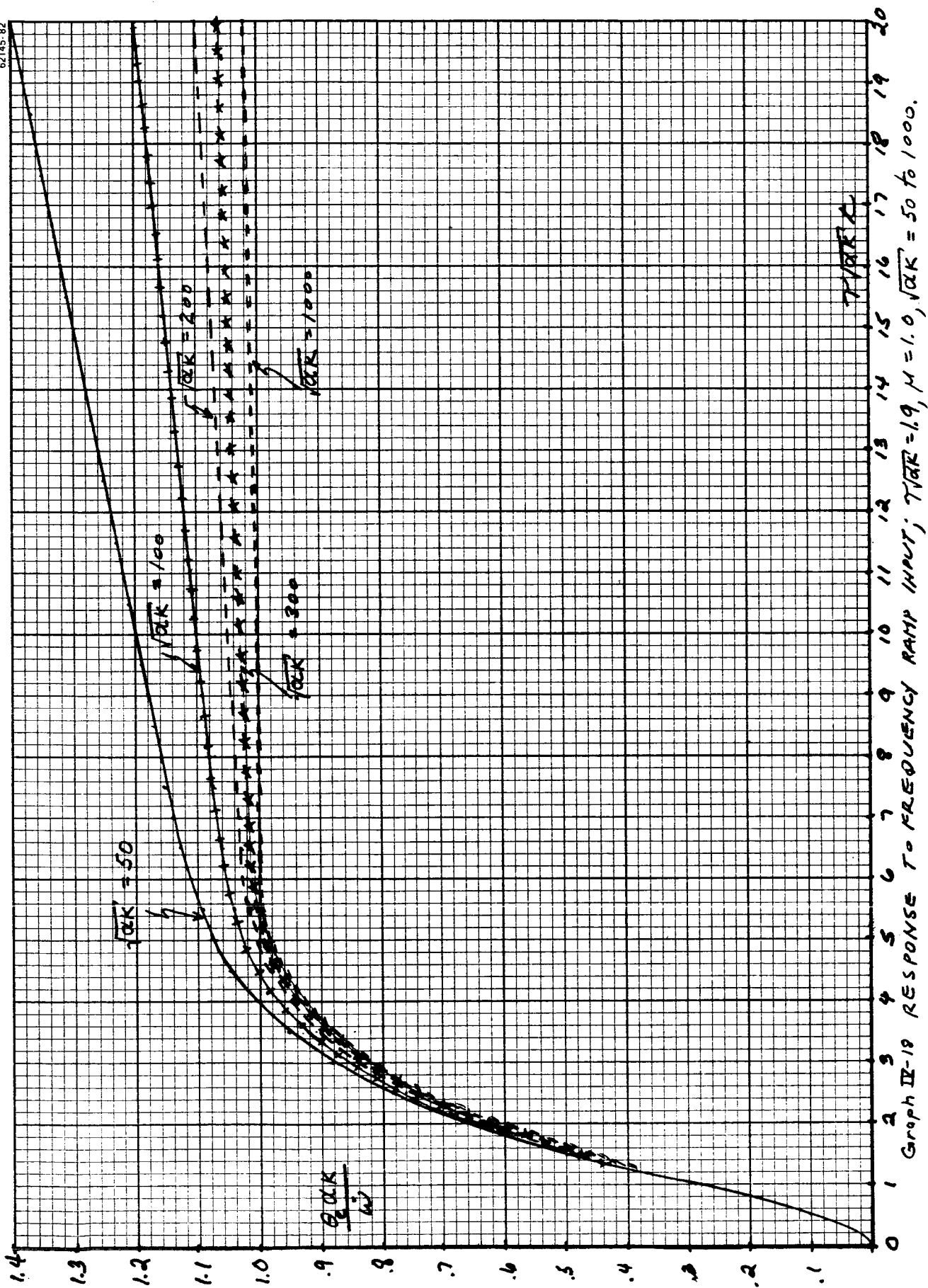
Graph II-15 RESPONSE FOR FREQUENCY RAMP INPUT;  $\gamma \sqrt{AK} = 1.0$ ,  $\mu = 10^6$ ,  $\sqrt{AK} = 50$  to 1000

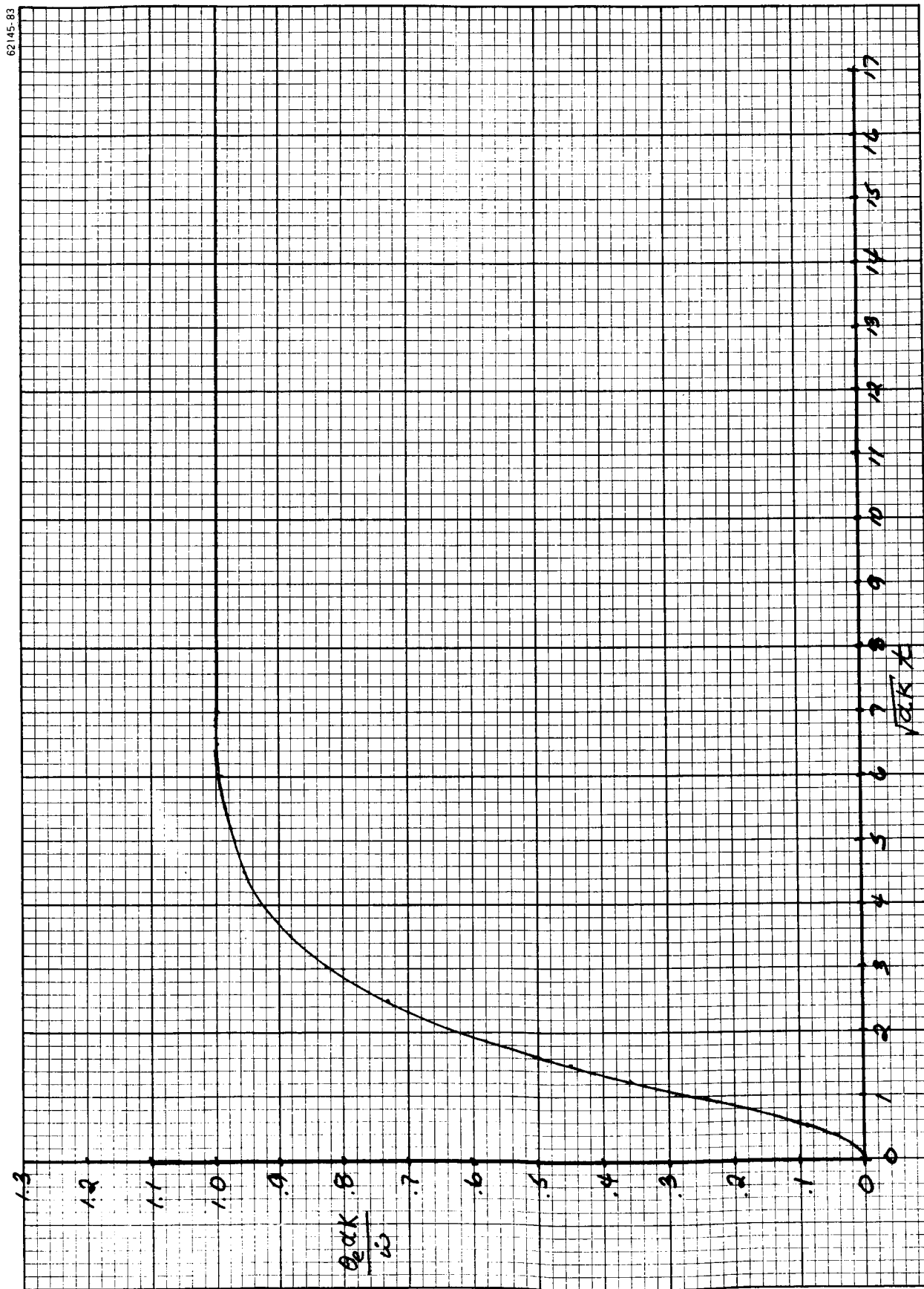


Graph IV-16 RESPONSE FOR FREQUENCY RAMP INPUT;  $T/GK = \sqrt{2}$ ,  $\mu = 1.0$ ,  $\sqrt{KR} = 50$  to 1000

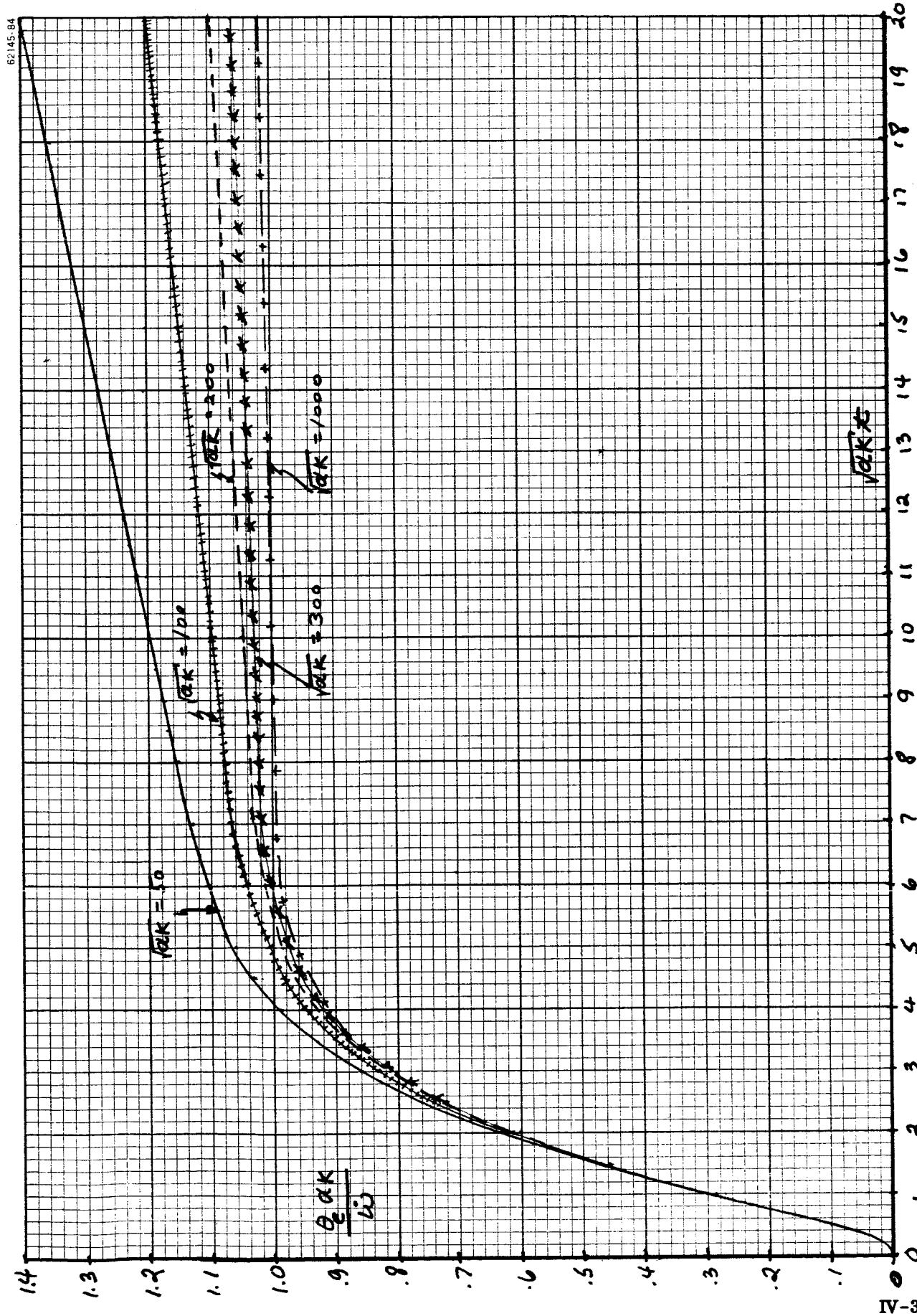




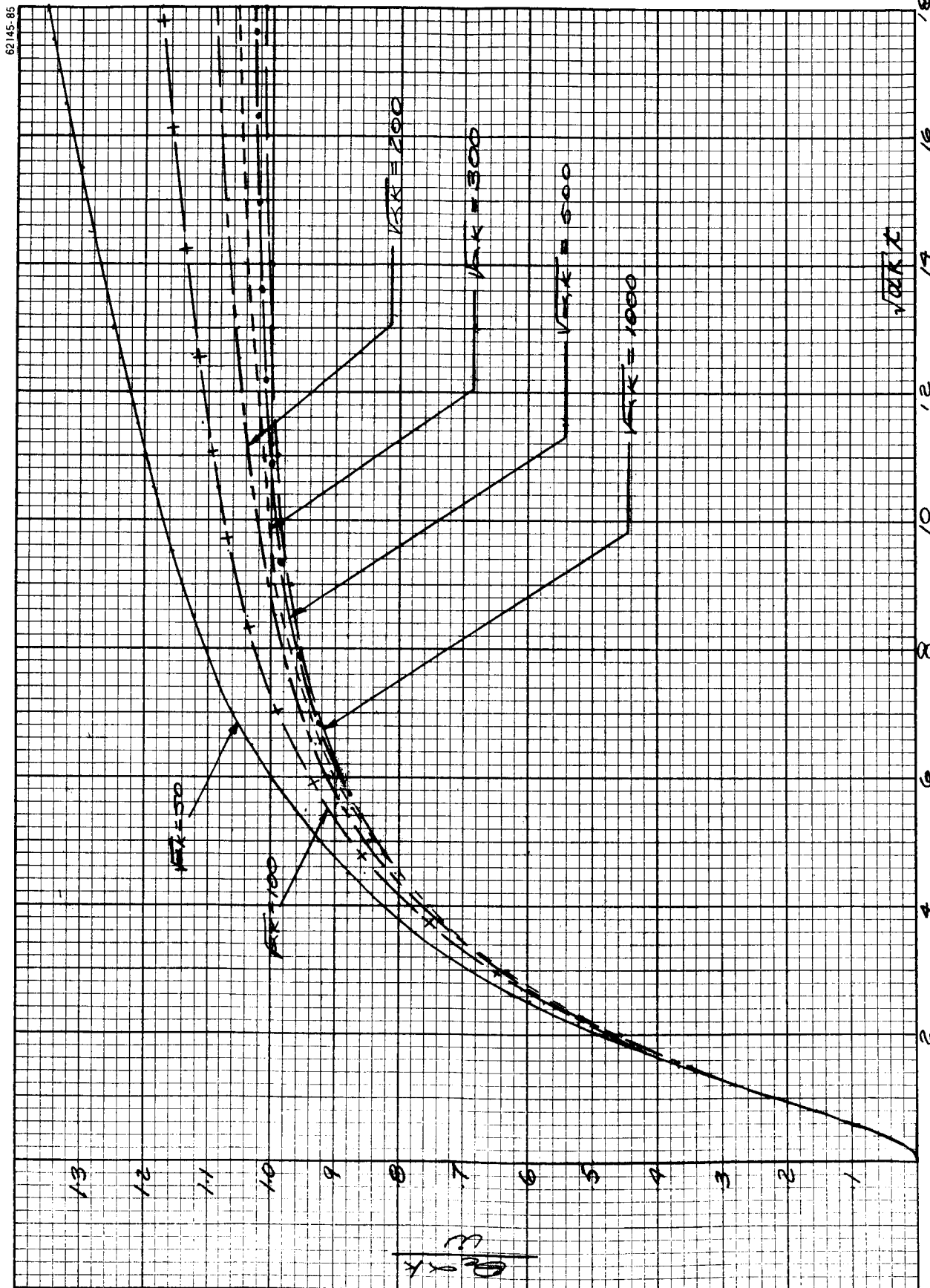


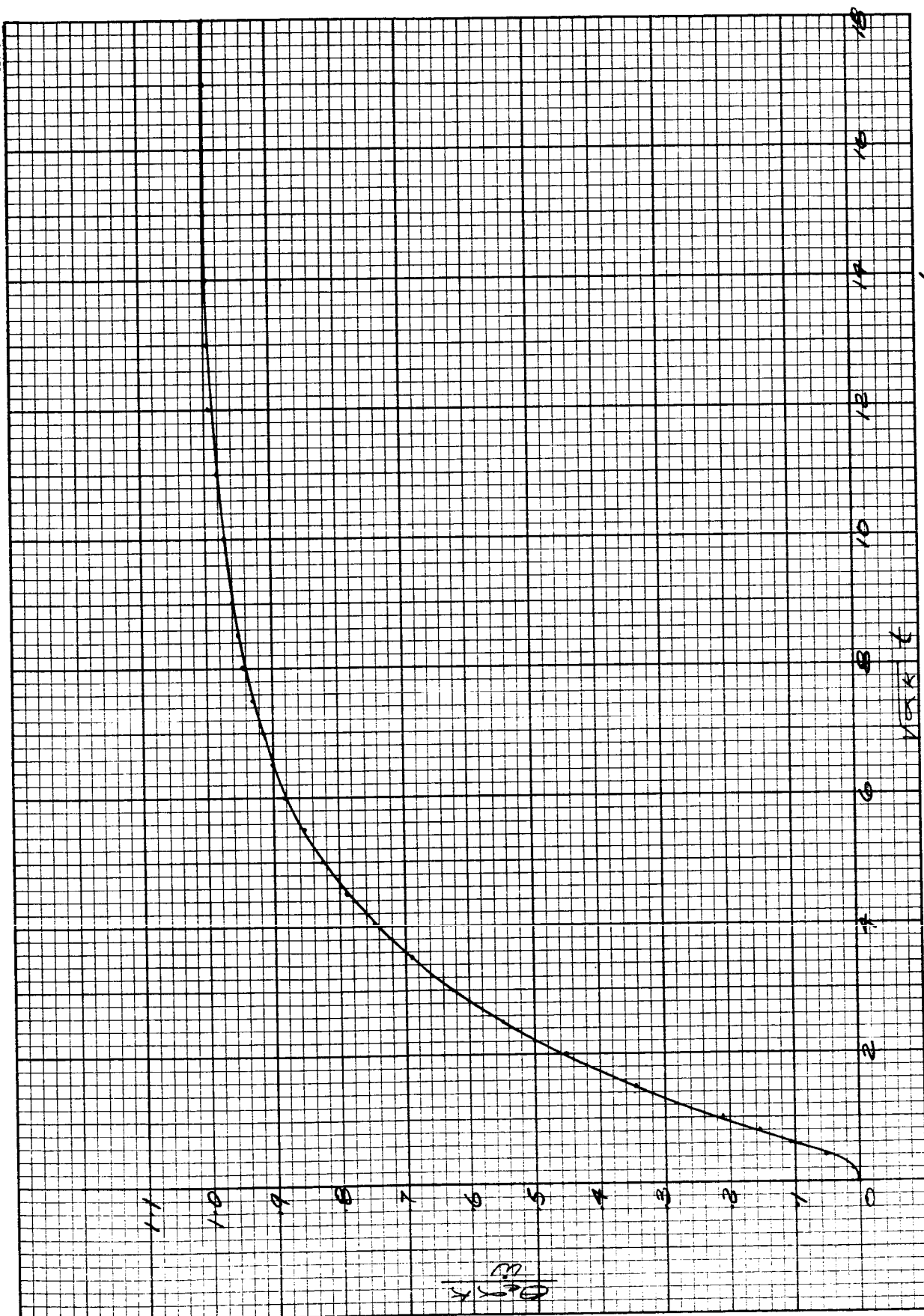


Graph II-19 RESPONSE TO FREQUENCY RAMP INPUT;  $\gamma\sqrt{OK} = 1.9$ ,  $\mu = 10^6$ ,  $\sqrt{OK} = 50$  to 1000

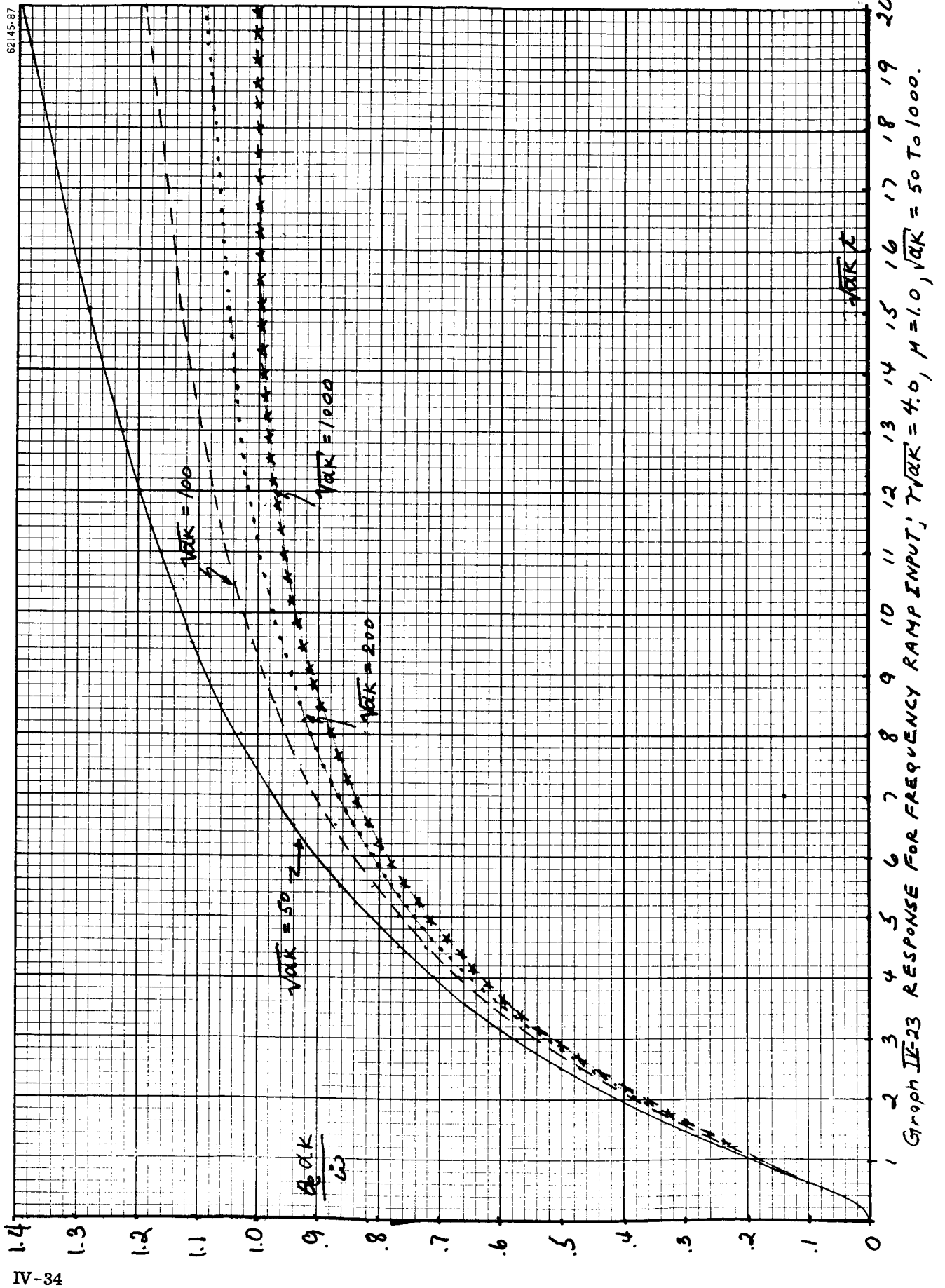


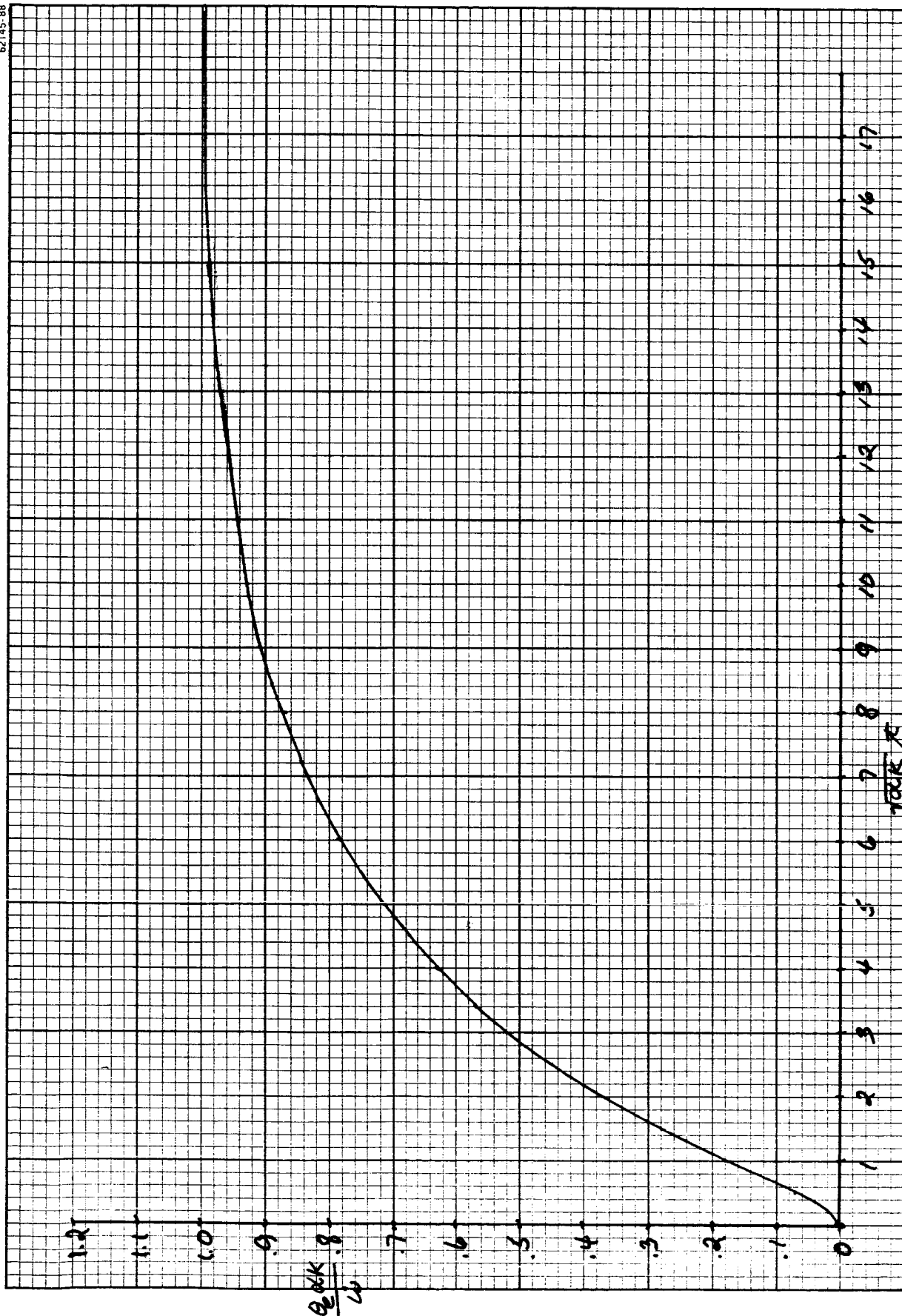
Graph IV-20 RESPONSE FOR FREQUENCY RAMP INPUT;  $\gamma/\alpha K = 2.0$ ,  $\mu = 1.0$ ,  $\sqrt{f}/\alpha K = 50$  TO  $1000$ .





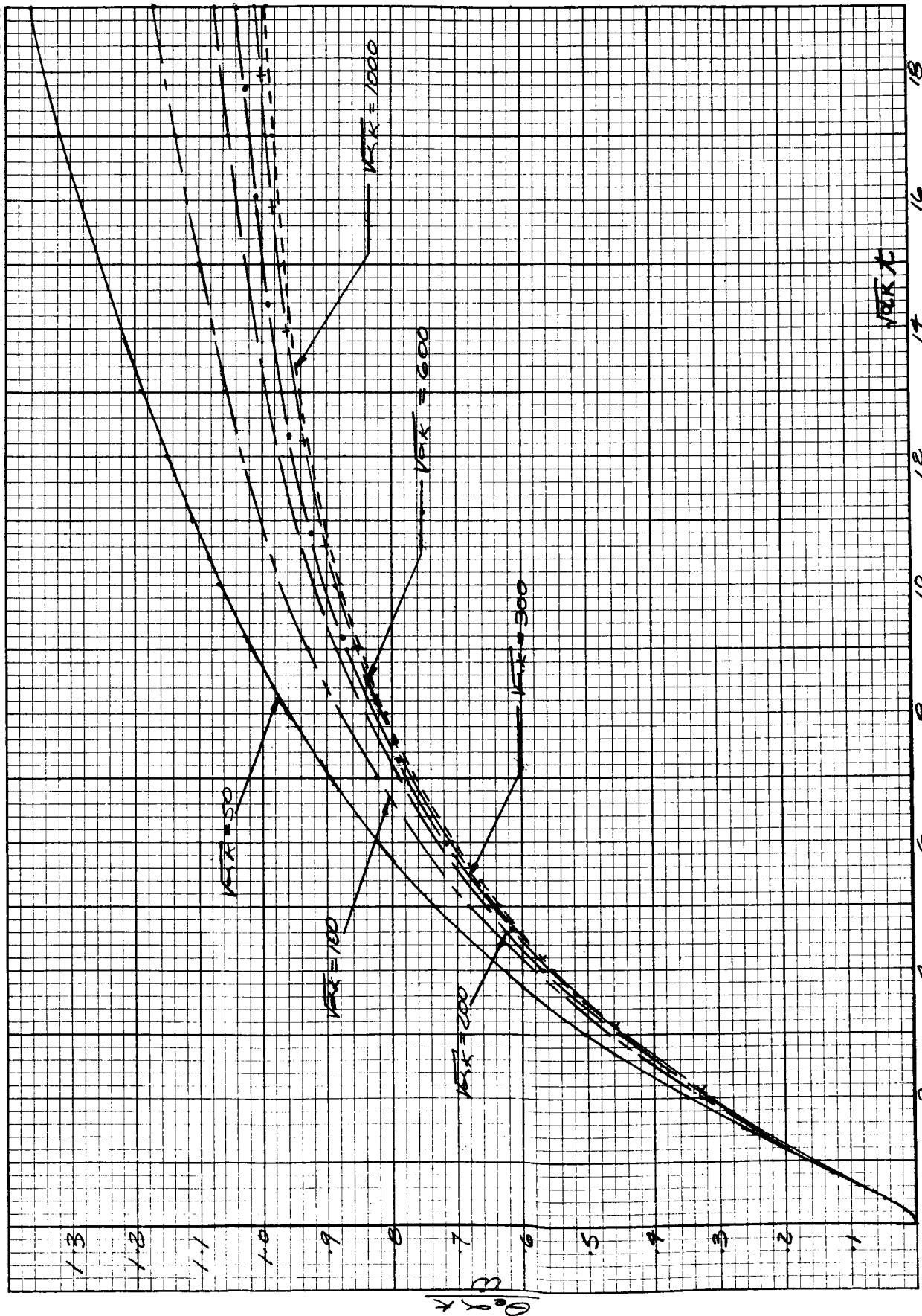
Graph IV-22 RESPONSE FOR FREQUENCY RAMP INPUT,  $\gamma\sqrt{K} = 3.0$ ,  $M = 10$ ,  $\sqrt{K}t = 50$  TO  $1000$ .





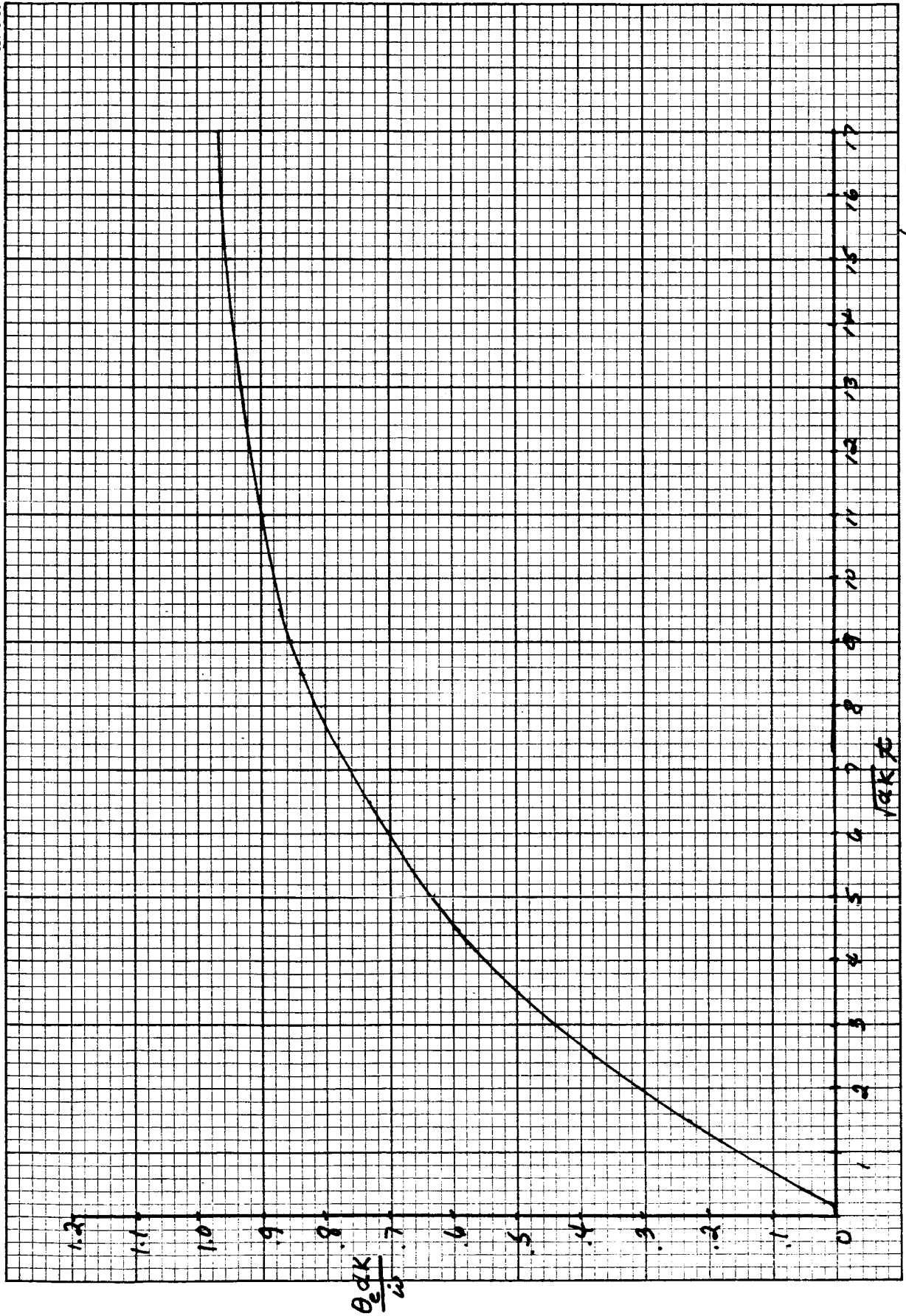
Graph II-24 RESPONSE FOR FREQUENCY RAMP INPUT,  $T_{0RK} = 4.0$ ,  $\mu = 10^6$ ,  $\sqrt{K} = 50$  TO  $1000$ .

62145-89



Graph IV-25 RESPONSE FOR FREQUENCY RAMP INPUT;  $T\sqrt{K} = 5.0$ ,  $\mu = 1.0$ ,  $\sqrt{K} = 50$  TO 1000.





Graph IV-26 RESPONSE FOR FREQUENCY RAMP INPUT;  $\gamma \sqrt{K} = 5.0$ ,  $\mu = 10^6$ ,  $\sqrt{K} \omega = 50$  TO 1000.